Measurement of flux-integrated ν_e and $\nu_e + \bar{\nu}_e$ charged-current interaction differential cross section on water

A Dissertation Presented

by

Yue Wang

to

The Graduate School

in Partial Fulfillment of the Requirements

for the Degree of

Doctor of Philosophy

in

Physics

Stony Brook University

September 2021

Stony Brook University

The Graduate School

Yue Wang

We, the dissertation committee for the above candidate for the Doctor of Philosophy degree, hereby recommend acceptance of this dissertation.

Chang Kee Jung – Dissertation Advisor
Professor, Department of Physics and Astronomy

Clark McGrew – Chairperson of Defense
Associate Professor, Department of Physics and Astronomy

Marilena Loverde
Adjunct Professor, Yang Institute of Theoretical Physic

Brett Viren
Physicist, Brookhaven National Lab

This dissertation is accepted by the Graduate School.

Abstract of the Dissertation

Measurement of flux-integrated ν_e and $\nu_e + \bar{\nu}_e$ charged-current interaction differential cross section on water

by

Yue Wang

Doctor of Philosophy

in

Physics

Stony Brook University

2021

The T2K experiment is a long base-line neutrino oscillation experiment which is designed to measure $\nu_\mu(\bar{\nu}_\mu)$ disappearance and $\nu_e(\bar{\nu}_e)$ appearance from the neutrino beam produced from a 30 GeV proton beam at J-PARC(Japan Proton Accelerator Research Complex). It consists of the J-PARC accelerator, a near detector complex (ND280) and a far detector (Super-Kamiokande). Intrinsic $\nu_e(\bar{\nu}_e)$ components in the $\nu_\mu(\bar{\nu}_\mu)$ is the major background in $\nu_e(\bar{\nu}_e)$ appearance measurement in T2K. Besides, a large systematic uncertainty in T2K $\nu_e(\bar{\nu}_e)$ appearance observation comes from uncertainties related with the neutrino cross-section modeling. Thus, in order to achieve more precise $\nu_e(\bar{\nu}_e)$ appearance measurements and to explore CP violation in the neutrino sector, the knowledge on ν_e and $\bar{\nu}_e$ interactions should be improved and the contamination of ν_e and $\bar{\nu}_e$ in the neutrino beam should be learned better. Since the far detector is a water Cherenkov detector, ν_e and $\bar{\nu}_e$ interactions measurements on water is particularly important. The design of π^0 Detector(P0D), a component of ND280, which includes fillable water bags, allows the measurement of on-water neutrino interaction cross-section. The details of selection strategies and systematic uncertainties are discussed in this thesis. A novel cross-section measurement method utilizing Markov-Chain Monte Carlo method is developed. A flux-integrated ν_e ($\nu_e + \bar{\nu}_e$) charged current interaction differential cross section on water is measured using the data collected by P0D in neutrino (anti-neutrino) beam mode. Results of both measurements are presented in this thesis.

Contents

Chapter 1

Neutrino Physics

Neutrinos are elementary particles in the Standard Model (SM). They play important roles in particle and nuclear physics, and astrophysics. W. Pauli postulated it in 1930 to explain the problem of energy conservation in beta-decay [1]. E. Fermi named it as "neutrino" in 1933 [2]. It is Italian for "little neutral one". In 1956, 26 years after Pauli proposed neutrinos, the "ghost particle" was observed for the first time in the experiment led by C. Cowan and F. Reines which used anti-electron neutrinos ($\bar{\nu}_e$) flux from a reactor. [3, 4].

1.1 Neutrinos in the Standard Model (SM)

The Standard Model is the theory which unifies strong, weak and electromagnetic interactions which are three of the four known fundamental forces in the universe. It is built based on the symmetry of $SU(3)_C \otimes SU(2)_L \otimes U(1)_Y$, where c represents color, L means left and Y is for hypercharge. $SU(3)_C$ is the color group for strong interaction and $SU(2)_L \otimes U(1)_Y$ is the symmetry for electroweak interaction. The symmetry of $SU(2)_L \otimes U(1)_Y$ is broken to be $U(1)_{EM}$ for electromagnetic interaction because of the spontaneous symmetry beaking (SSB) triggered by the vacuum expectation value (vev) of Higgs doublet as shown below.

$$SU(3)_C \otimes SU(2)_L \otimes U(1)_Y \xrightarrow{SSB} SU(3)_C \otimes U(1)_{EM} \tag{1.1}$$

There is one spin-0 boson,Hhiggs, and there are multiple spin-1 gauge fields as interaction mediators: eight massless gluons (g) for the strong interactions and one massless photon (γ) for electromagnetic interactions, and three massive bosons, charged $W^{\pm}$ and neutral Z bosons, for the weak interactions. Gluons and photon are massless as the propagators of gauge field $SU(3)_C$ and $U(1)_{EM}$, respectively, and the mass of $W^{\pm}$ and Z are obtained because of the SSB (or Higgs Mechanism in more detail) [5–7]. Besides, there are quarks and leptons which are spin-1/2 fermions and have 3 generations.

$$\begin{aligned} \text{3 generation quarks} : & \begin{pmatrix} u \\ d \end{pmatrix} \begin{pmatrix} c \\ s \end{pmatrix} \begin{pmatrix} t \\ b \end{pmatrix} \\ \text{3 generation lepton} : & \begin{pmatrix} \nu_e \\ e^- \end{pmatrix} \begin{pmatrix} \nu_\mu \\ \mu^- \end{pmatrix} \begin{pmatrix} \nu_\tau \\ \tau^- \end{pmatrix} \end{aligned} \tag{1.2}$$

The left-handed fermions are treated as doublets in math and right-handed fermions are singlets, i.e. $\begin{pmatrix} q_{uL} \\ q_{dL} \end{pmatrix}$, $\begin{pmatrix} \nu_{lL} \\ l_L^- \end{pmatrix}$,and l_R^-, q_{uR} and q_{dR}. No right-handed neutrino has been observed in any experiments, so it is not included in the SM. Figure 1.1 is the summary table of all elementary particles in SM.

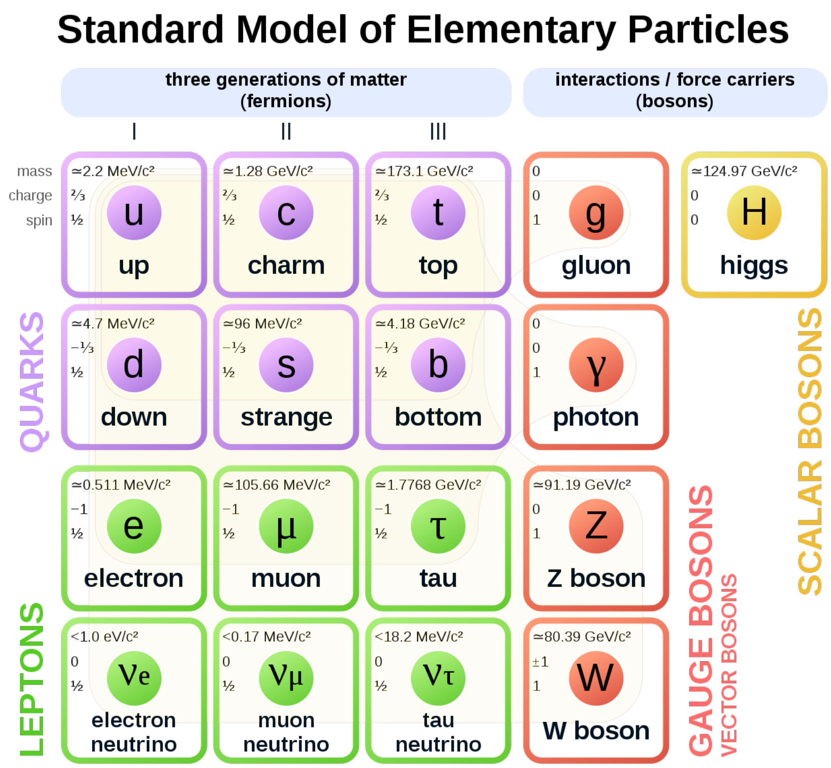

Figure 1.1: Elementary Particles in Standard Model. Figure is from [8]

More details of the electroweak interactions in SM will be introduced next. The electroweak Lagrangian can be written as the sum of three terms:

$$L = L_{\text{YM}} + L_{\text{Higgs}} + L_{\text{Y}} \tag{1.3}$$

where L_{YM} is the Yang–Mills Lagrangian for group $SU(2)_L \otimes U(1)_Y$, L_{Higgs} is the Lagrangian for Higgs and L_{Y} refers to Yukawa-Coupling.

From the Yang-Mills theory, the Lagrangian of the electroweak sector with symmetry group the $SU(2)_L \otimes U(1)_Y$ can be written as

$$L_{\mathrm{YM}} = -\frac{1}{4}W^i_{\mu\nu}W^{i\mu\nu} - \frac{1}{4}B_{\mu\nu}B^{\mu\nu} + \bar{\psi}_L i\gamma^\mu D_\mu \psi_L + \bar{\psi}_R i\gamma^\mu D_\mu \psi_R. \tag{1.4}$$

where D_μ is the covariant derivative, and $B_{\mu\nu}$ and $W^i_{\mu\nu}$ are the field strength tensor for the hypercharge and weak iso-spin group, respectively.

$$D_\mu \psi_L = (\partial_\mu + ig\tau^i W^i_\mu + ig'\frac{1}{2}Y_L B_\mu)\psi_L \tag{1.5}$$

$$D_\mu \psi_R = (\partial_\mu + ig'\frac{1}{2}Y_R B_\mu)\psi_R \tag{1.6}$$

$$B_{\mu\nu} = \partial_\mu B_\nu - \partial_\nu B_\mu \quad \text{and} \quad W^i_{\mu\nu} = \partial_\mu W^i_\nu - \partial_\nu W^i_\mu - g\epsilon_{ijk}\, W^j_\mu W^k_\nu \tag{1.7}$$

where B_μ is the gauge field of $U(1)_Y$ and W^i_μ $(i = 1,\ 2\ ,3)$ are the three $SU(2)_L$ gauge bosons. g and g' are coupling constant for $U(1)_Y$ and $SU(2)_L$, respectively. $\tau^i = \frac{1}{2}\sigma^i$ are generators of $SU(2)_L$. Gauge symmetry forbids the mass terms for gauge bosons and due to the different transformation properties of left- and right-handed fermions, the mass terms of fermions are not allowed, either.

From the last two terms in Eq 1.4, the interactions of fermions with gauge bosons are allowed via charged-current and neutral current interaction. Plug

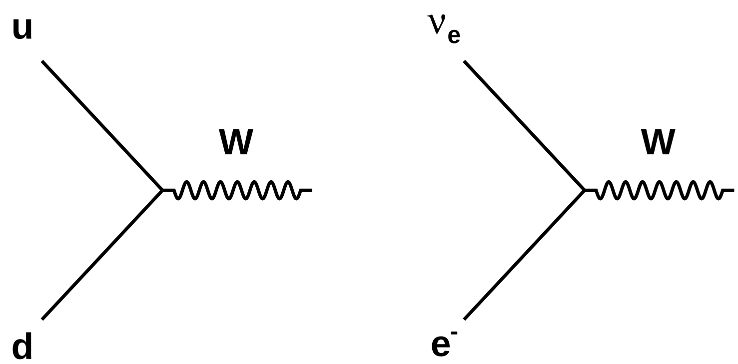

Figure 1.2: Feymann Diagram of Charged-Current Interaction Vertices

in the τ^i and the third term can be written as

$$\bar{\psi}_L i\gamma^\mu D_\mu \psi_L = \bar{\psi}_L i\gamma^\mu \partial_\mu \psi_L - \bar{\psi}_L \frac{g}{2}\gamma_\mu \begin{pmatrix} W_\mu^3 + \frac{g'}{g}B_\mu & W_\mu^1 - iW_\mu^2 \\ W_\mu^1 + iW_\mu^2 & -W_\mu^3 + \frac{g'}{g}B_\mu \end{pmatrix} \psi_L \quad (1.8)$$

For the off-diagonal terms in the matrix above, write $W_\mu^- = (W_\mu^1 + iW_\mu^2)/\sqrt{2}$ and its complex conjugate $W_\mu^+ = (W_\mu^1 - iW_\mu^2)/\sqrt{2}$. Remember that ψ_L is a doublet. For simplicity, use the first generation of fermions, $\begin{pmatrix} u_L \\ d_L \end{pmatrix}$ and $\begin{pmatrix} \nu_{eL} \\ e_L^- \end{pmatrix}$ as an example. The part of the Lagrange obtained from the off-diagonal term can be written as

$$L_{CC} = -\frac{g}{\sqrt{2}}\left\{W_\mu^\dagger[\bar{u}_L\gamma^\mu d_L + \bar{\nu}_{eL}\gamma^\mu e_L] + h.c.\right\} \quad (1.9)$$

which is the interaction named as Charge-Current (CC) interaction. Figure 1.2 shows the Feymann diagram for the CC vertices. For the diagonal term,

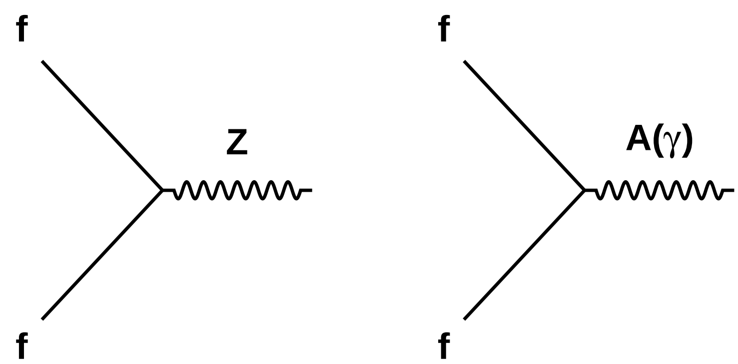

Figure 1.3: Feymann Diagram of Neutral-Current Interaction Vertices. Because γ often refers to the EM interactions, neutral-current in later chapters in this thesis only refers to the exchange of Z boson.

define $\tan\theta_\mathrm{W} = \frac{g'}{g}$ and a transformation

$$\begin{pmatrix} Z_\mu \\ A_\mu \end{pmatrix} = \begin{pmatrix} \cos\theta_W & -\sin\theta_W \\ \sin\theta_W & \cos\theta_W \end{pmatrix} \begin{pmatrix} W^3_\mu \\ B_\mu \end{pmatrix} \tag{1.10}$$

and then combine the part from diagonal term above with the term $\bar{\psi}_R i\gamma^\mu D_\mu \psi_R$, the Neutral Current (NC) interaction term can be obtained

$$L_{NC} = -\bar{\psi}^\mu_j \left\{ A_\mu (g\frac{\sigma^3}{2}\sin\theta_W + g' y_j \cos\theta_W) + Z_\mu (g\frac{\sigma^3}{2}\cos\theta_W - g' y_j \sin\theta_W)\psi_j \right\} \tag{1.11}$$

Figure 1.3 shows the Feymann diagram of the vertices

By far, the fermions, W and Z bosons are massless. However, experiment results have shown that quarks and charged leptons are massive. Thus, the Higgs term and Yukawa-coupling are added into the model.

Consider a $SU(2)_L$ doublet of a scalar field $\phi = \begin{pmatrix} \phi^+ \\ \phi^0 \end{pmatrix}$,

$$L_{\text{Higgs}} = (D_\mu \phi)^\dagger (D^\mu \phi) - \mu^2 \phi^\dagger \phi + \lambda(\phi^\dagger \phi)^2 \tag{1.12}$$

where $\mu^2 < 0$, $\lambda > 0$ and

$$D^\mu \phi = (\partial_\mu + ig\tau^i W_\mu^i + ig'\frac{1}{2} Y_\phi B_\mu)\phi \tag{1.13}$$

The minimum potential occurs at $|\phi| = \sqrt{\frac{\mu^2}{2\lambda}} \equiv \frac{v}{\sqrt{2}}$, where v is the vacuum expectation value (vev). Parameterize the scalar doublet into a general form

$$\phi(x) = \exp(i\frac{\sigma^i}{2}\theta^i(x))\frac{1}{\sqrt{2}} \begin{pmatrix} 0 \\ v + H(x) \end{pmatrix} \tag{1.14}$$

Then the term with covariant derivative in eq 1.12 becomes

$$D_\mu \phi^\dagger D^\mu \phi \xrightarrow{\theta^i = 0} \frac{1}{2}\partial_\mu H \partial^\mu H + (v + H)^2 \left\{ \frac{g^2}{4} W_\mu^\dagger W^\mu + \frac{g^2}{8\cos{\theta_W}^2} Z_\mu Z^\mu \right\} \tag{1.15}$$

The term v in eq 1.15 creates the mass term for $W^\pm$ and Z bosons and the predicted masses are

$$M_W = \frac{vg}{2} \qquad M_Z = \frac{vg}{2\cos\theta_W} \tag{1.16}$$

The masses of $W^\pm$ and Z bosons have been measured in experiments and the measured value agrees with the predicted masses (see summary in [9, 10]). Higgs boson has also been discovered [11, 12].

The Yukawa-coupling term decribes the interactions between fermions and the Higgs boson.

$$L_Y = -y^j(\bar{\psi}_L \phi \psi_R + \bar{\psi}_R \phi \psi_L) \tag{1.17}$$

where y_j is the coupling constant for each fermion. Again. use the first generation of fermions as an example.

$$\begin{aligned} L_Y = & - y^1 (\bar{u}_L \quad \bar{d}_L) \begin{pmatrix} \phi^+ \\ \phi^0 \end{pmatrix} d_R - y^2 (\bar{u}_L \quad \bar{d}_L) \begin{pmatrix} \phi^{0*} \\ -\phi^- \end{pmatrix} u_R \\ & - y^3 (\bar{\nu}_{eL} \quad \bar{e}_L) \begin{pmatrix} \phi^+ \\ \phi^0 \end{pmatrix} e_R + h.c. \end{aligned} \tag{1.18}$$

As mentioned before, because no right-handed neutrinos have been observed, they are not included in SM. As a result, there is no Yukawa-coupling term related to right-handed neutrino. Like before

$$L_Y \xrightarrow{\theta^i=0} L_Y = -\frac{1}{\sqrt{2}}(v+H)(y^1 \bar{d}_L \bar{d}_R + y^2 \bar{u}_L \bar{d}_u + y^3 \bar{e}_L \bar{e}_R) \tag{1.19}$$

The term v generates the mass terms for fermions, $-\frac{v}{\sqrt{2}}(y^1 \bar{d}_L \bar{d}_R + y^2 \bar{u}_L \bar{u}_R + y^3 \bar{e}_L \bar{e}_R)$. Thus, the predicted masses for the first generation of fermions are

$$m_u = \frac{y^2 v}{\sqrt{2}}, \qquad m_d = \frac{y^1 v}{\sqrt{2}}, \qquad m_e = \frac{y^3 v}{\sqrt{2}}, \qquad m_{\nu_e} = 0 \tag{1.20}$$

Because there is only left-handed neutrinos in the SM, there is no mass terms from Yukawa-coupling for neutrinos. Thus the neutrino is massless in the SM.

Overall, neutrinos in the SM have 3 flavours, ν_e, ν_μ and ν_τ, and are neutral and massless. They interact with matters through weak interactions only in the SM.

1.2 Neutrino Oscillation

The SM was developed in the early 1970s and since then, it has successfully explained almost all experimental results and predicted a lot of phenomena. It is the most successful theory by far to describe the subatomic world. However, as discussed above, the SM predicts that neutrinos are massless, but it has been proved to be wrong by the neutrino oscillation experiments. Neutrino oscillation is very important as it is one of the very few measurable phenomena at this moment that is beyond the SM.

1.2.1 Theory

Pontecorvo hypothesized that neutrinos may oscillate from one flavour to another, suggesting that neutrino mass states are different than their flavour states [13]. In 1998, the Super-Kamiokande experiment measured evidence for oscillations of atmospheric neutrinos [14]. In 2002, the SNO (Sudbury Neutrino Observatory) experiment also provided strong evidence of neutrino oscillations for the solar neutrinos [15]. Together the results from Super-Kamiokande and SNO show the strong evidence for neutrino oscillations. The Nobel Prize in physics in 2015 has been awarded to T. Kajita (Super-Kamiokande Collaboration) and A. B. McDonald (SNO Collaboration) for the discovery of neutrino oscillations. Neutrino oscillations suggest that neutrinos are not massless and have non-degenerate mass eigenstates, which is beyond the SM.

The theory of neutrino oscillation is developed by Maki, Nakagawa and Sakata [16] and Pontecorvo [13]. The PMNS matrix (Pontecorvo-Maki-Nakagawa-Sakata) named by them is used in formalised theory for neutrino oscillation. The flavour eigenstates ($|\nu_\alpha\rangle, = e, \mu, \tau$) are the states that neutrinos are generated via weak interactions. Considering that if the neutrinos are not massless, then neutrinos propagate via mass eigenstates ($|\nu_k\rangle,\ k = 1, 2, 3$). The flavour eigenstates can be expressed as linear superposition of the mass eigenstates:

$$|\nu_\alpha\rangle = \sum_k U^*_{\alpha k} |\nu_k\rangle \tag{1.21}$$

where $\alpha = e, \mu, \tau$ and $k = 1, 2, 3$ while U is the PMNS matrix which is unitary. An unitary matrix can be parametrized as

$$U = \begin{pmatrix} 1 & 0 & 0 \\ 0 & c_{23} & s_{23} \\ 0 & -s_{23} & c_{23} \end{pmatrix} \begin{pmatrix} c_{13} & 0 & s_{13}e^{-i\delta_{CP}} \\ 0 & 1 & 0 \\ -s_{13}e^{i\delta_{CP}} & 0 & c_{13} \end{pmatrix} \begin{pmatrix} c_{12} & s_{12} & 0 \\ -s_{12} & c_{12} & 0 \\ 0 & 0 & 1 \end{pmatrix} \begin{pmatrix} e^{i\alpha} & 0 & 0 \\ 0 & e^{i\beta} & 0 \\ 0 & 0 & 1 \end{pmatrix} \tag{1.22}$$

where $c_{ij} = \cos\theta_{ij}$ and $s_{ij} = \sin\theta_{ij}$. The two phases in last term which is diagonal is called Majorana phase which won't affect the neutrino oscillation probability as shown below.

Assume the neutrino travels in vacuum for now. The time evolution of a state $|\nu_\alpha(t = 0)\rangle = |\nu_\alpha\rangle$ is:

$$|\nu_\alpha(t)\rangle = e^{-iHt}|\nu_\alpha\rangle = \sum_k U^*_{\alpha k} e^{-iE_k t} |\nu_k(t = 0)\rangle \tag{1.23}$$

where E_k is the eigenvalue of the eigenstate $|\nu_k\rangle$.

The amplitude for a flavour change $\nu_\alpha \to \nu_\beta$ after time t is given by

$$A(\nu_\alpha \to \nu_\beta)(t) = \langle \nu_\beta | \nu(t) \rangle = \sum_k U^*_{\alpha k} U_{\beta k} e^{-iE_k t}. \tag{1.24}$$

and therefore the probability can be written as

$$P(\nu_\alpha \to \nu_\beta) \;=\; |A(\nu_\alpha \to \nu_\beta)|^2 = \sum_{k,j} U^*_{\alpha k} U_{\beta k} U_{\alpha j} U^*_{\beta j} e^{-i(E_k - E_j)t} \tag{1.25}$$

Because the neutrino travels ultra-relativistic and the mass of neutrino is expected to be very small, the energy can be approximately written as

$$E_k = \sqrt{p_k^2 + m_k^2} \approx E + \frac{m_k^2}{2E}, \qquad \text{if } |p_k| >> m_k \tag{1.26}$$

where E is the energy of the neutrino. Thus, Eq 1.25 can be re-written as:

$$P(\nu_\alpha \to \nu_\beta) = \sum_{k,j} U^*_{\alpha k} U_{\beta k} U_{\alpha j} U^*_{\beta j} \exp\left(-i\frac{\Delta m^2_{kj} L}{2E}\right). \tag{1.27}$$

where $\Delta m^2_{kj} = m_k^2 - m_j^2$. After plugging the PMNS matrix, Eq 1.27 becomes

$$\begin{aligned} P \quad (\nu_\alpha \to \nu_\beta) &= \delta_{\alpha\beta} - 4\sum_{k>l=1}^{3} \mathrm{Re}\left(U_{\alpha k} U^*_{\beta k} U^*_{\alpha l} U_{\beta l}\right) \sin^2\left(\frac{\Delta m^2_{kl} L}{4E}\right) \\ + \quad & 4\sum_{k>l=1}^{3} \mathrm{Im}\left(U_{\alpha k} U^*_{\beta k} U^*_{\alpha l} U_{\beta l}\right) \sin\left(\frac{\Delta m^2_{kl} L}{4E}\right) \cos\left(\frac{\Delta m^2_{kl} L}{4E}\right) \end{aligned} \tag{1.28}$$

By far, it is assumed that neutrino travels in vacuum which is not true when neutrino travels through the sun, supernova or earth. MSW (Mikheyev – Smirnov – Wolfenstein) effect attempts to take into account the matter effect and modify the oscillation probability by adding effective potential terms into the Hamiltonian.Because this thesis focuses on cross section measurement using data collect in near detectors before oscillation, the MSW effect out of the scope. More details about the MSW effect can be found for example in [17–19].

1.2.2 Long-Baseline Neutrino Experiments

The Super-Kamiokande experiment explored atmospheric neutrinos and the SNO experiment was based on solar neutrinos. Modern accelerator neutrino experiments such as T2K and NOνA produce neutrino beams itself by a proton accelerator. Such experiment usually consists of a near detector to measure the un-oscillated neutrino flux and a far detector to measured the oscillated neutrino flux after travelling some distance. As eq 1.28 shows, the oscillation probability depends not only on parameters in PMNS matrix, but also the ratio of travelling distance over the neutrino energy, L/E. The peak of the neutrino energy distribution, E, and the distance, L, will usually be adjust to be at the maximal oscillation positions. The measured event rate at far detector can generically be expressed as

$$R_{\text{far}}(\boldsymbol{x}) = \sum_{i}^{\text{processes}} \sum_{j}^{targets} \Phi(E_\nu)\sigma_i(E_\nu, \boldsymbol{x})\epsilon(\boldsymbol{x})N_j P(\nu_\alpha \to \nu_\beta) \tag{1.29}$$

where $R(\boldsymbol{x})$ is the total event rate for all processes as a function of the reconstructed kinematic variables $\boldsymbol{x}$, $\Phi(E_\nu)$ is the neutrino flux as a function of the neutrino energy E_ν, σ_i is the neutrino cross section for a particular mode i, ϵ is the detector efficiency and N_j is the number of target nuclei in the detector fiducial volume for target type j. From the equation, it is clear that to measure the oscillation probability, the neutrino flux, the neutrino cross section, and the detector efficiency must be known and well understood for precision measurement. Thus, for near detectors, besides the primary goal of measuring un-oscillated flux, another important role is to do cross-section measurements. Knowing neutrino-nucleus interaction cross-section well is essential for oscillation measurements.

1.3 Neutrino-Nucleus Interactions

Neutrinos interact with matters through weak interactions in the SM. In the energy region of sub-GeV and a few GeV where the T2K neutrino energy distributes, the cross section of neutrino-nucleus interactions is much larger than that of neutrino-electron interactions. Figure 1.4 shows a summary of ν_μ and $\bar{\nu}_\mu$ interaction cross sections w.r.t neutrino energy. Chapter 1.3.1 describes charged-current interactions between neutrinos and single nucleons. However, such a model is not sufficient to describe neutrino-nucleus interactions because of nuclear effects. Chapter 1.3.2 introduces such nuclear effects and the following chapter 1.3.3 introduces the other interactions models. The last chapter 1.3.4 introduces experiments which reported $\nu_e(\bar{\nu}_e)$ charged-current interaction cross sections on different targets.

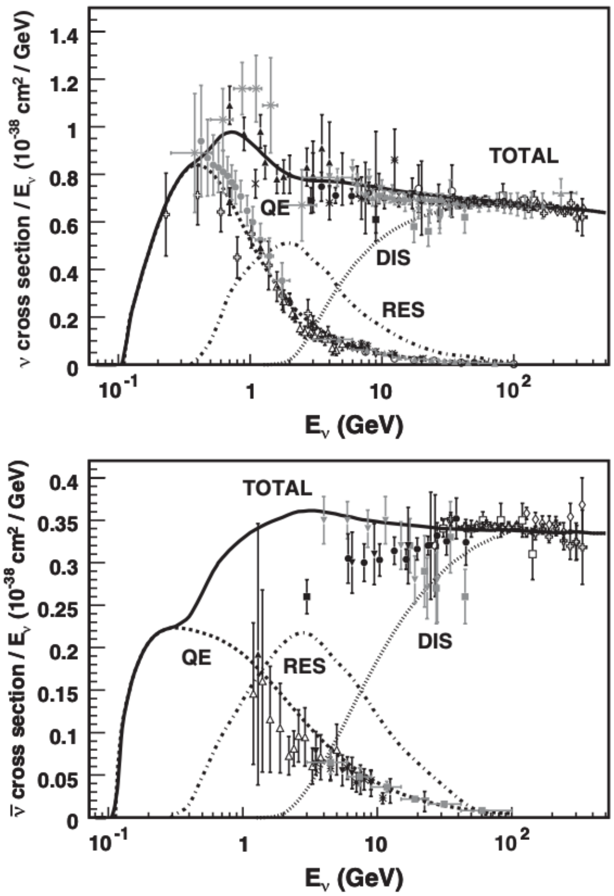

Figure 1.4: Muon (top) and anti-muon (bottom) neutrino charged current cross section measurements and predictions as a function of neutrino energy [20].

1.3.1 The Charged-Current Quasi-Elastic Interaction (CCQE)

CC interactions of neutrinos and nucleons exchange W bosons and produce charged leptons. Figure 1.5 shows the Feymann diagram of the CCQE process of neutrino and anti-neutrino. CCQE is called 'quasi-elastic' because the process is like elastic scattering but the nucleon is changed and the kinematics of the out-going charged lepton is not exactly the same as the incoming neutrino.

This process is important for several reasons.

1. In the sub-GeV energy region where the T2K beam peaks, CCQE is the dominant neutrino-nucleus interactions channel as shown in figure 1.4
2. The process has relatively well-studied theoretical models compared with other interaction channels.
3. Because it is a two-body process, it is possible to calculate the incoming neutrino energy from the measured out-going lepton's kinematics.

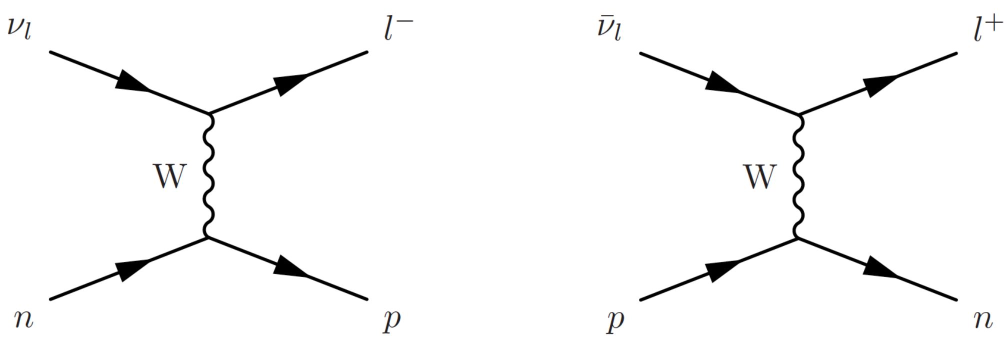

Figure 1.5: Feymann Diagram of CCQE process of neutrino (left) and anti-neutrino (right)

Using the neutrino process, $\nu_l \ + \ n \rightarrow \ p + \ l$ as an example. Assuming that the nucleon is at rest with bind energy E_b, from the conservation of energy and momentum, the reconstructed neutrino energy for the process will be

$$E_{\nu,recon} = \frac{m_p^2 - (m_n - E_b)^2 + m_l^2 + 2(m_n - E_b)E_l}{2(m_n - E_b - E_l - p_l \cos\theta_l)} \tag{1.30}$$

where m_p, m_n and m_l are the masses of proton, neutron and charged leptons respectively, E_b is the binding energy, and E_l, p_l and θ_l are the charged lepton's energy, momentum and direction w.r.t neutrino direction, respectively.

However, for the interaction channels which will be introduced next, there is no such a simple relation between the neutrino energy and charged leptons kinematics.

The QE interactions were intensively studied primarily using deuterium-filled bubble chambers[20, 21]. The differential cross section as a function of the four momentum transfer squared ($Q^2 = (p_\nu - k_l)^2 > 0$) can be parameterized and written as

$$\frac{d\sigma}{dQ^2} = \frac{G_F^2 M^2 |V_{ud}^2|}{8\pi E_\nu^2}\left(A \pm \frac{s-u}{M^2}B + (\frac{s-u}{M^2})^2 C\right) \tag{1.31}$$

where $\pm$ is for neutrino and anti-neutrino. G_F is the Fermi constant. M is the nucleon mass, m is the lepton mass, E_ν is the incoming neutrino energy, and $(s-u) = 4ME_\nu - Q^2 - m^2$. The factors A, B, and C are functions the familar vector F_1 and F_2, axial-vector (F_A), and pseudoscalar (F_P) form factors of nucleon.

$$\begin{aligned}
A(Q^2) &= \frac{(m_l^2 + Q^2)}{M^2}\Big[(1+\eta)\,F_A^2 - (1-\eta)\,F_1^2 \\
&\quad +\eta\,(1-\eta)\,F_2^2 + 4\eta F_1 F_2 \\
&\quad - \frac{m^2}{4M^2}\Big((F_1+F_2)^2 + (F_A + 2F_P)^2 \\
&\qquad - \left(\frac{Q^2}{M^2} + 4\right)F_P^2\Big)\Big] &(1.32)\\
B(Q^2) &= \frac{Q^2}{M^2}F_A(F_1+F_2) &(1.33)\\
C(Q^2) &= \frac{1}{4}\left(F_A^2 + F_1^2 + \eta F_2^2\right) &(1.34)
\end{aligned}$$

where $\eta = \frac{Q^2}{4M^2}$. The contribution of F_P is typically neglected in the analysis of the QE scattering as it is multiplied by $\frac{m^2}{M^2}$. The vector form factors F_1 and F_2 could be obtained from electron scattering using the conserved vector current (CVC). Thus, what is non-negligible and unknown here is the axial-vector form factor F_A. F_A is assumed for a dipole form shown as below.

$$F_A(Q^2) = \frac{g_A}{\left(1 + \frac{Q^2}{M_A^2}\right)^2} \tag{1.35}$$

where g_A and M_A are two empirical parameters. $g_A = 1.2694 \pm 0.0028$[22] is determined from beta decay. With measurements on deuterium and less-precise data on other heavier targets, M_A is fitted as $M_A = 1.026 \pm 0.0021$ [23].

1.3.2 Nuclear Effect

Modelling neutrino-nucleus interactions is complicated. Nucleons in nuclei are neither free nor at rest. Nucleons move around inside the nuclear potential and changes their momentum distributions before interactions which will affect cross sections. Such phenomenon is called Fermi Motion. Besides, neutrinos interact not only with single nucleons but correlated nucleons pairs or states of any number of nucleons. The detector cannot observe the neutrino-nucleus interaction at the nucleon level. When the particles generated at the vertex propagate through nuclear medium, many outgoing hadrons will re-interact, and as a result, the hadrons kinematics can be changed, the hadrons can be absorbed or extra particles can be emitted. Such re-interaction is called final

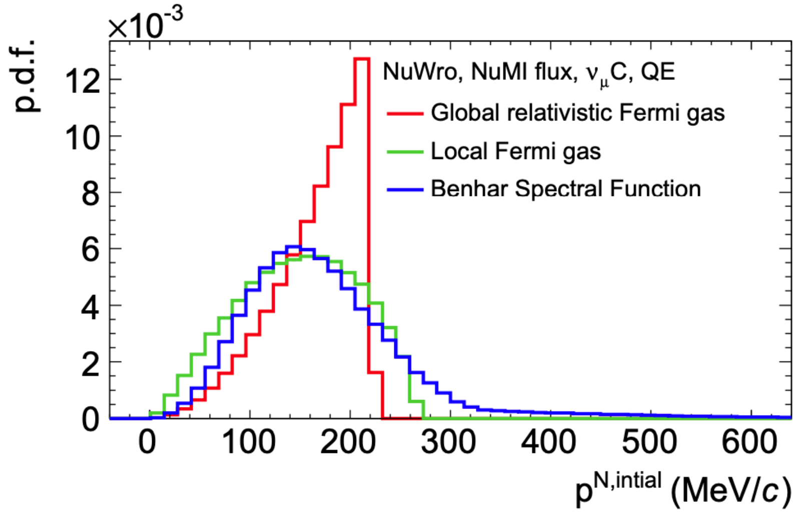

Figure 1.6: Comparison of the simulated nucleon momentum distributions for nuclear models of global relativistic Fermi gas (RFG), local Fermi gas (LFG), and Benhar spectral function (SF) using Carbon nucleus. Figure is from [27].

state interaction (FSI).

Fermi Motion

The nucleons in nuclei are undergoing random Fermi motions. It is difficult to accurately model the spectrum of nucleons in a nucleus with current existing theories and experimental results. There are three widely used nuclear models that attempting to predict the spectral functions in neutrino events generators. They are global relativistic Fermi gas (RFG), local Fermi gas (LFG) and Benhar spectral function (SF), respectively. Figure 1.6 shows a comparison of these model on a carbon nucleus. There are others models to describe Fermi Motions which are more sophisticated than these three [24–26]. Because they are not implemented in neutrino events generators, they will not be introduced in this thesis.

- Global Relativistic Fermi Gas (RFG)

  RFG is the simplest model that is commonly used to predict the spectral functions. It assumes that the nucleons don't interact with each other and the nuclear density is a constant, which means that the nucleons are under the same constant nuclear potential. Figure 1.7 shows cartoon of the model. Both protons and neutrons are fermions which obey the Pauli-Exclusion Principle. Because the nuclear density is a constant, nucleus can be treated as a sphere with radius $R = r_0 A^{1/3}$ and the Fermi energy E_F (or Fermi momentum p_F) which is the energy (momentum) of the highest energy state can be written as

$$p_F^p = \left(\frac{9\pi Z}{4A}\right)^{1/3} \frac{\hbar}{r_0} \tag{1.36}$$

$$p_F^n = \left(\frac{9\pi (A-Z)}{4A}\right)^{1/3} \frac{\hbar}{r_0} \tag{1.37}$$

$$E_F^p = \frac{{p_F^p}^2}{2m^p} = \frac{1}{2m^p} \left(\frac{9\pi Z}{4A}\right)^{2/3} \left(\frac{\hbar}{r_0}\right)^2 \tag{1.38}$$

$$E_F^n = \frac{{p_F^n}^2}{2m^n} = \frac{1}{2m^n} \left(\frac{9\pi (A-Z)}{4A}\right)^{2/3} \left(\frac{\hbar}{r_0}\right)^2 \tag{1.39}$$

  where the superscript p represents proton and superscript n represent neutron. A is the atomic number and Z is the number of protons in the nucleus.

- Local Fermi Gas (LFG)

  The assumption of constant nuclear density in RFG is not how the nature designs the nucleus. LFG is a more sophisticated model which uses local density approximation (LDA) [29] that the nuclear density is a

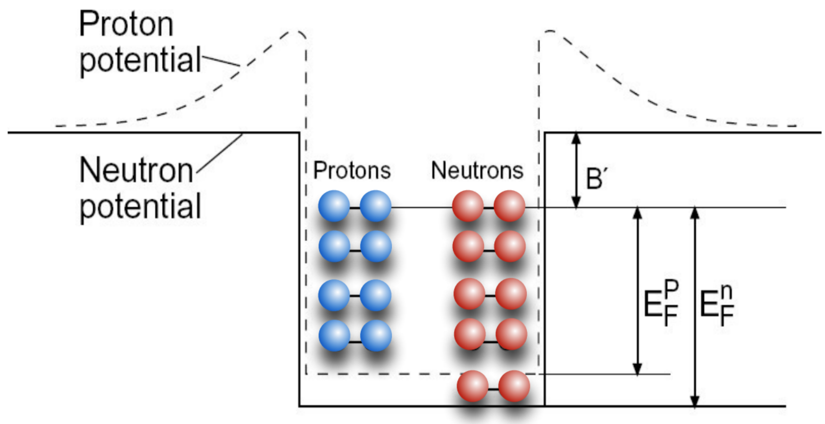

Figure 1.7: Cartoon of the Fermi Motion Model where E_F is the Fermi Energy. Figure is from [28].

function of radial position, $\rho(r)$. Such density distribution can be known from elastic electron scattering data [30]. The local Fermi momentum is assumed to depend on $\rho(r)$ (where r is a distance from the center of the nucleus) in the following way [31]. Figure 1.8 shows the comparison of Fermi momentum w.r.t radial position for carbon nucleus.

$$p_F^p = \left(3\pi^2 \rho(r) \frac{Z}{A}\right)^{1/3} \hbar \tag{1.40}$$

$$p_F^n = \left(3\pi^2 \rho(r) \frac{A-Z}{A}\right)^{1/3} \hbar \tag{1.41}$$

- Benhar Spectral Function (SF)

An assumption hold in the models mentioned above is that the nucleons don't interact with each other. However, such assumption is not true and from the electron scattering data, it is known that nucleon-nucleon interactions inside the nucleus can significantly affect the nucleon momentum

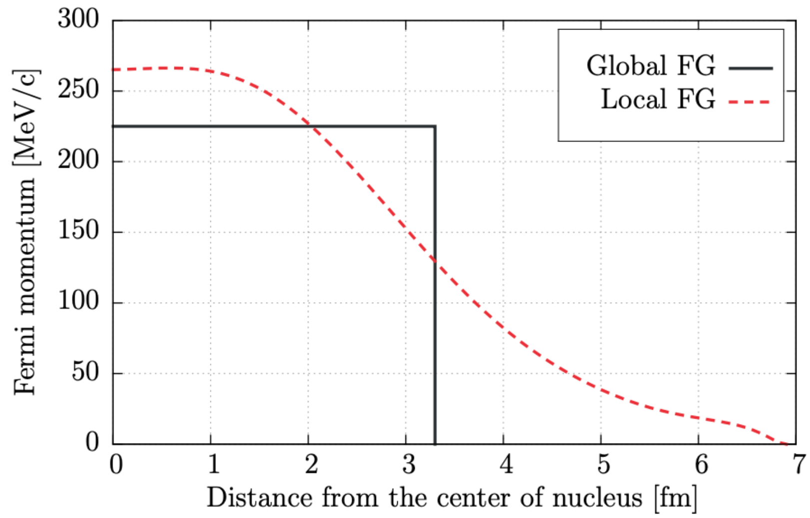

Figure 1.8: Comparison of the Fermi momentum for global and local Fermi gas in Carbon nucleus. Figure is from [31].

distributions [32, 33]. SF models considers such interactions. The probability distributions for the momentum of nucleons consist of two terms, a mean-field term for single particles and a term which describes the interactions of correlated pairs of nucleons [31]. The SF increase the neutrino interaction cross section at the high transferred energy and suppress the cross section at small transferred energy. Figure 1.9 shows a comparison of binding energy and initial momentum of the nucleon for the three models mentioned by far.

Nucleon-Nucleon correlation

By far, it is assumed that the neutrino interacts on single nucleons in nuclei and the cross section on a nucleus is an incoherent sum of interactions on single nucleons. However, electron-nucleus scattering experiments have inferred that such assumption does not hold and there would exist interactions on

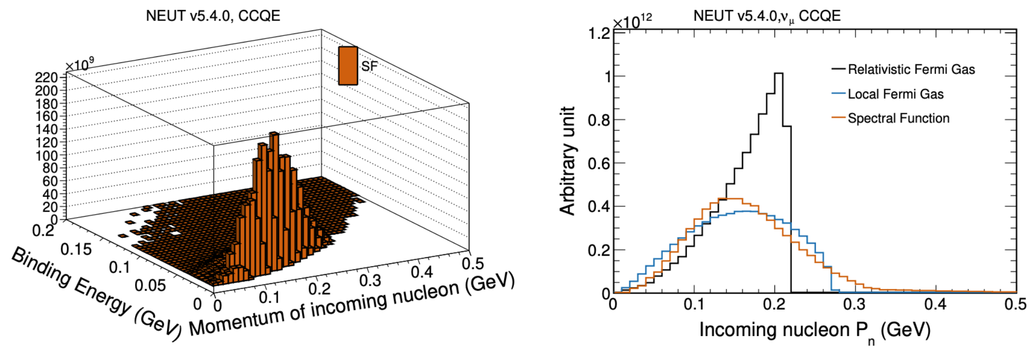

Figure 1.9: Binding energy vs momentum for RFG, LFG, SF in with NEUT v5.4.0. Figure is from [34].

bound-states of two or more nucleons in nuclei. New models are developed to describe such interactions (e.g [35, 36]). Random phase approximation (RPA) [35, 36] is applied to account for nuclear scattering effect. RPA describes the impact of the nuclear medium on an electroweak propagator.It affect significant especially at low Q^2 region. Figure 1.10 shows the comparison of Q^2 distribution for ν_μ CCQE interactions with and without RPA correction. The plot is generated using T2K on-axis detector flux in neutrino mode and Nieves RPA calculation in [35].

Final State Interactions

Final state interactions (FSI) describe the process that final state particles, especially hadrons which can interact with nuclei medium via strong interaction, re-interact with nuclei when passing through. Such interactions can change the kinematics of outgoing final state particles, absorb them or generate new particles. Figure 1.11 shows a schematic of possible FSI processes. As mentioned above, what measured by the detector is the particle exiting

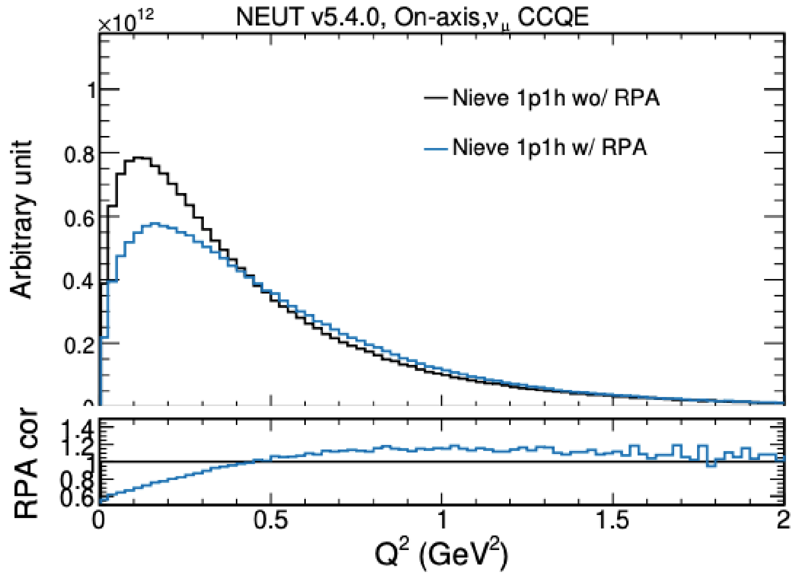

Figure 1.10: Q^2 distribution with and without RPA correction using T2K on-axis detector flux in neutrino mode and and Nieves RPA calculation implemented in T2K[35]. Figure is from [34]

from nuclei, so FSI directly affect the observed results of interactions. Thus, it is important to model or constrain FSI from experimental results as well as possible.

Cascade models are applied to model FSI. Interactions are simulated step by step and the interaction at each step is treated independently. The step size that hadrons propagating through the nucleus is discrete and tuned based on hadron scattering experimental results. The probability of interactions at each step is calculated based on the local nuclear density. For more details on how the FSI models are implemented in neutrino event generators, please refer to [31, 34, 37, 38].

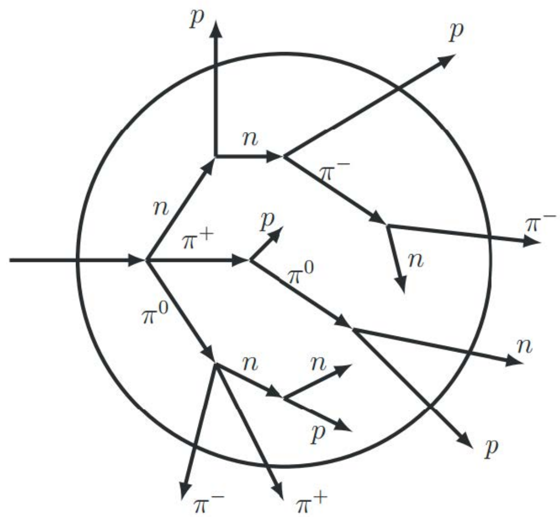

Figure 1.11: A schematic of final state interactions. Figure is from [31]

1.3.3 Other neutrino-nucleus models

Resonance production

When the energy of incoming neutrino in the center-of-mass framework is larger than the the mass of a delta baryon, the interaction could induce the resonance state and produce pions from delta baryon decay inside the nucleus. Such resonant pion productions can occur in both CC and NC interactions. Equations 1.42 show the CC channels of resonant production and 1.45 show the NC channels on nucleons. Figure 1.12 shows the Feymann diagram of resonance interactions using charge-current pion production processes as examples.

$$\nu_l + p \;\rightarrow\; l^- + p + \pi^+, \qquad \bar{\nu}_l + p \rightarrow l^+ + p + \pi^- \tag{1.42}$$

$$\nu_l + n \;\rightarrow\; l^- + p + \pi^0, \qquad \bar{\nu}_l + p \rightarrow l^+ + n + \pi^0 \tag{1.43}$$

$$\nu_l + n \;\rightarrow\; l^- + n + \pi^+, \qquad \bar{\nu}_l + n \rightarrow l^+ + n + \pi^- \tag{1.44}$$

$$\overset{(-)}{\nu}_l + p \;\rightarrow\; \overset{(-)}{\nu}_l + p + \pi^0 \tag{1.45}$$

$$\overset{(-)}{\nu}_l + p \;\rightarrow\; \overset{(-)}{\nu}_l + n + \pi^+ \tag{1.46}$$

$$\overset{(-)}{\nu}_l + n \;\rightarrow\; \overset{(-)}{\nu}_l + n + \pi^0 \tag{1.47}$$

$$\overset{(-)}{\nu}_l + n \;\rightarrow\; \overset{(-)}{\nu}_l + p + \pi^- \tag{1.48}$$

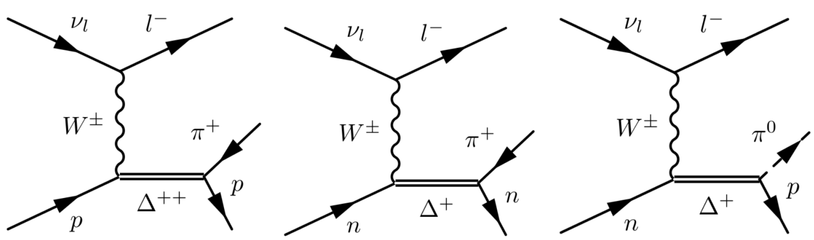

Figure 1.12: Charged current single pion production processes on a nucleon via different intermediate $\Delta(1232)$ resonances. Figure is from [34]

The neutrino event generators used in T2K, NEUT, with the version 5.4.0, adopted Rein and Sehgal's (RS) model [39] for resonant pion production. There are four parameters which are used to parameterize the model when implementing the RS model, NEUT-MARSRES for the axial vector mass constant , NEUT-MVRSRES for vector mass constant, NEUT-BGSCL for the non-resonant background scaling, and NEUT-NRTYPE.

CC Coherent Pion Production

Coherent scattering models treat the nucleus as a unit, i.e. the neutrino interact with the nucleus as a whole. Such interactions are allowed at low Q^2. Interaction processes in both CC and NC are shown below.

$$\overset{(-)}{\nu}_l + A \rightarrow l^{\overset{(+)}{-}} + A + \pi^{\overset{(-)}{+}} \tag{1.49}$$

$$\overset{(-)}{\nu}_l + A \rightarrow \overset{(-)}{\nu}_l + A + \pi^0 \tag{1.50}$$

Rein-Seghal coherent model [40] is often used to describe the coherent scattering in the energy region of GeV. At the lower energy region, Berger-Segnal model is used to attempt to address the disagreement. Overall, the cross section of this channel is very small at neutrino energies regions that T2K is of interest.

Deep Inelastic Scattering and Multiple Pion production

When neutrinos energies are high enough to resolve the individual quarks in the nucleon, they can interact with quarks and produce a jet of hadrons. Such interaction processes are called Deep Inelastic Scattering (DIS). Figure 1.4 shows that DIS will become dominant for ν_μ or $\bar{\nu}_\mu$ CC interaction when E_ν is larger than about 10GeV.

$$\overset{(-)}{\nu}_l + N \rightarrow l^{\overset{(+)}{-}} + X \quad N = p, n \tag{1.51}$$

$$\overset{(-)}{\nu}_l + N \rightarrow \overset{(-)}{\nu}_l + X \quad N = p, n \tag{1.52}$$

The cross-section of DIS processes can be written as

$$\frac{d^2\sigma}{dx\,dy} = \frac{G_F^2 M E_\nu}{\pi\left(1+\frac{Q^2}{M_W^2}\right)^2}\left\{\frac{y^2}{2}2xF_1(x,Q^2) + \left(1 - y - \frac{Mxy}{2E}\right)F_2(x,Q^2) \right.$$
$$\left. \pm y\left(1-\frac{y}{2}\right)xF_3(x,Q^2)\right\} \quad (1.53)$$

where

$$y = \frac{E_{had}}{E_\nu} \quad (1.54)$$

$$Q^2 = -m_l^2 + 2E_\nu(E_l - p_l\cos\theta_l) \quad (1.55)$$

$$x = \frac{Q^2}{2ME_\nu y} \quad (1.56)$$

y is called the inelasticity , $Q^2 = -q^2$ is the 4-momentum transfer and x is the Bjorken scaling variable. E_ν is the neutrino energy and E_l, p_l, and $\cos\theta_l$ are the energy, momentum and scattering angle of the outgoing lepton in lab framework, respectively. M is the nucleon mass, M_W is the mass of the W boson, and the $\pm$ refers to neutrino or antineutrino interactions. $F_i(x,Q^2)$ are the nucleon structure distributions and they are taken from parton distribution functions [41, 42].

Just to clarify that, in NEUT, when the hadronic invariant mass, W, in such interactions is less than 2GeV/c^2, it is called multiple π production (Multiπ), i.e. multiπ describes the DIS process when 1.3GeV/c^2 $< W <$ 2GeV/c^2 and DIS are for $W <$ 2GeV/c^2 in NEUT.

neutrino interaction cross section usually is not done on neutrino energies because of the model dependence on neutrino energy reconstruction. Instead, it's done on kinematics of FSI particles. For more details on the cross section measurement methods, please refer to the chapter 6.6

1.3.4 Previous measurements of ν_e and $\bar{\nu}_e$ interaction cross sections on nucleus

There are very few measurements on $\nu_e(\bar{\nu}_e)$ cross section on nucleus in GeV region. In 1978, the Gargamelle Experiment published a measurement of total inclusive ν_e and $\bar{\nu}_e$ interaction cross sections in the heavy liquid bubble chamber Gargamelle [43].

In 2014, T2K published a measurement of ν_e CC inclusive total cross section and differential cross section w.r.t. electrons kinematics on carbon [44]. Figure 1.13 shows a comparison of the inclusive total cross section from T2K in 2014 and from Gargamelle.

In 2016, MINERvA experiment published a result of flux-integrated ν_e CCQE-like differential cross sections on hydrocarbon. Figures 1.14 show the differential cross section as a function of the electron momentum and angle, respectively.

In 2020, following a different approach from the measurement in 2014 [44], T2K measured the ν_e CC and $\bar{\nu}_e$ CC inclusive differential cross section on carbon in FHC and RHC, separately [46]. The results are shown in figure 1.15.

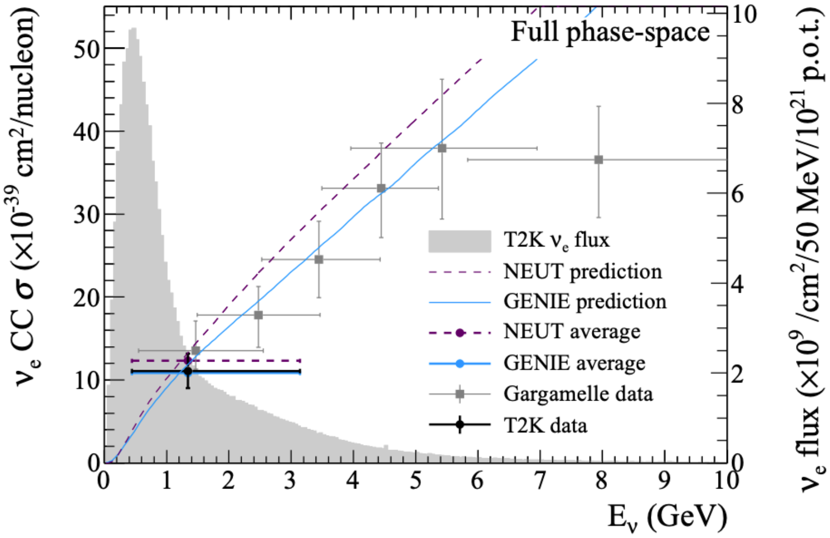

Figure 1.13: Total ν_e CC inclusive cross-section when unfolding through Q^2 in T2K. The T2K data point is placed at the ν_e flux mean energy. The vertical error represents the total uncertainty, and the horizontal bar represents 68% of the flux each side of the mean. The T2K flux distribution is shown in grey. Figure is from [44]

1.4 Motivation

T2K is a long baseline accelerator neutrino oscillation experiment measuring $\nu_e(\bar{\nu}_e)$ appearance and $\nu_\mu(\bar{\nu}_\mu)$ disappearance from the $\nu_\mu(\bar{\nu}_\mu)$ beam. Current major goals of long baseline accelerator neutrino experiments are measuring Dirac CP violation phase, δ_{CP}, and precise measurement of oscillation parameters. $\nu_e(\bar{\nu}_e)$ appearance measurement will be used for CP violation measurement and the interaction target in the far detector in T2K is water, H_2O. It is essential to have better understandings of the $\nu_e(\bar{\nu}_e)$ interactions especially on water for the future CP violation measurement in T2K for two reasons. First, the main background in $\nu_e(\bar{\nu}_e)$ appearance measurement is the intrinsic $\nu_e(\bar{\nu}_e)$ component in the neutrino beam in T2K which will be shown in section 2.1.

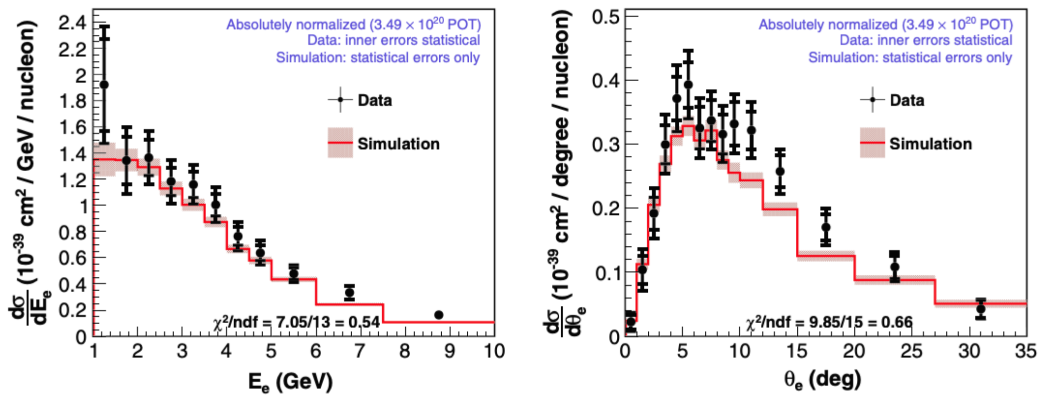

Figure 1.14: Miner$v$A Flux-integrated differential ν_e CCQE-like cross section versus electron energy (left) and electron angle (right). Inner errors are statistical; outer are statistical added in quadrature with systematic. The band represents the statistical error for the Monte Carlo curve. Figure is from [45]

Second, a large systematic uncertainty in T2K $\nu_e(\bar{\nu}_e)$ appearance observation comes from uncertainties related with the neutrino cross-section modelling. Predictions of signals in $\nu_e(\bar{\nu}_e)$ appearance rely on the modelling of the $\nu_e(\bar{\nu}_e)$ interaction which are constructed mainly based on the relations to the $\nu_\mu(\bar{\nu}_\mu)$ cross sections in current simulations. There have been many measurements on inclusive or exclusive $\nu_\mu(\bar{\nu}_\mu)$ cross sections (e.g. [20] as a review). It is known that $\nu_e(\bar{\nu}_e)$ and $\nu_\mu(\bar{\nu}_\mu)$ cross sections are not the same [47], but there are very few measurements on $\nu_e(\bar{\nu}_e)$ cross sections and no measurements on water (H_2O) target, as presented in section 1.3.4. Thus, measuring $\nu_e(\bar{\nu}_e)$ charged current (CC) cross sections especially on water is very important for the future CP violation measurement.

It is challenging to measure $\nu_e(\bar{\nu}_e)$ CC cross section in long baseline accelerator neutrino experiments because the neutrino beam is dominant by $\nu_\mu(\bar{\nu}_\mu)$. The number of $\nu_e(\bar{\nu}_e)$ is small comparing with $\nu_\mu(\bar{\nu}_\mu)$. The goal of selections would be selecting a small amount of electrons generated by $\nu_e(\bar{\nu}_e)$ CC inter-

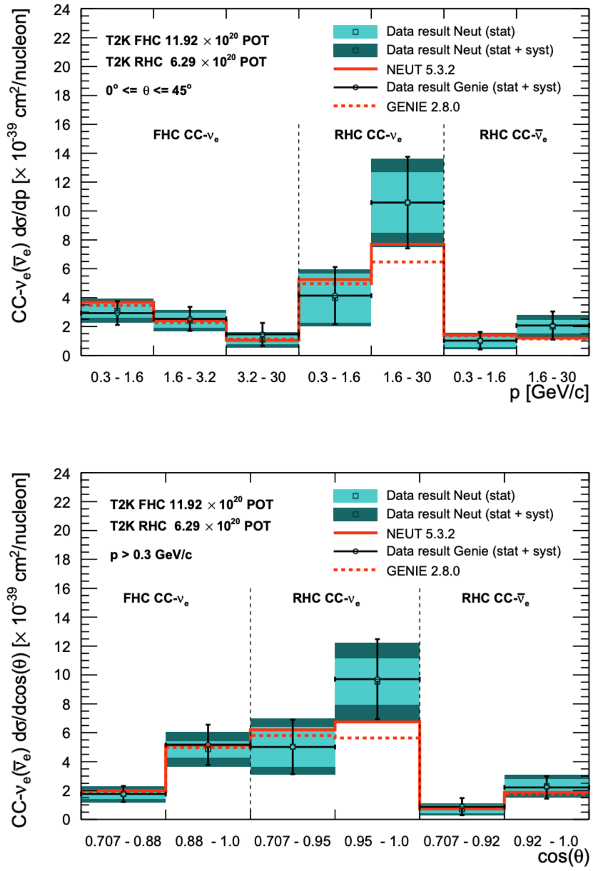

Figure 1.15: T2K flux-integrated $\nu_e(\bar{\nu}_e)$ CC inclusive differential cross section results in $d\sigma/dp_e$ and $d\sigma/d\cos\theta_e$ in a limited phases pace ($p > 300MeV/c$ and $\theta \leq 45\,$deg. Figure is from [46].

actions from numerous muons, protons and charged pions produced by $\nu_\mu(\bar{\nu}_\mu)$ CC interactions. Besides, photons generated from the decay π^0s which are produced in NC (or CC) interactions make it very difficult to select pure electron (anti-electron) samples because they both cause electron-magnetic showers which will be discussed in chapter 3.

In this thesis, the signal phase space is defined/constrained by a Boost Decision Tree (BDT) which will be presented in section 4.2. Selection strategies and systematic uncertainties will be discussed in chapter 4 and 5, respectively.

The result of flux-integrated ν_e CC differential cross section as a function of true total kinetic energy (see 6.7) on water target using data collected by P0D in FHC mode will be presented in section 8.1. Another independent measurement of flux-integrated $\nu_e + \bar{\nu}_e$ CC differential cross section on water in a limited phase space defined by the BDT using data collected by P0D in RHC mode will be presented in section 8.2.

Chapter 2

The T2K Experiment

The T2K (Tokai-to-Kamioka) [48] experiment is a long-baseline neutrino experiment which is designed to measure ν_μ disappearance and ν_e appearance from the ν_μ beam produced from a 30 GeV proton beam at J-PARC (Japan Proton Accelerator Research Complex) at Tokai, Japan. It consists of a neutrino beamline, a near detector complex (ND280) which are located at J-PARC and a far detector (Super-Kamiokande) located 295 km away from J-PARC. Figure 2.1 shows the cross-sectional schematic of the T2K.

T2K has been taking physics data since early 2010. It has successfully

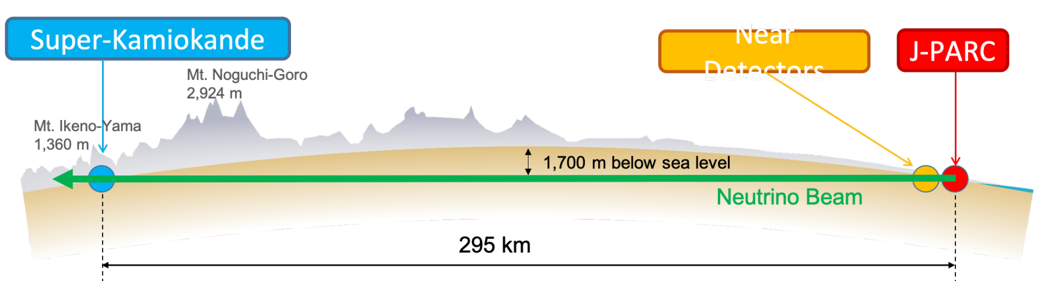

Figure 2.1: The Schematic of the T2K Experiment

completed the primary goal of measuring the unknown PMNS mixing angle θ_{13}. T2K continues to improve to make precision measurements on Δm^2_{23}, θ_{23} and θ_{13}. Furthermore, T2K moves to the measurement of CP violation at lepton sector. The recent results from T2K excludes values of δ_{CP} that result in a large increase in the observed anti-neutrino oscillation probability at three standard deviations (3σ) [49]. Besides, T2K has made some important neutrino-nucleus cross-section measurements. LIST SOME RESULTS OR PUBLICATIONS HERE ABOUT XSEC MEASUREMENT!!!

The chapter will give an overview of all components of the T2K experiment, from the beam source to the far detector.

2.1 The T2K Beam

2.1.1 J-PARC Accelator and T2K Neutrino Beamline

The J-PARC accelerator consists of three components: a linear accelerator (LINAC), a rapid-cycling synchrotron (RCS), and a main ring (MR) [48].The LINAC is used to accelerate an H^- beam and then the H^- beam is converted to an H^+ beam by charge-stripping foils at the RCS injection and is accelerated to up to 3 GeV by the RCS. The part of the proton beam (5%) are injected into the MR and accelerated up to 30 GeV. Figure 2.2 gives an overview of J-PARC.

An overview of the neutrino beamline is shown in Figure 2.3. Protons beam extracted from the MR goes to the T2K neutrino beamline. The neutrino beamline consists of two parts: the primary and secondary beamlines. The

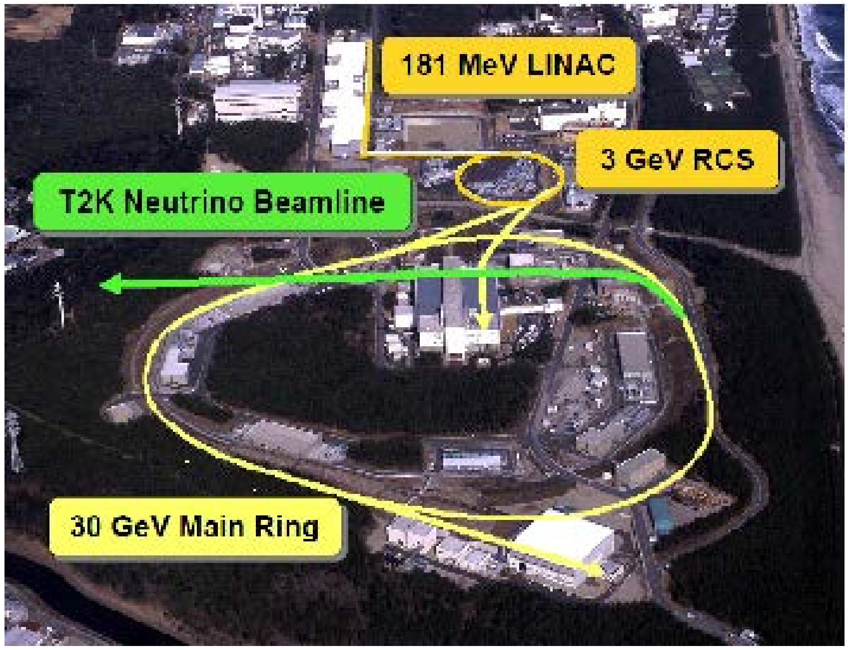

Figure 2.2: A Overview of the J-PARC Accelerators Complex

extracted proton beam is transported to point toward the SK in the primary beamline and impinges on a target to produce mesons which are mainly pions in the secondary beamline. The mesons are focused by magnetic horns and decay into neutrinos. By switching the polarity of the magnetic horns, the charge sign of the mesons focused by the horns can be reversed, and as result, a beam with enriched neutrinos or anti-neutrinos can be produced. Such magnetic configurations are called Forward Horn Current (FHC) or Reverse Horn Current (RHC). Figure 2.4 shows an overview of the neutrino production.

Neutrinos are products of decay of the mesons produced by the proton-nucleus interactions. The major components of mesons are charged pions/ Besides, there are some kaons. The major decay process are listed below.

- FHC: $\pi^+ \to \mu^+ + \nu_\mu$, $K^+ \to \mu^+ + \nu_\mu$

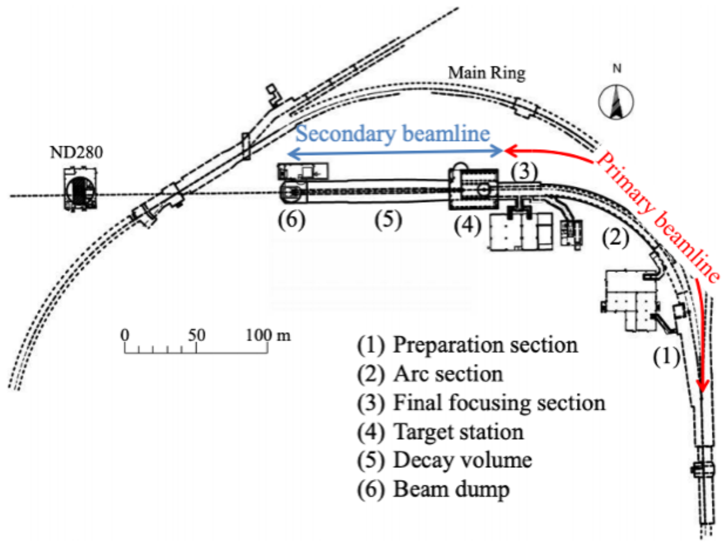

Figure 2.3: A Overview of the T2K Neutrino Beamline

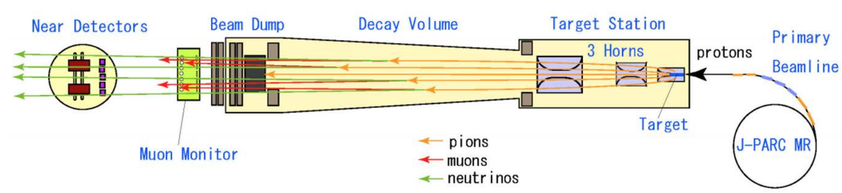

Figure 2.4: A Overview of the T2K Neutrino Beamline

- RHC: $\pi^- \to \mu^- + \bar{\nu}_\mu$, $K^- \to \mu^- + \bar{\nu}_\mu$

The two-body decay of pions allows the outgoing neutrino energy depends only weakly on the parent pion momentum beyond some scattering angle dependent threshold, which enables us to use the off-axis technique. More details about this will be introduced in next section 2.1.2. $\nu_\mu(\bar{\nu}_\mu$ becomes the dominant component in the neutrino beam produced in FHC (RHC) configuration. Muons produced by the decay of the mesons decay and kaons have another decay channel whose branch ratio is about 5% which is not negligible.

- $\mu^+ \rightarrow e^+ + \nu_e + \bar{\nu}_\mu, K^+ \rightarrow \pi^0 + \nu_e + e^+$
- $\mu^- \rightarrow e^- + \bar{\nu}_e + \nu_\mu, K^- \rightarrow \pi^0 + \bar{\nu}_e + e^-$

The length of the decay volume is chosen to maximise the meson to muon (anti-muon) neutrino conversion rate and minimize the electron (anti-electron) neutrino contamination in the beam, but inevitably, there are intrinsic $\nu_e(\bar{\nu}_e)$ components in the neutrino beam shown in figure 2.7, which is the major background in the $\nu_e(\bar{\nu}_e)$ appearance measurement in T2K and motivates this analysis as we discussed in section 1.4.

2.1.2 Off -axis Technique and Flux Prediction

As we mentioned before, the major source of neutrinos is the decay of pions which is a two-body decay. Use $\pi^+ \rightarrow \mu^+ + \nu_\mu$ as an example. From the conservation of energy and momentum and neglecting the mass of neutrino, we can derive that

$$E_{\nu_\mu} = \frac{m_\pi^2 - m_\mu^2}{2(E_\pi - \sqrt{E_\pi^2 - m_\pi^2} \cos\theta_{\pi\nu_\mu})} \tag{2.1}$$

The energy of produced neutrino is a function of angle between neutrino and pion $\theta_{\pi\nu_\mu}$. Figure 2.5 shows the neutrino energy vs pion input with different angles between pions and neutrino in the lab frame. By taking advantage of the relation with angle, SK are put at off-axis to get a narrow band of neutrino energy distribution. Figure 2.6 shows the un-oscillated ν_μ flux at SK with the ν_e appearance and and the ν_μ disappearance probability with respect to neutrino energy at different angle. T2K choose to place SK at 2.5° off-axis

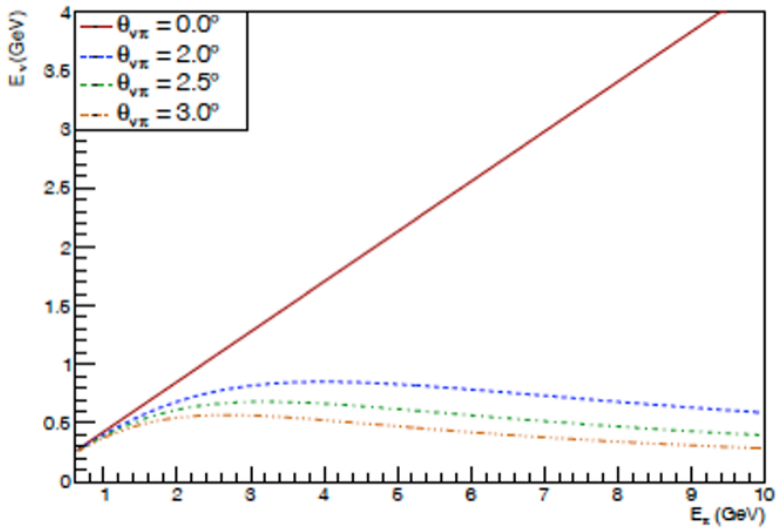

Figure 2.5: Neutrino energy in two-body pion decay as a function of the pion energy for different choices of the neutrino direction relative to the incoming pion direction in the lab frame. [50]

to ensure the peak energy is at 0.6GeV where the oscillation probability at SK is maximum and meanwhile the beam intensity and spread are balanced.

The flux prediction is an essential part of the successful prediction of neutrino interaction rates at the T2K detectors and is an important input to T2K neutrino oscillation and cross section measurements [51]. The neutrino flux is predicted by a Monte Carlo simulation based on experimental data [48]. The primary interaction of the 30 GeV proton with graphite target is simulated based on NA61/SHINE data. Other hadronic interactions inside the target are simulated by FLUKA[52][53]. Kinematic information for particles emitted from the target is saved and transferred to next simulations and interactions outside the target are simulated with GEANT3[54]. Figure 2.7 shows the most recent T2K flux prediction at ND280 and SK.

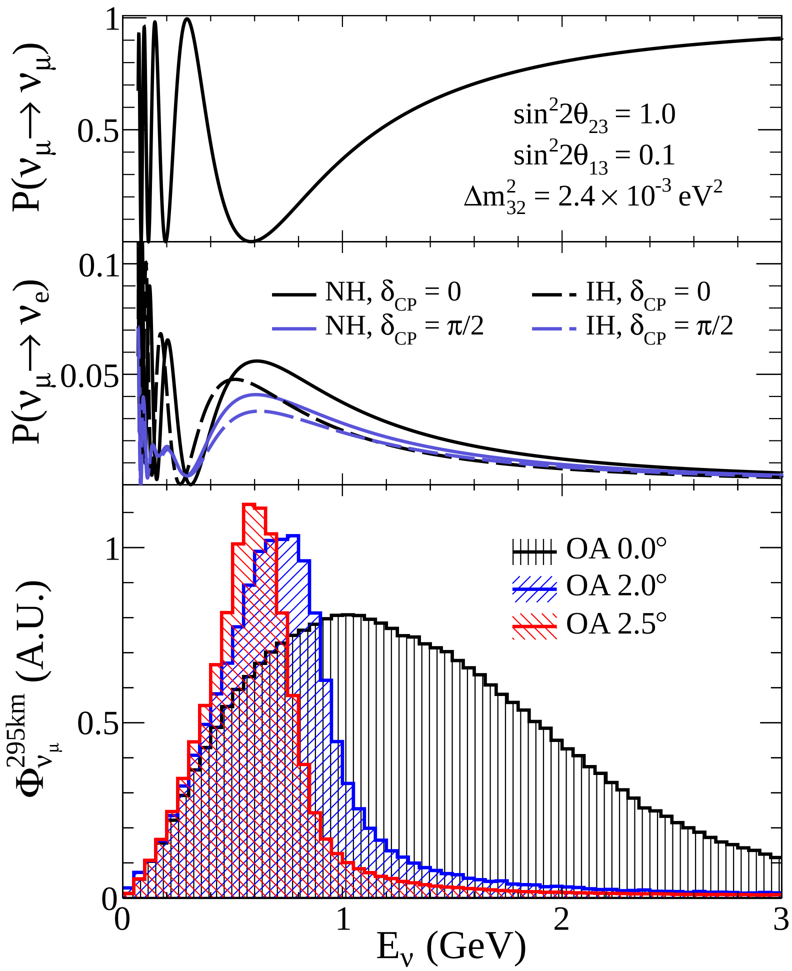

Figure 2.6: Comparison of the predicted un-oscillated ν_μ flux at SK (bottom) overlaid with the ν_e appearance probability at SK (middle) and the ν_μ disappearance probability (top) all given as a function of neutrino energy on the same scale.

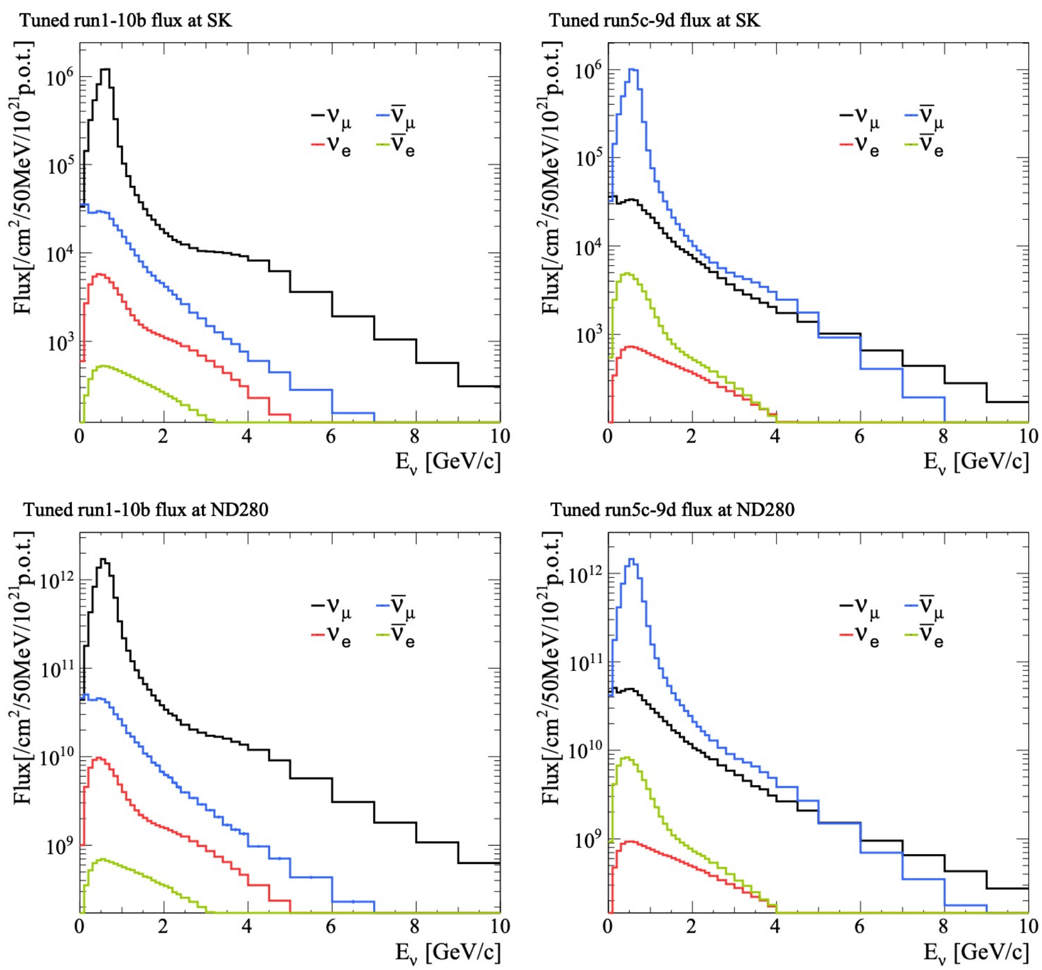

Figure 2.7: The neutrino flux at SK (top) and ND280 (bottom) tuned with NA61 replica 2010 data. Neutrino-mode is shown on the left and anti-neutrino mode on the right[55].

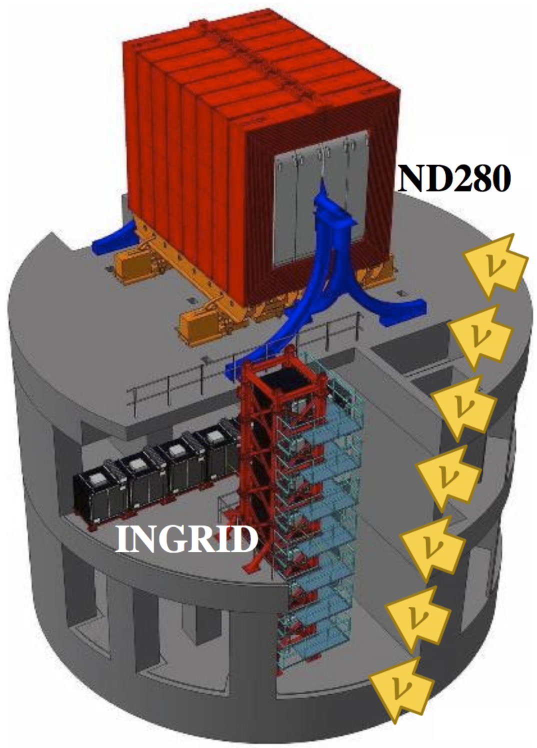

Figure 2.8: ND280 overview

ND280 shown in Figure 2.8 are a set of near detectors located 280m way from the neutrino beam production point. They are used to measure energy spectrum, flavor content, and interaction rates of the un-oscillated beam and further to predict the neutrino interactions at SK[48]. It consists of two parts, on-axis and off-axis.

2.1.3 INGRID

INGRID shown in Figure 2.9 is the detector placed on-axis and is used to monitor the neutrino beam direction and profile by neutrino interactions in iron, with sufficient statistics to provide daily measurements at nominal beam intensity [48].

INGRID is designed as a cross shape and the main cross spans 10 m$\times$10 m transverse to the neutrino direction. The cross consists of 14 identical modules arranged arranged along the horizontal and vertical axis, and 2 additional separate modules located at off-axis directions outside the main cross. Each module is structured as a sandwich of 9 iron plates and 11 tracking scintillator planes surrounded by veto scintillator planes, to reject interactions outside the module. Each of the 11 tracking planes consists of 24 scintillator bars in the horizontal direction glued to 24 perpendicular bars in the vertical direction. The purpose of the two off-axis modules is to check the axial symmetry of the neutrino beam. Other than the 16 modules described before, there is an different module, called the Proton Module has been added in order to detect with good efficiency the muons together with the protons produced by the neutrino beam in INGRID. The center of the cross corresponds to the neutrino beam center, defined as 0° with respect to the direction of the primary proton beamlin. With the sufficient statistics collected in each module, the beam center can be determined to a precision better than 0.4mrad at the near detector which is 280m downstream from the beam origin[48].

2.1.4 Off-axis Detectors

Off-axis detectors shown in Figure 2.10 are composed of one π^0 detector (P0D), three time projection chambers (TPCs) alternated two fine grained detectors (FGDs) following the neutrino beam direction. These sub-detectors are placed inside of a metal frame container, called the "basket". Electromagnetic calorimeters (ECal) surrounds the basket. The basket has dimensions of 6.5 m

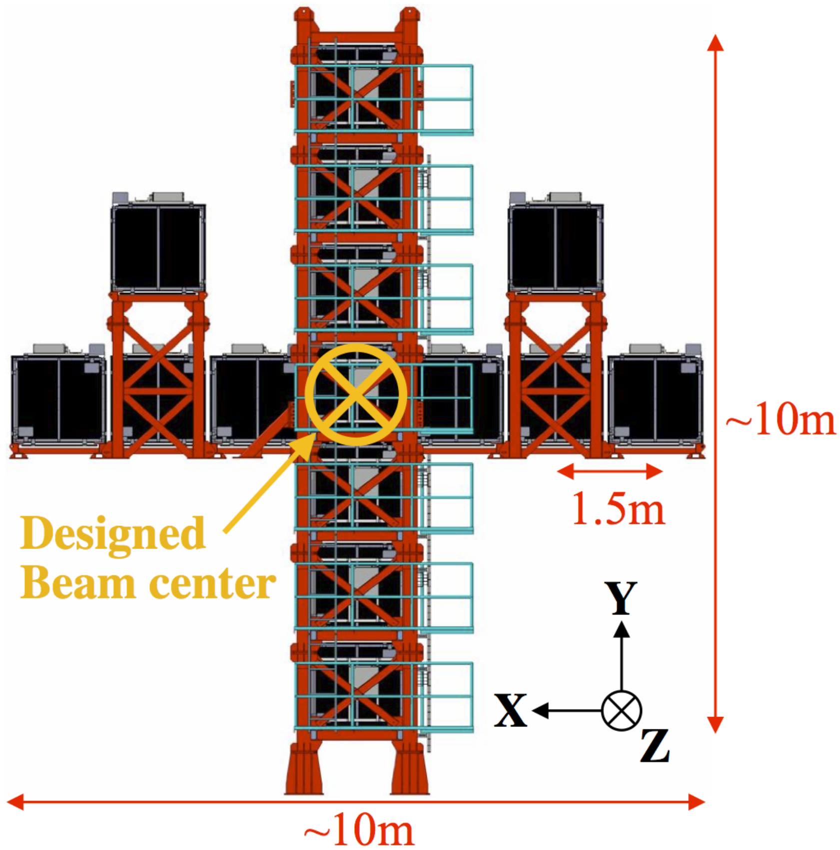

Figure 2.9: INGRID overview

× 2.6 m × 2.5 m (length × width × height) and is placed inside the recycled UA1 magnet. The magnet is instrumented with scintillator to perform as a muon range detector (SMRD). ND280 can be used to reduce the uncertainties on the flux prediction and measure event rate for neutrino interaction and provide constrains on cross-section modelling.

The detector which is used to perform a cross-section measurement in this thesis is P0D which will be introduced in detail in Chapter 3. SMRD can have the following functions: to measure muons escaping the detector at high angles relative to the beam direction; to form part of the trigger for cosmic ray muons that enter the ND280 detector; and to identify beam-related interactions in

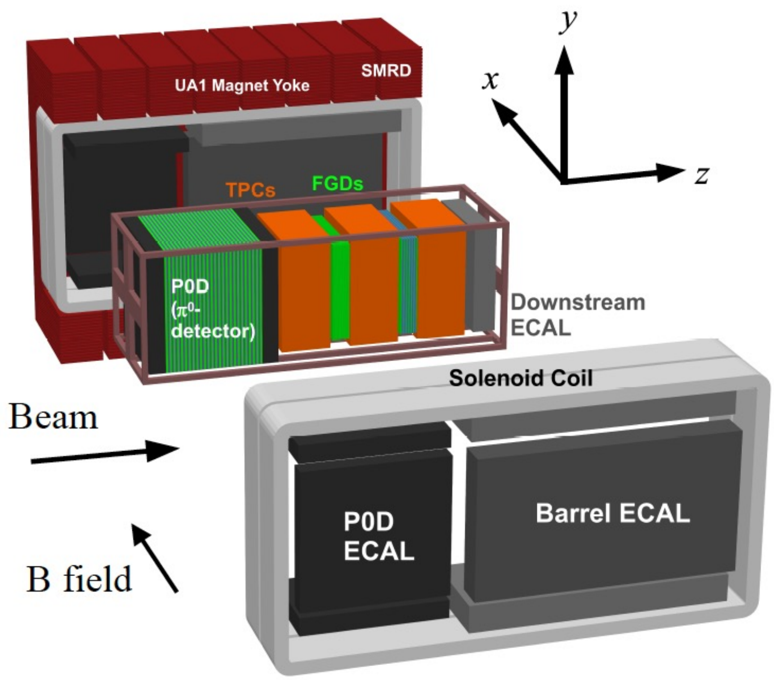

Figure 2.10: Overview of ND280 Off-axis detectors

the iron of the magnet and the surrounding cavity[56]. TPCs and FGDs will be introduced next.

2.1.5 UA1 magnet

The UA1 magnet provide a dipole magnetic field of 0.2 T. Trajectories of charge particles will be curved with the magnet field. The curvature can help to measure momenta with good resolution and determine the sign of charged particles. Knowing the sign of leptons from the neutrino interaction charged-current interaction will identify neutrino or anti-neutrino.

2.1.6 Time Projection Chambers (TPCs)

There are three TPCs along the beam direction with 2 FGDs in between. Each TPC shown in figure 2.11 consists of an inner box which holds an argon-based drift gas, contained within an outer box that holds CO2 as an insulating gas. Central cathode in the inner box create electric field at the same direction with the magnetic field. When charge particles travel in TPC, ionization will produces electrons and the electric field will make them drift away from the Central cathode and toward the readout panels. Charges collected at the readout panels and the arrival time and location at the panel determined by the 'micromegas' modules on the panel[57] will be used to reconstruct the trajectories of the charged particles in three dimensions. Different types of charged particles in TPC can be distinguished by the energy loss per distance, dE/dx [58]. PROBABLY ADD MORE DETAILS IN TERMS OF dE/dx LATER!!!

High resolution on readouts allows TPC to get the number and orientations of charged particles traversing the detectors in high precision. Besides the curvatures of charged particles caused by the magnetic field allows TPC to measure the momenta accurately.

The TPCs perform three key functions in the near detector. Firstly, with their excellent imaging capabilities in three dimensions, the number and orientations of charged particles traversing the detectors are easily determined and form the basis for selecting high purity samples of different types of neutrino interactions. Secondly, since they operate in a magnetic field, they are used to measure the momenta of charged particles produced by neutrino interactions elsewhere in the detector, and therefore determine the event rate as a function of neutrino energy for the neutrino beam, prior to oscillation. Finally, the amount of ionization left by each particle, when combined with the measured momentum, is a powerful tool for distinguishing different types of charged particles, and in particular allows the relative abundance of electron neutrinos in the beam to be determined.

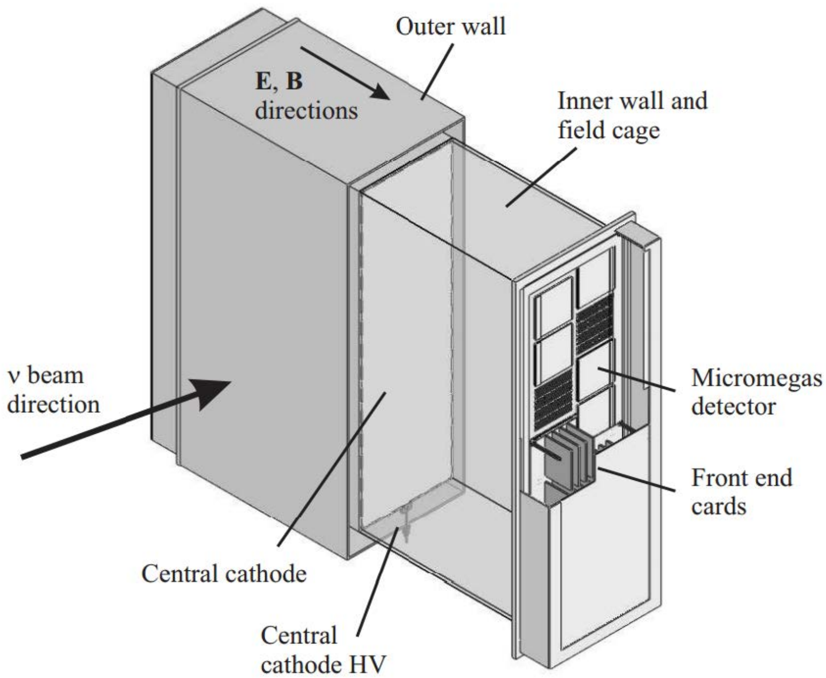

Figure 2.11: TPC Overview [48]

2.1.7 Fine Grained Detectors (FGD)

Two fine grained detectors (FGDs) provide target mass for neutrino interactions as well as tracking of charged particles coming from the interaction vertex.

Chapter 3

Pi-Zero Detector

Pi-Zero Detector (P0D) is the detector used in this analysis. The primary goal of the P0D is to measure the neutral current process $\nu + N \rightarrow \nu + X + \pi^0$ on water targets[48]. Furthermore, because irreducible intrinsic ν_e component in the neutrino beam is the main background in the appearance measurement at SK, P0D which uses water as targets can measure the ν_e CC interaction rate and cross-section on water. Details about the physical construction and event reconstruction will be described in this chapter.

3.1 Detector Description

Figure 3.1 shows the cross-sectional schematic of P0D where the neutrino beam is from left to right in the figure. The beam direction is defined as z direction, the upward direction is defined as y, and x direction points inwards to the paper. The blue color in figure 3.1 represents water targets. There are two parts containing water targets, Upstream Water Target (USWT) and Central

Water Target (CWT). The water bags are fillable in P0D so that P0D can run with water filled or emptied. As a result, there are two configuration for P0D, water-in configuration and water-out configuration. Conceptually, a subtraction between the two configurations enables measurements just on water targets.

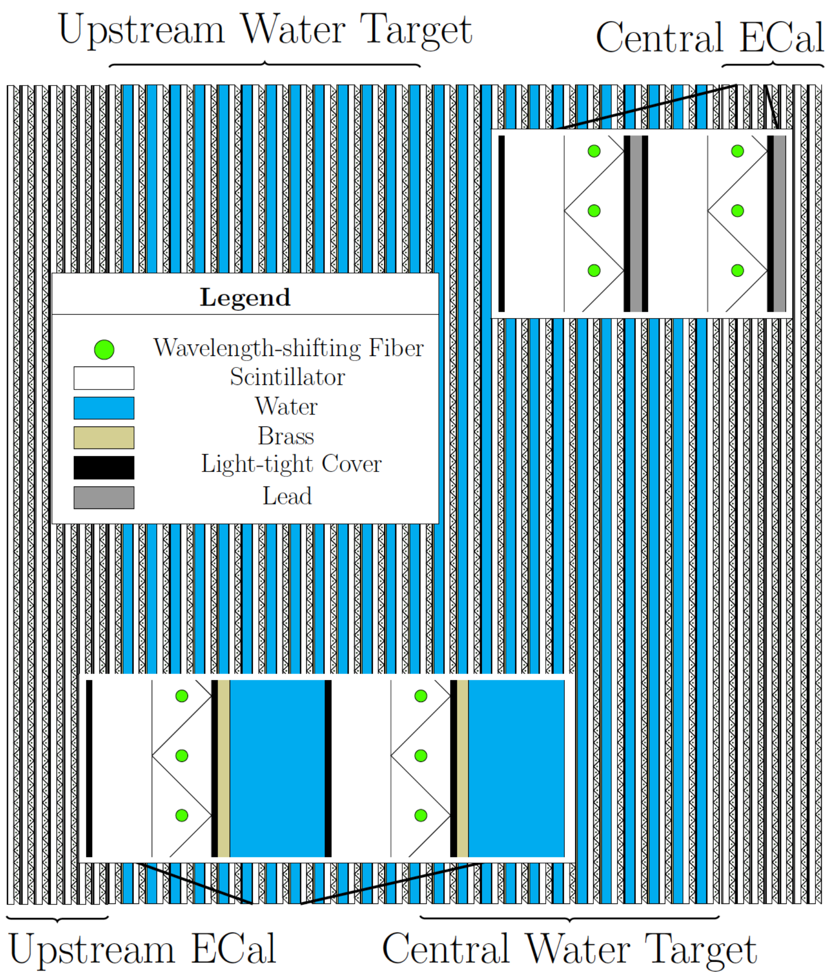

Figure 3.1: Schematic of P0D. The neutrino beam is from the left and going right [59].

Water target (WT) region consists of alternating two layers of scintillator bars, a layer of brass and a layer of water bags. The two layers of scintillator bars which is also called a P0D module (P0Dule) consist of one layers of 134 vertical scintillator bars (2133mm long) and another layer of 126 horizontal bars (2172mm long). The cross section of each scintillator bar is triangular with 33 mm base and 17 mm height. There is a single hole whose diameter is about 1.5mm filled with a Wave-Length Shift (WLS) fiber (Kuraray double-clad Y11 of 1 mm diameter) in each scintillator bar. Each fiber is mirrored on one end and the other end is optically read out using a Hamamatsu MPPC (Multi-Pixel Photon Counter) and each photodetector is read out with TFB electronic [59]. Figure 3.2 shows the WLS fiber in a scintillator bar and its connection to MPPC. When charged particles passing scintillator bars and exciting atoms and then emitting photons, the fiber can capture photons and transfer signals to MPPC to collect photons. A layer of reflective materials is added to the outside of each bar to reflect escaping light back into the bulk and increase the probability of capture by the center fiber. Location of scin-

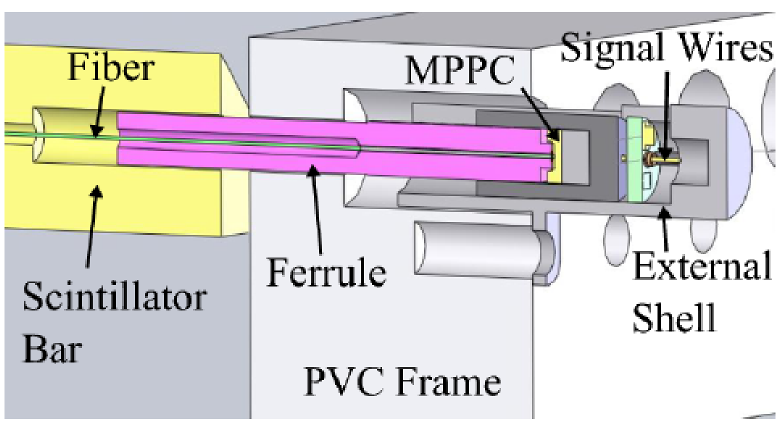

Figure 3.2: A view of the edge of a P0Dule showing how the WLS fibers exit the scintillator bars and couple to the MPPCs[59]

tillator bars provide position information. Such cross structures of scintillator bars of each P0Dule provide fine segmentation to reconstruct charged particles and photons travelling in P0D. There are 13 P0Dules in USWT and CTW, respectively.

Each layer of water bags consists of two single water bags with dimension 1006mm $\times$ 2062mm $\times$ 28mm next to each other in x direction. There are in total 25 layers of water bags (50 single water bags). Knowing the water mass is very important for P0D analysis as water is the interaction target. Other than estimating the water mass using density $\times$ volume, to determine water mass more precisely, several measurements on water mass are perform after different runs.

The most upstream and downstream parts are Upstream ECal (USECal) and Central ECal (CECal) which consist of alternative P0Dules and lead sheets. There are 7 P0Dules and 7 lead sheets in USECal and CECal, respectively. The width of lead is about 4.5mm. Scintillator bars at the two ends are used on trajectory reconstructions. Lead whose radiation length is 6.37 g/cm^2[60] provides a veto before and after the water target region to effectively reject particles entering from interactions outside of P0D and improve containment of electromagnetic showers.

3.2 Reconstruction

Figure 2.7 shows that, in ND280, neutrino flux peaks at 600MeV. Thus, electrons produced by charge-current interaction of electron neutrino (ν_e) have high energy (>> critical energy) and then the predominant channel of energy loss is Bremsstrahlung radiation. Photons from π^0 decay which are produced by neutral-current interaction lose energy predominantly by pair production. Besides, P0D contains high Z materials like brass and lead. Thus, when high energy electrons or photons passing through P0D, bremsstrahlung and pair production generate more electrons and photons and cause electromagnetic (EM) cascade, which is also called showering here.

Figure 3.3 shows the sequence of P0D reconstruction algorithms. After the preparation, all hits are first propagated to track reconstruction which is to reconstruct tracks caused by muons or protons if saying in a very simplified way. Those hits that are more likely from the EM cascade will then be passed to the shower reconstruction stage. Each steps will be introduced in this chapter following the sequence.

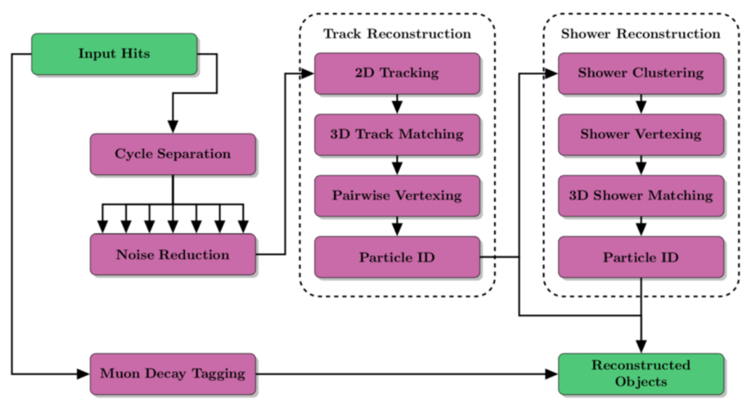

Figure 3.3: Sequential algorithm chain of the P0D reconstruction

3.2.1 Input and Preparation

The input to the reconstruction algorithm is the output of the calibration for either data hits collected by MPPC or Monte-Carlo simulated hits. As the PØD electronics (Trip-T here) collects data into 23 cycles, inputs hits are first divided into 23 cycles and in stages later only one vertex in each cycle is reconstructed. Then hits in each cycle go through noise check. Hits that cannot pass certain selection criteria are excluded as noise hits. The criteria is list below. Cycles with at least 5 cleaned hits continue to the next step in the reconstruction.

Hits Selection Criteria

- It has charge Q > 15 pe, and has a neighbor in the same view within 30 ns in time and 20 cm in space.
- It has charge Q > 7 pe, and has a neighbor in the same view within 30 ns in time and 10 cm in space.
- It has a neighbor within 30 ns in time and 3.5 mm in space (with no charge requirement).

3.2.2 Track Reconstruction

P0D track reconstruction can be generalized into 4 steps as shown in figure 3.3. The geometric information of scintillator bars can provide location information of hits in xz or yz plane. The first step is to reconstruct 2D tracks on xz and yz plane.

Hough transform is used to construct track seeds by selecting hits that conform to a straight line. The transform is constructed with bin sizes of 1.8° and 25 mm, and each seed must have a minimum of four hits. After seeds are constructed, a road following algorithm is applied to extended the track layer by layer. The road following algorithm will search the area within 60mm

What is of more interests is the view in 3D space. Thus, once the 2D tracks are reconstructed, tracks in xz and yz plane are paired or matched to construct 3D tracks. Every 2D track in xz plane is paired with every 2D track in yz plane. A probability is assigned to every pair and the probability is obtained by the number of overlapping layers, the relative disparity between the charges of the two tracks, and whether a track has already been matched. The most probable pair is selected each time after pairing all 2D tracks and then the rest 2D tracks are ran again following the matching algorithm until there is no pairing probability is above the given threshold.

Two types of 3D fit can be applied to the match tracks, Kalman filter and Parametric fitter. When the matched track passes more than 4 p0dules, Kalman filter is applied and the rest matched short tracks uses Parametric fitter. All 2D and 3D tracks are then passed to the stage of Particle Vertexing and a pairwise vertexing algorithm is applied. Reconstruction of trajectories are not the only things of interests. Knowing what types of particles the tracks may be is also very important. Tracks will be passed through particle identification (PID) process. There are 4 hypotheses for PID which are kLightTrack, kHeavyTrack, kEM and kOther, respectively. Hypothetically, the 4 hypotheses represents muons(kLightTrack), protons(kHeavyTrack), electrons and photons(kEM), and others(kOther), respectively. As shown in figure 3.4, short tracks through Parametric fitter is assign as kOther directly. For tracks through Kalman filter, the other three hypotheses are assigned with likelihoods. The tracks will be classified to the one whose likelihood is maximum. If tracks are classified as kEM, they will go to the shower reconstruction stage. Otherwise, they will go to final objects stage directly.

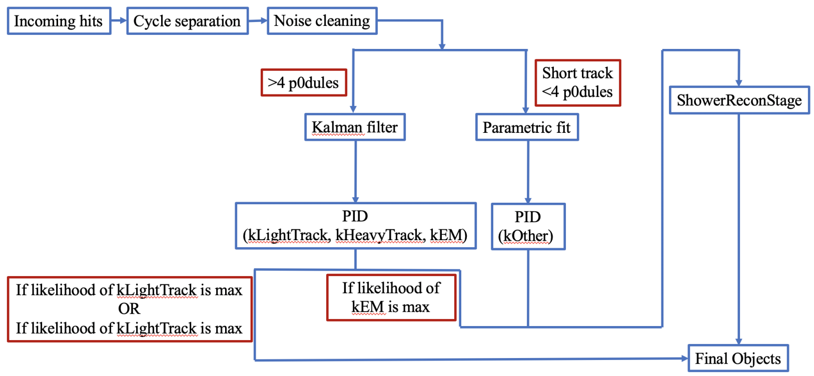

Figure 3.4: Flowchart of Particle Identification Process in Track Reconstruction in P0D

Likelihood of each PID hypothesis is calculated based on variables listed below.

- trackP0DuleAsymmetry
- trackMedianWidth
- trackWTCharge
- trackWTChargeRMS
- trackECalCharge
- trackECalChargeRMS
- trackECalChargeAsym
- trackLayerChargeVAngle

The probability density function of each variable for each PID is known. The log-likelihood of each PID hypothesis equals to the sum over the log-likelihood of all variables listed above. More details about the PID process will be discussed in the chapter 5.3.3 when discussing the systematic uncertainties of PID.

3.2.3 Shower Reconstruction

Hits of tracks which are classified as kEM or kOther or unused hits in track reconstruction stage will be passed to the shower reconstruction stage. Hits are first clustered and used to construct shower views in 2D space, xz an yz. Then, different from track reconstruction stage, shower vertex is determined before 3D matching. After that, 2D showers are paired to construct 3D views.

3.3 Energy Calibration

The reconstructed energy of electron is estimated via the linear relations with the reconstructed charges (PE) shown as equation 3.1 and 3.2 for water-in and water-out configuration, respectively. Since absorber materials for PØD water target (WT) and electromagnetic calorimeter (ECal) are different, each constant need to be derived separately.

$$E_e = k_{ECAL} * \sum_{i \in ECal} Q_i + k_{water-in,WT} * \sum_{i \in WT} Q_i \tag{3.1}$$

$$E_e = k_{ECAL} * \sum_{i \in ECal} Q_i + k_{water-out,WT} * \sum_{i \in WT} Q_i \tag{3.2}$$

where E_e is electron energy and Q is the charge of the reconstructed object, and the sum runs over the charges Q of the nodes in that part of the detector [61].

Table 3.1: Energy Calibration Constant

MeV/PE	Water-in WT	Water-out WT	ECal
Track Recon	0.1847 ± 0.0130	0.1340 ± 0.0207	0.1845 ± 0.0144
Shower Recon	0.1667 ±0.0064	0.1158 ±0.0125	0.1701 ± 0.0130

In order to estimate the three linear coefficient, according to T2K-TN-240 [61], electron particle gun MC samples are used in different geometries and energy regions. 10,000 electrons with energy uniformly distributed from 1MeV to 3GeV are created. For the constant in WT, a sample of electrons starts at the USWT and goes downstream, and all of the charge of the particle is required to be inside the WT to investigate that piece of the PØD. For the ECal, nd280mc configuration is modified to fill water target region with ECal layer. After running through nd280mc, elecSim, oaCalib and PØDRecon, the outputs are used to extract true electron energies E_e and charges Q from reconstructed track/shower. It was required that at least 90% of the true energy deposit must be in the PØD, to ensure that the particle is mostly contained inside the PØD. Then the distributions of Q/E_e fitted with Gaussian distribution. After that, the three linear coefficient are estimated shown in table 3.1

Chapter 4

Selection

In this chapter, the software used to generate Monte Carlo (MC) simulations and summary of data used in this thesis will be presented in section 4.1. The signal definitions in limited phase space defined by a Boost Decision Tree (BDT) used in the two analyses in FHC and RHC respectively will be described in section 4.2. Although measurements in FHC and RHC are independent to each other, the selection strategies to select signal samples are almost the same. Thus, the strategies will be presented in section 4.3 and selected results in FHC and RHC will be shown in section 4.4. Besides, control samples to constrain the background in the selected signal sample will be discussed in section 4.5 and 4.6.

4.1 Software and MC/Data Samples

The nominal MC samples are generated by production 6T where the version of neutrino event generator is NEUT 5.4.0. As discussed in Chapter 3, P0D has two configurations, water-in and water-out. The beam has two modes, forward-horn-current (FHC) and reverse-horn-current(RHC). Thus, there are 4 configurations for P0D measurements shown in the table 4.1. The total POT breakdown is listed in the table 4.2. It is a summary of POT of data used in the fitter and obtained by the function, GetPOT(), in the class of DataSample in Highland2.

Table 4.1: P0D and Beam Configuration

	Water-in	Water-out
FHC	water-in+FHC	water-out+FHC
RHC	water-in+RHC	water-out+RHC

Table 4.2: Data POT used for P0D Analysis from run1 to run10

POT(e+20)	Water-in+FHC	Water-out+FHC	Water-in+RHC	Water-out+RHC
Run1	NOTU	0	0	0
Run2	0.42680	0.35989	0	0
Run 3	0	NOTU	0	0
Run 4	1.57898	1.52004	0	0
Run 5	NOTU	0	0.16578	0
Run 6	0	0	0	3.50175
Run 7	0	0	2.43921	0
Run 8	1.57958	4.02461	0	0

4.2 Signal Definition

As discussed in chapter 3, when high energy(>> critical energy) e^- (or e^+) travelling through P0D, bremsstrahlung and pair production generate more e^-, e^+ and photons, and cause EM cascade. Thus, although the magnetic field applied will bent the trajectory of charged particles, it is very difficult to distinguish such curvatures for e^- and e^+ in P0D due to the EM cascade, which means that e^- and e^+ is almost non-distinguishable in P0D. From the past experimental results [43, 46], it is known that the $\bar{\nu}_e$ CC cross section is smaller than ν_e cross section. Figure 2.7 shows that the flux of ν_e is higher than the flux of $\bar{\nu}_e$ in FHC and smaller than the flux of $\bar{\nu}_e$ in RHC. Thus, it is expected that the number of $\bar{\nu}_e$ CC interactions is much smaller than the number of ν_e CC interaction in FHC and as a result, in FHC the signal is defined for ν_e CC alone. However, the number of ν_e CC interactions is expected to be at a comparable level with $\bar{\nu}_e$ CC interactions in RHC. Thus, the signal is defined to be $\nu_e + \bar{\nu}_e$ CC interactions in RHC. The signal in FHC and RHC are defined separately as below.

- in FHC mode, ν_e Charged-Current (CC) interactions on water generating $1e^-$ + 0 visible proton + 0 visible charged pion

- in RHC mode, $\nu_e + \bar{\nu}_e$ Charged-Current (CC) interactions on-water generating $1e^{\pm}$ + 0 visible proton + 0 visible charged pion

The limited phase space of $1e^-$ (or $1e^{\pm}$) + 0 visible proton + 0 visible charged pion is defined by a function using Boost Decision Tree.

In P0D Shower Reconstruction, protons (or charged pions) are not visible (or distinguishable) from electrons under some scenarios. For example,

- If the energy of a proton (or a charged pion) is very low in the absolute scale, then the proton (or charged pion) is not visible.
- If the kinetic energy of a proton (or a charged pion) is very low comparing with the kinetic energy of an electron, then it's likely that hits from the proton (or charged pion) will be mis-reconstructed into the shower caused by the electron.
- When a proton (or a charged pion) has very high angle (i.e. going backward) with respect to the beam direction, then the proton (or charged pion) will be hard to be recognized by the reconstruction algorithms which are built mainly for particles moving forward.
- When a proton (or a charged pion) is very close to an electron, then it is very likely that the proton (or the charged pion) and the electron will be reconstructed into one shower instead of two separate showers.

Thus, knowing the kinematic conditions where the protons (or charged pions) are visible (or distinguishable) is important to define the signal. However, the edges of kinematic regions where we can effectively reconstruct objects for protons and charged pions are complicated. They do not just depend on kinematics of protons (or charged pions), but also depend on their relations with electrons kinematics. Thus, the idea of using Boost Decision Tree (BDT) to provide a function to define the kinematic region is brought up. BDT for protons and charged pions are trained separately using samples from particle gun simulations. Using proton as an example here. In the simulation, the electrons kinetic energies are from 600MeV to 3GeV with angles w.r.t beam distributed uniformly from 0° to 45°. The protons kinetic energies are from 150MeV to 400MeV with angle from 0° to 180° w.r.t to the beam. Feature engineering of the BDT is based on the domain knowledge on physics and the detector. The BDT has 4 features, proton kinetic energy (KE_p), the ratio of electron kinetic energy energy over proton kinetic energy (KE_e/KE_p), angle of proton (θ_p) and angle between proton and electron (θ_{ep}). The goal is to predict whether the proton (charged pion) is visible at reconstruction level from the truth information, so it can be treated as a classification problem and the loss function used is binary cross-entropy. The software used to train BDT is XGBoost.

To give more intuitions on what type of events that the BDT may classify as signal or non-signal, tables 4.3 and 4.4 show the fraction of events that are classified as signal channel by channel in FHC and RHC. Most of CCQE and MEC events are classified as signal which is expected because it is expected that there is no charged pions produced in for example CCQE. Most of CC DIS and Multi π events are classified as non-signal as expected.

4.3 Signal Sample Selections

The selection cuts aim to select reconstructed objects of electrons (and positrons) produced by the ν_e (and $\bar{\nu}_e$) CC interaction. P0D contains high Z material, brass in the Water Targets Region and lead in the ECals, which causes the electrons to shower. As a result, the curvatures of reconstructed trajectories of electrons and positrons in the magnetic field are not applicable to distin-

Table 4.3: Split of each NEUT5.4.0 interaction channel by BDT classification in FHC before selections. Sum over the two columns at each row equals to 1.

(a) Water-in

Category	BDT Signal	BDT non-Signal
ν_e CCQE	76.83%	23.17%
ν_e CCRES	57.21%	42.79%
ν_e CCMEC	74.23%	25.77%
ν_e CCCOH	51.65%	48.35%
ν_e CCDIS	20.78%	79.22%
ν_e CC LowWMP	39.86%	60.14%

(b) Water-out

Category	BDT Signal	BDT non-Signal
ν_e CCQE	76.54%	23.46%
ν_e CCRES	56.84%	43.16%
ν_e CCMEC	74.74%	25.26%
ν_e CCCOH	56.28%	43.72%
ν_e CCDIS	20.76%	79.24%
ν_e CC LowWMP	38.59%	61.41%

guish electrons and positrons in P0D. Thus, their behaviors in P0D are non-distinguishable and selection strategies developed for electrons are applicable to positrons. Therefore, the selection strategies to select signal samples in FHC and RHC are the same except that cut values may be different. Selection cuts will be presented step by step in this section.

In P0D Reconstruction, as described in Chapter 3.2, ideally an electron should go through the track reconstruction stage and then go through shower reconstruction stage. As a result, such an electron will have an associated reconstructed object after track reconstruction stage and another object after shower reconstruction stage. Just to clarify again, objects after track recon-

Table 4.4: Split of each NEUT5.4.0 interaction channel by BDT classification in RHC before selections. Sum over the two columns at each row equals to 1.

(a) Water-in

Category	BDT Signal	BDT non-Signal
$\nu_e + \bar{\nu}_e$ CCQE	89.33%	10.67%
$\nu_e + \bar{\nu}_e$ CCRES	68.56%	31.44%
$\nu_e + \bar{\nu}_e$ CCMEC	88.25%	11.75%
$\nu_e + \bar{\nu}_e$ CCCOH	53.49%	46.51%
$\nu_e + \bar{\nu}_e$ CCDIS	25.46%	74.54%
$\nu_e + \bar{\nu}_e$ CC LowWMP	47.86%	52.14%

(b) Water-out

Category	BDT Signal	BDT non-Signal
$\nu_e + \bar{\nu}_e$ CCQE	87.89%	12.11%
$\nu_e + \bar{\nu}_e$ CCRES	66.68%	33.32%
$\nu_e + \bar{\nu}_e$ CCMEC	86.87%	13.13%
$\nu_e + \bar{\nu}_e$ CCCOH	47.73%	52.27%
$\nu_e + \bar{\nu}_e$ CCDIS	26.63%	73.37%
$\nu_e + \bar{\nu}_e$ CC LowWMP	49.47%	50.53%

struction stage are called tracks and objects after shower reconstruction stage are called showers in this thesis.

4.3.1 Three-Dimensional Reconstructed Object

To ensure a good reconstruction quality, first of all, this cut requires the vertex is valid, i.e. the vertex is reconstructed in all three dimensions. As mentioned before, ideally an electron should go through the track reconstruction stage and then go through shower reconstruction stage. Then it is required that there is at least one object in track reconstruction stage that is reconstructed in all three dimensions and at least one object in shower reconstruction stage that is reconstructed in all three dimensions. After the valid dimension check, the object whose reconstructed energy is highest among all valid objects after track reconstruction stage is selected as candidate track and the shower whose reconstructed momentum is highest among all valid objects after shower reconstruction stage is selected as candidate shower.In a short summary, this cut requires

- Three-Dimensional Vertex
- Three-Dimensional Candidate Track
- Three-Dimensional Candidate Shower

4.3.2 Fiducial Volume Cut

This cut requires that the vertex is inside the Fiducial Volume (FV) of P0D. T2K-TN-073[62] has a detailed study of FV in P0D and table 4.5a summarizes the definition of P0D FV in it.

Figures from 4.1 to 4.4 show the N-1 distribution of vertex positions after track recon stage along three dimensional coordinates which are the distributions obtained after applying all cuts but the cut on vertex position along that coordinate in all configuration. The N-1 distributions show that the FV cut can effectively remove events which happens outside of the P0D FV. Along the Z axis, because the cut on the number of layers that the candidate track passes which will be discussed in section 4.3.5, has some effects on shrinking the FV edge on the downstream of P0D. Thus, the downstream edge of the FV is explicitly shrunk and redefined it as table 4.5b shows.

Table 4.5: Fiducial Volume of P0D

(a) Fiducial Volume of P0D in TN073

Dimention	Minimun(mm)	Maximum(mm)
X	-836	764
Y	-871	869
Z	-2969	-1264

(b) Fiducial Volume of P0D in this Analysis

Dimention	Minimun(mm)	Maximum(mm)
X	-836	764
Y	-871	869
Z	-2969	-1536

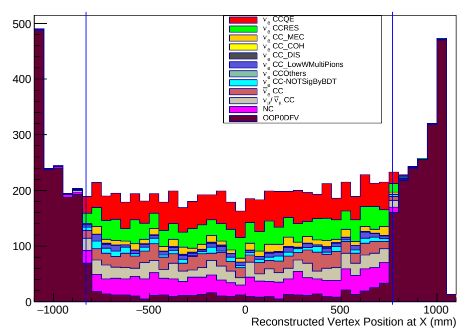

(a) Vertex Position along X (mm)

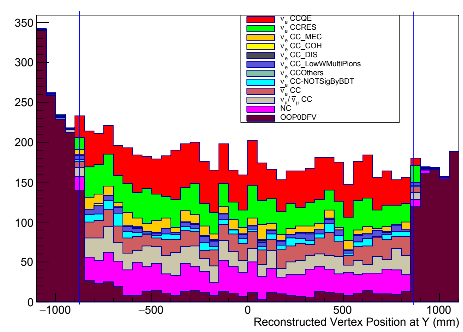

(b) Vertex Position along Y(mm)

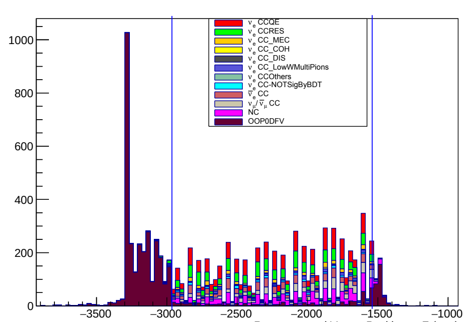

(c) Vertex Position along Z(mm)

Figure 4.1: N-1 Plot of Vertex Position (water-in + FHC)

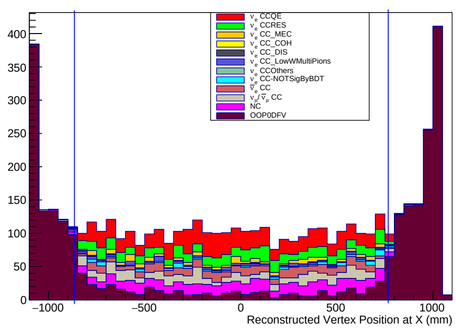

(a) Vertex Position along X (mm)

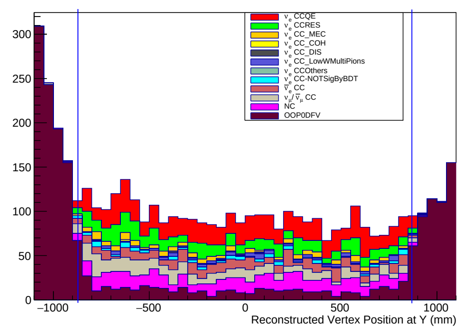

(b) Vertex Position along Y(mm)

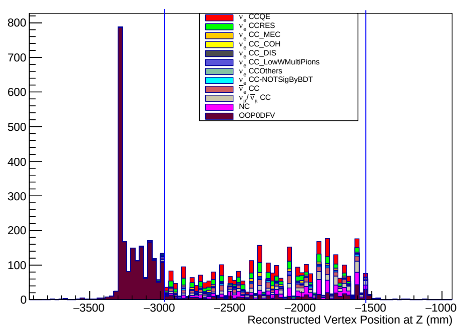

(c) Vertex Position along Z(mm)

Figure 4.2: N-1 Plot of Vertex Position (water-out + FHC)

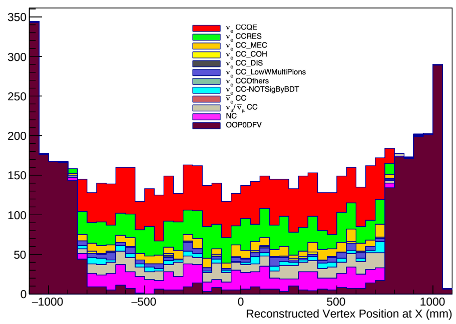

(a) Vertex Position along X (mm)

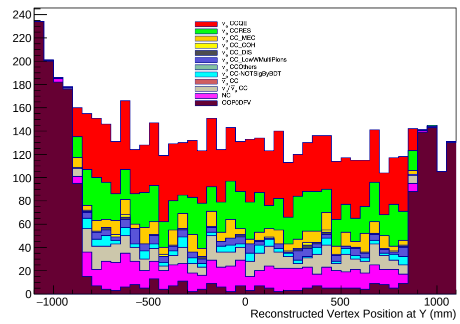

(b) Vertex Position along Y(mm)

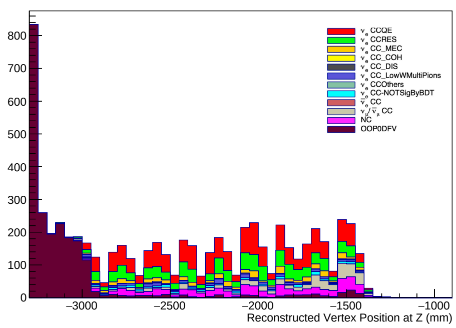

(c) Vertex Position along Z(mm)

Figure 4.3: N-1 Plot of Vertex Position (water-in + RHC)

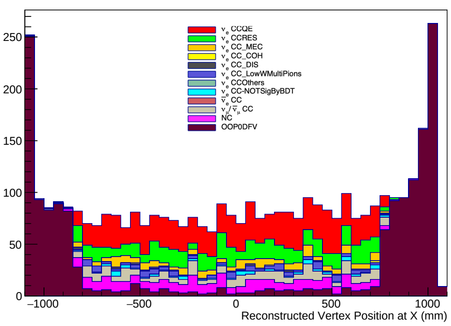

(a) Vertex Position along X (mm)

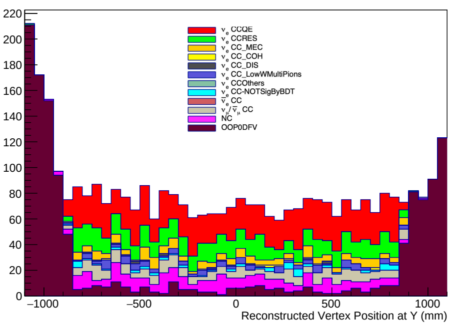

(b) Vertex Position along Y(mm)

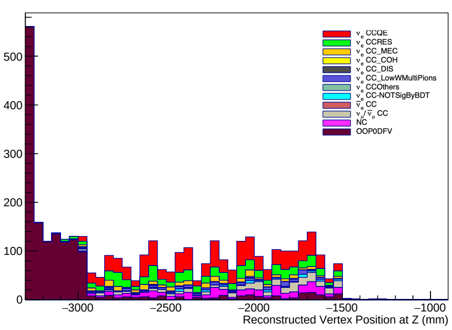

(c) Vertex Position along Z(mm)

Figure 4.4: N-1 Plot of Vertex Position (water-out + RHC)

4.3.3 Hit Fraction Cut

As discussed in the chapter 3, when a reconstructed track is classified as a shower-like object, the track object will move to shower reconstruction stage, so hits associated with the track will be propagated to reconstruct showers. Thus, it is expected that for a track and a shower caused by the same particle, the set of hits used to reconstruct the shower contains hits used in the track, i.e. the fraction of the number of same hits in a shower and its associated track over the number of hits in the associated track should be 1 in theory. Due to some noise effects, the value in reality will not be exactly 1, but it should be very close to 1. When selecting the candidate track and candidate shower, it is necessary to do such a sanity check to ensure that they are from the same set of hits. The cut value is chosen to be 90%. Figures 4.5 show the N-1 distributions for all 4 configurations, respectively.

4.3.4 Shower Direction Cut

The structure of P0D scintillator bar as shown in figure 4.6 [59] is triangular with two equal sides. Its height is 17 ± 0.5mm and width is 33 ± 0.5mm. Its cross section is approximately a right angle. Thus, particles with an angle of more than $45°$ with respect to the beam direction would hit more than two adjacent bars in a layer. As the P0D reconstruction algorithm (P0DRecon) is designed to deal with two adjacent bar hits in a layer, such events with more than two active adjacent bars would cause mis-reconstruction. Thus, a cut is applied to require that the angle of the candidate shower w.r.t the beam direction is smaller than $45°$ [61]. As s reference, figures 4.7 show the N-1 plots

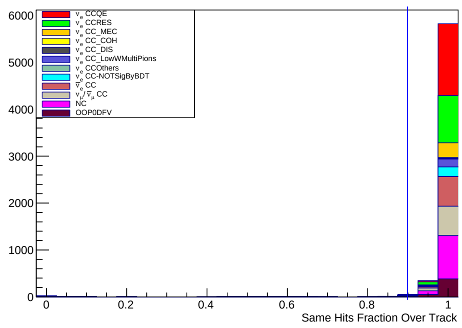

(a) water-in + FHC

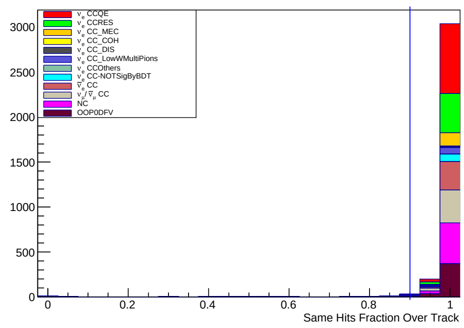

(b) water-out + FHC

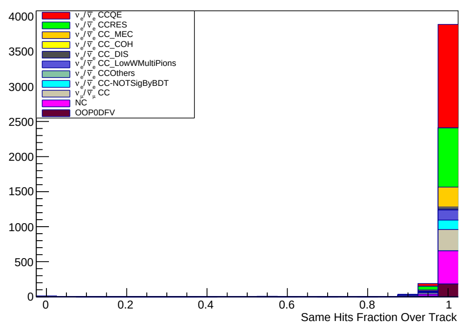

(c) water-in + RHC

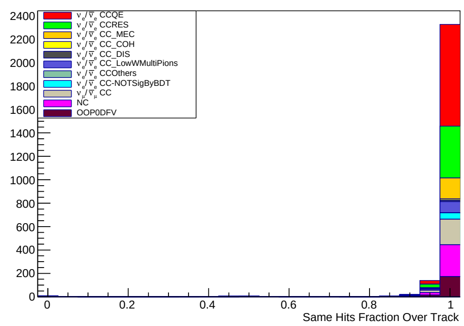

(d) water-out + RHC

Figure 4.5: N-1 Plot of Hit Fraction

of the angle distributions for all 4 configurations.

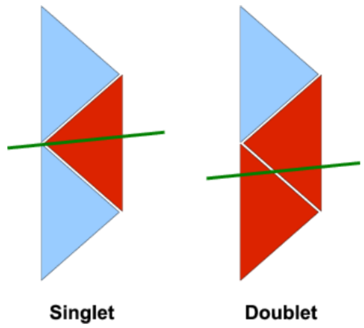

Figure 4.6: P0D Scintillator Bar Structure

4.3.5 Number of Layers that the Candidate Track Passes

This cut is applied for multiple reasons.

- EM showers caused by electrons from ν_e CC interactions tends to travel longer than EM showers caused by for example NC interactionunder the same neutrino energy.

- For interactions producing backward-going protons, P0DRecon may use hits at the end of backward-going protons as the start point and reconstruct a forward-going trajectory. Figures 4.8 show that there are much more fraction of $\nu_\mu/\bar{\nu}_\mu$ CC background events in FHC than those in RHC when the reconstructed trajectory is short. Backward-going protons from $\nu - N$ interactions is the part of the causes while as neutrons produced from $\bar{\nu} - N$ interactions are not detectable for P0D.

By optimizing the criteria of efficiency*purity, the chosen cuts values are shown in the table 4.6 for all configurations.

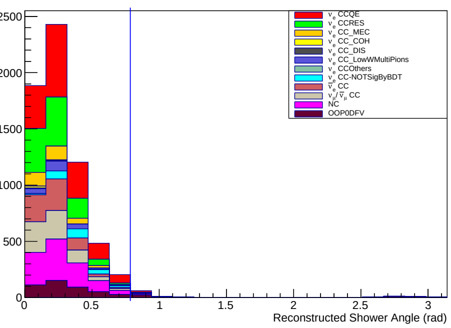

(a) water-in + FHC

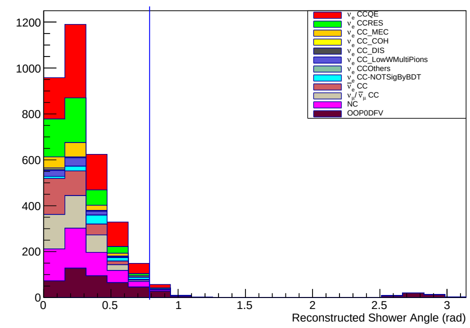

(b) water-out + FHC

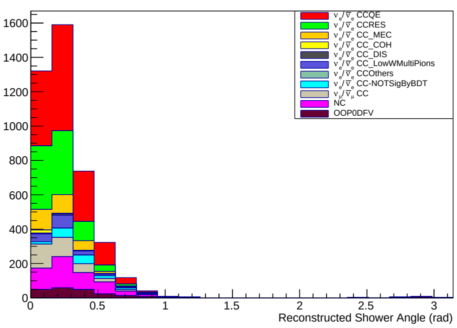

(c) water-in + RHC

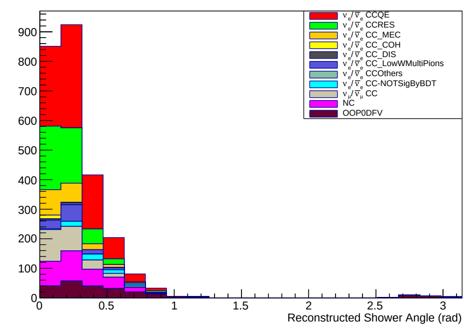

(d) water-out + RHC

Figure 4.7: N-1 Plot of Reconstructed Shower Angle

4.3.6 Track Median Width (TMW) Cut

The median width (MW) is first defined in T2K-TN-053 [63]. Because of EM showers, tracks reconstructed with hits from from electrons, are generally wider than tracks from muons which typically have only 1 or 2 hits per layer in adjacent bars. This motivates an electron-muon separation variable based on the width of the track measured in each scintillator layer through which the track passes. In each scintillator layer, the energy-weighted standard deviation of the position of the hits reconstructed in the track is calculated as follows:

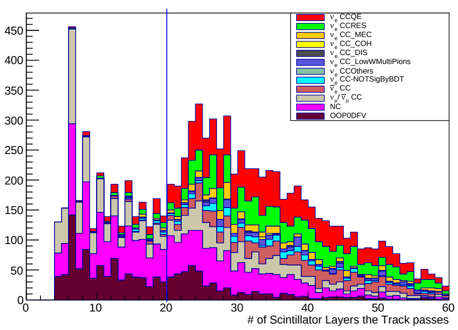

(a) water-in + FHC

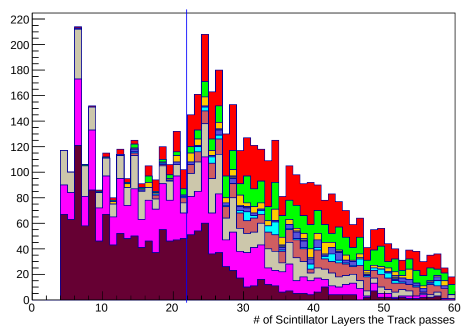

(b) water-out + FHC

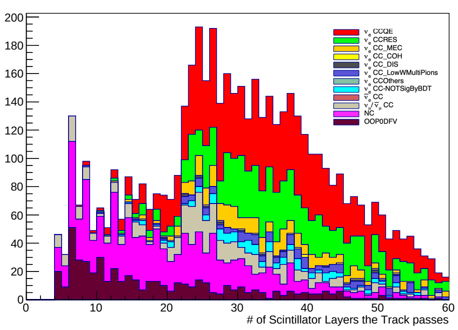

(c) water-in + RHC

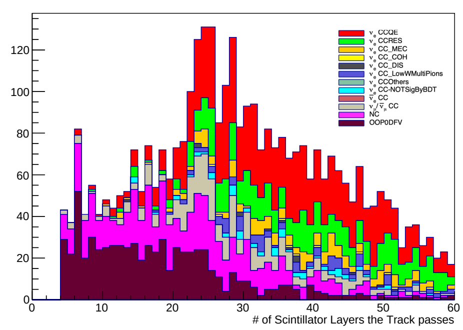

(d) water-out + RHC

Figure 4.8: N-1 Plot of Number of Layers the Candidate Track Passing

Table 4.6: Values of Cuts on Number of Layers the Candidate Track Passing

	Water-in	Water-out
FHC	20	22
RHC	18	20

- If the two hits with the highest deposited energy (after calibration) are in adjacent strips, replace them with a single hit. The new hit's position is at the energy-weighted average position of the two original hits, and its energy is the sum of the energies of the original hits. Any other hits in the layer are left unchanged. This procedure gives MIP-like layers a very small (almost always zero) width. Electrons shower, so the likelihood that the two highest energy deposits will be in adjacent bars is much lower. In studies it was shown that if bars are not merged, this strong difference between shower and MIP-like events is not seen clearly. Merging gives a stronger separation between the two hypotheses.

- The energy-weighted standard deviation of the hit positions in layer l is $\omega_l = \sqrt{\frac{\sum_j E_j(x_j - \bar{x})^2}{\sum_j E_j}}$

  where $\bar{x}$ is the average position of all hits positions in layer l. x_j is j-th hit position in layer l and E_j is its deposited energy after calibration

- For the set of hits used in the candidate track, calculate energy-weighted standard deviations of the hit positions in each layer for all layers. After removing repeated values and sorting, the median value is taken as the track median width(TMW)

Events whose candidate tracks' TMW are less than 1mm are rejected.

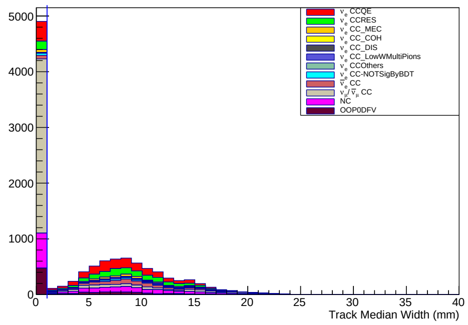

(a) water-in + FHC

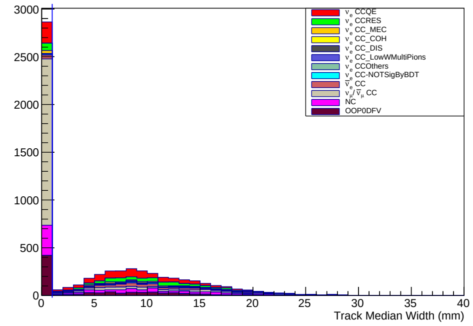

(b) water-out + FHC

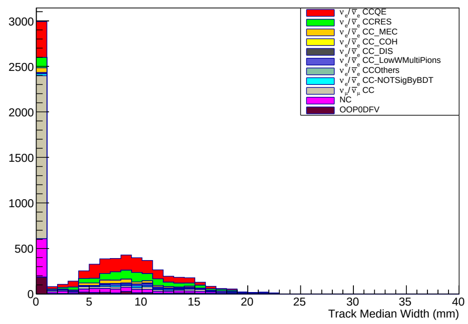

(c) water-in + RHC

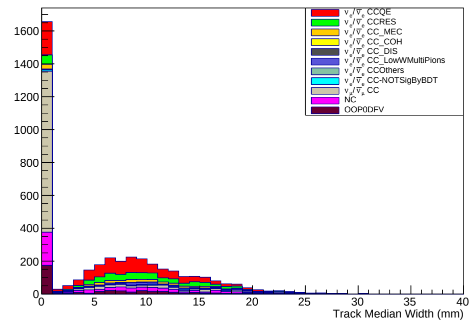

(d) water-out + RHC

Figure 4.9: N-1 Plot of Track Median Width

From figures 4.9, it is obvious that this cut removes a lot of $\nu_\mu/\bar{\nu}_\mu$ CC events effectively.

4.3.7 Shower Median Width (SMW) Cut

P0DRecon at shower reconstruction stage looks for hits in a cone from the reconstructed vertex position and use them to reconstruct one or more showers. Thus, if several particles trajectories are overlapped to each other, it is likely that hits caused by them will be combined into one reconstructed shower. For example, NC1π^0 interactions produce π^0 which will decay into two photons. In the lab frame, the two photons can fly in parallel and as a result, showers caused by the two photons will be reconstructed as one. ν_e ($\bar{\nu}_e$) CC interactions produce one e^- (e^+) which should cause one shower in P0D. It is expected that showers from single particles are relatively narrower than showers contains multiple particles, when their energies are comparable. Therefore, events with a very wide candidate shower are more likely to be background events whose showers are caused by hits from several EM particles. Shower median width (SMW) is a quantitative variable to measure the wideness of showers. The method to calculate SMW is the same as the way for TMW. Figures 4.10 show the N-1 plots of SMW which confirm that events with very wide showers are more likely to be background events such as NC interactions or ν_μ CC with multiple pions produced. After optimizing efficiency*purity, the cut values are chosen as table 4.7 shows.

Table 4.7: Values of Cuts on Shower Median Width

	Water-in	Water-out
FHC	25mm	29mm
RHC	25mm	29mm

4.3.8 Shower Charge Fraction (SCF) Cut

This analysis aims to select events with $1e^-$ + 0 visible proton + 0 visible charged pion in FHC and $1e^\pm$ + 0 visible proton + 0 visible charged pion in RHC. Therefore, it is expected that only one reconstructed shower caused by the electron from the interactions will be seen. Because the definition of 0 visible proton + 0 visible charged pion is given by a BDT function, explicitly requiring single reconstructed shower object may introduce a large systematic

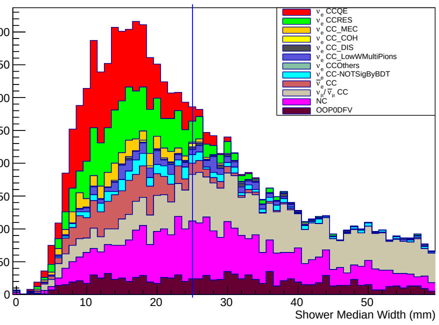

(a) water-in + FHC

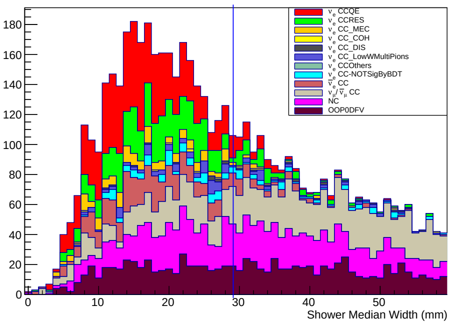

(b) water-out + FHC

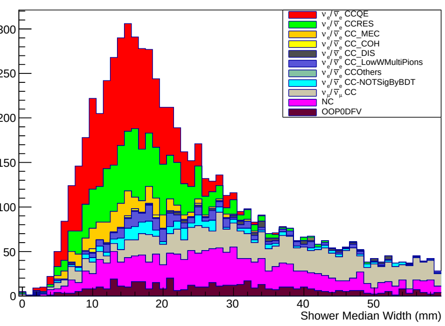

(c) water-in + RHC

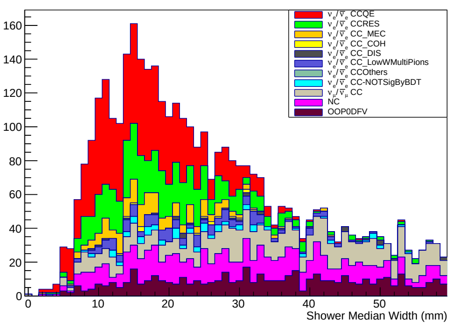

(d) water-out + RHC

Figure 4.10: N-1 Plot of Shower Median Width

uncertainty. To avoid it, instead a variable called shower charge fraction (SCF) is introduced, which is the ratio of charges in the shower over the total charges collected for the event. If SCF equals to 1, it is equivalent to the situation that only one shower object is reconstructed with all hits collected. The cut value is chosen to be 90% for all 4 configurations (SCF>0.9). Figures 4.11 show the N-1 plot of SCF.

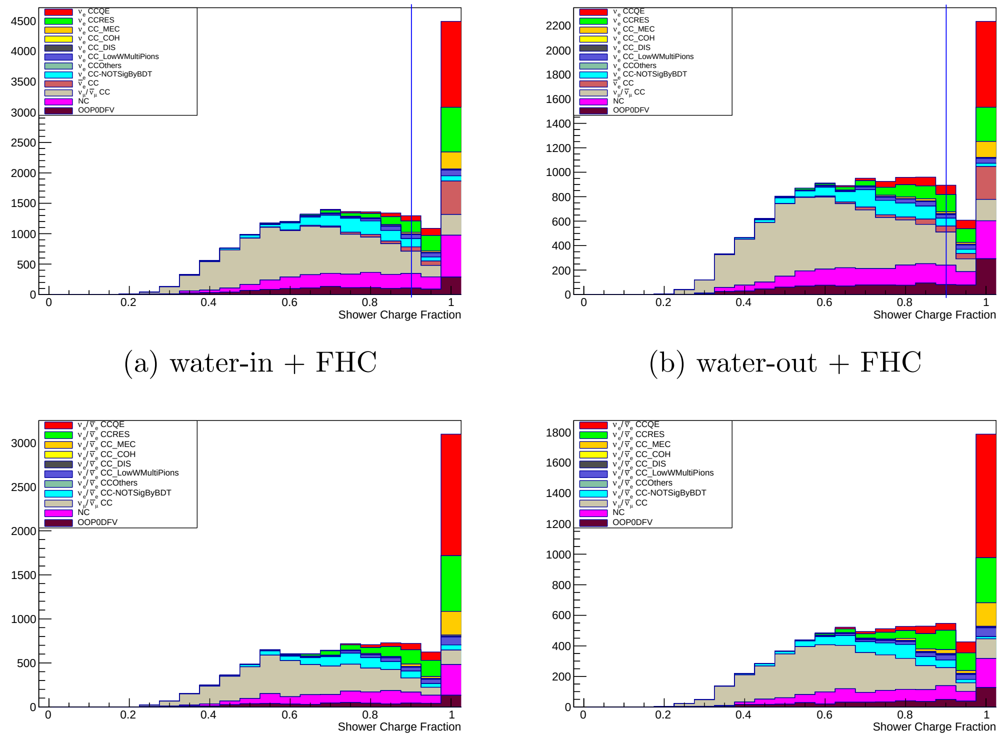

(a) water-in + FHC

(b) water-out + FHC

(c) water-in + RHC

(d) water-out + RHC

Figure 4.11: N-1 Plot of Shower Median Width

4.4 Selected Signal MC Sample

Figures 4.12 and 4.13 show the selected signal samples in FHC, and 4.14 and 4.15 show the selected signal samples in RHC.

4.4.1 Purity and Efficiency

Tables 4.8 show the purity and efficiency of different interaction channels in FHC, and 4.9 show them in RHC. Figures 4.16 show how purity and efficiency of signal in the selected sample change when applying the cuts in 4.3 in sequence. In the beginning, when no cut is applied, the purity of signal is close

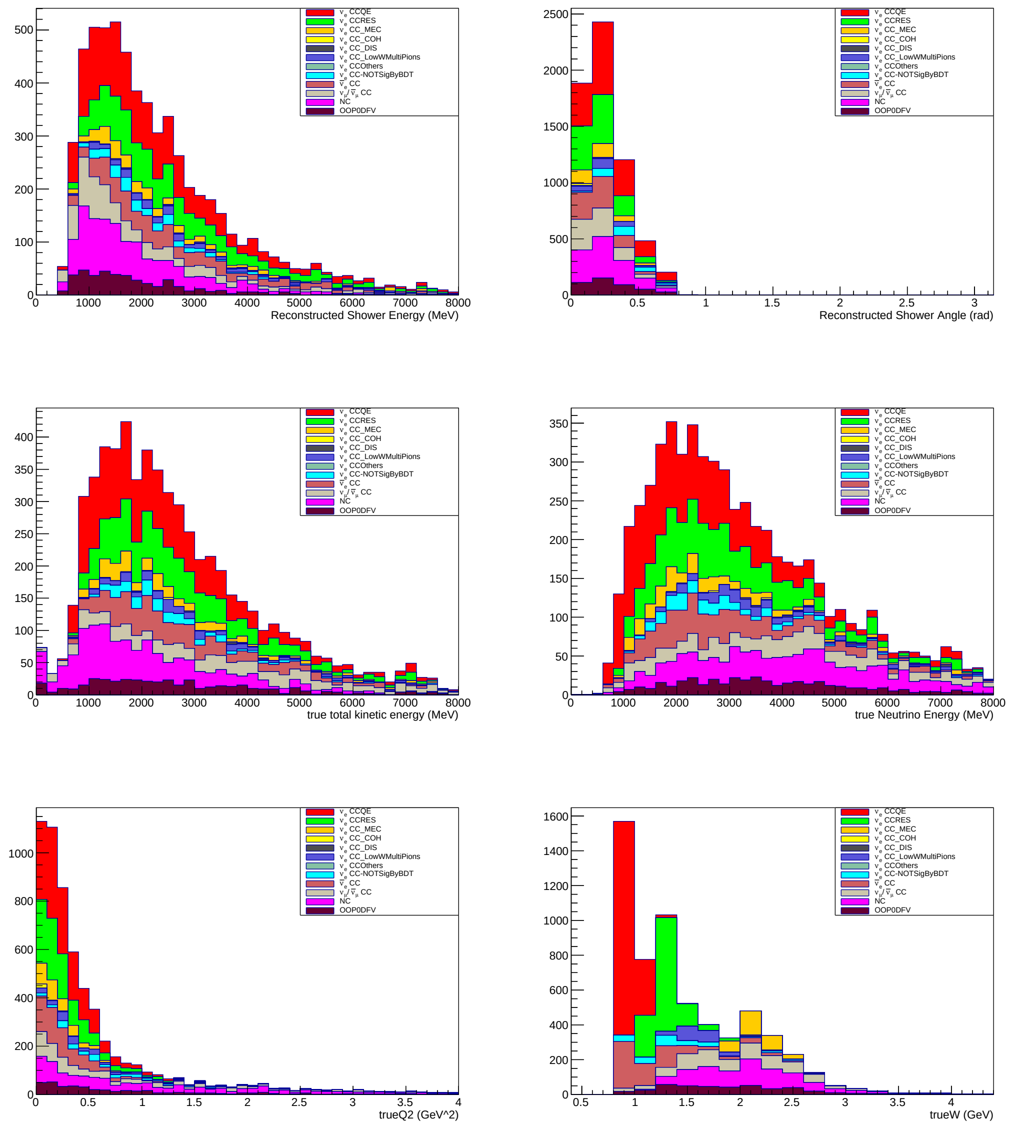

Figure 4.12: Selected Signal Samples in the configuration of water-in + FHC

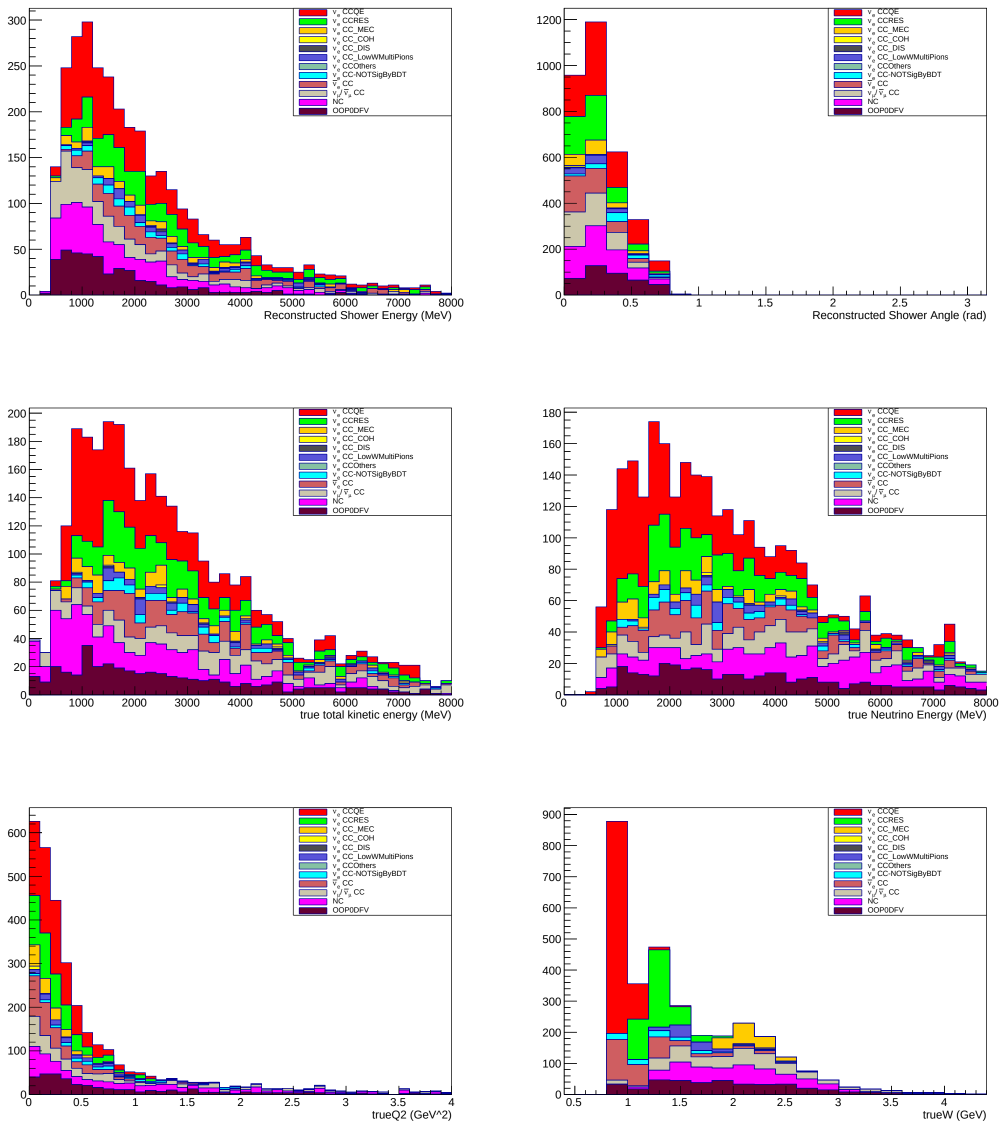

Figure 4.13: Selected Signal Samples in the configuration of water-out + FHC

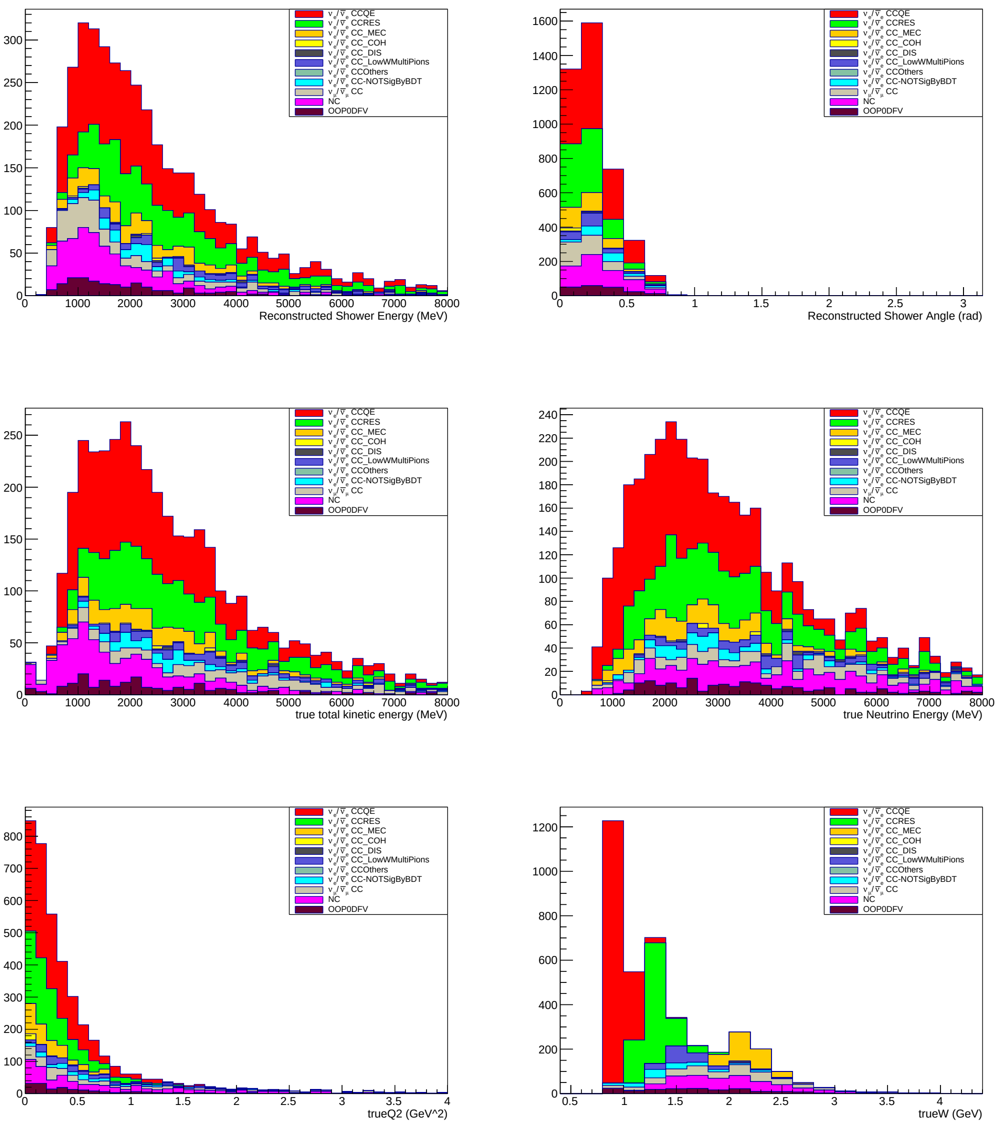

Figure 4.14: Selected Signal Samples in the configuration of water-in + RHC

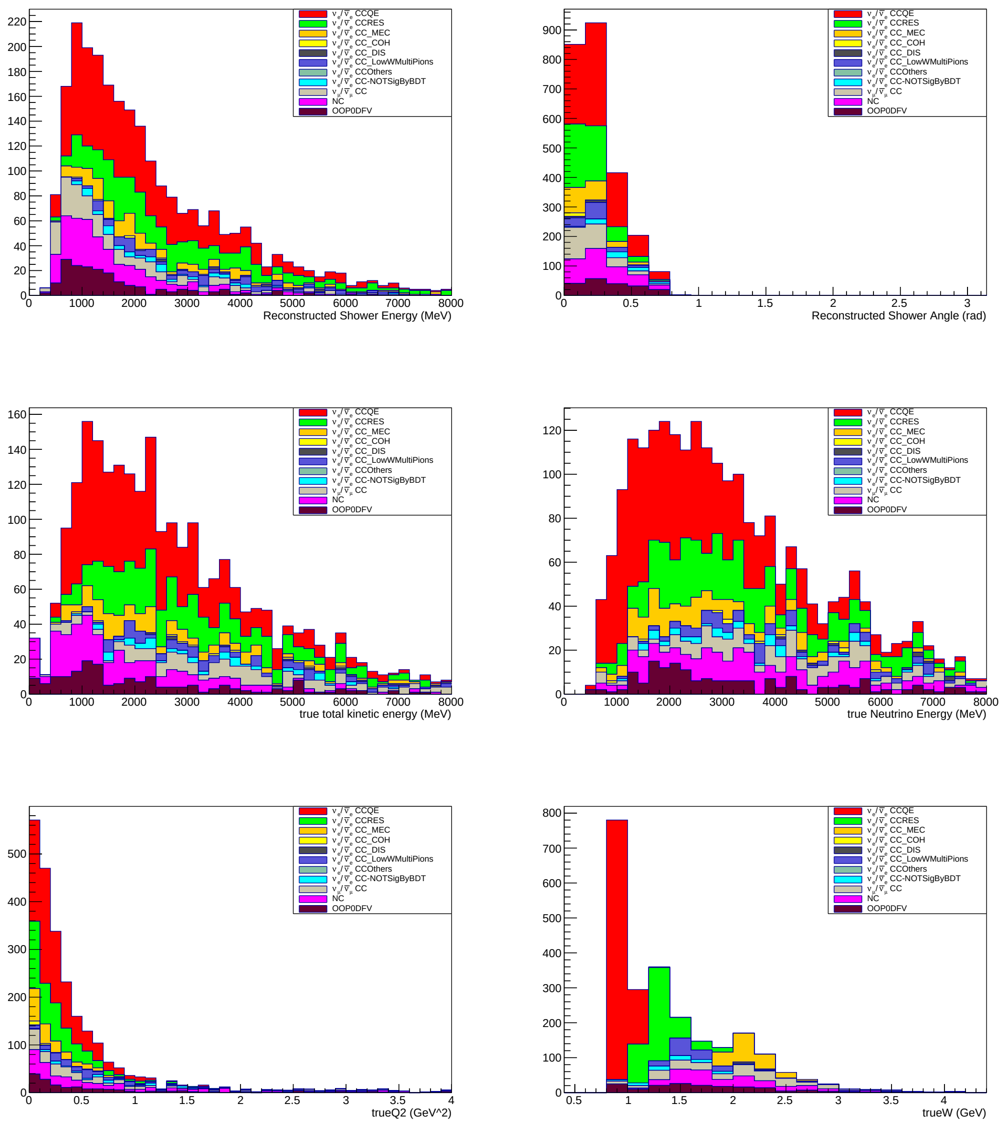

Figure 4.15: Selected Signal Samples in the configuration of water-out + RHC

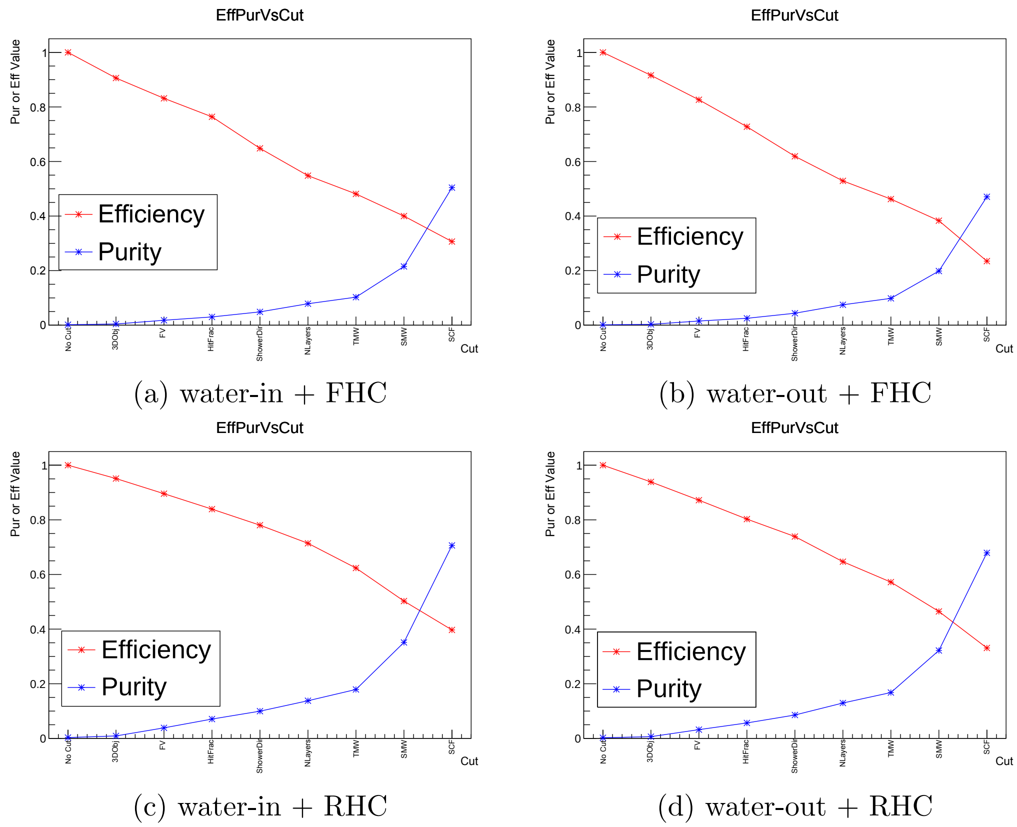

(a) water-in + FHC

(b) water-out + FHC

(c) water-in + RHC

(d) water-out + RHC

Figure 4.16: Evolution of purity and efficiency of ν_e CC signal in FHC (or $\nu_e/\bar{\nu}_e$ CC signal in RHC) by BDT following selection cuts sequence in 4.3

to 0 because the neutrino beam is dominant by $\nu_\mu(\bar{\nu}_\mu)$, which is part of the reason why this analysis is challenging as discussed in section 1.4.

4.5 $\nu_\mu/\bar{\nu}_\mu$ CC Control Sample Selections

$\nu_\mu/\bar{\nu}_\mu$ CC background is one of the major background in the selected sample. The components of $\nu_\mu/\bar{\nu}_\mu$ CC background in terms of NEUT channels will be presented in section 4.5.1. Having control samples (also called sideband in this thesis) to constrain the background can help to reduce and even eliminate model dependence when extracting the cross section of signal from the select

Table 4.8: Purity and Efficiency of Selected Sample in terms of interaction channels in FHC

(a) Water-in

Category	Purity	Efficiency
ν_e CCQE Signal	24.68%	33.54%
ν_e CCRES Signal	17.01%	30.72%
ν_e CCMEC Signal	4.96%	36.96%
ν_e CCCOH Signal	0.34%	37.29%
ν_e CCDIS Signal	0.34%	5.10%
ν_e CC LowWMP Signal	3.09%	17.51%
(ν_e CC total Signal	50.42%	30.09%)
ν_e CC NOT-Signal	3.53%	2.91%
$\bar{\nu}_e CC$	10.47%	42.17%
$\nu_\mu/\bar{\nu}_\mu CC$	11.74%	0.07%
NC	16.84%	0.62%
OOFV	6.99%	<0.01%

(b) Water-out

Category	Purity	Efficiency
ν_e CCQE Signal	24.85%	26.98%
ν_e CCRES Signal	14.32%	21.77%
ν_e CCMEC Signal	4.64%	28.44%
ν_e CCCOH Signal	0.25%	28.57%
ν_e CCDIS Signal	0.37%	4.44%
ν_e CC LowWMP Signal	2.64%	12.89%
(ν_e CC total Signal	47.07%	23.09%)
ν_e CC NOT-Signal	2.83%	1.92%
$\bar{\nu}_e CC$	10.17%	33.13%
$\nu_\mu/\bar{\nu}_\mu CC$	12.26%	0.06%
NC	15.12%	0.41%
OOFV	12.57%	<0.01%

Table 4.9: Purity and Efficiency of Selected Sample in terms of interaction channels in RHC

(a) Water-in

Category	Purity	Efficiency
$\nu_e/\bar{\nu}_e$ CCQE Signal	37.06%	47.17%
$\nu_e/\bar{\nu}_e$ CCRES Signal	22.05%	36.17%
$\nu_e/\bar{\nu}_e$ CCMEC Signal	7.45%	48.39%
$\nu_e/\bar{\nu}_e$ CCCOH Signal	0.51%	35.00%
$\nu_e/\bar{\nu}_e$ CCDIS Signal	0.46%	4.86%
$\nu_e/\bar{\nu}_e$ CC LowWMP Signal	3.88%	19.03%
($\nu_e/\bar{\nu}_e$ CC total Signal	71.41%	38.57%)
$\nu_e/\bar{\nu}_e$ CC NOT-Signal	3.52%	3.82%
$\nu_\mu/\bar{\nu}_\mu CC$	8.15%	0.07%
NC	12.18%	0.67%
OOFV	4.74%	<0.01%

(b) Water-out

Category	Purity	Efficiency
$\nu_e/\bar{\nu}_e$ CCQE Signal	36.40%	41.10%
$\nu_e/\bar{\nu}_e$ CCRES Signal	19.17%	28.49%
$\nu_e/\bar{\nu}_e$ CCMEC Signal	7.47%	39.06%
$\nu_e/\bar{\nu}_e$ CCCOH Signal	0.48%	32.43%
$\nu_e/\bar{\nu}_e$ CCDIS Signal	0.56%	5.40%
$\nu_e/\bar{\nu}_e$ CC LowWMP Signal	4.32%	18.64%
($\nu_e/\bar{\nu}_e$ CC total Signal	68.40%	32.61%)
$\nu_e/\bar{\nu}_e$ CC NOT-Signal	2.34%	2.21%
$\nu_\mu/\bar{\nu}_\mu CC$	9.64%	0.08%
NC	11.90%	0.52%
OOFV	7.71%	<0.01%

samples. Section 4.5.2 presents the selection of control samples for $\nu_\mu/\bar{\nu}_\mu$ CC background.

4.5.1 $\nu_\mu/\bar{\nu}_\mu$ CC Background in the Selected Signal Sample

The selected signal sample has about 13% to 14% $\nu_\mu/\bar{\nu}_\mu$ CC background in FHC and about 8% to 9% $\nu_\mu/\bar{\nu}_\mu$ CC background in RHC. Table 4.10 and 4.11 shows the break down $\nu_\mu/\bar{\nu}_\mu$ CC background w.r.t interaction channels in NEUT in FHC and RHC configurations, respectively. Figure 4.17 shows the distribution of Longest Track Angle. More plots of $\nu_\mu/\bar{\nu}_\mu$ CC background will be presented later as comparisons with the $\nu_\mu/\bar{\nu}_\mu$ CC sidebands.

4.5.2 Selection of $\nu_\mu/\bar{\nu}_\mu$ CC Sidebands

As the tables 4.10 and 4.11 and figures 4.17 show, the major contributions of the $\nu_\mu/\bar{\nu}_\mu$ CC background are from CC Deep Inelastic Scattering (DIS), Resonant interaction(RES) and low W multi-pion production (lowWMP). Thus, the selections of $\nu_\mu/\bar{\nu}_\mu$ CC sidebands focus on selecting events from these interaction channels.

As mentioned before, P0D reconstruction will reconstruct a muon as a track (ideally). Therefore, it is expected to see a long track for a muon. Because the interaction channels that contribute most to the $\nu_\mu/\bar{\nu}_\mu$ CC background such DIS tend to produce multiple outgoing particles, it is expected to see multiple reconstructed objects. Thus, selection strategies applied are listed as below.

- Valid reconstructed vertex

Table 4.10: Breakdown of $\nu_\mu/\bar{\nu}_\mu$ CC background in selected signal sample w.r.t interaction channels in FHC

(a) Water-in

Category	Fraction in $\nu_\mu/\bar{\nu}_\mu$ CC background	Fraction in Selected Signal Sample
$\nu_\mu/\bar{\nu}_\mu$ CCQE	4.58%	0.54%
$\nu_\mu/\bar{\nu}_\mu$ CCRES	26.31%	3.09%
$\nu_\mu/\bar{\nu}_\mu$ CCMEC	2.49%	0.29%
$\nu_\mu/\bar{\nu}_\mu$ CCCOH	3.14%	0.37%
$\nu_\mu/\bar{\nu}_\mu$ CCDIS	47.12%	5.53%
$\nu_\mu/\bar{\nu}_\mu$ CCLowWMP	16.36%	1.92%

(b) Water-out

Category	Fraction in $\nu_\mu/\bar{\nu}_\mu$ CC background	Fraction in Selected Signal Sample
$\nu_\mu/\bar{\nu}_\mu$ CCQE	4.01%	0.49%
$\nu_\mu/\bar{\nu}_\mu$ CCRES	27.75%	3.38%
$\nu_\mu/\bar{\nu}_\mu$ CCMEC	4.26%	0.52%
$\nu_\mu/\bar{\nu}_\mu$ CCCOH	4.76%	0.58%
$\nu_\mu/\bar{\nu}_\mu$ CCDIS	45.61%	5.59%
$\nu_\mu/\bar{\nu}_\mu$ CCLowWMP	13.78%	1.69%

Table 4.11: Breakdown of $\nu_\mu/\bar{\nu}_\mu$ CC background in selected signal sample w.r.t interaction channels in RHC

(a) Water-in

Category	Fraction in $\nu_\mu/\bar{\nu}_\mu$ CC background	Fraction in Selected Signal Sample
$\nu_\mu/\bar{\nu}_\mu$ CCQE	8.63%	0.70%
$\nu_\mu/\bar{\nu}_\mu$ CCRES	22.68%	1.85%
$\nu_\mu/\bar{\nu}_\mu$ CCMEC	2.88%	0.23%
$\nu_\mu/\bar{\nu}_\mu$ CCCOH	5.11%	0.42%
$\nu_\mu/\bar{\nu}_\mu$ CCDIS	43.45%	3.54%
$\nu_\mu/\bar{\nu}_\mu$ CCLowWMP	17.25%	1.41%

(b) Water-out

Category	Fraction in $\nu_\mu/\bar{\nu}_\mu$ CC background	Fraction in Selected Signal Sample
$\nu_\mu/\bar{\nu}_\mu$ CCQE	5.49%	0.53%
$\nu_\mu/\bar{\nu}_\mu$ CCRES	29.80%	2.87%
$\nu_\mu/\bar{\nu}_\mu$ CCMEC	3.14%	0.30%
$\nu_\mu/\bar{\nu}_\mu$ CCCOH	5.88%	0.57%
$\nu_\mu/\bar{\nu}_\mu$ CCDIS	43.14%	4.16%
$\nu_\mu/\bar{\nu}_\mu$ CCLowWMP	12.55%	1.21%

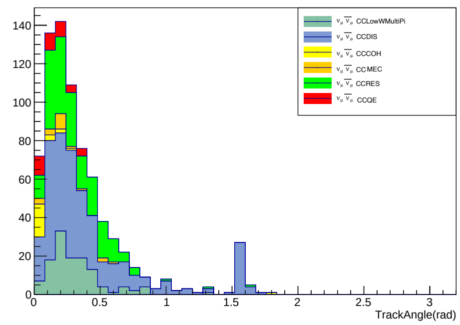

(a) water-in + FHC

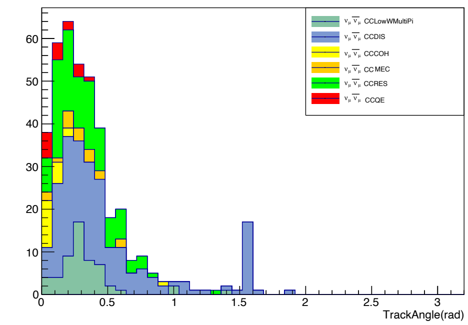

(b) water-out + FHC

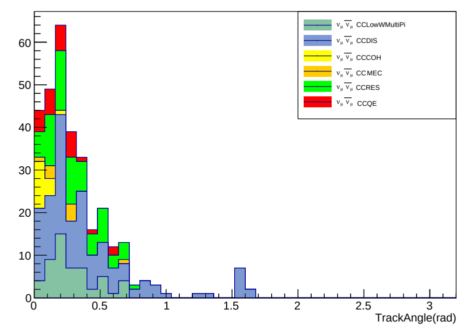

(c) water-in + RHC

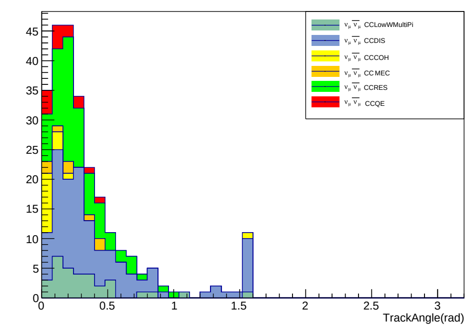

(d) water-out + RHC

Figure 4.17: Distribution of Longest Track Angle of $\nu_\mu/\bar{\nu}_\mu$ CC background in selected signal sample

- Fiducial volume cut as chapter 4.3.2 defines
- More than 3 valid reconstructed objects and among them, there are at least two valid reconstructed tracks (mainly considering one outgoing muon and at least one proton).
- The number of layers that the longest track passes is more than 23

4.5.3 Selected $\nu_\mu/\bar{\nu}_\mu$ CC Sidebands

Tables 4.12 and 4.13 show the breakdown of selected $\nu_\mu/\bar{\nu}_\mu$ CC sidebands w.r.t NEUT channels in FHC and RHC, respectively. CC DIS, LowWMP and RES are the three major channels in the sidebands. Figures from 4.18 to 4.21 show comparisons of distributions of some true variables for $\nu_\mu/\bar{\nu}_\mu$ CC background and $\nu_\mu/\bar{\nu}_\mu$ CC sidebands in all 4 configurations.

Table 4.12: Breakdown of $\nu_\mu/\bar{\nu}_\mu$ CC Sidebands w.r.t interaction channels in FHC

(a) Water-in

Category	Fraction
$\nu_\mu/\bar{\nu}_\mu$ CCQE	1.68%
$\nu_\mu/\bar{\nu}_\mu$ CCRES	18.06%
$\nu_\mu/\bar{\nu}_\mu$ CCMEC	0.32%
$\nu_\mu/\bar{\nu}_\mu$ CCCOH	0.38%
$\nu_\mu/\bar{\nu}_\mu$ CCDIS	36.69%
$\nu_\mu/\bar{\nu}_\mu$ CCLowWMP	22.72%
$\nu_e/\bar{\nu}_e$ CC	1.43%
NC	6.76%
OOFV	9.00%

(b) Water-out

Category	Fraction
$\nu_\mu/\bar{\nu}_\mu$ CCQE	1.98%
$\nu_\mu/\bar{\nu}_\mu$ CCRES	20.81%
$\nu_\mu/\bar{\nu}_\mu$ CCMEC	0.63%
$\nu_\mu/\bar{\nu}_\mu$ CCCOH	0.36%
$\nu_\mu/\bar{\nu}_\mu$ CCDIS	32.70%
$\nu_\mu/\bar{\nu}_\mu$ CCLowWMP	22.95%
$\nu_e/\bar{\nu}_e$ CC	1.67%
NC	7.03%
OOFV	11.87%

4.6 NC1π^0 Control Sample Selections

NC background is another major background in the selected sample. Similarly, the components of NC background in terms of NEUT channels will be presented in section 4.6.1. and the selection of control samples for NC background will be present in section 4.6.2

Table 4.13: Breakdown of $\nu_\mu/\bar{\nu}_\mu$ CC Sidebands w.r.t interaction channels in RHC

(a) Water-in

Category	Fraction
$\nu_\mu/\bar{\nu}_\mu$ CCQE	1.36%
$\nu_\mu/\bar{\nu}_\mu$ CCRES	18.52%
$\nu_\mu/\bar{\nu}_\mu$ CCMEC	0.28%
$\nu_\mu/\bar{\nu}_\mu$ CCCOH	0.68%
$\nu_\mu/\bar{\nu}_\mu$ CCDIS	37.57%
$\nu_\mu/\bar{\nu}_\mu$ CCLowWMP	23.17%
$\nu_e/\bar{\nu}_e$ CC	2.00%
NC	6.82%
OOFV	9.58%

(b) Water-out

Category	Fraction
$\nu_\mu/\bar{\nu}_\mu$ CCQE	1.54%
$\nu_\mu/\bar{\nu}_\mu$ CCRES	20.58%
$\nu_\mu/\bar{\nu}_\mu$ CCMEC	0.55%
$\nu_\mu/\bar{\nu}_\mu$ CCCOH	0.77%
$\nu_\mu/\bar{\nu}_\mu$ CCDIS	31.03%
$\nu_\mu/\bar{\nu}_\mu$ CCLowWMP	23.62%
$\nu_e/\bar{\nu}_e$ CC	2.35%
NC	7.62%
OOFV	11.92%

4.6.1 NC Background in the Selected Signal Sample

The major background in the selected signal sample is from NC interaction. Tables 4.14, 4.15, 4.16 and 4.17 show the break down NC background w.r.t interaction channels in NEUT and topology in all 4 configurations, respectively. Similarly, plots of NC background will be presented later as comparisons with the NC sidebands.

4.6.2 Selections of NC Sidebands

As tables 4.14, 4.15, 4.16 and 4.17 show, the major contributions of NC background are from NC DIS w.r.t NEUT interactions and are from NC1π^0 w.r.t topology. To select NC1π^0 events, the aim is to select events which contains two showers reconstructed from the two photons decayed from the π^0. The selection strategies are inspired by P0D NC 1π^0 analysis [64, 65]. The selection strategies are listed below.

Table 4.14: Breakdown of NC background in selected signal sample w.r.t interaction channels and topology in FHC and water-in configuration

(a) Water-in + FHC, w.r.t Reaction

Category	Fraction in NC background	Fraction in Selected Signal Sample
NCRES π^0	18.58%	3.13%
NCRES $\pi^\pm$	1.50%	0.25%
NCRES Others	5.58%	0.94%
NCCOH π^0	18.50%	3.11%
NCDIS	42.65%	7.18%
NCLowWMP	12.83%	2.16%
NC Others	0.35%	0.06%

(b) Water-in + FHC, w.r.t Topology

Category	Fraction in NC background	Fraction in Selected Signal Sample
NC $1\pi^0$	77.17%	13.00%
NC $> 1\pi^0$	6.19%	1.04%
NC $>= 1\pi^\pm, 0\pi^0$	8.50%	1.43%
NC Others	8.14%	1.37%

Table 4.15: Breakdown of NC background in selected signal sample w.r.t interaction channels and topology in FHC and water-out configuration

(a) Water-out + FHC, w.r.t Reaction

Category	Fraction in NC background	Fraction in Selected Signal Sample
NCRES π^0	22.15%	3.35%
NCRES $\pi^{\pm}$	1.02%	0.15%
NCRES Others	5.08%	0.77%
NCCOH π^0	19.62%	2.98%
NCDIS	42.48%	6.42%
NCLowWMP	9.35%	1.41%
NC Others	0.20%	0.03%

(b) Water-out + FHC, w.r.t Topology

Category	Fraction in NC background	Fraction in Selected Signal Sample
NC $1\pi^0$	80.49%	12.17%
NC $> 1\pi^0$	6.91%	1.04%
NC $>= 1\pi^{\pm}, 0\pi^0$	6.10%	0.92%
NC Others	6.50%	0.98%

Table 4.16: Breakdown of NC background in selected signal sample w.r.t interaction channels and topology in RHC and water-in configuration

(a) Water-in + RHC, w.r.t Reaction

Category	Fraction in NC background	Fraction in Selected Signal Sample
NCRES π^0	20.12%	2.45%
NCRES $\pi^\pm$	2.46%	0.32%
NCRES Others	4.07%	0.50%
NCCOH π^0	25.41%	3.09%
NCDIS	35.57%	4.33%
NCLowWMP	11.79%	1.44%
NC Others	0.41%	0.05%

(b) Water-in + RHC, w.r.t Topology

Category	Fraction in NC background	Fraction in Selected Signal Sample
NC $1\pi^0$	82.32%	10.03%
NC $> 1\pi^0$	5.08%	0.62%
NC $>= 1\pi^\pm, 0\pi^0$	6.30%	0.77%
NC Others	6.30%	0.77%

Table 4.17: Breakdown of NC background in selected signal sample w.r.t interaction channels and topology in RHC and water-out configuration

(a) Water-out + RHC, w.r.t Reaction

Category	Fraction in NC background	Fraction in Selected Signal Sample
NCRES π^0	25.42%	3.01%
NCRES $\pi^\pm$	1.68%	0.20%
NCRES Others	7.26%	0.86%
NCCOH π^0	25.70%	3.05%
NCDIS	27.09%	3.21%
NCLowWMP	12.01%	1.42%
NC Others	0.84%	0.10%

(b) Water-out + RHC, w.r.t Topology

Category	Fraction in NC background	Fraction in Selected Signal Sample
NC $1\pi^0$	77.37%	9.18%
NC $> 1\pi^0$	5.31%	0.63%
NC $>= 1\pi^\pm, 0\pi^0$	7.54%	0.89%
NC Others	9.78%	1.16%

- Valid reconstructed vertex
- Fiducial Volume cut as chapter 4.3.2 defines.
- At least two valid reconstructed showers and the number of scintillator layers that showers passes is larger than 8.
- Containment Cut: All objects produced in the interaction are contained in P0D.
- μ decay Cut: No μ decay clusters is tagged.
- Single Shower Charge Fraction Cut: Ratio of charges in the most energetic reconstructed shower over the total charges in the interaction is less than 90%. This cut is anti SCF Cut discussed in section 4.3.8 in the signal sample selection.
- Two Showers Charge Fraction: Ratio of charges in the most two energetic reconstructed showers over the total charges in the interaction is more than 85%.
- π^0 angle Cut: Reconstructed angle of π^0 is less than $60°$.
- Invariant Mass Cut: Reconstructed invariant mass is in the range (65, 205) MeV/c^2, where the invariant mass is calculated as

$$\text{invmass} = (|\boldsymbol{p}_{s1}| + |\boldsymbol{p}_{s2}|)^2 - (\boldsymbol{p}_{s1} + \boldsymbol{p}_{s2})^2 \tag{4.1}$$

  where $p_{1\mu} = (|\boldsymbol{p}_{s1}|, \boldsymbol{p}_{s1})$ and $p_{2\mu} = (|\boldsymbol{p}_{s2}|, \boldsymbol{p}_{s2})$ are reconstructed 4-momentum of the two most energetic showers.

4.6.3 Selected NC Sidebands

Tables 4.18 and 4.19, 4.20 and 4.21 show the breakdown of selected NC1π^0 sideband w.r.t NEUT channels and topology in all configurations, respectively. Figures from 4.22 to 4.27 show comparisons of distributions of true neutrino energy, true Q^2 and true W for NC1π^0 background and NC1π^0 sideband in all 4 configurations. Figures 4.30 and 4.31 show the distributions of reconstructed invariant mass of the selected sidebands in all 4 configurations w.r.t to NEUT interaction channels and topology, respectively. Because it is expected that the distribution of reconstructed invariant mass would peak at the π^0 mass which is known to be about 135 MeV/c^2, the distribution of reconstructed invariant mass can be used as a cross-check to make sure the energy reconstruction and the shower identification here are not absurdly wrong. As figures 4.30 and 4.31 show, the invariant mass of each selected NC1π^0 sample in FHC peaks at the bin which contains 135 MeV/c^2. For RHC, although the number of events in the bin of 105-125 MeV/c^2 is more than that in bin 125-145 MeV/c^2, the difference in within in the statistical uncertainty, so it may due to the statistical fluctuations.

The comparisons of NC backgrounds in the selected signal samples and selected NC1π^0 sidebands in figures from 4.22 to 4.29 show that the NC1π^0 sideband does not cover the background of high true neutrino energy, high Q^2 or high W. This is inevitable if the strategy to select NC1π^0 events is by trying to identify and select two photons from π^0 decay. Interactions with high input neutrino energies will likely produce high energy π^0 whose open angle will more likely be small in the lab frame, which means the two decayed photons will fly closely to each other, which makes it very difficult (impossible if too close) for the detector to recognize them as two showers instead of one. As a result, such events will not be selected into the sideband. Besides, due to the similarity of photons and electrons behaviours in P0D, it is also very difficult to select pure NC samples with very small π^0 open angle by selecting single shower as they are not distinguishable from ν_e CC events.

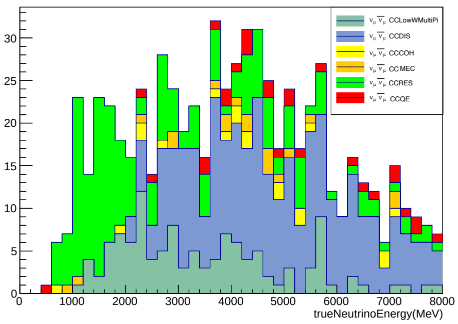

(a) true E_ν in $\nu_\mu/\bar{\nu}_\mu$ CC the background

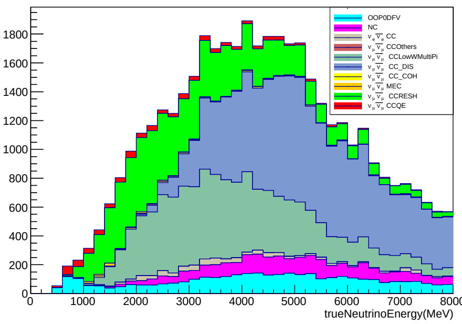

(b) true E_ν in $\nu_\mu/\bar{\nu}_\mu$ CC the sidebands

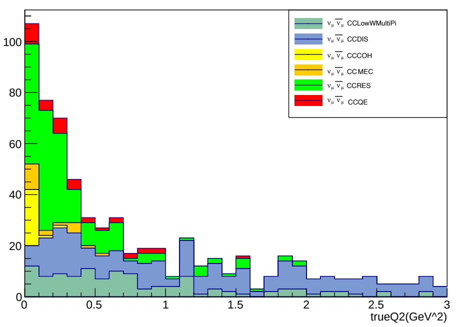

(c) true Q^2 in $\nu_\mu/\bar{\nu}_\mu$ CC the background

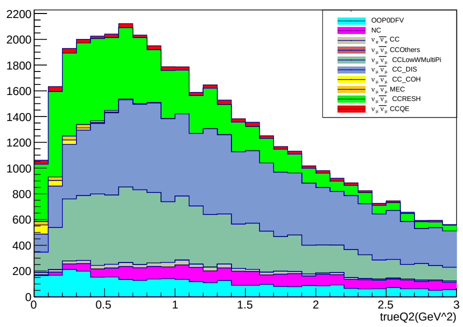

(d) true Q^2 in $\nu_\mu/\bar{\nu}_\mu$ CC the sidebands

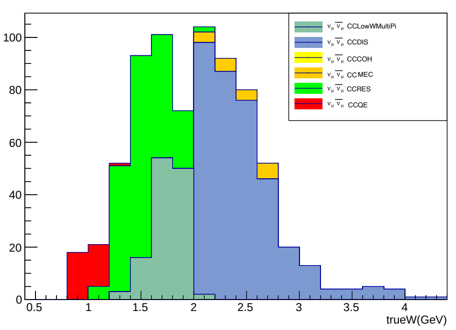

(e) true W in $\nu_\mu/\bar{\nu}_\mu$ CC the background

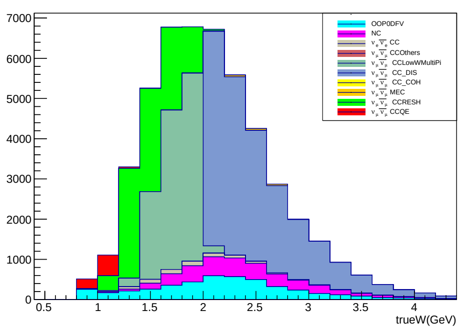

(f) true W in $\nu_\mu/\bar{\nu}_\mu$ CC the sidebands

Figure 4.18: Comparison of $\nu_\mu/\bar{\nu}_\mu$ CC background and sidebands in FHC and water-in configuration

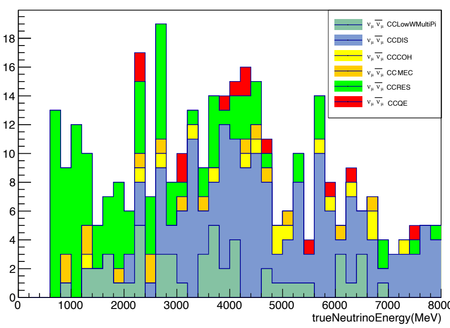

(a) true E_ν in $\nu_\mu/\bar{\nu}_\mu$ CC the background

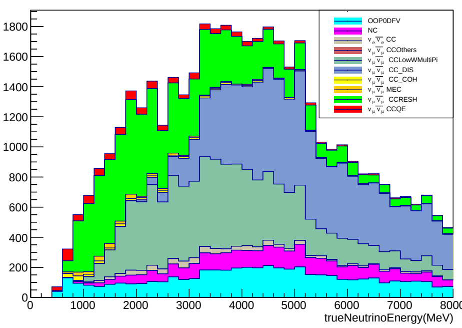

(b) true E_ν in $\nu_\mu/\bar{\nu}_\mu$ CC the sidebands

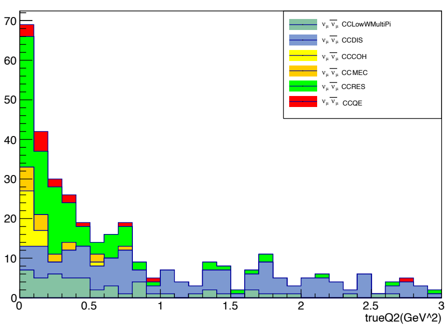

(c) true Q^2 in $\nu_\mu/\bar{\nu}_\mu$ CC the background

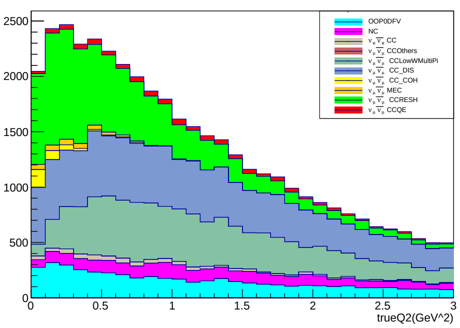

(d) true Q^2 in $\nu_\mu/\bar{\nu}_\mu$ CC the sidebands

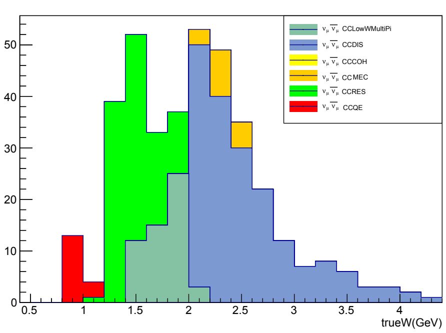

(e) true W in $\nu_\mu/\bar{\nu}_\mu$ CC the background

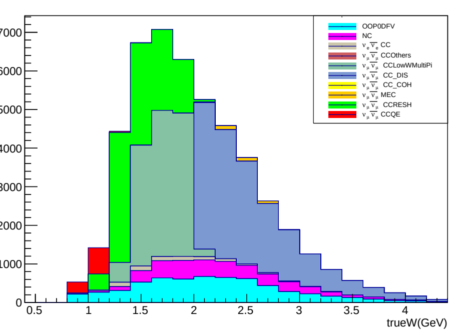

(f) true W in $\nu_\mu/\bar{\nu}_\mu$ CC the sidebands

Figure 4.19: Comparison of $\nu_\mu/\bar{\nu}_\mu$ CC background and sidebands in FHC and water-out configuration

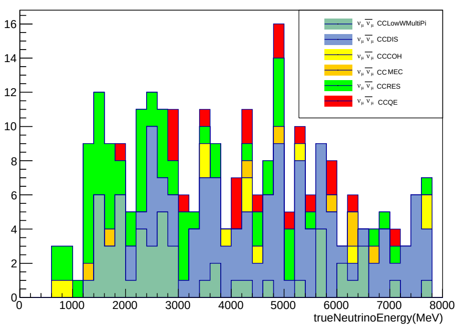

(a) true E_ν in $\nu_\mu/\bar{\nu}_\mu$ CC the background

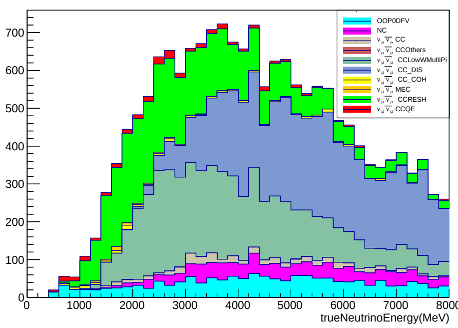

(b) true E_ν in $\nu_\mu/\bar{\nu}_\mu$ CC the sidebands

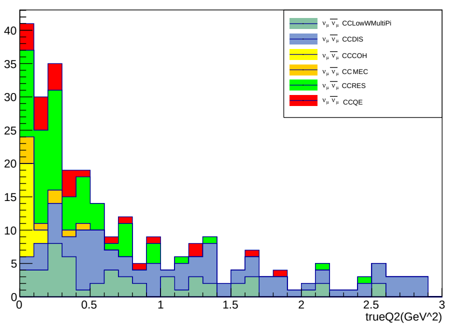

(c) true Q^2 in $\nu_\mu/\bar{\nu}_\mu$ CC the background

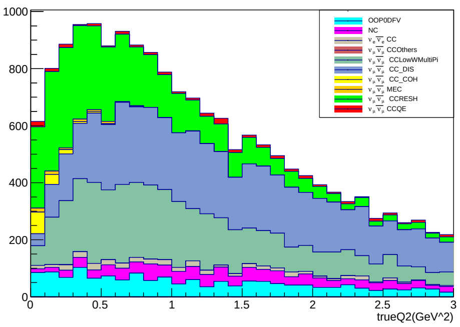

(d) true Q^2 in $\nu_\mu/\bar{\nu}_\mu$ CC the sidebands

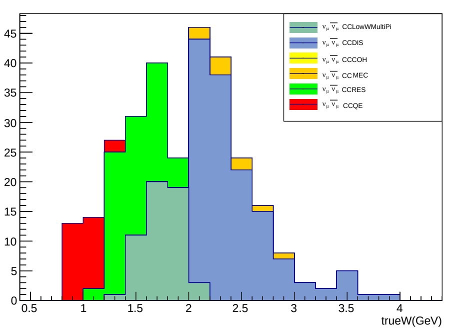

(e) true W in $\nu_\mu/\bar{\nu}_\mu$ CC the background

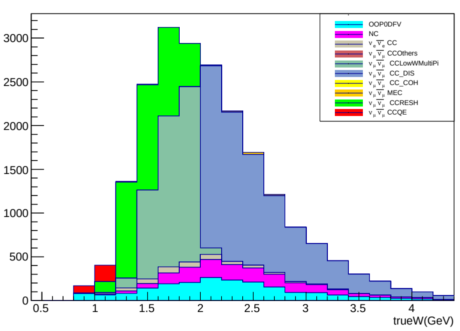

(f) true W in $\nu_\mu/\bar{\nu}_\mu$ CC the sidebands

Figure 4.20: Comparison of $\nu_\mu/\bar{\nu}_\mu$ CC background and sidebands in RHC and water-out configuration

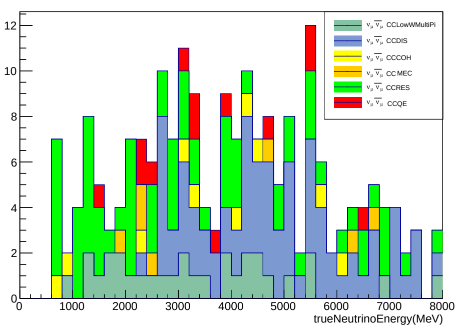

(a) true E_ν in $\nu_\mu/\bar{\nu}_\mu$ CC the background

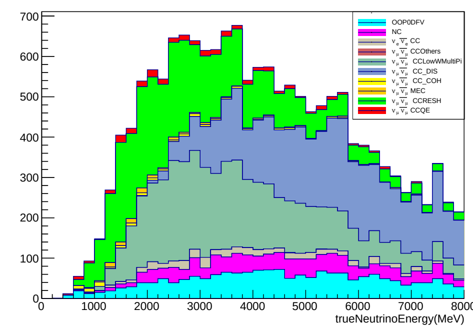

(b) true E_ν in $\nu_\mu/\bar{\nu}_\mu$ CC the sidebands

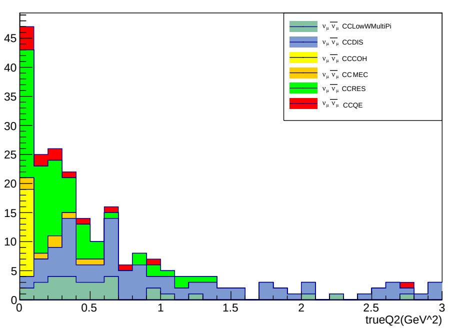

(c) true Q^2 in $\nu_\mu/\bar{\nu}_\mu$ CC the background

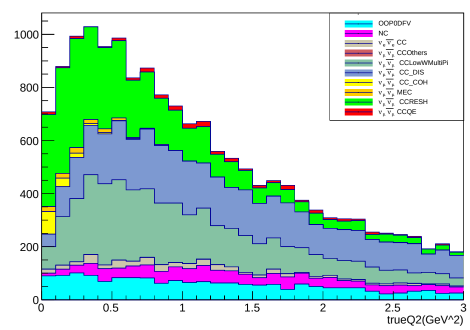

(d) true Q^2 in $\nu_\mu/\bar{\nu}_\mu$ CC the sidebands

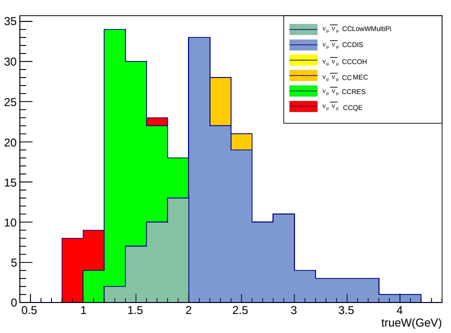

(e) true W in $\nu_\mu/\bar{\nu}_\mu$ CC the background

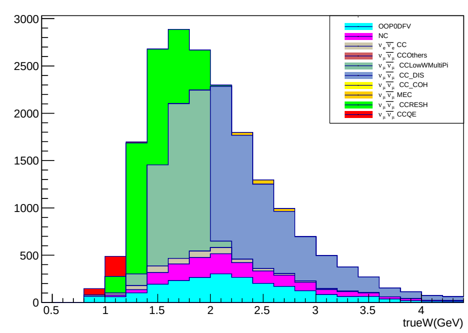

(f) true W in $\nu_\mu/\bar{\nu}_\mu$ CC the sidebands

Figure 4.21: Comparison of $\nu_\mu/\bar{\nu}_\mu$ CC background and sidebands in RHC and water-out configuration

Table 4.18: Breakdown of NC1π^0 sideband w.r.t interaction channels and topology in FHC and water-in configuration

(a) Water-in + FHC, w.r.t Reaction

Category	Fraction in NC1π^0 sideband
NCRES π^0	39.11%
NCRES $\pi^\pm$	3.14%
NCRES Others	1.76%
NCCOH π^0	8.86%
NCDIS	0.92%
NCLowWMP	7.45%
NC Others	1.16%
$\nu_e/\bar{\nu}_e$ CC	1.86%
$\nu_\mu/\bar{\nu}_\mu$ CC	22.00%
OOFV	13.74%

(b) Water-in + FHC, w.r.t Topology

Category	Fraction in NC1π^0 sideband
NC $1\pi^0$	53.24%
NC $> 1\pi^0$	2.15%
NC $>= 1\pi^\pm, 0\pi^0$	3.99%
NC Others	3.02%
CC $1\pi^0$	10.07%
CC $> 1\pi^0$	0.52%
CC $>= 1\pi^\pm, 0\pi^0$	6.81%
CC Others	6.46%
OOFV	13.74%

Table 4.19: Breakdown of NC1π^0 sideband w.r.t interaction channels and topology in FHC and water-out configuration

(a) Water-out + FHC, w.r.t Reaction

Category	Fraction in NC1π^0 sideband
NCRES π^0	34.04%
NCRES $\pi^\pm$	3.04%
NCRES Others	1.17%
NCCOH π^0	7.88%
NCDIS	0.53%
NCLowWMP	5.51%
NC Others	1.17%
$\nu_e/\bar{\nu}_e$ CC	1.34%
$\nu_\mu/\bar{\nu}_\mu$ CC	22.76%
OOFV	22.55%

(b) Water-out + FHC, w.r.t Topology

Category	Fraction in NC1π^0 sideband
NC $1\pi^0$	46.48%
NC $> 1\pi^0$	1.06%
NC $>= 1\pi^\pm, 0\pi^0$	3.61%
NC Others	2.18%
CC $1\pi^0$	7.53%
CC $> 1\pi^0$	0.28%
CC $>= 1\pi^\pm, 0\pi^0$	6.29%
CC Others	10.00%
OOFV	22.55

Table 4.20: Breakdown of NC1π^0 sideband w.r.t interaction channels and topology in RHC and water-in configuration

(a) Water-in + RHC, w.r.t Reaction

Category	Fraction in NC1π^0 sideband
NCRES π^0	35.83%
NCRES $\pi^\pm$	4.59%
NCRES Others	2.62%
NCCOH π^0	18.11%
NCDIS	0.98%
NCLowWMP	9.19%
NC Others	1.05%
$\nu_e/\bar{\nu}_e$ CC	2.23%
$\nu_\mu/\bar{\nu}_\mu$ CC	11.02%
OOFV	14.37%

(b) Water-in + RHC, w.r.t Topology

Category	Fraction in NC1π^0 sideband
NC $1\pi^0$	60.89%
NC $> 1\pi^0$	3.08%
NC $>= 1\pi^\pm, 0\pi^0$	4.92%
NC Others	3.48%
CC $1\pi^0$	5.12%
CC $> 1\pi^0$	0.59%
CC $>= 1\pi^\pm, 0\pi^0$	3.54%
CC Others	4.00%
OOFV	14.37

Table 4.21: Breakdown of NC1π^0 sideband w.r.t interaction channels and topology in RHC and water-out configuration

(a) Water-out + RHC, w.r.t Reaction

Category	Fraction in NC1π^0 sideband
NCRES π^0	33.81%
NCRES $\pi^\pm$	3.46%
NCRES Others	2.11%
NCCOH π^0	17.10%
NCDIS	0.29%
NCLowWMP	7.01%
NC Others	1.15%
$\nu_e/\bar{\nu}_e$ CC	1.54%
$\nu_\mu/\bar{\nu}_\mu$ CC	7.88%
OOFV	25.65%

(b) Water-out + RHC, w.r.t Topology

Category	Fraction in NC1π^0 sideband
NC $1\pi^0$	56.35%
NC $> 1\pi^0$	1.54%
NC $>= 1\pi^\pm, 0\pi^0$	3.46%
NC Others	3.65%
CC $1\pi^0$	2.88%
CC $> 1\pi^0$	0.19%
CC $>= 1\pi^\pm, 0\pi^0$	3.08%
CC Others	3.27%
OOFV	25.67

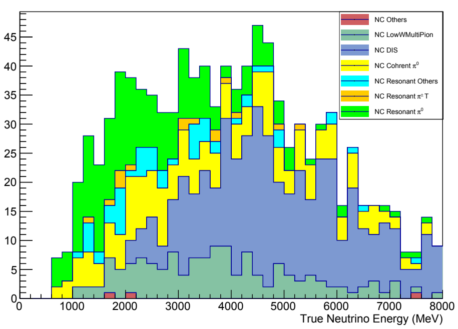

(a) true E_ν in NC the background

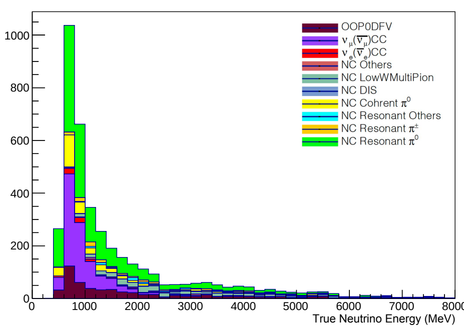

(b) true E_ν in NC1π^0 the sidebands

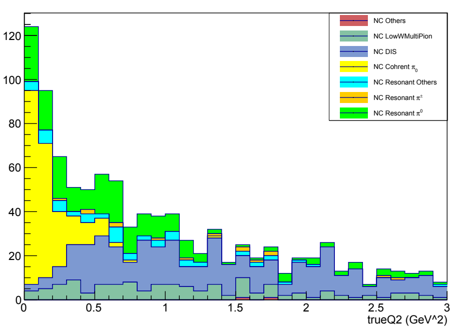

(c) true Q^2 in NC the background

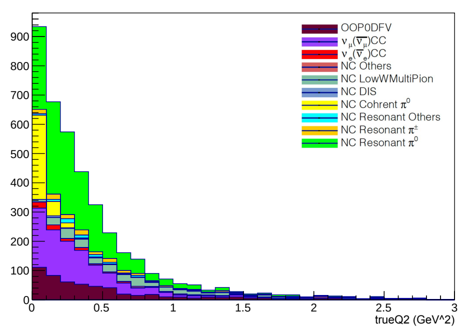

(d) true Q^2 in NC1π^0 the sidebands

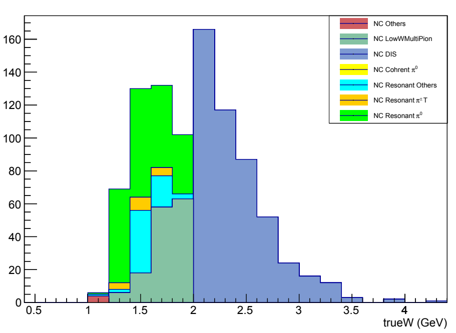

(e) true W in NC the background

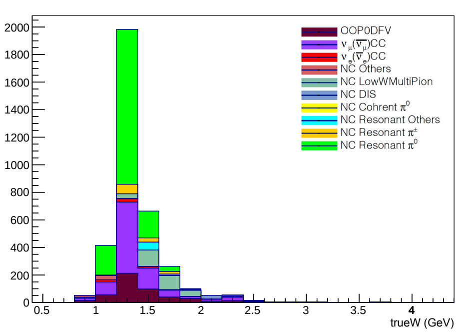

(f) true W in NC1π^0 the sidebands

Figure 4.22: Comparison of NC background and sidebands w.r.t NEUT interaction channels in FHC and water-in configuration

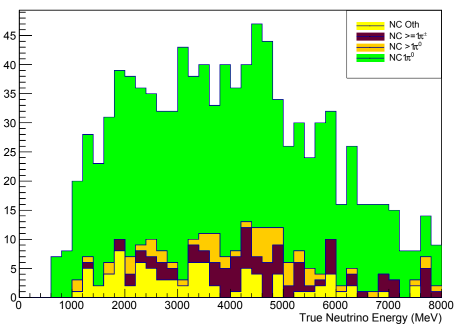

(a) true E_ν in NC the background

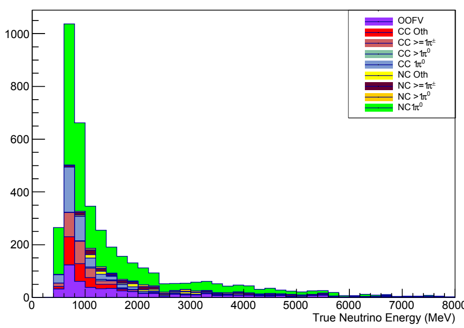

(b) true E_ν in NC1π^0 the sidebands

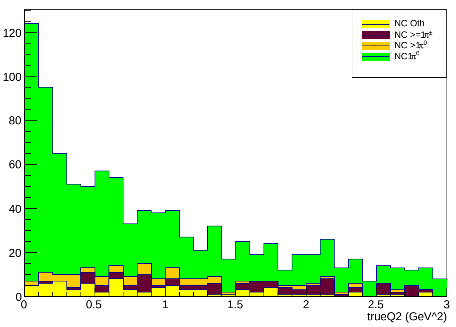

(c) true Q^2 in NC the background

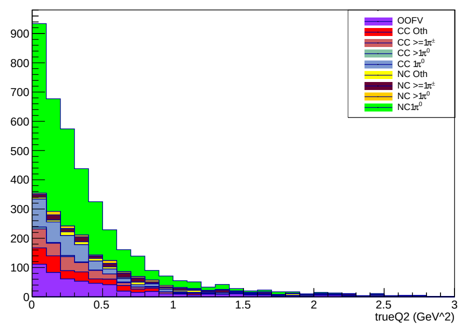

(d) true Q^2 in NC1π^0 the sidebands

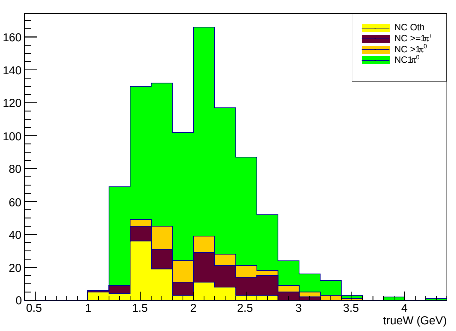

(e) true W in NC the background

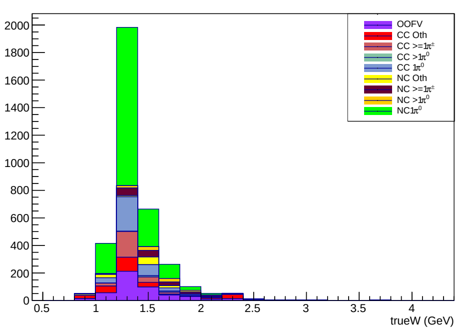

(f) true W in NC1π^0 the sidebands

Figure 4.23: Comparison of NC background and sidebands w.r.t Topology in FHC and water-in configuration

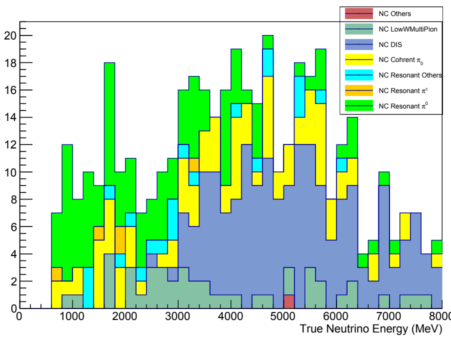

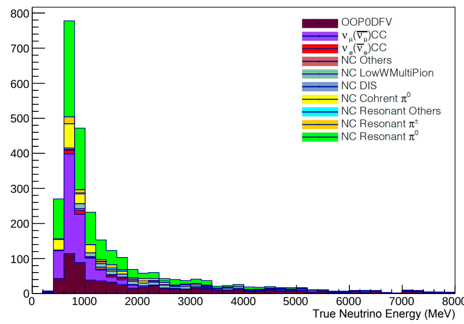

(a) true E_ν in NC the background (b) true E_ν in NC1π^0 the sidebands

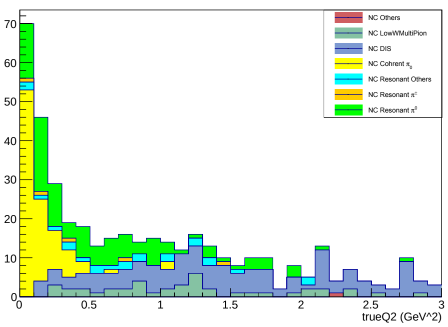

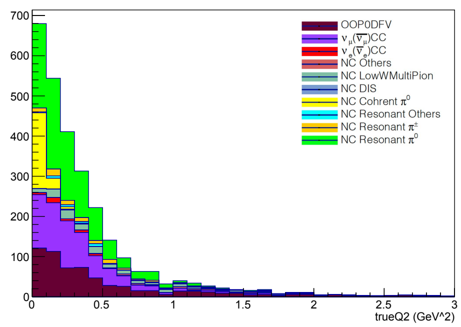

(c) true Q^2 in NC the background (d) true Q^2 in NC1π^0 the sidebands

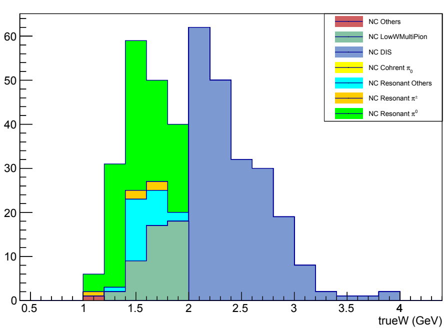

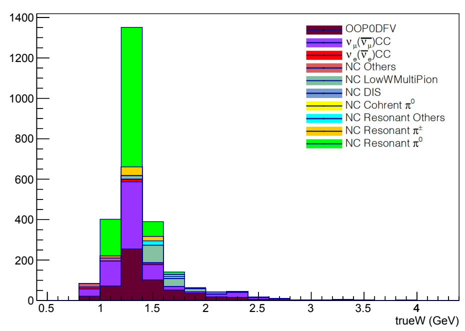

(e) true W in NC the background (f) true W in NC1π^0 the sidebands

Figure 4.24: Comparison of NC background and sidebands w.r.t NEUT interaction channels in FHC and water-out configuration

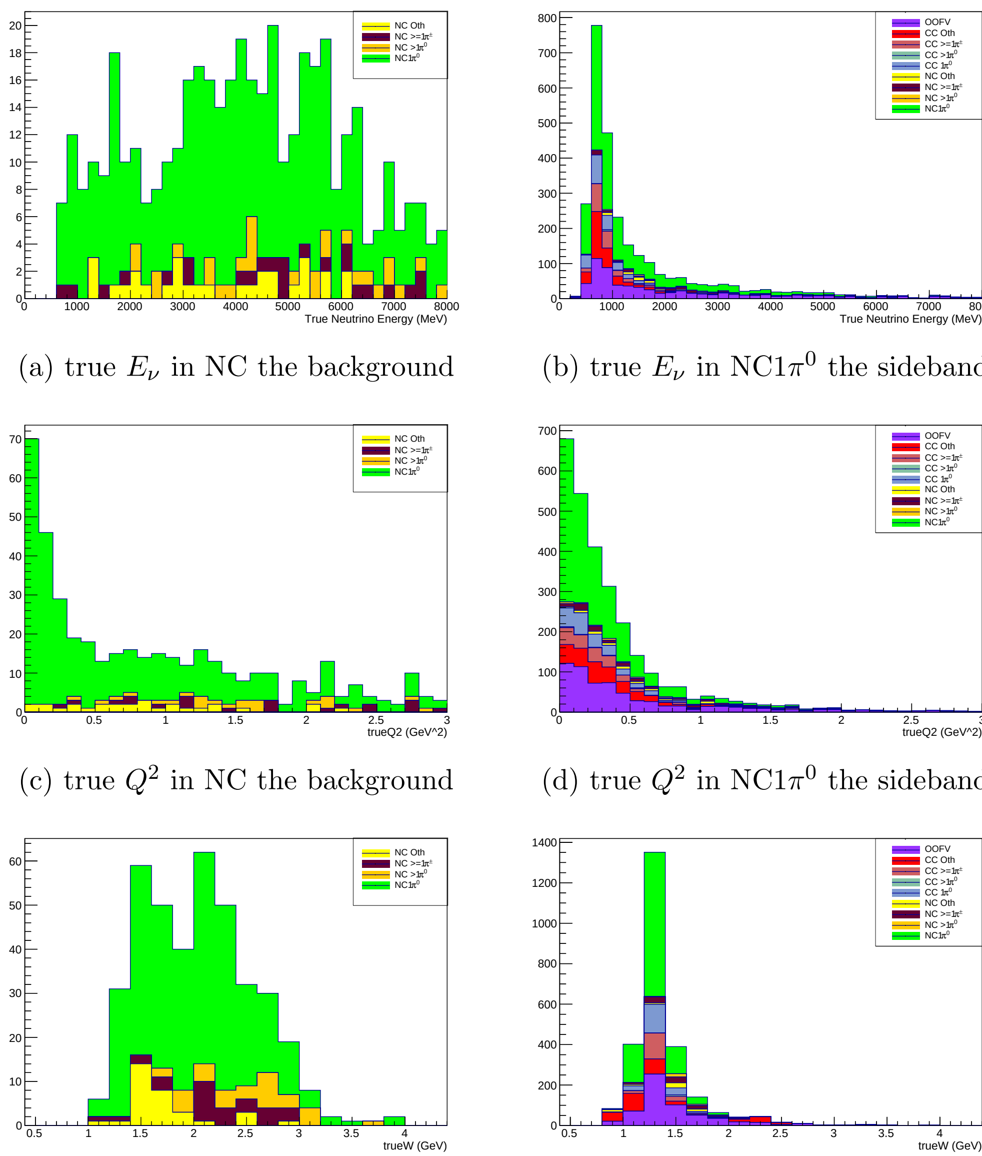

(a) true E_ν in NC the background (b) true E_ν in NC$1\pi^0$ the sidebands

(c) true Q^2 in NC the background (d) true Q^2 in NC$1\pi^0$ the sidebands

(e) true W in NC the background (f) true W in NC$1\pi^0$ the sidebands

Figure 4.25: Comparison of NC background and sidebands w.r.t Topology in FHC and water-out configuration

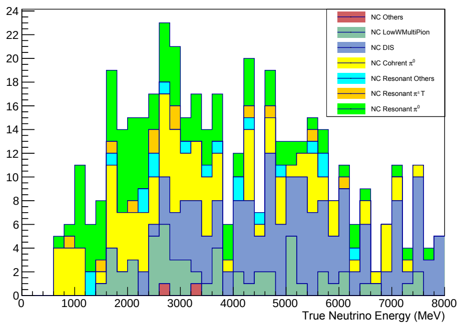

(a) true E_ν in NC the background

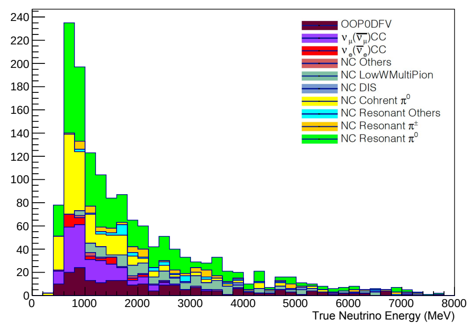

(b) true E_ν in NC1π^0 the sidebands

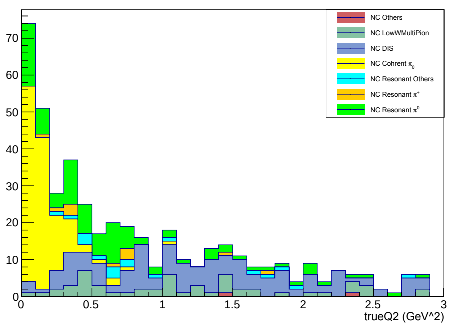

(c) true Q^2 in NC the background

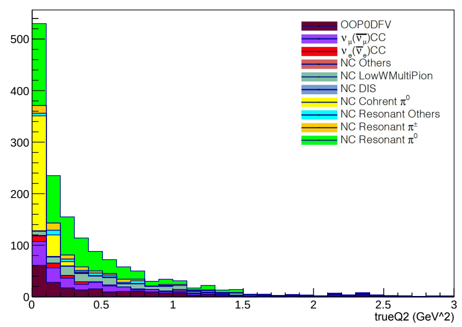

(d) true Q^2 in NC1π^0 the sidebands

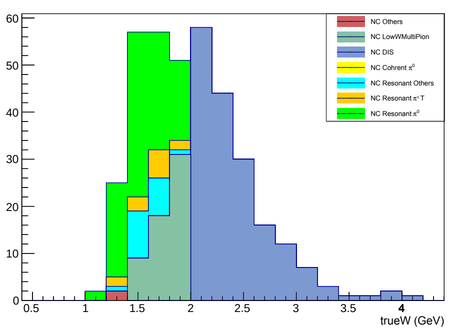

(e) true W in NC the background

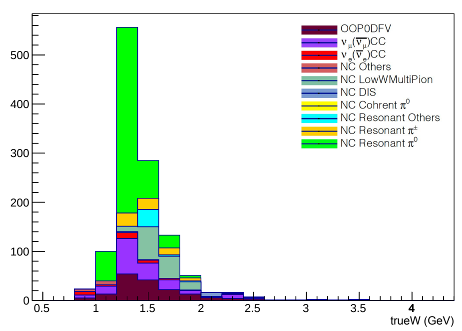

(f) true W in NC1π^0 the sidebands

Figure 4.26: Comparison of NC background and sidebands w.r.t NEUT interaction channels in RHC and water-in configuration

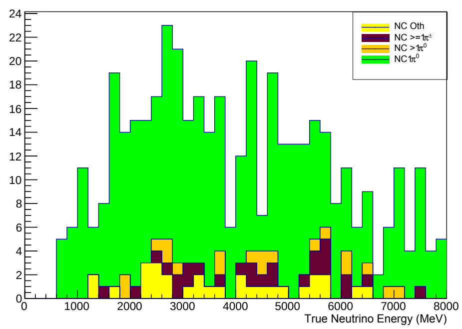

(a) true E_ν in NC the background

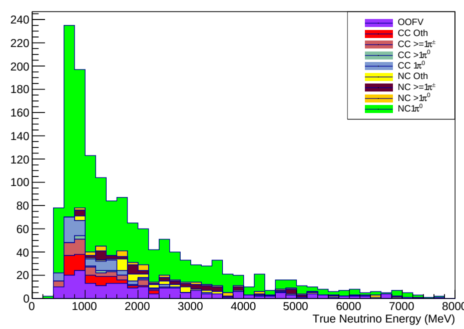

(b) true E_ν in NC1π^0 the sidebands

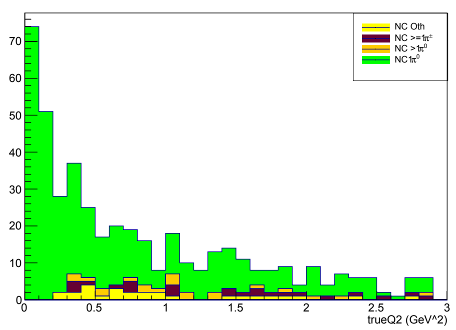

(c) true Q^2 in NC the background

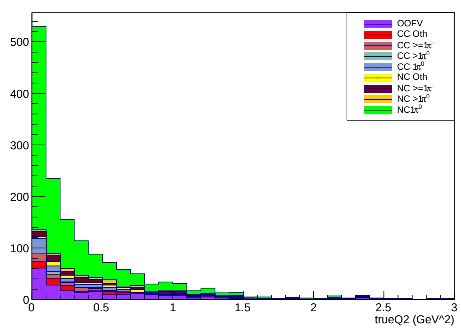

(d) true Q^2 in NC1π^0 the sidebands

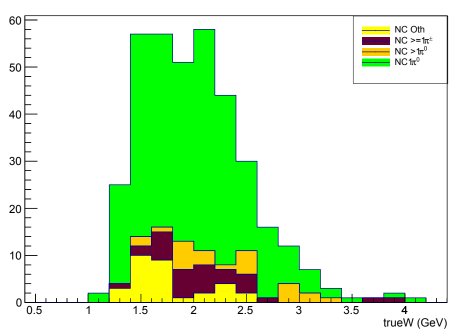

(e) true W in NC the background

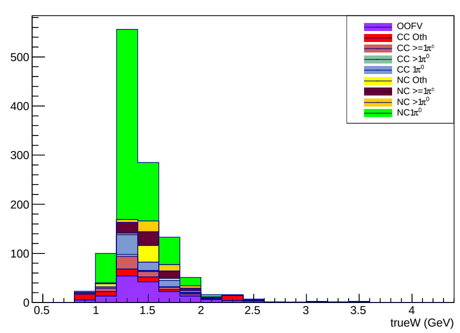

(f) true W in NC1π^0 the sidebands

Figure 4.27: Comparison of NC background and sidebands w.r.t Topology in RHC and water-in configuration

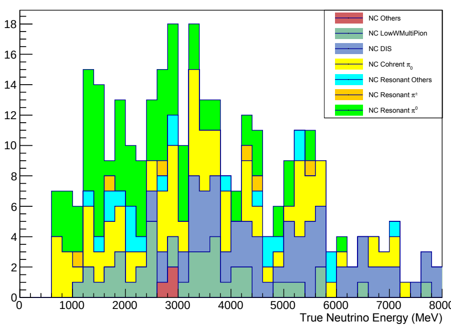

(a) true E_ν in NC the background

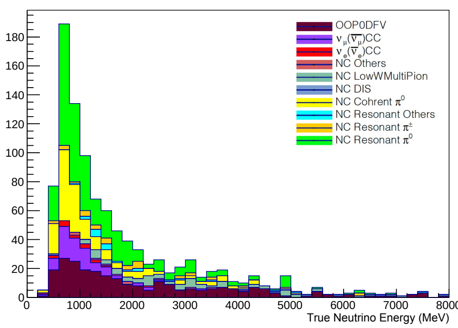

(b) true E_ν in NC1π^0 the sidebands

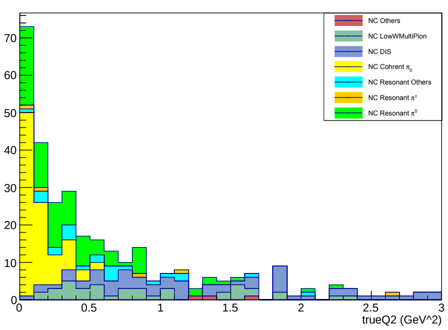

(c) true Q^2 in NC the background

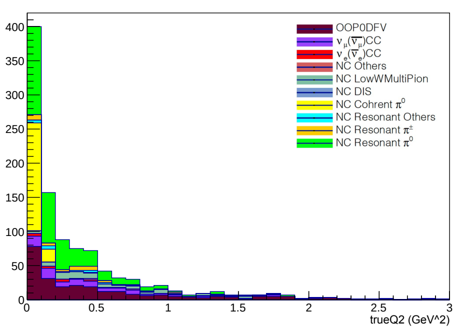

(d) true Q^2 in NC1π^0 the sidebands

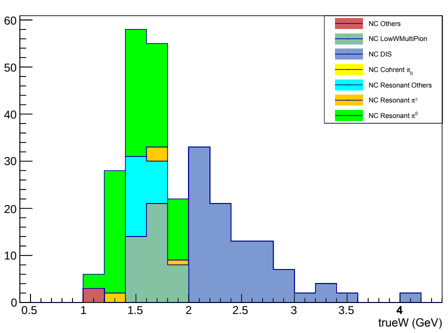

(e) true W in NC the background

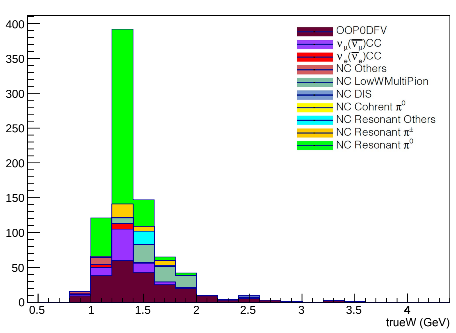

(f) true W in NC1π^0 the sidebands

Figure 4.28: Comparison of NC background and sidebands w.r.t NEUT interaction channels in RHC and water-out configuration

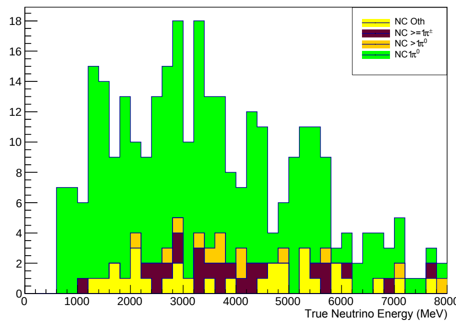

(a) true E_ν in NC the background

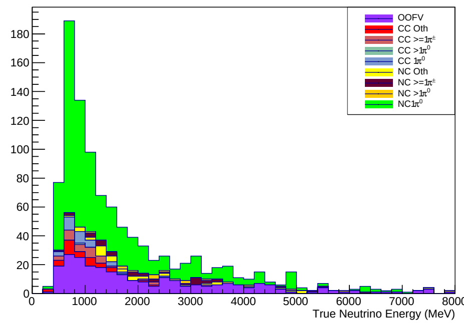

(b) true E_ν in NC$1\pi^0$ the sidebands

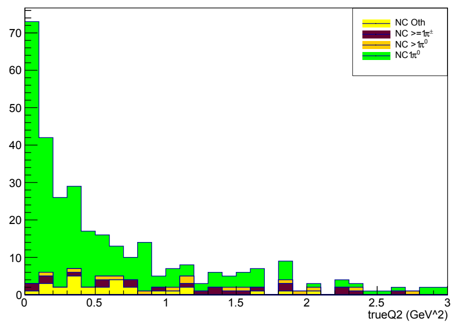

(c) true Q^2 in NC the background

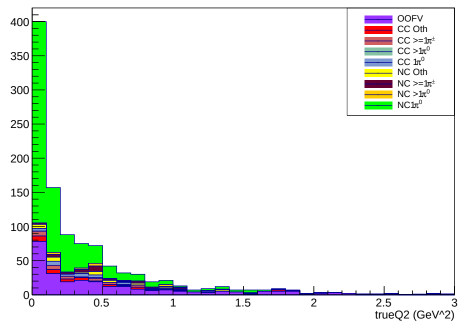

(d) true Q^2 in NC$1\pi^0$ the sidebands

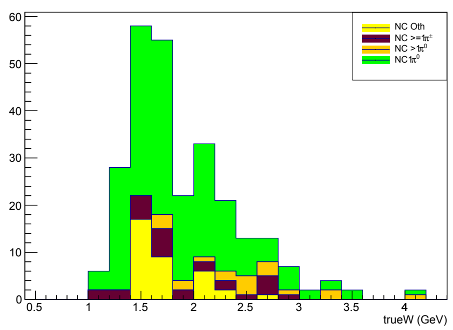

(e) true W in NC the background

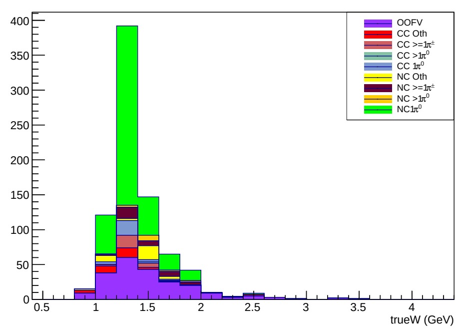

(f) true W in NC$1\pi^0$ the sidebands

Figure 4.29: Comparison of NC background and sidebands w.r.t Topology in RHC and water-out configuration

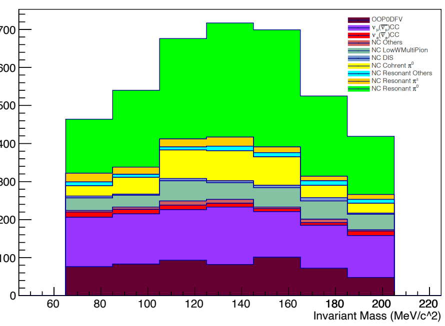

(a) water-in + FHC

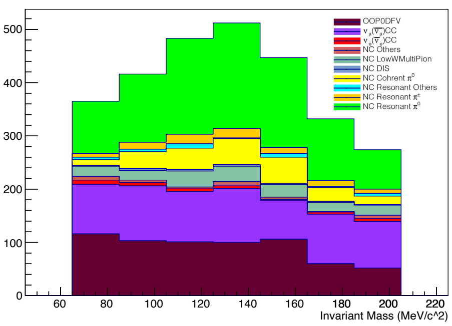

(b) water-out + FHC

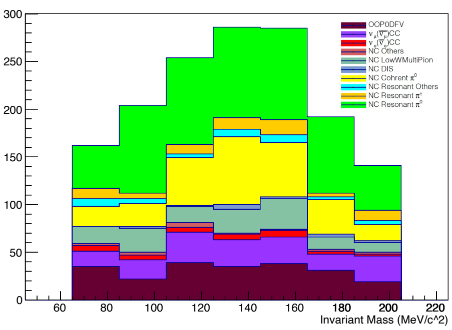

(c) water-in + RHC

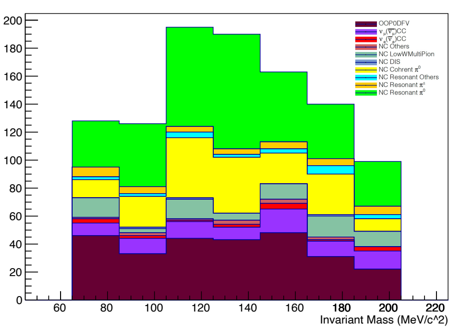

(d) water-out + RHC

Figure 4.30: Reconstructed Invariant Mass of selected NC1π^0 sideband in all 4 configuration w.r.t NEUT interaction channel

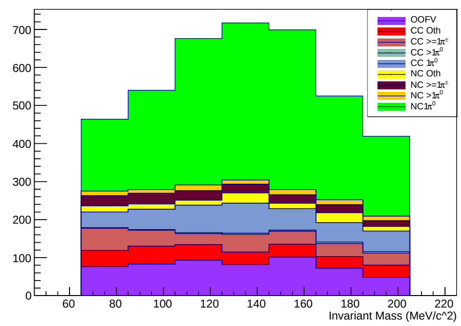

(a) water-in + FHC

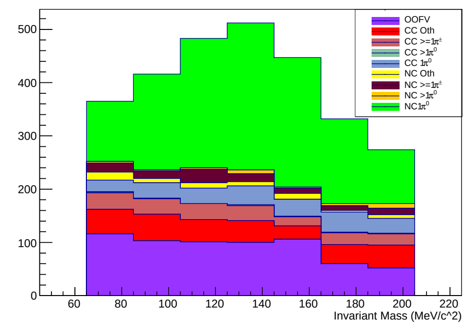

(b) water-out + FHC

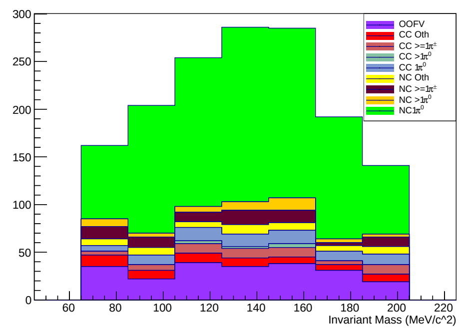

(c) water-in + RHC

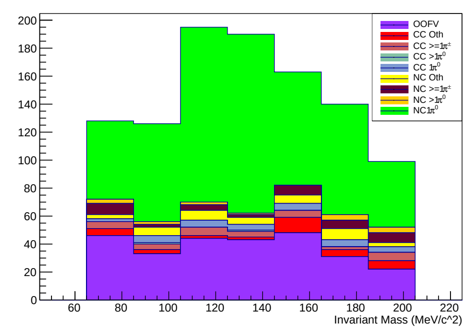

(d) water-out + RHC

Figure 4.31: Reconstructed Invariant Mass of selected NC1π^0 sideband in all 4 configuration w.r.t Topology

Chapter 5

Systematic Uncertainties

The MC are simulated based on current knowledge of flux, cross section models and detector reconstructions. However, none of them are perfectly known. Uncertainties on them must be considered and propagated when extracting cross sections.

5.1 Flux

The flux systematic uncertainties are parametrized by scale factors binned in true neutrino energy. The binning and covariance matrix of flux parameters are provided by the beam group. The version used in current fitter is 13av7p1 [66]. Tables 5.1 show the binning for flux and figures 5.1 show the covariance matrix for flux at ND280 in FHC and RHC, respectively.

Table 5.1: Neutrino Energy Binning for flux at ND280

(a) Neutrino Energy Binning for flux in FHC at ND280

ν flavour	Nbins	Binning (GeV)
ν_μ	11	0, 0.4, 0.5, 0.6, 0.7, 1.0, 1.5, 2.5, 3.5, 5, 7, 30
$\bar{\nu}_\mu$	5	0, 0.7, 1.0, 1.5, 2.5, 30
ν_e	7	0, 0.5, 0.7, 0.8, 1.5, 2.5, 4, 30
$\bar{\nu}_e$	2	0, 2.5, 30

(b) Neutrino Energy Binning for flux in RHC at ND280

ν flavour	Nbins	Binning (GeV)
ν_μ	5	0, 0.7, 1.0, 1.5, 2.5, 30
$\bar{\nu}_\mu$	11	0, 0.4, 0.5, 0.6, 0.7, 1.0, 1.5, 2.5, 3.5, 5, 7, 30
ν_e	2	0, 2.5, 30
$\bar{\nu}_e$	7	0, 0.5, 0.7, 0.8, 1.5, 2.5, 4, 30

5.2 Cross-Section

A set of parameters to parametrize the uncertainty in the nominal MC from the neutrino interaction models are used here. The uncertainties and the covariance matrix for some parameters are from the T2K BANFF systematic parameters for 2019-2020 oscillation analysis[67]. Other than them, parameters for NC DIS/MPi interactions are developed just for this analysis. Parameters can be categorized into two types, normalization parameters and shape parameters. Normalization parameters have the same effect on every event. Shape parameters on the other side, may have different effects on events if for example, their true neutrino energies or true momentum transfers are different. Thus, normalization parameters are directly applied in the fitter to weight every event and the shape parameters are applied via response functions (also

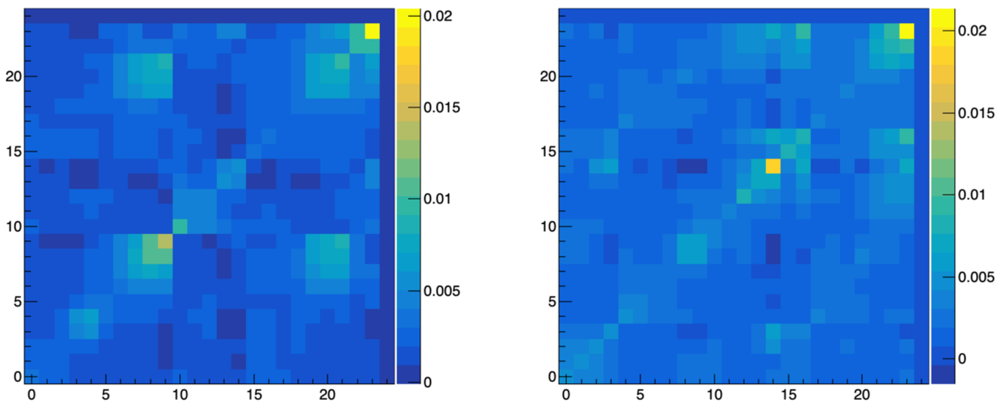

(a) Flux covariance matrix in FHC. Indices 0-10 represent ν_μ bin1 to bin11. Indices 11-15 represent $\bar{\nu}_\mu$ bin1 to bin5. Indices 16-22 represent ν_e bin1 to bin7. Indices 23-24 represent $\bar{\nu}_e$ bin1 to bin2.

(b) Flux covariance matrix in RHC. Indices 0-4 represent ν_μ bin1 to bin5. Indices 5-15 represent $\bar{\nu}_\mu$ bin1 to bin11. Indices 16-17 represent ν_e bin1 to bin2. Indices 18-24 represent $\bar{\nu}_e$ bin1 to bin7

Figure 5.1: Flux covariance matrix at ND280 from BANFF input of version 13av7p1

called splines in this thesis later) which are generated by T2K-Reweight. The versions/branches of the T2K-Rewight, NIWG-Reweight and NEUT used to generate the response functions in this analysis are listed below.

- T2K-Reweight: OA2021Development[68]
- NIWG-Reweight: OA2021Tidy[69]
- NEUT: PreOA2021DevelopmentMerge[70]

Table 5.2 summarises all cross-section modelling parameters used in this analysis.

Table 5.2: Summary Cross-section Modelling Parameters applied in this analysis

Parameter	Type	Nominal Value	Prior value	Uncertainty
$\mathrm{M_A^{QE}}$	Shape	1.21	1.03	0.2
$\mathrm{M_A^{RES}}$	Shape	0.95	1.07	0.15
$\mathrm{C_A^5}$	Shape	1.01	0.96	0.15
ISO BKG	Shape	1.30	0.96	0.31
CC BY DIS	Shape	0	0	1
CC BY MPi	Shape	0	0	1
CC AGKY MPi	Shape	0	0	1
CC DIS Norm nu	Norm	1	1	1
CC MPi Norm nu	Norm	1	1	1
CC DIS Norm nubar	Norm	1	1	1
CC MPi Norm nubar	Norm	1	1	1
2p2h Norm nu	Norm	1	1	0.5
2p2h Norm nubar	Norm	1	1	0.5
NC Resonant Norm	Norm	1	1	0.3
NC Coherent Norm	Norm	1	1	0.3
$\bar{\nu}_e/\bar{\nu}_\mu$ ratio	Norm	1	0.1	
NC BY DIS	Shape	0	0	1
NC BY MPi	Shape	0	0	1
NC AGKY Mult	Shape	0	0	1
NC MultiPi Shape	Shape	0	0	1
NC DIS/MPi Norm	Norm	1	1	1
CExLowMomProb(FEFCX)	Shape	0.697	0.697	0.43
AbsProb(FEFABS)	Shape	1.404	1.404	0.31
InelProb(FEFINEL)	Shape	1.002	1.002	1.009
QELowMomProb(FEFQE)	Shape	1.069	1.069	0.30
QEHighMomProb(FEFQEH)	Shape	1.824	1.824	0.47
CExHighMomProb(FEFCXL)	Shape	1.8	1.8	0.30

5.3 Detector

5.3.1 Fiducial Volume

Sources of Fiducial Volume systematic uncertainties can be decoupled to two cases. One is the vertex resolution of reconstruction due to P0D structure and reconstruction algorithm. Another one is the migration of background events who interaction vertices are away from where particles are generated because of the physics of detection. For example, for NC1π^0 interactions, the π^0 is produced at where the interaction happens and then π^0 decay into photons which generates $e^{\pm}$ via pair production. Until the first pair of $e^{\pm}$ is generated, the interaction cannot be detected by the detector. For the first case of vertex resolution, because of algorithm and P0D structure, it can be divided to subcases according to how many reconstructed objects and where the interaction happens, in scintillator bars or NOT, i.e.

- case1: vertex resolution because of P0D structure and reconstruction algorithm
  - subcase 1.1: single reconstructed object
    * subcase 1.1.1: true vertex in scintillator bars
    * subcase 1.1.2: true vertex NOT in scintillator bars, e.g. in water bags or brass sheets
  - subcase 1.2: multiple reconstructed objects
- case2: background events migration because of physics

Figure 5.2, 5.3 and 5.4 are the distribution of difference between reconstructed vertex position and true vertex position along x, y and z direction for events passing the cuts of Valid Vertex, FV. On one xy plane which is perpendicular to the beam direction, P0D structure is uniform(ideally). The distribution at x and y direction is symmetric with respect to 0 from figures 5.2 and 5.3as excepted. Figure 5.4 clearly shows that the distribution is not symmetric along z direction and there are several spikes. From the left plot, most events are from $\nu_\mu CC$ interactions so the effect of case 2 can be ignored in this sample for now. Those spikes show the motivation why the subcase 1.1 is split into two subcases.

For the spikes in the bin [37.5-42.5mm), the interactions targets are mostly brass shown in the plot on the right side. As introduced in chapter 3, the P0D Water Target region consists of alternative structures of two layers of scintillator bars, a layer of brass and a layer of water bags. Thus, for an interaction on brass, if particles go forward which is the mostly likely case, then the first hit which can be collected is in the first scintillator layer after the water bag. Height of water bag(size along z direction) is about 28mm, height of brass sheet is about 1.28mm and height of triangular scintillator bar is about 17mm. The hit position will be chosen as the center of the scintillator bar. So the hit position is about 37.78mm (28+1.28+17/2mm) away from the interaction vertex. Because in the reconstruction algorithm, if there is only one reconstructed obejct, the starting point will be the vertex position. If there is a long track, it's very likely that the starting point of this long track which usually is the position of the first in this track will be chosen as the vertex position. As a result, there will be a high spike around 37.78mm in the distribution of (ReconVertexPositionZ - TrueVertexPositionZ), which is what has been seen in the plot. Besides this very high peak, there are several smaller spikes in the negative side, for example, in the bin of [-12.5, -7.5mm) and [-32.5, 27.5mm). They are caused by backward going particles in the interaction. Besides the obvious spikes, there are more events on the positive side than the negative side. They locate in between the bin [-2.5, 2.5mm) and the bin [37.5-42.5mm) which the bin of the highest spike, and most of them are from interactions on oxygen which means that these events happen on water. They are caused by the same reason as that for the brass.

For the subcase 1.1.2,

- For the case that events happen in Upstream ECal, if the single particle of such an event goes to Water Target, it has to pass the first two scintillator layers which is after Upstream ECal and before water bags. Thus, for such events, their vertices would be chosen in the first layer of scintillator bars. The choice of FV on the upstream side excludes such events so such case wouldn't affect the selected results.

- For the case that events happen in Water Target, because the FV on the downstream side is chosen in between two scintillator layers so the interactions happen in the water bags or brass before that two scintillator layers would be kept. Although there could a shift on vertex position but the total number of events will not be affected.

- For the case that events happen in Central ECal, unless the particles go backward, it would not affect events in FV. In principle, such case happens only when there are multiple particles generated but reconstructed

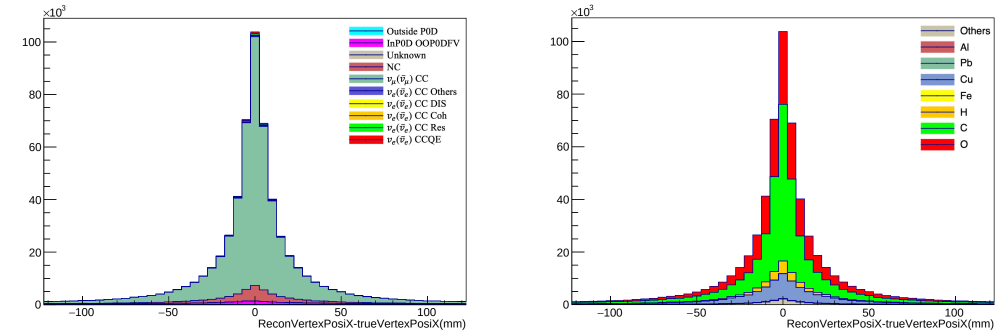

Figure 5.2: (ReconVertexPositionX - TrueVertexPositionX) of events passing valid vertex cut, Fiducial volume cut and additional cut on vertex position at Z in the configuration of water-in and FHC beam

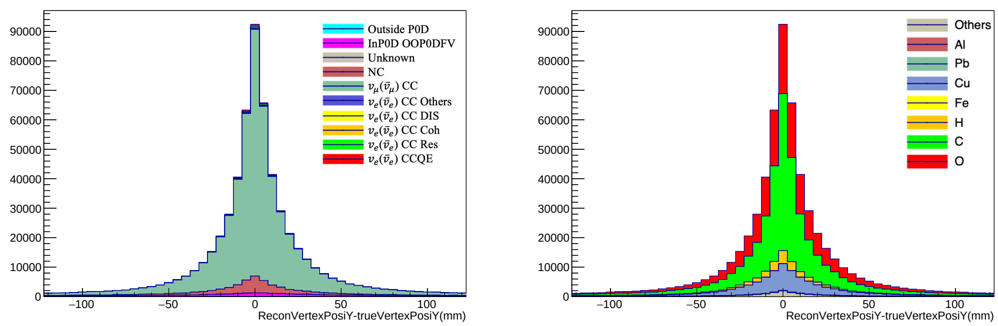

Figure 5.3: (ReconVertexPositionY - TrueVertexPositionY) of events passing valid vertex cut, Fiducial volume cut and additional cut on vertex position at Z in the configuration of water-in and FHC beam

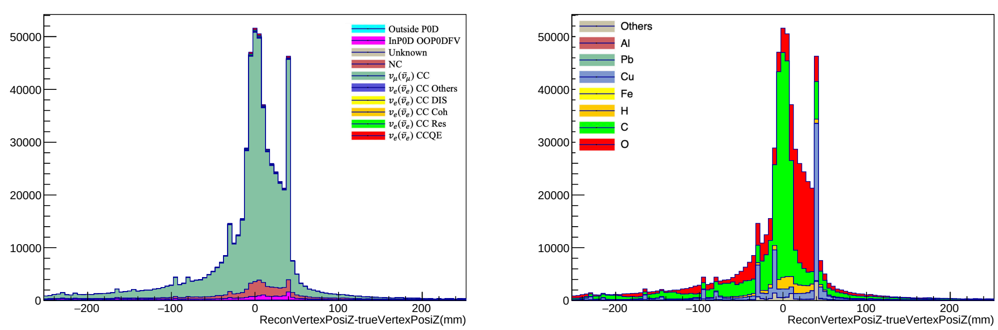

Figure 5.4: (ReconVertexPositionZ - TrueVertexPositionZ) of events passing valid vertex cut, Fiducial volume cut and additional cut on vertex position at Z in the configuration of water-in and FHC beam

Table 5.3: Vertex Resolution

configuration	Resolution at X(mm)	Resolution at Y(mm)	Resolution at Z(mm)
water-in	22.5	22.9	46.6
water-out	22.9	22.5	47.3

as one. Otherwise, it violates the conservation of momentum. The fraction of events in such case is very small.

In subcase 1.2, with multiple outgoing particles, the shift of vertex positions in subcase 1.1.2 in principle can be avoided when tracking back multiple trajectories and then locating the pairwise vertex. The vertex resolution is defined by he half the distance from the 16 % and 84 % quantiles of distributions of (ReconVertexPosition - TrueVertexPosition).

Figure 5.5, 5.6 and 5.7 shows the distribution of (ReconVertexPosition - TrueVertexPosition) along X, Y and Z in waterin and FHC configuration after requiring more than one reconstructed objects. Figure 5.8, 5.9 and 5.10 shows the distribution in waterout and FHC configuration. The plots clearly show that after requiring multiple objects, the spikes drops significantly and the distributions along z becomes more symmetric. The resolution is summarized in table 5.3

To study the data-mc difference in terms of vertex resolution, a sample has been selected using cuts listed below. It aims to select ν_μ CC interactions with multiple outgoing particles.

- Valid vertex
- More than 1 valid objects which are from Track Recon stages directly in

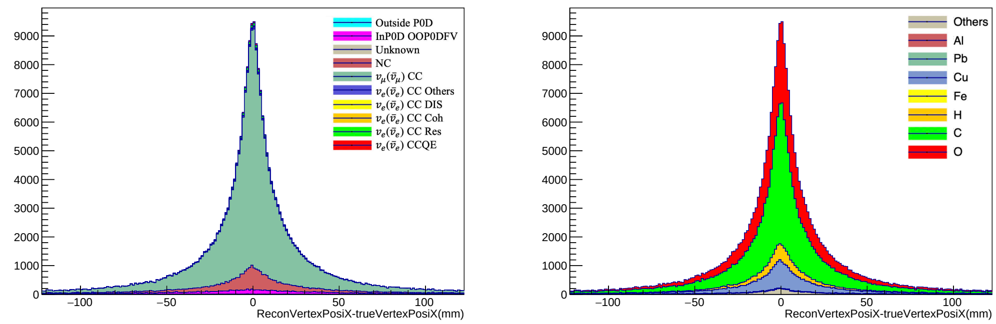

Figure 5.5: Vertex Resolution on X (water-in and FHC)

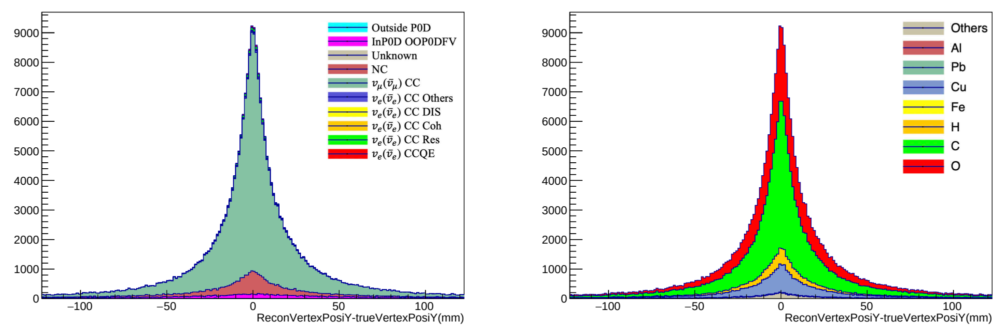

Figure 5.6: Vertex Resolution on Y (water-in and FHC)

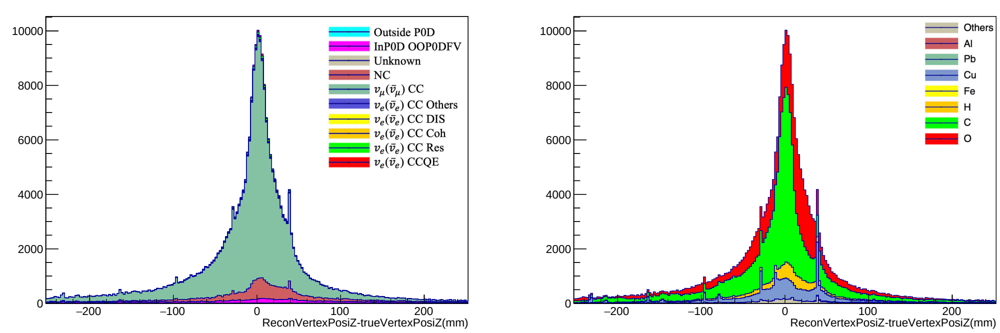

Figure 5.7: Vertex Resolution on Z (water-in and FHC)

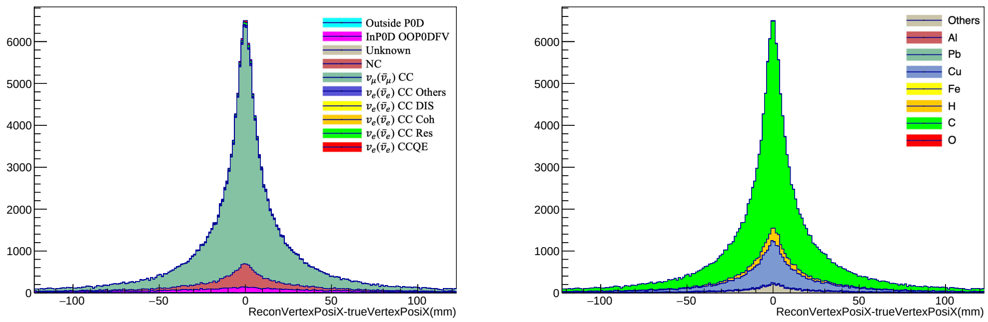

Figure 5.8: Vertex Resolution on X (water-out and FHC)

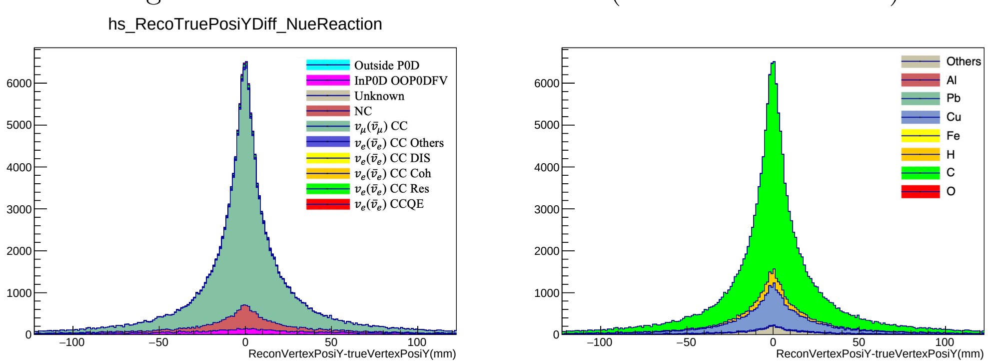

Figure 5.9: Vertex Resolution on Y (water-out and FHC)

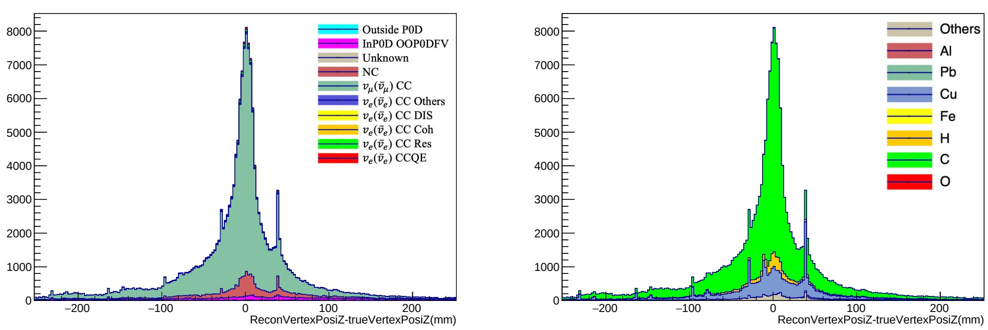

Figure 5.10: Vertex Resolution on Z (water-out and FHC)

final stage

- No Valid tracks
- Fiducial Volume cut

The data-mc comparisons are shown in figure 5.11 for water-in and FHC configuration.The mean and standard deviation of both truncated data and MC distribution are calculated. The relative difference between data standard deviation and MC standard deviation is very small (∼1%). Besides, both Chi-2 test or K-S test show than data-MC agrees well. Thus, uncertainties on vertex resolution is negligible.

For the case 2, it mainly caused by NC events from which the photons decayed from π^0 are detected until electrons are generated by pair production. In such case, the path from the point where the interaction happens to the point where electrons are generated cannot be seen. Thus, in the reconstruction, no matter how perfect the reconstruction algorithm is, such deviations from reconstructed vertex to true vertex caused by physics is inevitable.From the Monte Carlo study, it is found that the fraction of NCπ^0 events which are out of P0D FV (OOP0DFV) are about 2% .Thus, it is decided to apply 100% uncertainty on on such events.

5.3.2 Angular Resolution

A cut is applied on the shower direction to remove events whose candidate shower's angle along z axis is more than 45°. Events whose candidate showers close to this angle may migrate in or out which can effect the final selected

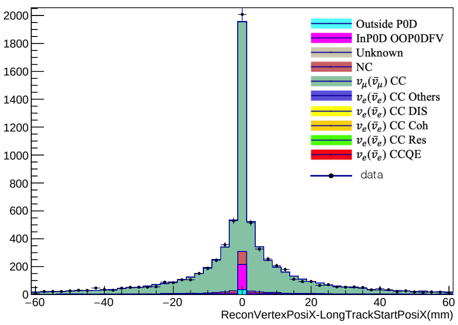

(a) VertexPositionX - longTrackStartingPositionX (mm)

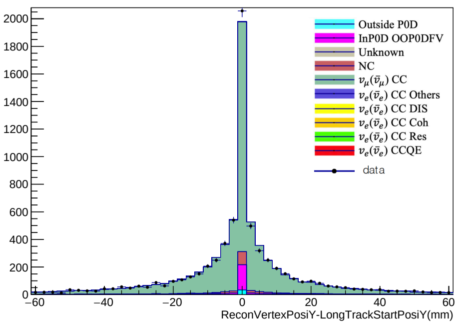

(b) VertexPositionY - longTrackStartingPositionY (mm)

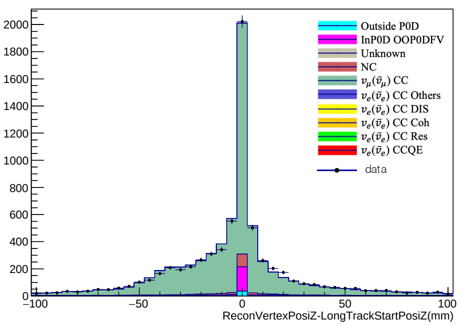

(c) VertexPositionZ- longTrackStartingPositionZ (mm)

Figure 5.11: Distribution of difference between VertexPosition and longTrackStartingPosition of control sample (waterin and FHC)

samples. In the previous analysis shown in T2K-TN-240 [61], the uncertainty caused by the angular resolution is smaller than 0.01 for both water-in and water-out configurations as well for on-water ratio. Therefore it is concluded that the systematic uncertainty coming from the angular resolution is negligible.

5.3.3 Particle Identification (PID) Systematic Uncertainties

The selections are based on the candidate track and candidate shower whose reconstructed energies are the highest among all objects after track and shower reconstruction stage, respectively. Whether hits from an electron goes to shower reconstruction stage will affect the number of selected signals and whether a muon, proton or other non-EM particle goes to shower reconstruction stage will affect the number of selected backgrounds. PID systematic uncertainties in this analysis are to study the systematic uncertainties on efficiency of identifying an electron as EM. Figure 3.4 briefly shows the reconstruction flow of P0D. As introduced in chapter 3, for each reconstructed object in track reconstruction stage, there are 4 types of PID hypotheses. They are classified as kLightTrack, kHeavyTrack, kEM and kOther. kOther is assigned under the case when the object travels less that 4 P0Dules. In the signal selections as section 2.1.6 mentioned, events are removed when their candidate tracks travel less than certain number of layers listed in table 4.6. The cut values are larger than 8 layers (for 4 P0Dules) in all 4 configurations, so events with candidate tracks classified as kOther will not be selected in the final sample. Thus, PIDs to study are the other three, kLightTrack, kHeavyTrack and kEM. Among the three PIDs, the reconstruct object is classified to the one whose likelihood is maximum. If it's classified as kEM, the object will go to the shower reconstruction stage. Otherwise, it will go to final objects stage directly. Likelihood of each PID hypothesis is calculated based on variables listed below.

- trackP0DuleAsymmetry
- trackMedianWidth
- trackWTCharge
- trackWTChargeRMS
- trackECalCharge
- trackECalChargeRMS
- trackECalChargeAsym
- trackLayerChargeVAngle

The probability density function (pdf) of each variable for each PID is known. The log likelihood of each PID hypothesis equals to the sum over the log likelihood of all variables listed above. Use trackP0DuleAsymmetry as an example to explain in more details below.

TrackP0DuleAsymmetry is a 2D variable. It means charge asymmetry between two adjacent P0Dules, $\frac{\text{diff}}{\text{sum}}$, VS P0Dules from the end. P0Dules from the end means that it is counted backward from the last P0Dule which the object goes through and marked as 0 , 1, 2, 3, 4 for last five P0Dules. Starting from 6th P0Dule counting backward, every P0Dule is marked as 5. The charge asymmetry in one P0Dule is calculated using charges in the P0Dule and its previous P0Dule. The first P0Dule the object goes through, i.e. the last one if counting backward, is not included as it does not have any "previous" P0Dule.

Figures 5.12 show the pdf of the variable trackP0DuleAsymmetry for kLight-Track, kHeavyTravk and kEM when the object stops in Water Target region when P0D is in water-out configuration, respectively. After getting the vector of charge asymmetry vs P0Dule from the end, search in the the pdf such as figure 5.12 and sum over all log likelihood given by each pair of charge asymmetry vs P0Dule in the vector. Then the log likelihood given by this variable for this object can be obtained.

Sand muons are used as the control samples to study data-MC difference for PIDs. What should be pointed out is that using sand muon as control samples can help to study the systematic uncertainties of PID for muons, but in principle, it is not equivalent to systematic uncertainties of PIDs for electrons. However, there is no electron control samples to use. As a result, it is assumed here that the systematic uncertainties of PIDs for electrons is same with that for muons. The systematic uncertainties eventually will be applied to the efficiency of the selection.

The control sample selection strategies are listed below:

- Among reconstructed objects after track recon stage, choose the longest one and call it candidate sandmuon-like object.
- For the candidate sandmuon-like object, it is required to have hits in the first layer of first P0Dule in P0D. This is to select objects coming from outside of P0D.
- For the candidate sandmuon-like object, it is required to have no hits in the last layers of last P0Dule and no hits in the side bar, which means the object stops in P0D.
- The candidate sandmuon-like object goes to WT region in P0D and pass

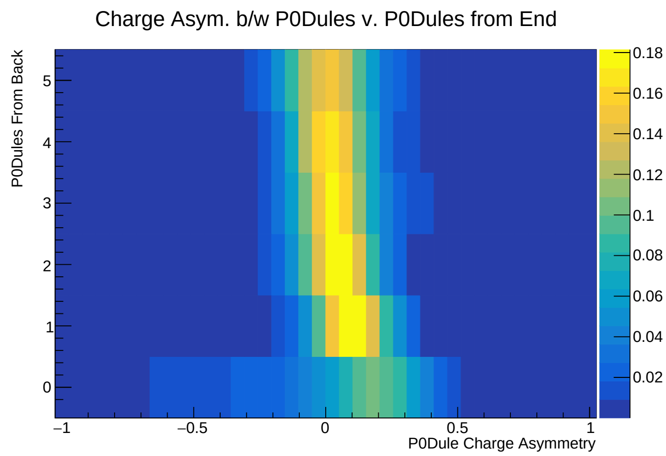

(a) trackP0DuleAsymmetry_wateroutconfig_WatertargetContained_LightTrack

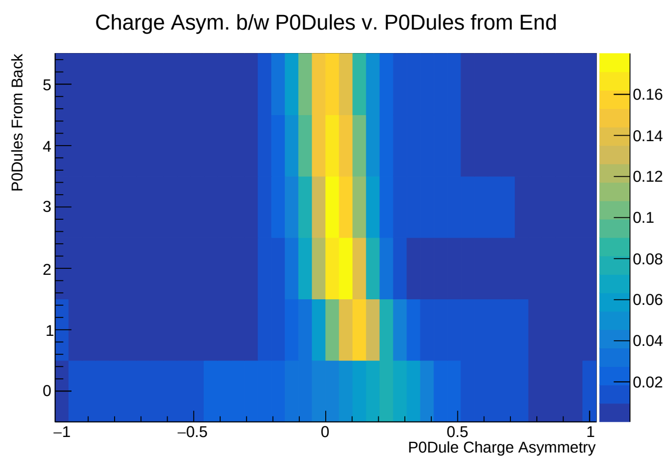

(b) trackP0DuleAsymmetry_wateroutconfig_WatertargetContained_HeavyTrack

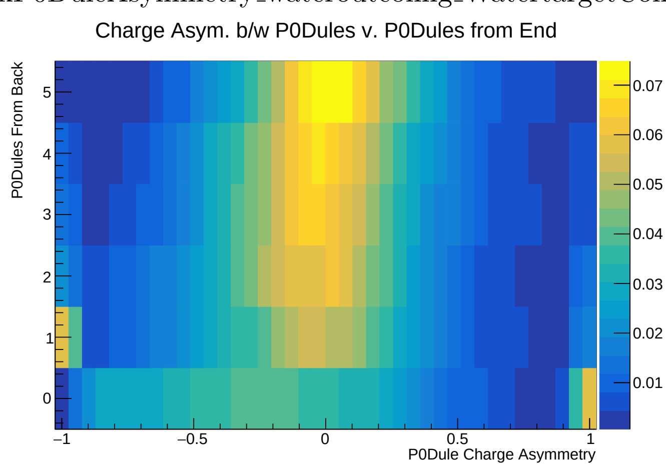

(c) trackP0DuleAsymmetry_wateroutconfig_WatertargetContained_EM

Figure 5.12: pdf of trackP0DuleAsymmetry_WatertargetContained in wateroutconfig for all PIDs

$>$10 P0Dules in WT, which means it passes $>$17 P0Dules in P0D because Upstream ECal has 7 P0Dules.

- The reconstructed energy is $>$300MeV to remove electron/positron.

The goal is to build a map for each variable between data and MC using the control sample. The approaches to build the map are list below.

- Get cumulative distribution of each variable from sand muon samples.
- For each variable, use the variable value in data which has the same cumulative probability value to replace the variable value in MC
- Such one-to-one relation is called the map between data and MC for each variable

The map built from the control samples is applied to the Magnet MC of neutrino interactions and new likelihoods are calculated based on mapped new values of variables. Then the difference on the number of classifications of kEM can be obtained and changes on the selection efficiency can be studied.

Once again, trackP0DuleAsymmetry is used as an example to show how the map is built and applied. For other variables, please see the details in Appendix A. As mentioned above, trackP0DuleAsymmetry is a 2D variable of charge asymmetry vs P0Dule from the end. The distribution of charge asymmetry of each P0Dule is considered separately, i.e. the map is built for charge asymmetry in each P0Dule. Figures from 5.13a to 5.18b show the data-MC comparisons of charge asymmetry from P0Dule0 to P0Dule5 counting backward. From the map between data and MC for charge asymmetry of each P0Dule obtained from sand muon control samples, the mapped values of

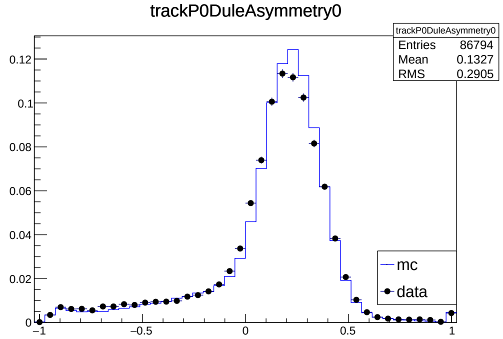

(a) Distribution of charge asymmetry of P0Dule 0 counting backward

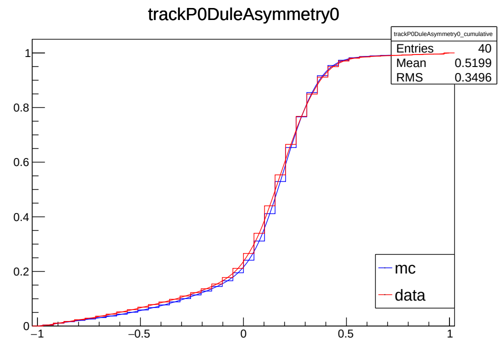

(b) Cumulative distribution of charge asymmetry of P0Dule0 counting backward

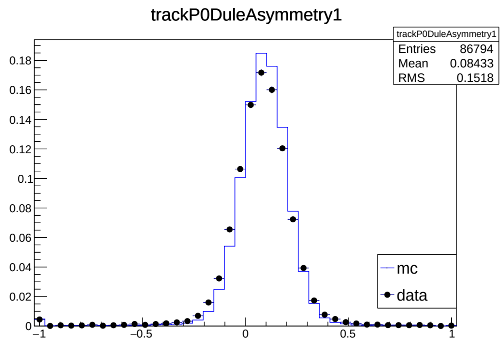

(a) Distribution of charge asymmetry of P0Dule1 counting backward

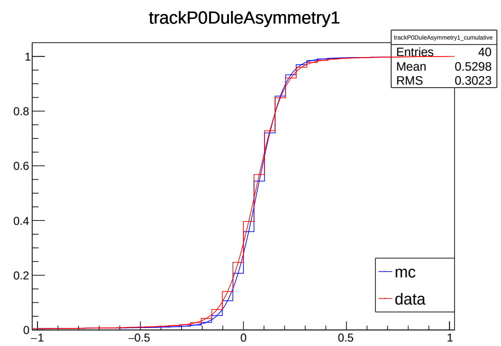

(b) Cumulative distribution of charge asymmetry of P0Dule1 counting backward

trackP0DuleAsymmetry for the Magnet MC sample can be obtained. By doing this for every variables, the likelihood of each objects for each PID hypothesis can be recalculated and then the effect on the selected events can be estimated.

Table 5.4 shows the comparison of numbers of events for PIDs for the water-in configuration before and after mapping with certain Magnet MC sample. Table 5.5 shows the percentage. The table shows that after mapping, electron identification shows a difference of approximately 0.4% and muon mis-

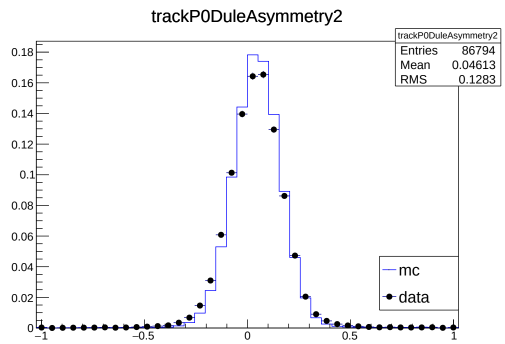

(a) Distribution of charge asymmetry of P0Dule2 counting backward

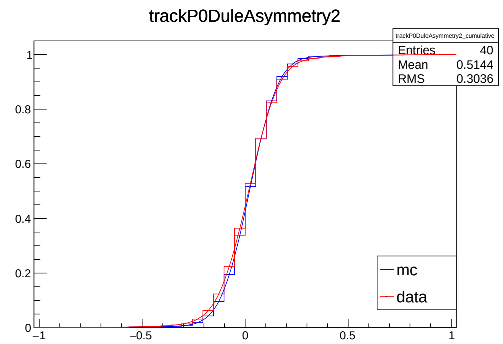

(b) Cumulative distribution of charge asymmetry of P0Dule2 counting backward

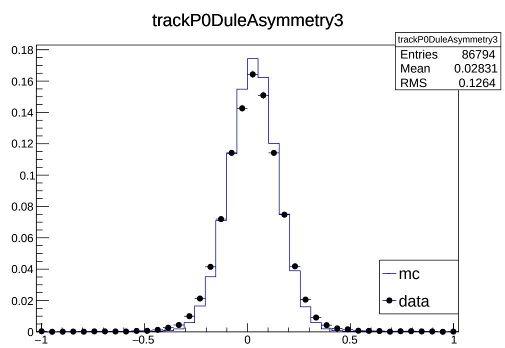

(a) Distribution of charge asymmetry of P0Dule3 counting backward

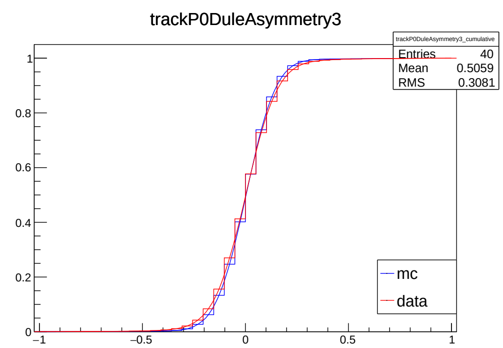

(b) Cumulative distribution of charge asymmetry of P0Dule3 counting backward

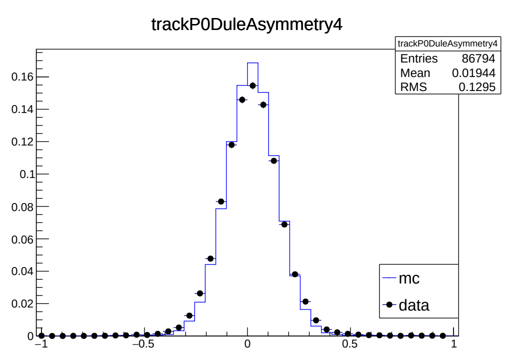

(a) Distribution of charge asymmetry of P0Dule4 counting backward

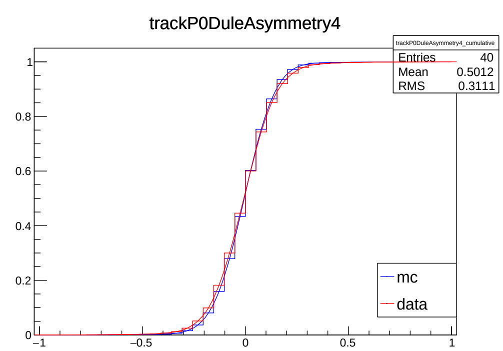

(b) Cumulative distribution of charge asymmetry of P0Dule4 counting backward

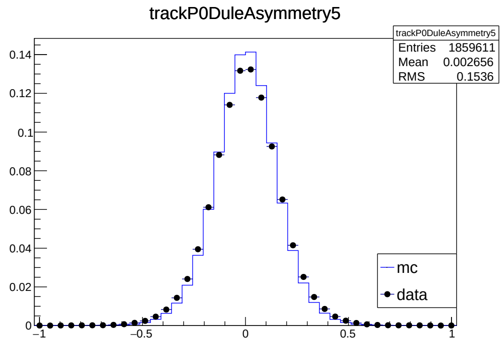

(a) Distribution of charge asymmetry of P0Dule5 counting backward

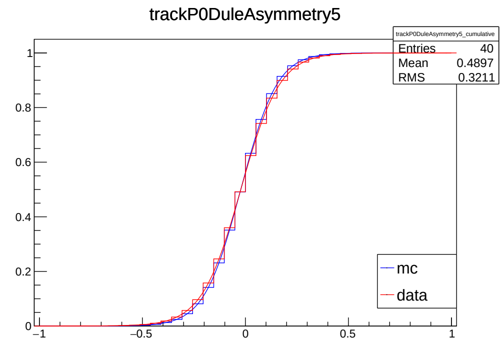

(b) Cumulative distribution of charge asymmetry of P0Dule5 counting backward

idetification shows a difference of approximately 1%. Thus, 1% of uncertainty selection efficiency is assigned in water-in configuration. Similar study has been done for water-out configuration as well and 1.8% of uncertainty is assigned to selection efficiency in water-out configuration.

Table 5.4: Comparison of numbers of events for the PID at the tracking stage for the water-in configuration before and after mapping

Counts	True Muon	True Proton	True Electron
Before Mapping			
LightTrack	747413	10412	195
HeavyTrack	462380	180080	1813
EM	54642	86049	73794
After Mapping			
LightTrack	671000	10578	127
HeavyTrack	525575	175409	1556
EM	67860	90554	74119

Table 5.5: Comparison of percentage of events for the PID at the tracking stage for the water-in configuration before and after mapping

Counts	True Muon	True Proton	True Electron
Before Mapping			
LightTrack	59.11%	3.77%	0.26%
HeavyTrack	36.57%	65.12%	2.39%
EM	4.32%	31.12%	97.35%
After Mapping			
LightTrack	53.07%	3.83%	0.17%
HeavyTrack	41.57%	63.43%	2.05%
EM	5.37%	32.75%	97.78%

5.3.4 Hit Fraction

Hit Fraction cut is a sanitary check cut. This cut it to check whether hits used to reconstruct the candidate shower contains hits used in the candidate track. This is to make sure that the reconstruction algorithm does not do something obviously wrong. Its uncertainty is negligible.

5.3.5 Track Median Width

As mentioned in the section 4.3.6, TMW cut removes events whose TMW is bin 0-1mm. The geometry of each scintillator bar in P0D is given in section 4.3.4. Each Bar is triangular and its height and width are 17 ± 0.5mm and 33 ± 0.5, respectively. Thus, having a median width less than 1mm is equivalent to the fact the the trajectory only hits one or two adjacent bars in each layer and TMW is actually equal to 0. Any scaling factor on TMW will not change the value when TMW=0.

5.3.6 Shower Median Width

To estimate the systematic uncertainty of SMW, control samples which are enriched with EM showers are selected. As in the selected signal enriched sample, electrons energies peak around 1GeV, the energies of EM showers from NCπ^0 is too low to match the signal. Thus, the goal is to select EM showers from ν_μ CC interactions which produce π^0. In the selected control samples, about 98% events are from ν_μ interaction and only 2% are from ν_e interactions.

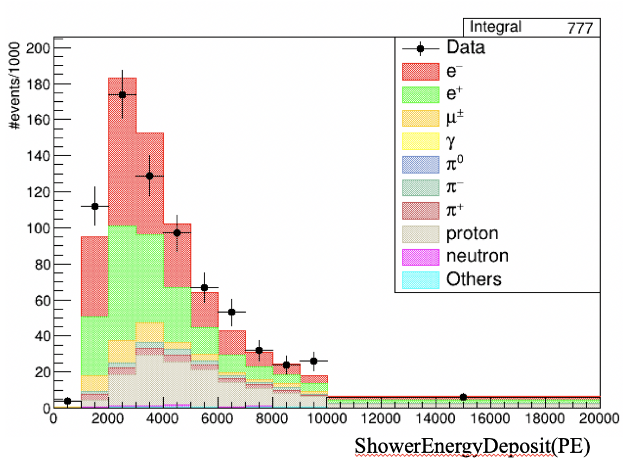

Figure 5.19: EM Shower Energy Deposition in Control Sample in water-in and FHC

The energy depositions of the selected showers in the control samples are shown in figure 5.19. As table 5.6a shows, for the truth of selected showers in the control samples, other than electrons (and positrons), protons' fraction is relatively high. Showers caused by electrons (or positrons) are because of bremsstrahlung radiation and pair production of photon, but showers caused by protons are due to hadronic interactions. Thus, in principle, show-

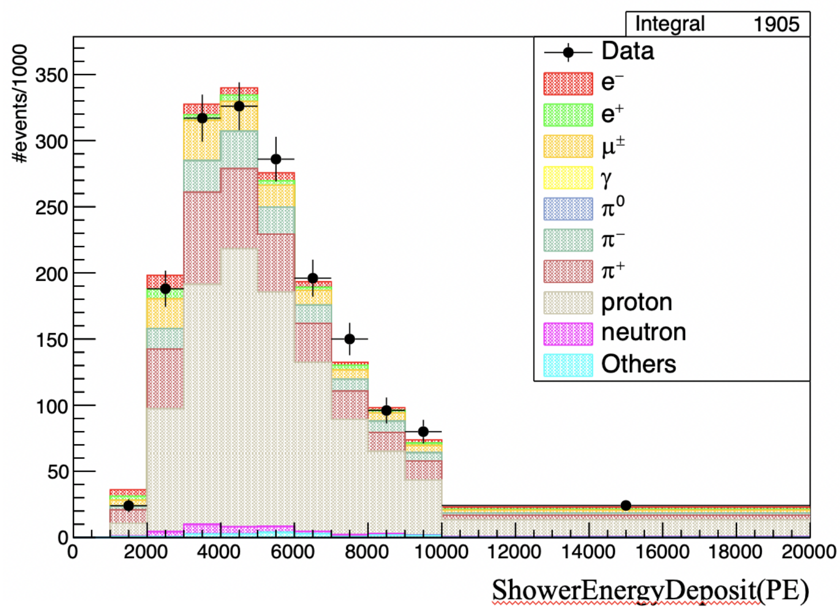

Figure 5.20: Hadron Shower Energy Deposition in Control Sample.

ers caused by electrons(or positrons) should not be treated the same as the showers caused by protons. Then, another control sample of showers caused by protons is selected. The shower energy depositions are shown in figure 5.20. Table 5.6b shows that $\pi^{\pm}$ occupies a large fraction. Because $\pi^{\pm}$ causes showers due to hadronic interactions too, it's not unreasonable to categorize them in the hadron shower control samples with protons.

A scaling parameter is assigned to shower median width. From left plots in figures 5.21a and 5.21b, the bin 0-1 mm have much more events than other bins. Considering such a bin will affect the fitting more than other bins and the TMW cut has removed almost all events in bin 0-1mm in the signal sample, the bin 0-1mm is removed when fitting the scaling parameter. The parameter for hadron showers is fitted first and then the best fit value is used as known parameter to fit the scaling parameter of EM showers. The fitted results are

Table 5.6: Particle Truth in EM and Hadron Shower Control Sample

(a) EM Shower Control Sample

Category	Fraction
e^-	37.45%
e^+	31.42%
$\mu^\pm$	5.76%
$\pi^\pm$	6.49%
proton	18.06%
neutron	0.45%
others	0.31%

(b) Hadron Shower Control Sample

Category	Fraction
e^-	3.50%
e^+	2.06%
$\mu^\pm$	8.75%
$\pi^\pm$	26.11%
proton	57.06%
neutron	1.26%
others	1.26%

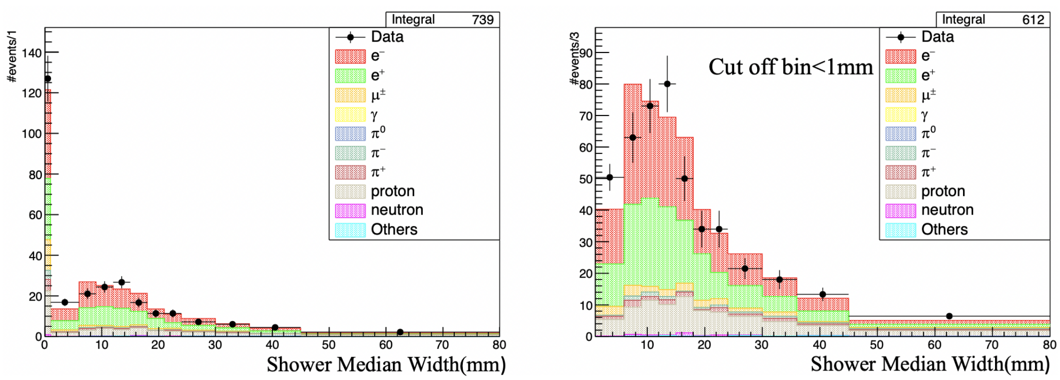

(a) EM Shower Median Width in Control Sample.

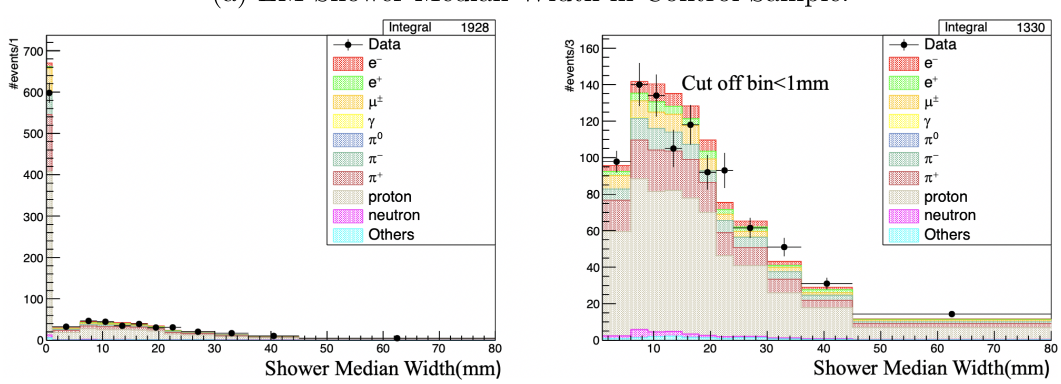

(b) Hadron Shower Median Width in Control Sample.

Table 5.7: Scaling Parameter on SMW

SMW Scaling Parameter	Fitted result
EM Shower SMW Scaling Parameter	0.96 ± 0.06
Hadron Shower SMW Scaling Parameter	1.06 ± 0.03

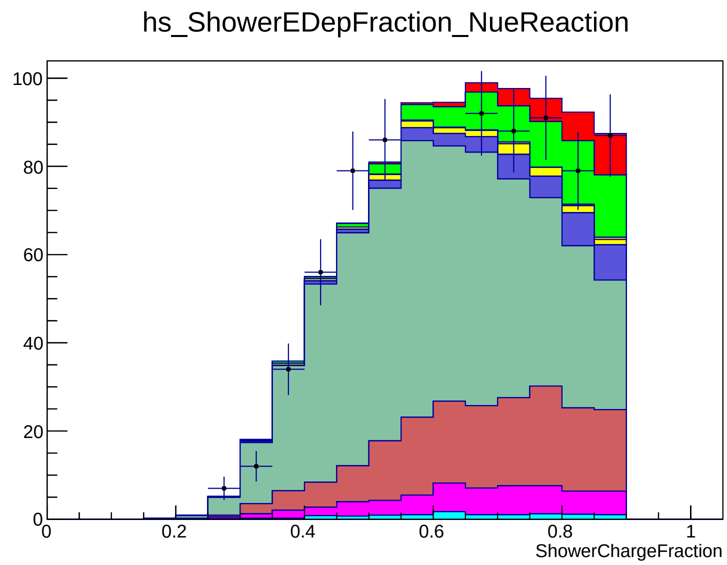

Figure 5.22: Shower Charge Fraction in Control Sample.

shown in table 5.7

5.3.7 Shower Charge Fraction

A scaling factor is assigned to shower charge fraction, too. The control samples used here are events which pass all other cuts but SCF Cut. Figure 5.22 shows the data-MC comparison of distribution of SCF. Fitted results of the scaling factor is shown in table 5.8.

Table 5.8: Scaling Parameter on SCF

Configuration	Fitted result
Water-in Configuration	1.006 ± 0.01
Water-out Configuration	1.006 ± 0.01

5.3.8 Shower Energy Scale

Shower energy calibrations have been introduced in section 3.3. As a reminder, the reconstructed energy of electron is estimated via the linear relations with the reconstructed charges (PE) shown as equation 3.1 and 3.2 for water-in and water-out configuration, respectively. The estimated values and uncertainties of the coefficient are given in table 3.1. The uncertainties are propagated to get uncertainties of reconstructed shower energies.

5.3.9 Water Mass

Because of the difference between as-built mass and simulated mass, the events whose true vertices are in inside P0D Fiducial Volume are re-weighted by ratio of the as-built mass over simulated mass. The re-weighting parameters are different for water targets and other targets. Interactions on the water targets are corrected with the water mass while events happening on other materials such as scintillator or brass are corrected with the dry mass. Table 5.9 listed the fiducial mass of water-in and water-out configuration for Run1 and Run2 as well as production 6 MC. Run1 and Run2 has different mass because the entire the water sensor system was replaced between those runs. The masses and their uncertainties for the water-in and water-out configurations are not

Table 5.9: The as-built fiducial mass and Production 6 MC fiducial volume masses for water-in and water-out configuration

	Water-in Configuration(kg)	Water-out Configuration(kg)
Run1	5460.86 ± 37.78	3558.86 ± 34.23
Run2	5480.30 ± 37.40	3578.30 ± 33.80
P6 MC	5393.22 ± 0.56	3469.14 ± 0.55

Table 5.10: The as-built fiducial water and non-water mass and Production 6 MC fiducial water and non-water

	Water Mass(kg)	Non-Water Mass(kg)
Run1	1902.00 ± 15.99	3558.86 ± 34.23
Run2	1902.00 ± 16.01	3578.30 ± 33.80
P6 MC	1924.08 ± 0.11	3469.14 ± 0.55

uncorrelated as the water-in configuration is composed of water and the non-water mass which should be identical with the water-out configuration. From table 5.9, the fiducial mass of water and non-water materials can be deducted as table 5.10 shown.

5.3.10 Detector Systematic Uncertainties For NC1π^0 Sideband Only

This section will describe detector systematic uncertainties used for NC1π^0 sideband only. However, they are not all of the detector systematic uncertainties applied for NC1π^0 sideband. Just to emphasize, some of the systematic uncertainties which have discussed before such as scaling of shower charge fraction 5.3.7, will be applied NC1π^0 sideband, too. As mentioned in the section

Table 5.11: Nominal Value and Uncertainties of the Scaling Factor on Two Showers Charge Fraction

Parameter	Water-in	Water-out
Signal Scale	0.022 ± 0.015	0.032 ± 0.015
Background Scale	0.005 ± 0.004	0.005 ± 0.004

4.6, the selection of NC1π^0 sideband used significant parts of selection strategies of P0D NC1π^0 analysis [64, 65]. Thus, studies of detector systematic uncertainties for NC1π^0 can be directly used here.

Systematics from Cut on Two Showers Charge Fraction

According to T2K-TN-364 [65], a scaling factor as eq 5.1 shows can be applied to the cut value of two shower charge fraction which is the ratio of charges of the most two energetic reconstructed showers over the total charges in the interaction as defined in section 4.6.2. Table 5.11 shows the estimated nominal value and uncertainties of the scaling factor for NC1π^0 signal events and background events under water-in and water-out configuration.

$$(TwoShowersChargeFraction)' = (1-scale)*(TwoShowersChargeFraction) \tag{5.1}$$

Systematics from Photon Energy Scale and Invariant mass

Invariant mass is a cut variable and is the binning variable for the NC1π^0 at the meanwhile. Thus, any changes on invariant mass could potentially affect the final results and uncertainties on the invariant mass must be propagated to the final results.

Invariant mass is calculated as Eq4.1 shows, where the reconstructed momentum of the two most energetic showers, $|\boldsymbol{p}_{s1}|$ and $|\boldsymbol{p}_{s2}|$of showers, are estimated as

$$p_\gamma = k_{ECAL} * \sum_{i \in ECal} Q_i + I_{ECAL} + k_{water-in,WT} * \sum_{i \in WT} Q_i + I_{water-in,WT} \quad (5.2)$$

$$p_\gamma = k_{ECAL} * \sum_{i \in ECal} Q_i + I_{ECAL} + k_{water-out,WT} * \sum_{i \in WT} Q_i + I_{water-out,WT} \quad (5.3)$$

A comprehensive studies has been done to estimated the constant coefficients in NC1π^0 analysis in T2K-TN-144 [64]. The estimated values are shown in the table 5.12. The uncertainties sources of the invariant mass are from the photon energy scale and the angular resolution of showers. As discussed in the section 5.3.2, the uncertainties from the angular resolution is negligible in P0D comparing other uncertainties sources. The uncertainties of invariant mass are from the uncertainties of the photon energy scales. They are propagated to the final results in the fitter.

Table 5.12: Photon Energy Scale

	Water-in WT	Water-out WT	ECal
Slope(k) (MeV/PEU)	0.197 ± 0.019	0.121 ± 0.011	0.262 ± 0.025
Intercept(I) (MEV)	14.1 ± 14.2	1.3 ± 13.0	16.0 ± 29.6

Systematics from Muon Decay Tag

Events which have non-zero muon decay clusters are rejected in the NC1π^0 sidebands selections. Thus, the efficiency and accuracy of muon decay tag will affect the results. Chapter 4.3.5 in T2K-TN-364 [65] has detailed discussions on how to deal with the systematic uncertainties caused by muon decay tag. As a summary here, events are categorized as CC events ans NC events, and for CC events, a correction on efficiency is applied and for NC events, a fake rate is applied. Table 5.13 shows the parameters.

Table 5.13: Muon Decay Efficiency and Fake Rate Parameters

	Water-in	Water-out
Fake Rate on NC	0.01065 ± 0.005	-0.0124 ± 0.007
Efficiency on CC	0.015 ± 0.007	-0.023 ± 0.0085

Chapter 6

Cross-Section Extraction Strategy

The previous analysis of measuring ν_e CC interaction rate on water in P0D [61, 71] fitted the data for water-in and water-out configurations separately and did the direct subtraction to get the measured event rate. In this thesis, instead of subtracting directly to get a point estimation of event rate in frequentist inference, data for water-in and water-out configurations are fitted simultaneously using the Markov Chain Monte Carlo (MCMC) method to do Bayesian inference to extract the posterior probabilistic distributions of cross sections on water.

Bayesian inference and the MCMC method will be introduced in the sections 6.1 and 6.2, respectively. How the information of interests is extracted from the posterior distribution and how to evaluate the model will be presented in section 6.4. After construct the mathematical foundation of Bayesian inference for the analysis, the definition of likelihood and binning choice used in the fitter will be discussed in section 6.5 and 6.7, respectively. The method of extracting cross sections from the posterior distributions after fitting will be explained in section 6.6.

6.1 Bayesian Inference

Bayesian inference is a method of statistical inference where the Bayes' Theorem shown in eq 6.1 is used to compute the posterior probability of a hypothesis H given the condition E.

$$P(H|E) = \frac{P(E|H)P(H)}{P(E)} \tag{6.1}$$

Note that

- $D_n = \{\boldsymbol{X}_1, \boldsymbol{X}_2, ..., \boldsymbol{X}_n\}$ is the observed data set where $\boldsymbol{X}_i$ is a measured data point
- $\boldsymbol{\theta} = \{\theta_1, \theta_2, ..., \theta_k\}$ is a set of parameters
- $\pi(\boldsymbol{\theta})$ is the probability density of parameters $\boldsymbol{\theta}$, which represents the prior beliefs about parameters $\boldsymbol{\theta}$ before the measurement with data. It is called the prior distribution.
- $p(\boldsymbol{X}|\boldsymbol{\theta})$ is statistical model/hypothesis representing the knowledge and beliefs about data given parameters $\boldsymbol{\theta}$

Then, the posterior distribution of parameters $\boldsymbol{\theta}$ after seeing the data determined by the Bayes' Theorem 6.1 is

$$\begin{aligned} P(\boldsymbol{\theta}|\boldsymbol{X}_1, \boldsymbol{X}_2, ..., \boldsymbol{X}_n) &= \frac{P(\boldsymbol{X}_1, \boldsymbol{X}_2, ..., \boldsymbol{X}_n|\boldsymbol{\theta})\pi(\boldsymbol{\theta})}{P(\boldsymbol{X}_1, \boldsymbol{X}_2, ..., \boldsymbol{X}_n)} \\ &= \frac{L(\boldsymbol{\theta})\pi(\boldsymbol{\theta})}{P(\boldsymbol{X}_1, \boldsymbol{X}_2, ..., \boldsymbol{X}_n)} \\ &\propto L(\boldsymbol{\theta})\pi(\boldsymbol{\theta}) \end{aligned} \tag{6.2}$$

where $L(\boldsymbol{\theta}) = P(\boldsymbol{X}_1, \boldsymbol{X}_2, ..., \boldsymbol{X}_n|\boldsymbol{\theta})$ is also called the likelihood function. With the data set D_n, $P(\boldsymbol{X}_1, \boldsymbol{X}_2, ..., \boldsymbol{X}_n) = \int P(\boldsymbol{X}_1, \boldsymbol{X}_2, ..., \boldsymbol{X}_n|\boldsymbol{\theta})\pi(\boldsymbol{\theta})d\boldsymbol{\theta}$ is independent from $\boldsymbol{\theta}$. The posterior distribution then is proportional to the product of likelihood function and prior distribution as Eq 6.2 shows. It is often not easy to calculate the integral $\int P(\boldsymbol{X}_1, \boldsymbol{X}_2, ..., \boldsymbol{X}_n|\boldsymbol{\theta})\pi(\boldsymbol{\theta})d\boldsymbol{\theta}$. Fortunately, to sample a desired distribution using MCMC, what is needed is a function proportional to the desired distribution. Thus, with the MCMC method, the posterior distribution can be sampled with given $L(\boldsymbol{\theta})\pi(\boldsymbol{\theta})$.

With the estimated posterior distributions across the full parameters spaces, for some parameters of interests, their distributions can be estimated by marginalization. For example, if parameter θ_1 is the one to be measured, then

$$p(\theta_1|\boldsymbol{X}_1, \boldsymbol{X}_2, ..., \boldsymbol{X}_n) = \int P(\theta_1, \theta_2, ..., \theta_k|\boldsymbol{X}_1, \boldsymbol{X}_2, ..., \boldsymbol{X}_n)d\theta_2, ..., d\theta_k \tag{6.3}$$

6.2 Markov Chain Monte Carlo Method

Monte Carlo method is to obtain some numerical results by randomly sampling from a desired distribution. The sampled results can be used to for example simulate certain process or estimate some parameters. There are many algorithms to do random sampling. For instance, rejection sample is one of the most basic sampling algorithm which uniformly sample points and reject those whose probability is above the desired value. Such method will be very inefficient with high-dimensional distribution. Markov Chain is a stochastic model that the probability of next state depends only on the present state. For example, consider a discrete process X_n, Markov Chain state would satisfy the property that $P(X_{n+1} = x|X_n = x_n, X_{n-1} - x_{n-1}, ..., X_1 = x_1) = P(X_{n+1} = x|X_n = x_n)$. Markov Chain Monte Carlo method, as the name suggests, is to sample a desired distribution by constructing Markov Chains. MCMC is more efficient to sample multi-dimensional distributions comparing with the generic Montel Carlo algorithms. There are a class of algorithms to construct the Markov Chain. What is used in this thesis is Adaptive Metropolis Hasting Algorithm.

6.2.1 Adaptive Metropolis Hasting Algorithm

Metropolis Hasting Algorithm is named after N. Metropolis who first developed this method [72] and W. K. Hastings who extended it into more general cases [73].

The implementation of the algorithm is described below. Figure 6.1 also shows a flowchart of the process. Note that $p(\boldsymbol{\theta})$ is the desired probability distribution and $f(\boldsymbol{\theta})(\propto p(\boldsymbol{\theta}))$ is a function that can be obtained n a fairly easy way and is proportional to the desired distribution. In this thesis, $p(\boldsymbol{\theta})$ is the posterior distribution $P(\boldsymbol{\theta}|\boldsymbol{X}_1, \boldsymbol{X}_2, ..., \boldsymbol{X}_n)$ and $f(\boldsymbol{\theta})$ is the $L(\boldsymbol{\theta})\pi(\boldsymbol{\theta})$ in

Eq 6.2.

The processes to implement the Metropolis Hasting Algorithm:

- Initialization: Choose an initial state $\boldsymbol{\theta} = \boldsymbol{\theta}_0$ (which could be either a random state or a given state). Choose a arbitrary probability density function function $g(\boldsymbol{\theta}'|\tilde{\boldsymbol{\theta}})$ which actually represents the transition function from state $\tilde{\boldsymbol{\theta}}$ to state $\boldsymbol{\theta}'$. Usually a symmetric function is chosen for $g(\boldsymbol{\theta}'|\tilde{\boldsymbol{\theta}})$, i.e $g(\boldsymbol{\theta}'|\tilde{\boldsymbol{\theta}}) = g(\tilde{\boldsymbol{\theta}}|\boldsymbol{\theta}')$.

- Start iteration from t=0 (initial state)

  - At a step t, propose a random state $\boldsymbol{\theta}'$ from $g(\boldsymbol{\theta}'|\boldsymbol{\theta}_t)$.
  - Calculate acceptance ratio $\alpha = \frac{f(\boldsymbol{\theta}')}{f(\boldsymbol{\theta}_t)} \left(= \frac{p(\boldsymbol{\theta}')}{p(\boldsymbol{\theta}_t)}, \text{because} f(\boldsymbol{\theta}) \propto p(\boldsymbol{\theta})\right)$
  - Generate a random number u from uniform distribution in $[0, 1]$.

    if $u < \alpha$, accept $\boldsymbol{\theta}'$ as the next step, i.e. $\boldsymbol{\theta}_{t+1} = \boldsymbol{\theta}'$.

    if $u > \alpha$, reject $\boldsymbol{\theta}'$ and current step as next step, i.e. $\boldsymbol{\theta}_{t+1} = \boldsymbol{\theta}_t$.

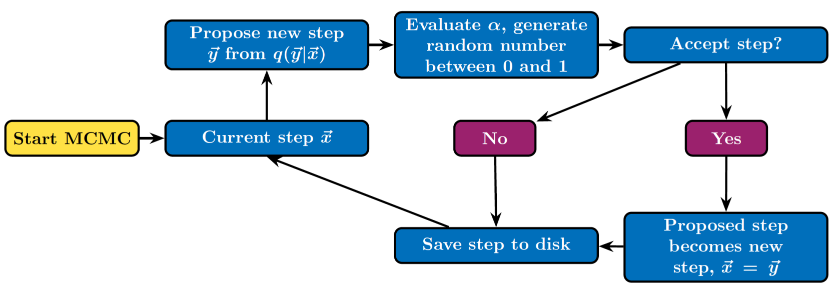

Figure 6.1: Flow Chart of Metropolis Hasting Algorithm. Figure taken from [56]

It has been shown that the MCMC will eventually reach the stationary state after infinite amount of steps. However, in practice, running infinitely long steps is impossible. What is wanted is that after certain amount of finite steps, the chain approximately reaches the stationary state. There are many factors that could affect the "convergence" to the stationary state. One of those factors is the actual distribution of $g(\boldsymbol{\theta}'|\boldsymbol{\theta}_t)$. Often, $g(\boldsymbol{\theta}'|\boldsymbol{\theta}_t)$ is chosen as a Gaussian distribution which centers at $\boldsymbol{\theta}_t$, i.e. $g(\boldsymbol{\theta}'|\boldsymbol{\theta}_t) = N(\boldsymbol{\theta}_t, \text{cov})$ where cov is the covariance matrix of all parameters. Use MCMC in 1D as an example. Consider two distributions $g_1(\theta'|\theta_t) = N(\theta_t, \sigma)$ and $g_2(\theta'|\theta_t) = N(\theta_t, 2\sigma)$. $g1$ and $g2$ have the same center but different width which is also called step size here. Because g_2 is wider than g_1 (in other words, the step size of g_2 is larger than g_1), so the next step proposed by g_2 is more likely to be further away from the current state than the step proposed by g_1. Thus the expected effects caused by the step size on the chain are

- If the step size is too small, then the proposed state $\boldsymbol{\theta}'$ would be very close to current state $\boldsymbol{\theta}_t$, $\boldsymbol{\theta}' \approx \boldsymbol{\theta}_t$. Thus, the chain is "trapped" around its initial state and does not move away from the initial state quickly

- If the step size is too large, then the proposed state $\boldsymbol{\theta}'$ is far away from the current state $\boldsymbol{\theta}_t$. If the current state is around the most probable value, the proposed state would be at the tail and then ratio $\alpha = \frac{f(\boldsymbol{\theta}')}{f(\boldsymbol{\theta}_t)}$ becomes very small and the probability to accept the proposed state is small. As a result, the chain may stay at some states for a long time.

Figure 6.2 shows an example of how the step size affects the "convergence" in 1D. The three chains shown in the figure have the same stationary distribution which is the normal distribution, $N(0, 1)$. The step size of (a) is a proper one. The chain starts from some value far away from the most probable value and then it converges to the mean value, 0, of the normal distribution quickly and moves mostly in the region of $[-2\sigma, 2\sigma]$ where $\sigma = 1$ here. The step size of (b) is so small that the chain does not leave the initial value much within the number simulated steps. The size in (c) is too large and many proposed states are rejected so the chain stays at certain states for a long time as discussed above. Tuning the step size to an appropriate value is difficult but important in the MCMC technique. An improvement of the Adaptive Metropolis Hasting Algorithm used in this thesis comparing with the process described above is that

- The step size is not fixed. It can be adapted according to the acceptance rate. It would increase the step size if too many points were accepted and decrease it if too few points were accepted.

- Instead of proposing the next step depending on only the current step, it builds a covariance matrix of all the accepted steps

6.2.2 Burn-in

As mentioned in the previous section, what is wanted is that after certain amount of finite steps, the chain approximately reaches the stationary state. Then the question coming along is how to determine how many steps is needed to reach the stationary state Use (a) in figure 6.2 as an example. The initial value is about -10 which is away from the region of high probability. With more steps ran by the MCMC, the proposed values moves to the region of high probability and fluctuates there. The procedure of dropping the steps before reaching the stationary state is called burn-in. The samples which are

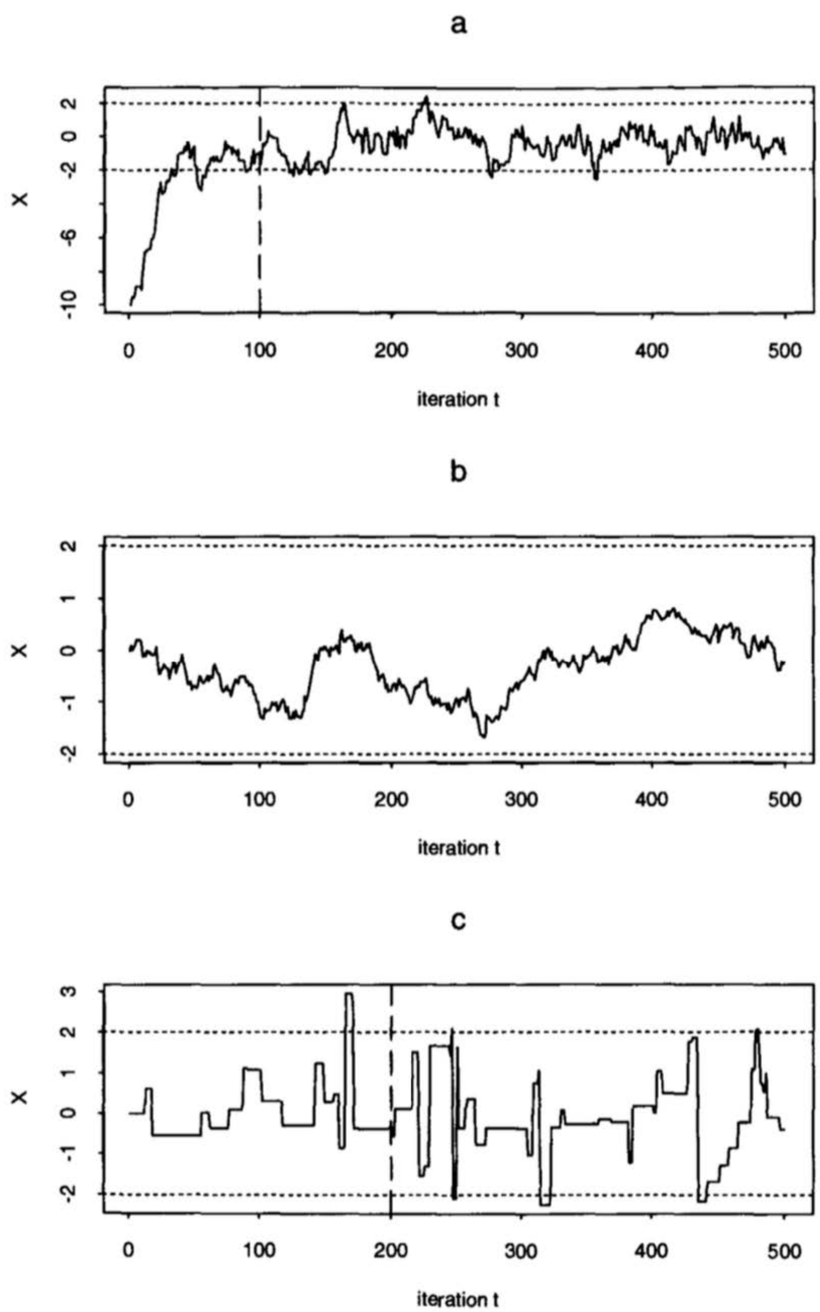

Figure 6.2: 500 iterations from MCMC chains using the Metropolis-Hastings algorithm with stationary distribution N(0, 1). (a)$g(\tilde{\boldsymbol{\theta}}|\boldsymbol{\theta}') = N(\boldsymbol{\theta}', 0.5)$(or step size = 0.5), (b) $g(\tilde{\boldsymbol{\theta}}|\boldsymbol{\theta}') = N(\boldsymbol{\theta}', 0.1)$ (or step size = 0.1), (c) $g(\tilde{\boldsymbol{\theta}}|\boldsymbol{\theta}') = N(\boldsymbol{\theta}', 10)$ (or step size = 10). Figure is from [74].

dropped are also called burn-in. As the vertical dashed line shows, the steps before 100 are discarded. Burn-in is to find a good start point for the chain. In this thesis, the number of steps (or samples) to throw away is determined by the the evolution of log-likelihood. Figure 6.3 shows the evolution of log-likelihood for the fist 120,000 steps in one chain when fitting to the real data in FHC (see more details in chapter 8). The log-likelihood increase quickly. In this thesis, burn-in first 40,000 steps.

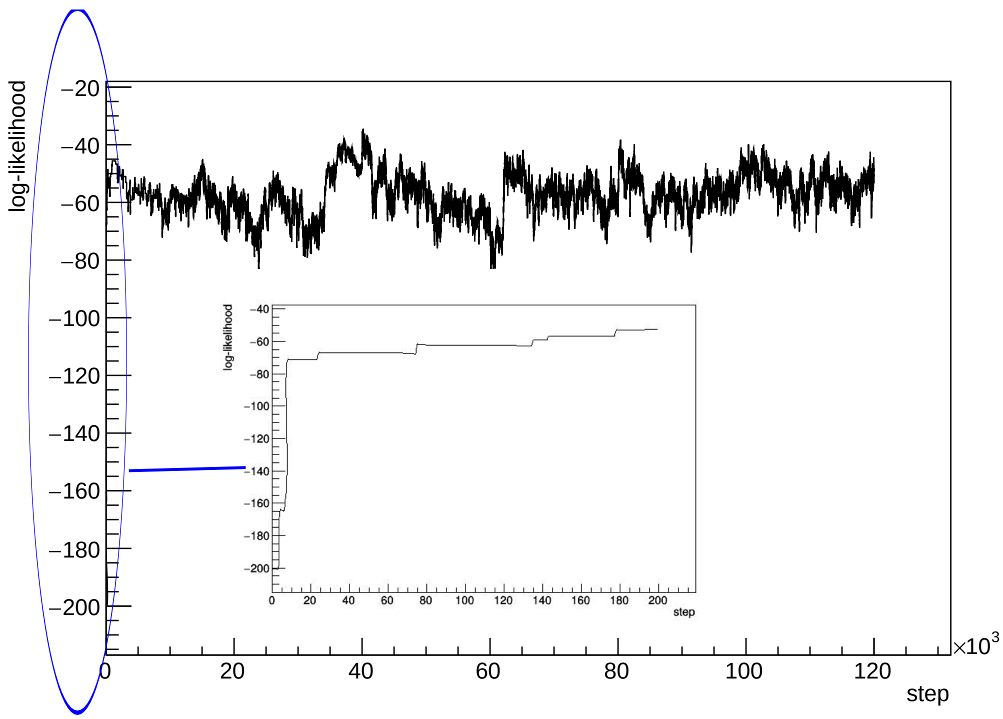

Figure 6.3: Log-Likelihood evolution w.r.t the steps in one MCMC chain when fitting to the real data in FHC.

6.3 Auto-Correlation

Move back to the example of (a) in figure 6.2. After burn-in 100 steps, the chain ran another 400 steps to get the sampled distribution. Thus, besides steps to burn-in, another question is that after reaching the stationary state, how many steps is needed to sample enough points to get the approximately complete numerical distribution. For example, if only 50 steps are sampled after the 100-th step, there will not exist any points at the region where $x > 0$, which means that the positive half of the normal distribution is missed due to limited number of points. In principle, sampling as many points as possible can increase the statistics and solve such problem. However, in practice, what is wanted is to get the approximately complete numerical distribution as soon as possible. Thus, knowing how many points is sufficient is important. Auto-correlation is used to estimate it.

Auto-correlation is a quantity which is often used in time-series analysis. It is the Pearson correlation between values of the process at different times, as a function of the time lag. Considering a stationary series X_t, the auto-correlation between t_1 and t_2 would imply statistical dependence between time $t1$ and $t2$. In other words, if the auto-correlation is very small, it may imply that the events in the series at $t1$ and $t2$ are independent. The mathematical definition of auto-correlation between time $t1$ and $t2$ [75] is :

$$\rho(t_1, t_2) = \frac{E\left[(X_{t1} - \mu_{t1})(X_{t2} - \mu_{t2})\right]}{\sigma_{t1}\sigma_{t2}} \tag{6.4}$$

where E represents the expect value. If the mean μ and standard deviation σ

of the process are time-independent, the auto-correlation of lag τ is defined as

$$\rho_\tau = \frac{E\left[(X_t - \mu)(X_{t+\tau} - \mu)\right]}{\sigma^2} \tag{6.5}$$

A obvious property for ρ_τ is that when $\tau = 0$, $\rho_0 = 1$. In this thesis, the mean and standard deviation of every step after burn-in is assumed to be time-independent. They are estimated using the mean value and standard deviation of all steps. The estimation of auto-correlation in this thesis is given below.

Note that θ_t where $t = 0, 1, ..., N$ are the accepted steps in MCMC, then

$$\begin{aligned}
\hat{\mu} &= \frac{1}{N}\sum_{t=0}^{N}\theta_t \\
\hat{\sigma} &= \frac{1}{N-1}\sum_{t=0}^{N}(\theta_t - \hat{\mu})^2 \\
\hat{\rho}_\tau &= \frac{1}{N-\tau}\sum_{t=0}^{N-\tau}\frac{(\theta_t - \hat{\mu})(\theta_{t+\tau} - \hat{\mu})}{\hat{\sigma}^2}
\end{aligned} \tag{6.6}$$

where the hat sign means that the values are estimators not truth.

Figures 6.4 show all parameters' $\hat{\rho}_\tau$ estimated from one MCMC chain when fitting to the real data in FHC. The lag τ distributes from 0 to 40,000. As the figures show, $\hat{\rho}_\tau$ of most parameters drop below 0.2 within 10,000 steps. There are few parameters that need about 20,000 step to reach 0.2. $\hat{\rho}_\tau$ of one parameter of POIs bounces back to 0.4 after about 20,000 steps and then drops again. This parameter bounces back and forth periodically.

It is assumed in this analysis that for τ_0, if $\hat{\rho}_{\tau_0} < 0.2$, the state at t and $t+\tau_0$ are independent. It is expected that such assumption holds in good confidence

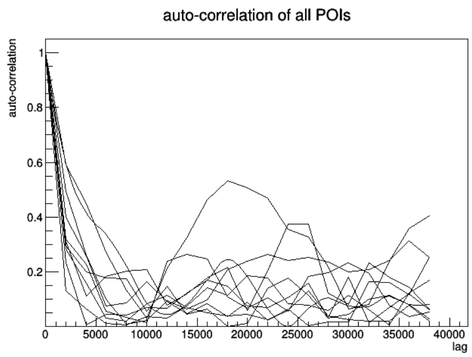

(a) Auto-correlation of all 10 POIs.

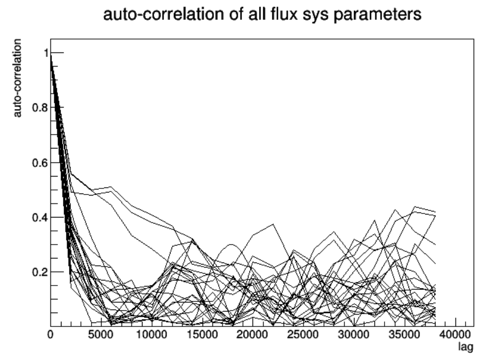

(b) Auto-correlation of all 25 parameters for systematic uncertainties from flux.

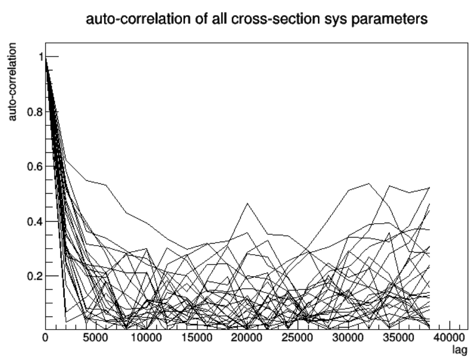

(c) Auto-correlation of all 25 parameters for systematic uncertainties from cross-section modelling.

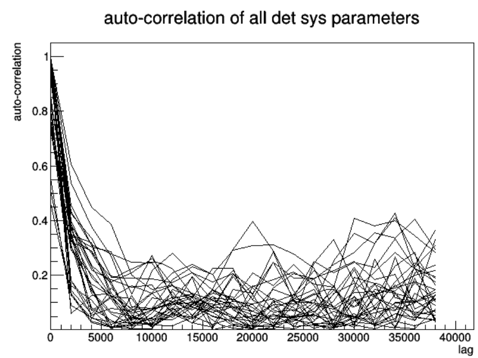

(d) Auto-correlation of all 25 parameters for systematic uncertainties from detector.

Figure 6.4: Auto-correlations of all parameters as a function of lag from 0 to 40,000 in one MCMC chain when fitting to the real data in FHC. The chain length is 80,000.

because as mentioned above, small auto-correlation of lag τ may indicate that two events with lag τ are independent for a stationary series and it is expected that the chain approximately locates at the stationary state after burn-in. Thus, the τ_0 is the size of an independent step and the number of independent samples would be equal be the number of accepted steps in MCMC after burn-in divided by the independent size, i.e. $\mathrm{N_{independent\ point}} = \mathrm{N_{steps}}/\tau_0$. In this analysis, τ_0 is chosen as 20,000 from figure 6.4. There should be more than 100 $N_{independent\ point}$ to sample a distribution. Thus $\mathrm{N_{steps}} = \mathrm{N_{independent\ point}} \times \tau_0 \geq 2,000,000$. For the results shown in chapter 8, $\mathrm{N_{steps}}$ is more than 12,000,000 in MCMC.

6.4 Parameter Extraction and Model Evaluation from Posterior Distribution

The sampled posterior distribution is the results of the analysis. In principle, the posterior distribution contains all information and publishing it is the final step. However, as discussed in chapter 5, there are 93 parameters in this analysis which means that the sampled posterior distribution is in 93 dimension. It is very difficult to visualize and interpret a distribution in such a high dimensional space. Besides, although all parameters are treated equal in the fitter, there are some parameters that are of more interests than others. Thus, marginalization technique will be used to extract information of parameters of interests(poi).

6.4.1 Marginalization

Once getting the posterior distribution, by marginalizing over other parameters shown in Eq 6.7, the marginalized distribution of the parameters of interests (poi) can be obtained.

$$P(\boldsymbol{\theta}_{poi}|D_n) = \frac{\int P(\boldsymbol{\theta}_{poi}, \boldsymbol{\theta}_{oth}|D_n)d\boldsymbol{\theta}_{oth}}{\int P(\boldsymbol{\theta}_{poi}, \boldsymbol{\theta}_{oth}|D_n)d\boldsymbol{\theta}_{oth}d\boldsymbol{\theta}_{poi}} \tag{6.7}$$

where $P(\theta_{poi}, \theta_{oth}|D_n)$ is the sampled posterior distribution $P(\boldsymbol{\theta}|\boldsymbol{X}_1, \boldsymbol{X}_2, ..., \boldsymbol{X}_n)$ following the notations introduced in section 6.1. Integrating over parameters in high dimension is often difficult to calculate but the MCMC is natural on dealing with it. By plotting distributions using the accepted values at each step, the marginalized distributions can be obtained numerically.

6.4.2 Credible Interval (C.I.)

With the marginalization method, a 1D distribution for each parameter can be obtained. From the section 6.6, the distribution of cross section can be obtained, too. The credible interval (C.I.) of probability α is a range $[\theta_a, \theta_b]$ where the probability $P(\theta_a < \theta < \theta_b)$ is equal to α, where $\alpha \in [0, 1]$. There exist more than one intervals for a given probability α. The credible interval chosen in this thesis is highest density interval (HDI), which is the shortest credible interval that contains the most probable point. For example, figure 6.5 shows the marginalized cross section posterior distribution at one bin. The interval in between the two green lines are the HDI with probability $\alpha = 68\%$ and the interval between the two red lines are HDI with probability $\alpha = 95\%$.

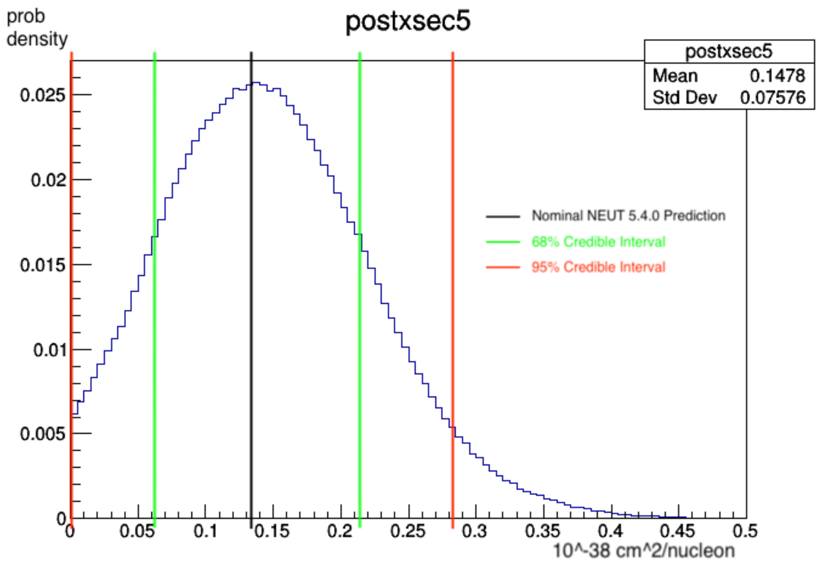

Figure 6.5: An example of a marginalized cross section distribution at bin5 in true space (>3.4 GeV)

In later chapters, they will be called 68% C.I and 95% C.I.

6.4.3 Posterior Predictive Distribution (PPD)

In Frequentist statistics, every parameter has a single best-fit value and the predicted distribution can be drawn by updating the parameters into the best-fit point. In Bayesian statistics, a posterior distribution instead of single values for all parameters is obtained and posterior predictive distribution of $\tilde{x}$ is the marginalized distribution of $\tilde{x}$ given $\boldsymbol{\theta}$ over the posterior distribution under the measured dataset $D_n = \{\boldsymbol{X}_1, \boldsymbol{X}_2, ..., \boldsymbol{X}_n\}$, i.e.

$$p(\tilde{x}) = \int P(\tilde{x}|\boldsymbol{\theta}, D_n)P(\boldsymbol{\theta}|D_n)d\boldsymbol{\theta} \tag{6.8}$$

In other words, the posterior predictive distribution is the distribution of unobserved values conditional on the observed values [76]. Although a point estimation can be done by using the mode of the posterior distribution and the method to get predicted distribution in Frequentist statistics can still be used, it is not adapted in this thesis. There are two reasons why the "best-fit" distribution in Frequentist statistics is not used in Bayesian statistics, or at least in this analysis. One is that the uncertainty of $\boldsymbol{\theta}$ is considered in posterior predictive distribution. Another reason is that to draw the "best-fit" distribution, the mode of the posterior distribution is needed and it is computationally consuming and even prohibitive to find the mode for high-dimensional distributions.

The implementation of posterior predictive distribution as a function of reconstructed shower energy (or other binning variables) in this analysis is described below.

- Randomly sample N points from the posterior distribution.
- For each sampled point, get the predicted distribution of reconstructed shower energy.
- Combine the distribution of N points and then there are N numbers of entries for each bin. Each entry is a number of events predicted at that bin given the point. Do a Gaussian fit for each bin and the fitted mean value is taken as the predicted value at that bin.

Figure 6.6 shows an example of the posterior predictive distribution. The block at each bin is a 2D histogram where the color bar on the right side represent

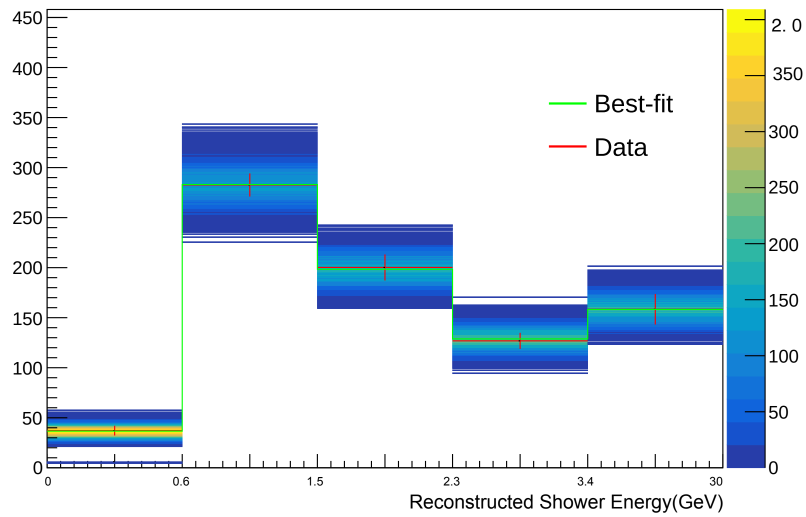

Figure 6.6: An example of posterior predictive distribution. 5000 points are sampled to get this plot.

the number of event. The green line is called the "best-fit" and it is mean value of the fitted Gaussian function at each bin. The red line is the number of events within statistical error in that bin in data or fake data.

6.4.4 Posterior Predictive P-Value (PPP)

P-value is a quantity often used in hypothesis testing. It is the probability of observing a test result which is more extreme than or as extreme as the results that have been observed, under the assumption that the null hypothesis is true. If the p-value is smaller than the significance level which is a pre-defined value, then the null hypothesis will be rejected. When obtaining the posterior distribution, a question coming along naturally is how well the model fits. A quantity named posterior predictive p-value (PPP) is developed by A. Gelman et al [77] to evaluate the goodness-of-fit in Bayesian analysis.

The implementation of posterior predictive p-value in this analysis is described below.

- Randomly sample N points from the posterior distribution.
- For each sampled point $\boldsymbol{\theta}_i$ among the N points, get the predicted distribution of reconstructed shower energy, label as $predMC_i$.
  - Calculated the χ^2 of data distribution of the predicted MC, i.e. $\chi^2(data, predMC_i)$
  - Statistically fluctuate $predMC_i$ and label the new distribution as $statpredMC_i$. Calculate the χ^2 between two distribution,
i.e $\chi^2(statpredMC_i, predMC_i)$
- Combine the calculated χ^2 of N points and the fraction of points for which $\chi^2(data, predMC) < \chi^2(statpredMC, predMC)$ is the posterior predictive p-value.

Figure 6.7 shows an example of the PPP. According to the implementation listed above, the value of PPP is actually the proportion below the diagonal line of $x = y$ drawn in the plot.

The PPP often does not have a uniform distribution under the null hypothesis but instead tends to have a distribution more concentrated near 0.5 [78]. In general, a PPP very close to 0 indicates that the model may be false. By convention, when using p-value which follows a uniform distribution, p-value=0.05 is selected as a criteria of rejecting a model or not. However, nonuniform distributions of PPP makes it difficult to reject a false model. The relevance of the PPP depends on the practical cases. The value of 0.05

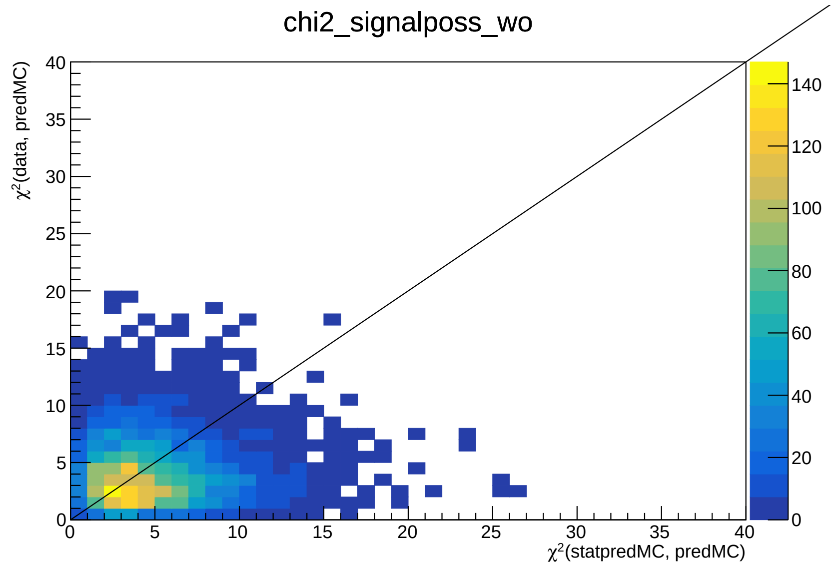

Figure 6.7: An example of posterior predictive p-value. PPP=0.571 here and 5000 points are sampled to get this plot.

is still chosen here as the criteria for most cases, but as you will see in later chapters, for some cases, the PPP<0.05 is accepted.

6.5 Likelihood Definition

So far how to estimate the distributions of poi and how to evaluate the model using the Bayesian approaches have been discussed. Now the question coming naturally is how to implement what have been discussed step by step.

First of all, the likelihood function in Eq 6.2 should be defined. To make it computational easier, the log of the likelihood is used in this thesis. Just to clarify, unless stated otherwise both likelihood and loglikelihood in later chapters represents log of the likelihood. The log of the desired distribution is

$$logP(\boldsymbol{\theta}|\boldsymbol{X}_1, \boldsymbol{X}_2, ..., \boldsymbol{X}_n) = logL(\boldsymbol{\theta}) + log\pi(\boldsymbol{\theta}) \tag{6.9}$$

To make it easier to read, use $logL_{stat}$ to represent $logL(\boldsymbol{\theta})$ and $logL_{prior}$ to represent $log\pi(\boldsymbol{\theta})$ later. The likelihood is defined as the extended binning likelihood [79]

$$logL_{stat} = \sum_{ir=1}^{RecoBin} N_{ir}^{data} - N_{ir}^{MC} + N_{ir}^{data} log\frac{N_{ir}^{MC}}{N_{ir}^{data}} \tag{6.10}$$

and the prior distribution is chosen to be a multi-dimensional Gaussian distributions

$$logL_{prior} = -\frac{1}{2}V^{\dagger}(cov)^{-1}V \tag{6.11}$$

where V is the vector of nuisance parameters, cov is the covriance matrix of the parameters and $(cov)^{-1}$ is the inverse matrix.

The data in water-in (wi) and water-out (wo) configuration are fitted simultaneously. Beside the signal enriched samples, background control samples (CS) are selected to constrain the background as stated in Chapter 4. These samples are also fitted simultaneously. Thus, the total likelihood is

$$\begin{aligned} logL = {} & logL_{sig,wi} + logL_{NCCS,wi} + logL_{\nu_\mu CCCS,wi} \\ & + logL_{sig,wo} + logL_{NCCS,wo} + logL_{\nu_\mu CCCS,wo} \end{aligned} \tag{6.12}$$

Uncertainties sources from flux, cross-section models and detectors are parameterized and introduced in Chapter 5. Other than these nuisance parameters, parameters of interests (poi) are applied at each bin for signal in truth space freely. All of these parameters could vary the number of events in MC.

Eq 6.13 and Eq 6.14 show mathematically how these parameters affect the number of events at each reconstructed bin in the selected signal sample. Just to be clear that, in the fitter, the variations or reweights are performed on event by event not bin by bin. The equations are not exactly what happen in the fitter but the final effect should be the same.

$$
\begin{aligned}
N_{ir,F}^{waterin,FHC} =& d_{ir,F}^{waterinFHC} \sum_{jt=1}^{TrueBin} S_{ir,jt}^{waterinFHC} \times \\
& \Bigg\{ a_{jt,F}^{\nu_e CC,onwater} \sum_{k}^{int\ types} \sum_{n}^{E_\nu} f_{n,jt}^{\nu_e} N_{jt}^{\nu_e CC,onwater} \prod_{a}^{models} \omega(a)_{jt,k} \\
& + b_{jt,F}^{\nu_e CC,notwater} \sum_{k}^{int\ types} \sum_{n}^{E_\nu} f_{n,jt}^{\nu_e} N_{jt}^{\nu_e CC,notwater} \prod_{a}^{models} \omega(a)_{jt,k} \\
& + \sum_{k}^{int\ types} \sum_{n}^{E_\nu} f_{n,jt}^{\nu_e} N_{jt}^{\nu_e CC,onwater,notsigbyBDT} \prod_{a}^{models} \omega(a)_{jt,k} \\
& + \sum_{k}^{int\ types} \sum_{n}^{E_\nu} f_{n,jt}^{\nu_e} N_{jt}^{\nu_e CC,notwater,notsigbyBDT} \prod_{a}^{models} \omega(a)_{jt,k} \\
& + \sum_{k}^{bk\ int\ types,} \sum_{n}^{E_\nu} f_{n,jt}^{bk} N_{jt,k}^{bk,onwater} \prod_{a}^{models} \omega(a)_{jt,k} \\
& + \sum_{k}^{bk\ int\ types,} \sum_{n}^{E_\nu} f_{n,jt}^{bk} N_{jt,k}^{bk,notwater} \prod_{a}^{models} \omega(a)_{jt,k} \Bigg\}
\end{aligned}
\tag{6.13}
$$

$$
\begin{aligned}
N_{ir,F}^{waterout,FHC} =& d_{ir,F}^{wateroutFHC} \sum_{jt=1}^{TrueBin} S_{ir,jt}^{wateroutFHC} \\
& \Bigg\{ g_{jt,F}^{\nu_e CC,notwater} \sum_{k}^{int\ types} \sum_{n}^{E_\nu} f_{n,jt}^{\nu_e} N_{jt}^{\nu_e CC,notwater} \prod_{a}^{models} \omega(a)_{jt,k} \\
& + \sum_{k}^{int\ types} \sum_{n}^{E_\nu} f_{n,jt}^{\nu_e} N_{jt}^{\nu_e CC,notwater,notsigbyBDT} \prod_{a}^{models} \omega(a)_{jt,k} \\
& + \sum_{k}^{bk\ int\ types} \sum_{n}^{E_\nu} f_{n,jt}^{bk} N_{jt,k}^{bk,notwater} \prod_{a}^{models} \omega(a)_{jt,k} \Bigg\}
\end{aligned}
\tag{6.14}
$$

where ir represent bin i in reconstruction space (r), jt means bin j in true space (t), *int types* means signal interaction types from the interaction generators (NEUT5.4.0 here), and *bk int types* means background interaction types in the selected sample. d_{ir} represents the effects caused by the detectors systematic uncertainties, $S_{ir,jt}$ represent the transfer matrix from true space to the reconstruction space. $f_{n,jt}$ is the weight caused by the neutrino flux at energy bin E_n to the true binning variable at bin j. $\omega(a)_{jt,k}$ is the weights of interaction type k on true bin j. As mentioned above, other than nuisance parameters, pois are applied on signal events. $a_{jt,F}^{\nu_e CC,onwater}, b_{jt,F}^{\nu_e CC,notwater}$ are the free parameters applied on signal events whose interaction targets are water and non-water materials respectively in water-in configuration. $g_{jt,F}^{\nu_e CC,notwater}$ is the free parameters applied on signal events interacting on non-water materials in water-out configuration. The only difference between water-in and water-out configuration is whether P0D is filled with water or empty. The detector's non-water materials should be the same despite the water-in or water-out configuration, so the free parameter $b_{jt,F}^{\nu_e CC,notwater}$ and $g_{jt,F}^{\nu_e CC,notwater}$ is set to be the same, i.e. $b_{jt,F}^{\nu_e CC,notwater} = g_{jt,F}^{\nu_e CC,notwater}$. Such condition allows us to use data in water-out configuration to constrain interactions on non-water materials and to extract interaction cross-section just on water target.

6.6 Cross-Section Extraction

T2K neutrino flux is not mono-energetic as explained in chapter 2.1.2, instead the neutrino energy is spread and peaked at certain energy with the off-axis technique shown in figure 2.7. The reconstruction of neutrino energy is highly model dependent because of nuclear effect. To reduce and even remove model dependence on differential cross section measurement, usually choose the kinematics of particles exiting from nucleus, for example, outgoing charged lepton kinematics.

There are 3 common ways to extract cross section in neutrino physics [80].

- the flux-unfolded cross-section:

$$\frac{d\sigma}{dx_j} = \frac{N_j^{MCsignal}}{\epsilon_j^{MC} \int_{E_\nu,min}^{E_\nu,max} w_i(E_\nu)\phi(E_\nu)dE_\nu N_{nucleons}} \times \frac{1}{\Delta x_j} \tag{6.15}$$

  where $w_i(E_\nu)$ is the neutrino energy distribution at bin j. This method relies on the reconstruction of incoming neutrino energy for each event, which has been shown to be strongly model-dependent. The advantage of this method is that the results can be used to compare with differently models directly.

- the flux-averaged cross-section:

$$\frac{d\sigma}{dx_j} = \frac{N_j^{MCsignal}}{\epsilon_j^{MC} \int_{E_\nu,min}^{E_\nu,max} \phi(E_\nu) dE_\nu N_{nucleons}} \times \frac{1}{\Delta x_j} \tag{6.16}$$

- the flux-integrated cross-section (The method chosen in this thesis):

$$\frac{d\sigma}{dx_j} = \frac{N_j^{MCsignal}}{\epsilon_j^{MC} \Phi N_{nucleons}} \times \frac{1}{\Delta x_j} \tag{6.17}$$

  where x_j is the binning variable and Δx_j is the bin width of bin j. Φ is the integrated flux. Since the binning variables are often chosen as the kinematics of final state particles, for example the momentum of muons, which can be directly measured by the detector, there is no neutrino interaction model is introduced when getting the value of x_j. Thus, the measured results by this way are model-independent, which is very important. However, because the integrated flux is used here, the results are experiment(flux)-dependent. Thus, to compare models to the results, proper flux need to be used.

As discussed above in chapter 6.4, to extract distributions of some parameters, the marginalization technique is used. Though cross section is not the parameter directly applied in the fitter, it is a function of parameters in the fitter. Thus mathematically the distribution of cross section can be obtained by probability density function transformation from variables X to variable

Y=g(X). Numerically, following Eq 6.17, where

$$\begin{aligned} N_j^{MCsignal} &= a_{jt}^{signal\ \ onwater} N_{jt,afterSel,postfit}^{signal,onwater} \\ &= a_{jt}^{signal\ \ onwater} \sum_{k}^{int\ types} \sum_{n}^{E_\nu} f_{n,jt}^{\nu_e} N_{jt,afterSel}^{signal,onwater} \prod_{a}^{models} \omega(a)_{jt,k} \end{aligned} \tag{6.18}$$

implemented in the fitter as shown below. and

$$\epsilon_i = \frac{N_{jt,afterSel,postfit}^{signal,onwater}}{N_{jt,beforeSel,postfit}^{signal,onwater}} \tag{6.19}$$

plug equations 6.18 and 6.19 in and the formula to extract of cross section distribution can be re-written as

$$\begin{aligned} \frac{d\sigma}{dx_i} &= \frac{a_{jt}^{signal\ \ onwater} N_{jt,\ beforeSel,postfit}^{signal,onwater}}{\Phi N_{nucleons}} \times \frac{1}{\Delta x_i} \\ &= \frac{a_{jt}^{signal\ \ onwater} \sum_{k}^{int\ types} \sum_{n}^{E_\nu} f_{n,jt}^{\nu_e} N_{jt,beforeSel}^{signal,onwater} \prod_{a}^{models} \omega(a)_{jt,k}}{\Phi N_{nucleons}} \times \frac{1}{\Delta x_i} \end{aligned} \tag{6.20}$$

Just to clarify that postfit in $N_{jt,beforeSel,postfit}^{signal,onwater}$ doesn't mean that $N_{jt,beforeSel}^{signal,onwater}$ are used in the fitter directly. It just means that the signal events before applied selections are varied with the parameters in posterior distributions.

6.7 Binning

Because the neutrino energy reconstruction is highly model-dependent as mentioned in section 6.6, neutrino energy is not used as binning variable in this thesis. For signal samples, the binning variables in the reconstructed space is the reconstructed energy of the selected candidate shower. The corresponding variables in the true space is the total true kinetic energy of all primary charged particles, primary photons and primary π^0s. In other words, the goal of the analysis is to measure the differential cross section as a function of the total true kinetic energy of all primary charged particles, primary photons and primary π^0s. The reason why not using true electron energy is because the SCF cut in 4.3.8 requires that charges in the selected candidate shower count more than 90% of charges collected for the event, which means that charges deposited by for example generated protons will very likely be used in the reconstruction of the candidate shower. This also agrees with the signal definition of $1e^-$ (or $1e^\pm$ in RHC) + 0 visible proton + 0 visible charged pions. Thus considering the energy of electron alone is not enough. The energy of other particles which can deposit energies should be taken into consideration.

As Eq 6.12 indicates, the sidebands contribute to the final results by adding the likelihood obtained from sidebands MC and data. Thus, the binning variables used for sidebands can be different from binning variables used for signal. For $\nu_\mu/\bar{\nu}_\mu$ CC sidebands, the binning variables is the reconstructed angle of the longest track w.r.t the beam direction. The corresponding true variable is the angle of $\mu^\pm$ w.r.t the beam direction. For NC1π^0, the binning variable is the reconstructed invariant mass whose distribution is expected to be peaked at the mass of π^0 at rest, $135 MeV/c^2$.

The binning choice is important to make a measurement as precise as possible. If the binning is too coarse, the results do not give much information about the shape of the cross section, while on the other hand if the binning is too fine, due to the limited statistics, there could be bins that have very few events or even become empty. The criteria of binning are listed below

- The bin width is greater than the resolution of the binning variables.
- The number of events at each bin is not too small. If possible, keep the number of events at each bin to be > 100. (This is hard to satisfy in RHC mode due to the very limited statistics.)
- The signal efficiency across all bins to be as flat as possible.
- The transfer matrix between true and reconstructed space is as diagonal as possible.

Summaries of binning choice for the signal sample, $\nu_\mu/\bar{\nu}_\mu$ CC sideband and NC $1\pi^0$ sideband are shown in tables 6.1, 6.2 and 6.3, respectively.

Table 6.1: Summary of the binning choice for ν_e ($\nu_e + \bar{\nu}_e$) CC signal by BDT in FHC (RHC). The binning is the same for both water-in and water-out configuration.

Bin Name	Energy Region (GeV)
Bin 1	0 - 0.6
Bin 2	0.6 - 1.5
Bin 3	1.5 - 2.3
Bin 4	2.4 - 3.4
Bin 5	> 3.4

Table 6.2: Summary of the binning choice for $\nu_\mu/\bar{\nu}_\mu$ CC sideband in FHC and RHC. The binning is the same for both water-in and water-out configuration.

Bin Name	Angle Region (rad)
Bin 1	0 - 0.2
Bin 2	0.2 - 0.3
Bin 3	0.3 - 0.4
Bin 4	0.4 - 0.5
Bin 5	0.5 - 0.6
Bin 6	0.6 - 0.785
Bin 7	0.785 - 1.57

Table 6.3: Summary of the binning choice for NC $1\pi^0$ sideband in FHC and RHC. The binning is the same for both water-in and water-out configuration.

Bin Name	Invariant Mass Region (MeV/c^2)
Bin 1	65 - 85
Bin 2	85 - 105
Bin 3	105 - 125
Bin 4	125 - 145
Bin 5	145 - 165
Bin 6	165 -185
Bin 7	185 - 205

Chapter 7

Cross-Section Extraction Framework Validation

A comprehensive set of tests and studies have been done to validate the cross section extraction framework in this thesis. Unless stated explicitly, otherwise the MC samples are generated using NEUT 5.4.0 in this thesis. All studies are done with MC POTs scaled to real data POTs shown in tables 8.1 and 8.3.

7.1 Asimov Fit

In Asimov fit study, the input fake data are identical to the input MC. Thus, every parameter and measured cross section values are expected to be at the nominal values. Asimov Fit study doesn't use all MC files, instead, part of MC were randomly chosen and used. Table 7.1 and 7.2 shows the MC POTs used in the Asimov fit for FHC and RHC, respectively. Figures 7.1 show the comparisons of nominal (pre-fit) selected signal samples, $\nu_\mu(\bar{\nu}_\mu)$ CC sidebands

Table 7.1: MC POTs of Samples used in Asimov Fit in FHC

POTs	water-in	water-out
FHC	1.58e+21	1.41e+21

Table 7.2: MC POTs of Samples used in Asimov Fit in RHC

POTs	water-in	water-out
RHC	3.33e+21	3.47e+21

and NC1π^0 sidebands for MC and Asimov fake data in FHC. The nominal fake data align with the MC as expected.

7.1.1 Fitted Results

As mentioned in chapter 6.4, it is very difficult to visualize the posterior distribution in high dimension. Instead, marginalization technique can be used to extract information of parameters. The Bayesian analysis technique used in this thesis can provide the 1D marginalized distribution of each parameter and cross section. Figures 7.2 show fitted cross section results of Asimov Fit in FHC. Mode of the 1D marginalized distribution at each bin agrees with the nominal cross section predicted by the MC which is simulated by NEUT 5.4.0 here.

7.2 NEUT with biased CC DIS and Multi π productions

As table 4.10 and 4.11 show, $\nu_\mu(\bar{\nu}_\mu)$ CC DIS contributes most among all $\nu_\mu(\bar{\nu}_\mu)$ CC backgrounds. A fake data set is generated with biased CC DIS and Multi π channels to validate the fitting framework. As mentioned in section 5.2, CC DIS models can be parameterized with several parameters, CC_BY_DIS, CC_BY_Mpi and CC_AGKY_Mpi. The fake data set is generated by varying these 3 parameters for 1.5 σ. Figure 7.3 show the comparisons of selected samples from nominal MC and fake data with biased CC DIS and Multiπ in FHC.

Figures 7.4 show fitted cross section results using the fake data and MC from NEUT 5.4.0 in FHC. For the energy region of 0.6-1.5GeV and 1.5-2.3GeV, the mode of the 1D marginalized distribution is almost aligned with the nominal cross section. For the energy region of 2.3-3.4GeV and >3.4GeV, though the mode deviates from the nominal value a bit, the difference between the nominal value and the mode is small comparing with the standard deviation of the distribution. The nominal is within the 68% credible interval of the posterior distribution.

To quantify the goodness-of-fit, as discussed in section 6.4.4, posterior predictive p-value (PPP) is also calculated for each sample. Each plot in figures 7.5 show the PPP value of each sample. PPP values indicates no dis-agreement on fake data and post-fit MC distributions. Figures 7.6 provide the posterior predictive distribution (PPD) as discussed in section 6.4.3 to visualize agreement between fake data and post-fit MC.

Similar to the study in FHC, fake data sets in RHC with varying CC DIS and Multi π parameters for 1.5 σ are generated for water-in and water-out configuration with NEUT 5.4.0. Figures 7.7 show the fitted cross section results with biased CC DIS and Multi π in RHC. Figures 7.8 shows the PPP of the fitted results of each sample and figures 7.9 show PPD to visualize the comparisons between fake data and post-fit distributions.

7.3 NEUT with biased NC DIS and Multi π productions

Besides $\nu_\mu(\bar{\nu}_\mu)$ CC background, another large background source is NC interaction. From tables 4.14, 4.15, 4.16 and 4.17, it is known that NC DIS is the largest contributor of NC background. A fake data set is generated by double the number of events of NC DIS and Multiπ. Figure 7.10 show the comparison of selected samples from nominal MC and fake data with doubled NC DIS and Multiπ background. Figure 7.11 show fitted cross section results. The mode of the marginalized distribution is very close to the nominal value predicted by the MC. Figures 7.12 show the PPP for each sample. PPP values indicates no dis-agreement on fake data and post-fit MC distributions.

Results for fake data study with doubled NC DIS and Multi π events in RHC are shown in figures 7.13 and 7.14 .

Table 7.3: POTs of Samples used in Fake Data Study with GENIE in FHC

POTs	water-in	water-out
MC (NEUT 5.4.0)	3.61e+21	3.61e+21
Fake Data (GENIE 2.8.0)	3.51e+21	3.53e+21

7.4 Fake Data Study using GENIE generator

Fake data sets in this study are generated with neutrino event generators GENIE with version 2.8.0. MC used is generated by NEUT 5.4.0 as MC used in other studies. Table 7.3 shows the POTs used for both fake data and MC in the study in FHC. All distributions are scaled to real data POT in the fitter.

The interaction models for some channels in GENIE v2.8.0 are different from them in the NEUT 5.4.0. Table 7.4 shows comparisons between NEUT 5.4.0 and GENIE 2.8.0 and figures 7.15 show comparisons of selected samples between fake data simulated with GENIE 2.8.0 and MC with NEUT 5.4.0 in FHC.

Reaction type	NEUT v5.4.0	GENIE v2.8.0
CCQE scattering =	SF or RFG and RPA $M_A^{QE} = 1.21\ GeV/c^2$ $p_F^{^{12}C} = 217\ MeV/c\ p_F^{^{16}O} = 225\ MeV/c$ $E_B^{^{12}C} = 25\ MeV/c\ E_B^{^{16}O} = 27\ MeV/c$	RFG $M_A^{QE} = 0.99\ GeV/c^2$ $p_F^{^{12}C} = 221\ MeV/c\ p_F^{^{16}O} = 225\ MeV/c$ $E_B^{^{12}C} = 25\ MeV/c\ E_B^{^{16}O} = 27\ MeV/c$
Multinucleon (2p2h mainly)	Nieves model	Not included
CC-RES π production	Rein-Sehgal model ($W < 2\,GeV$)	Rein-Sehgal model ($W < 1.7\,GeV$)
CC-DIS	GRV98 PDF Bodek-Yang corrections at low Q2	GRV98 PDF Bodek-Yang corrections at low Q2
Hadronization	KNO scaling ($W < 2\,GeV$) PYTHIA/JETSET ($W > 2\,GeV$)	AGKY($W < 2.3\,GeV$) AGKY+PYTHIA/JETSET ($2.3 < W < 3\,GeV$) PYTHIA/JETSET ($W > 3\,GeV$)
FSI	Intra-nuclear cascade	Intra-nuclear cascade

Table 7.4: Comparisons of the models used in NEUT v5.4.0 and GENIE v2.8.0 to simulate CC interactions.

Figures 7.16 show the measured cross section results at each bin. For bin 2 and bin 5 where the total true kinetic energy is in [0.6, 1.5] GeV or >3.4GeV, the mode of the marginalized posterior distribution is very close to truth of the fake data. For bin3 where the total true kinetic energy is in [1.5, 2.3] GeV, the truth value of the fake data is very close to the lower side boundary of 68% C.I. For bin 4 where the total true kinetic energy is in [2.4, 3.4] GeV, the truth value of the fake data is very close to the upper side boundary of 68% C.I.

Figures 7.17 show the PPP of the fitted results and 7.18 show the PPD.

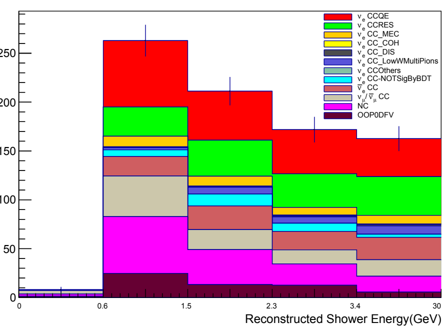

(a) Selected signal sample in water-in + FHC configuration

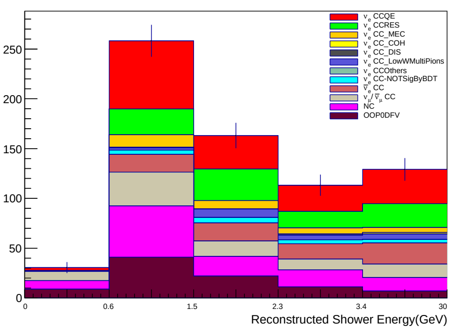

(b) Selected signal sample in water-out + FHC configuration

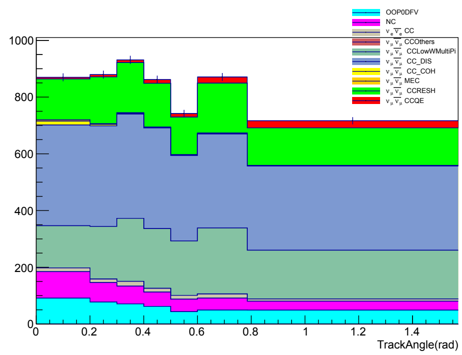

(c) Selected $\nu_\mu(\bar{\nu}_\mu)$ CC sidebands in water-in + FHC configuration

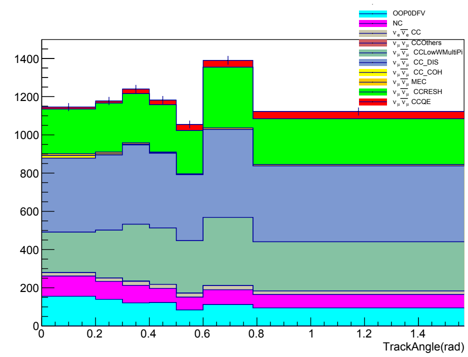

(d) Selected $\nu_\mu(\bar{\nu}_\mu)$ CC sidebands in water-out + FHC configuration

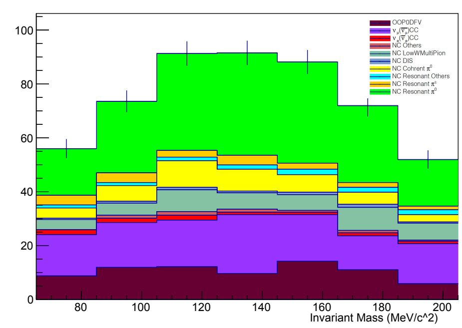

(e) Selected NC $1\pi^0$ sideband in water-in + FHC configuration

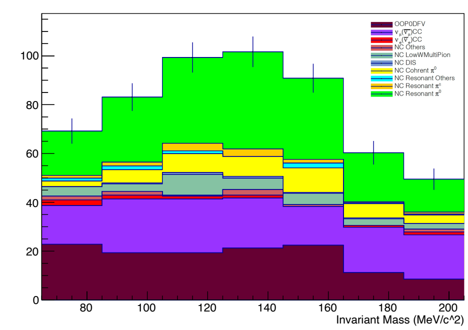

(f) Selected NC $1\pi^0$ sideband in water-out + FHC configuration

Figure 7.1: Comparison of selected nominal (pre-fit) MC and Asimov fake data in FHC. Colorful Stack is the selected MC sample and the cross marker is the selected Asimov fake data sample. The binning in the plots of the signal sample are not equally divided. Refer to the labels on the x-axis for the value of each bin.

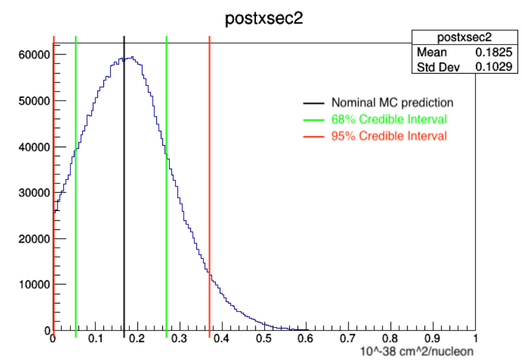

(a) Marginalized cross section distribution at bin2 in true space (0.6-1.5 GeV)

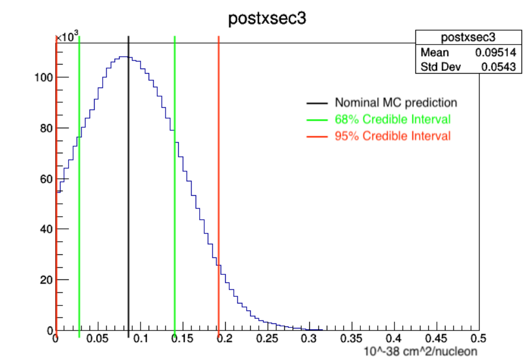

(b) Marginalized cross section distribution at bin3 in true space (1.5-2.3 GeV)

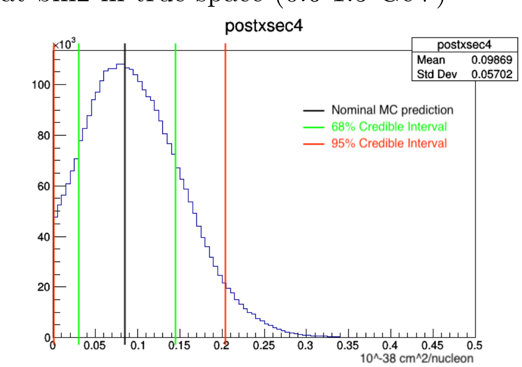

(c) Marginalized cross section distribution at bin4 in true space (2.3-3.4 GeV)

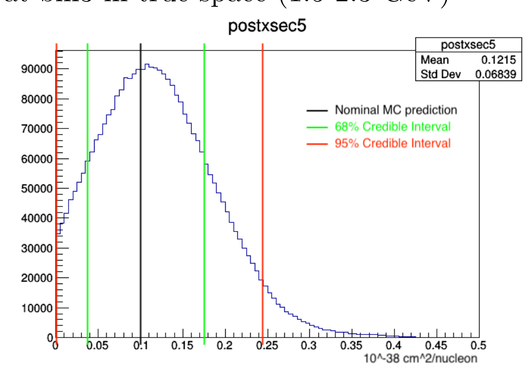

(d) Marginalized cross section distribution at bin5 in true space (>3.4 GeV)

Figure 7.2: Comparison of nominal cross section on water in NEUT 5.4.0 and marginalized posterior distribution of measured cross section on water from Asimov fit. Regions between green (red) lines are 68%(95%) credible intervals of the posterior distribution.

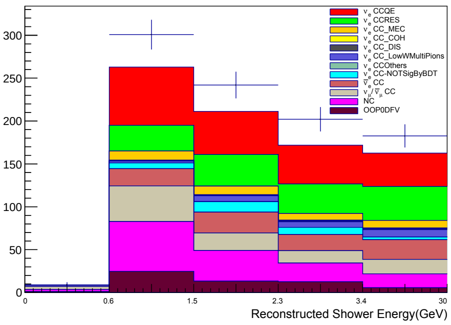

(a) Selected signal sample in water-in + FHC configuration

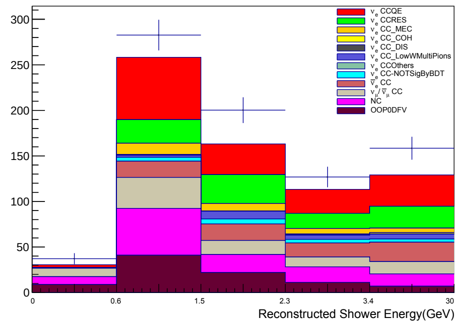

(b) Selected signal sample in water-out + FHC configuration

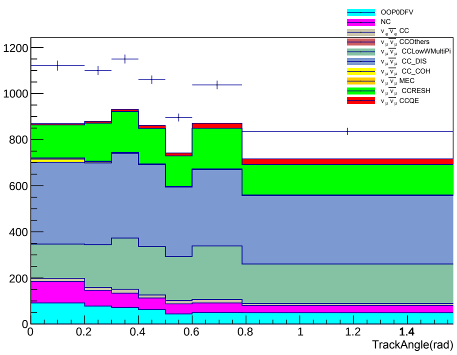

(c) Selected $\nu_\mu(\bar{\nu}_\mu)$ CC sidebands in water-in + FHC configuration

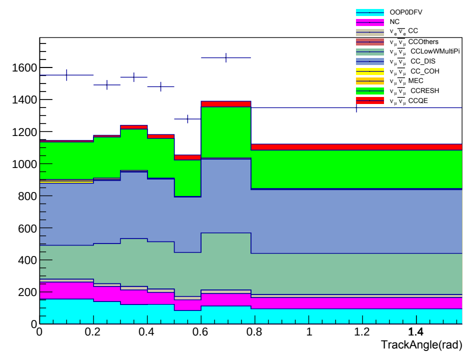

(d) Selected $\nu_\mu(\bar{\nu}_\mu)$ CC sidebands in water-out + FHC configuration

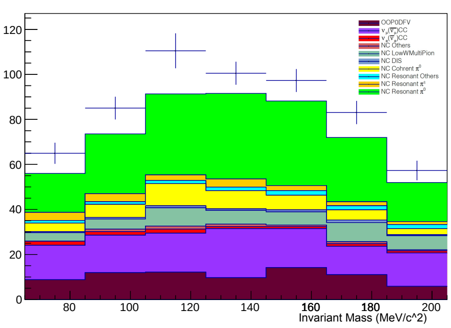

(e) Selected NC $1\pi^0$ sideband in water-in + FHC configuration

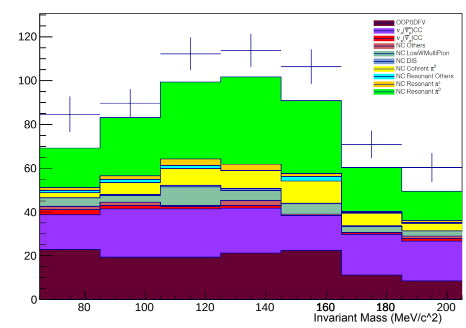

(f) Selected NC $1\pi^0$ sideband in water-out + FHC configuration

Figure 7.3: Comparison of selected nominal (pre-fit) MC and fake data with biased CC DIS and Multiπ in FHC. Colorful Stack is the selected MC sample and the cross marker is the selected fake data sample. The binning in the plots of the signal sample are not equally divided. Refer to the labels on the x-axis for the value of each bin.

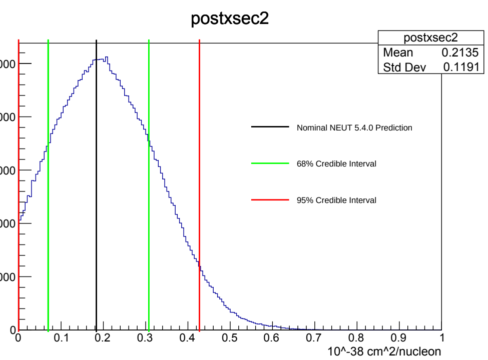

(a) Marginalized cross section distribution at bin2 in true space (0.6-1.5 GeV)

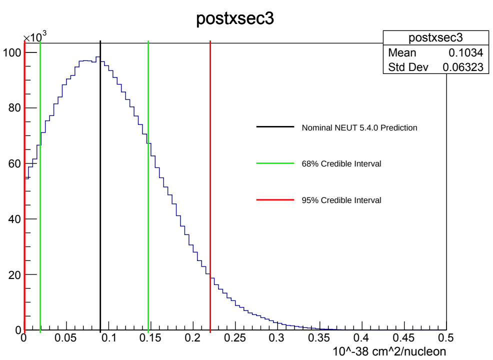

(b) Marginalized cross section distribution at bin3 in true space (1.5-2.3 GeV)

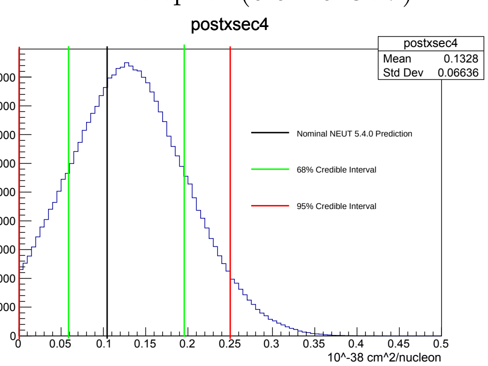

(c) Marginalized cross section distribution at bin4 in true space (2.3-3.4 GeV)

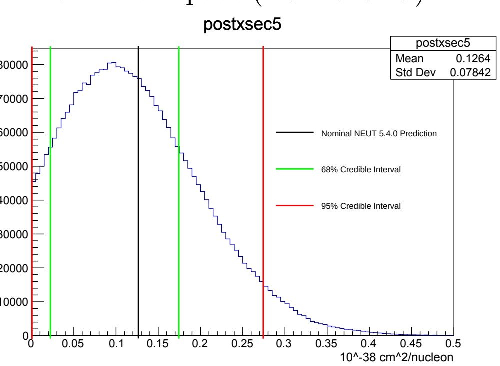

(d) Marginalized cross section distribution at bin5 in true space (>3.4 GeV)

Figure 7.4: Comparison of nominal cross section on water in NEUT 5.4.0 and marginalized posterior distribution of measured cross section on water using generated fake data set with biased CC DIS and Multiπ. Regions between green (red) lines are 68%(95%) credible intervals of the posterior distribution.

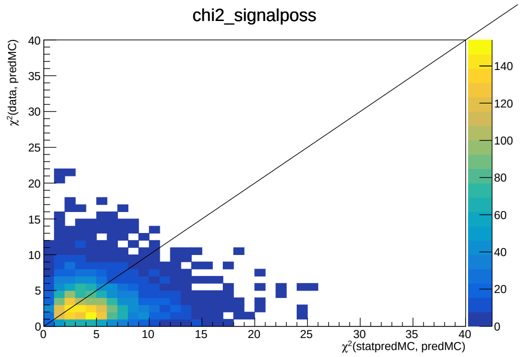

(a) PPP=0.647 for signal sample in water-in + FHC configuration

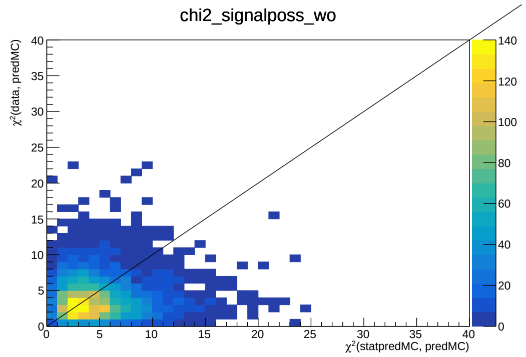

(b) PPP=0.573 for signal sample in water-out + FHC configuration

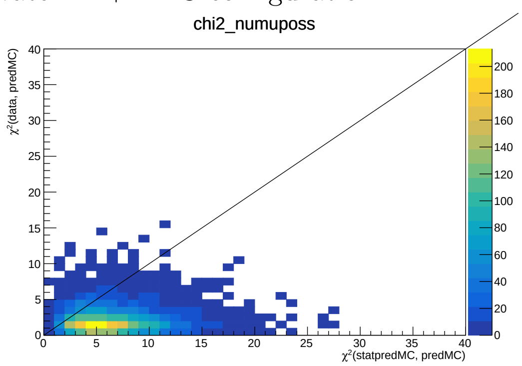

(c) PPP=0.911 for $\nu_\mu(\bar{\nu}_\mu)$ CC sideband in water-in + FHC configuration

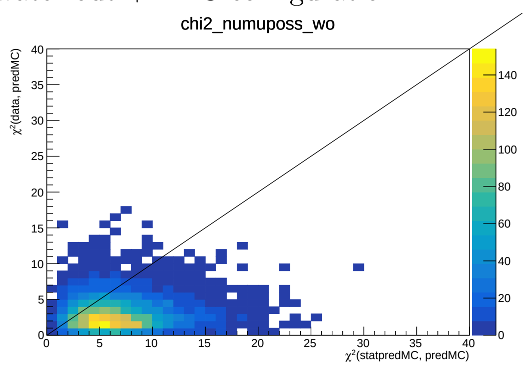

(d) PPP=0.836 for $\nu_\mu(\bar{\nu}_\mu)$ CC sideband in water-out + FHC configuration

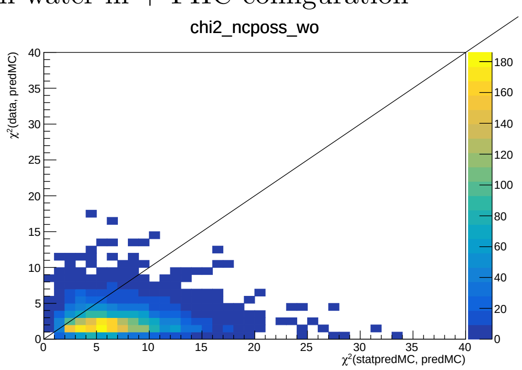

(e) PPP=0.879 for NC $1\pi^0$ sideband in water-in + FHC configuration

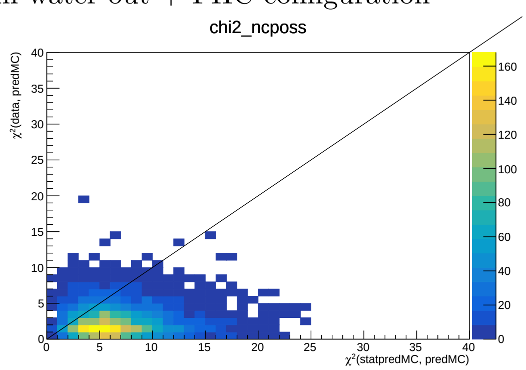

(f) PPP=0.870 for NC $1\pi^0$ sideband in water-out + FHC configuration

Figure 7.5: Posterior Predictive P-value (PPP) for each of all 6 samples in FHC after fitting with fake data set with biased CCDIS and Multiπ.

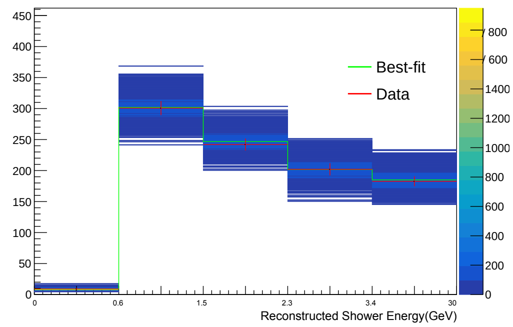

(a) Signal sample PPD in water-in + FHC configuration

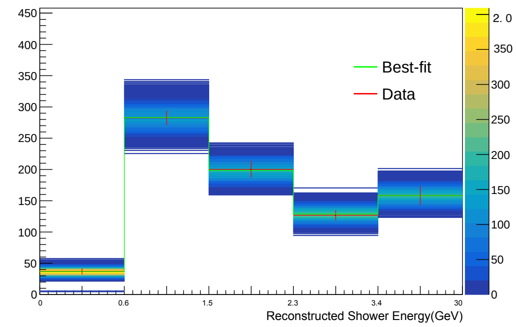

(b) Signal sample PPD in water-out + FHC configuration

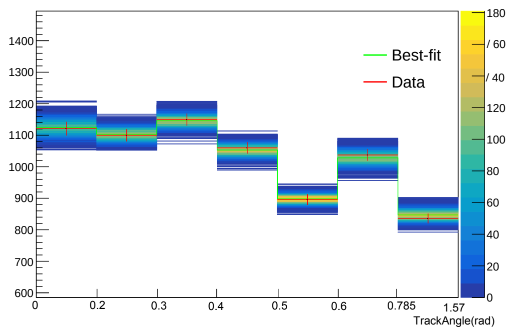

(c) $\nu_\mu(\bar{\nu}_\mu)$ CC sideband PPD in water-in + FHC configuration

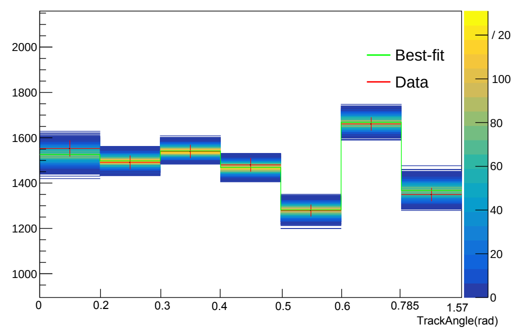

(d) $\nu_\mu(\bar{\nu}_\mu)$ CC sideband PPD in water-out + FHC configuration

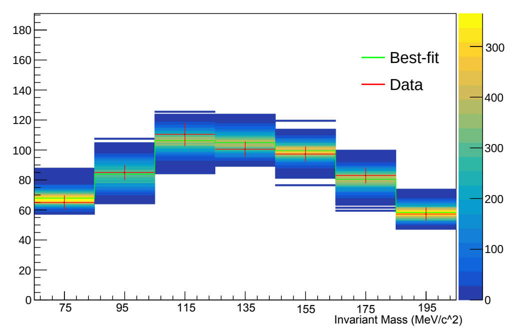

(e) NC $1\pi^0$ sideband PPD in water-in + FHC configuration

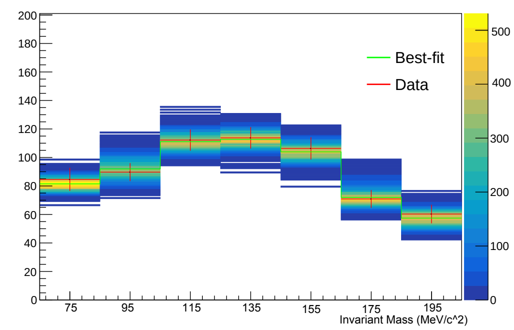

(f) NC $1\pi^0$ sideband PPD in water-out + FHC configuration

Figure 7.6: Posterior Predictive Distribution (PPD) of all 6 samples in FHC in FHC after fitting with fake data set with biased CCDIS and Multiπ. Red cross represent data and green lines are the "best-fit" values in MC. The distribution of each bin after sampling 5000 points on posterior distribution is shown as the colored 2D histogram.

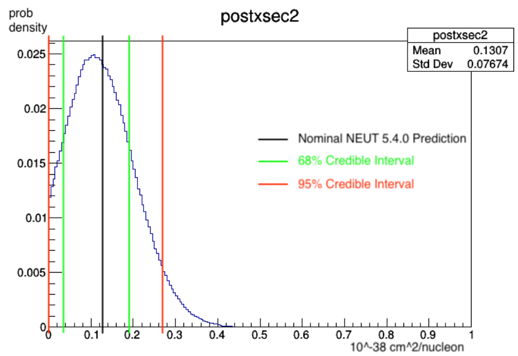

(a) Marginalized cross section distribution at bin2 in true space (0.6-1.5 GeV)

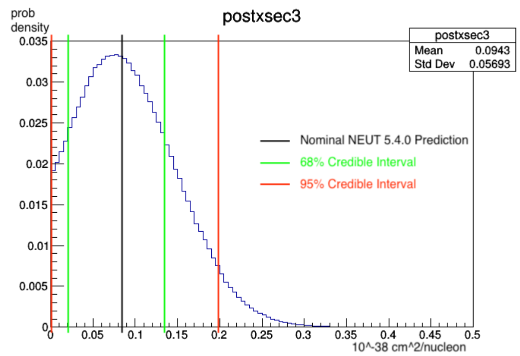

(b) Marginalized cross section distribution at bin3 in true space (1.5-2.3 GeV)

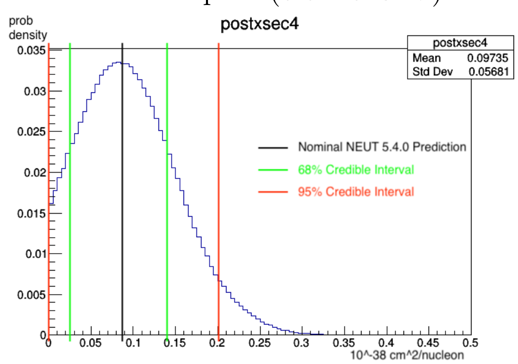

(c) Marginalized cross section distribution at bin4 in true space (2.3-3.4 GeV)

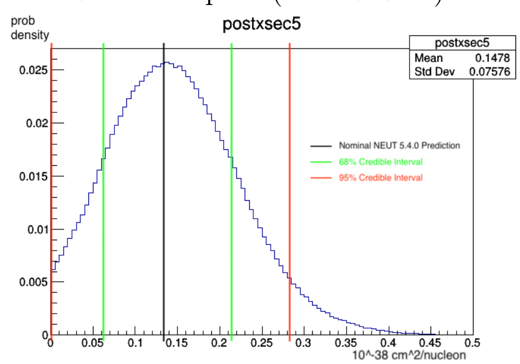

(d) Marginalized cross section distribution at bin5 in true space (>3.4 GeV)

Figure 7.7: Comparison of nominal cross section on water in NEUT 5.4.0 and marginalized posterior distribution of measured cross section on water using generated fake data set with biased CC DIS and Multiπ in RHC. Regions between green (red) lines are 68%(95%) credible intervals of the posterior distribution.

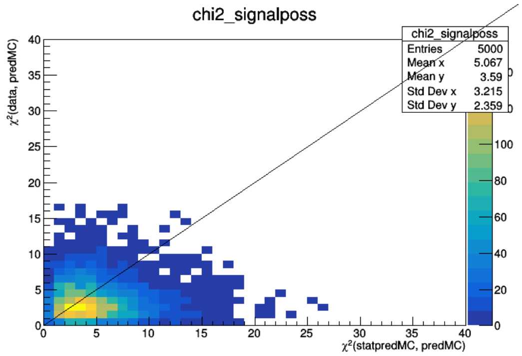

(a) PPP=0.646 for signal sample in water-in + RHC configuration

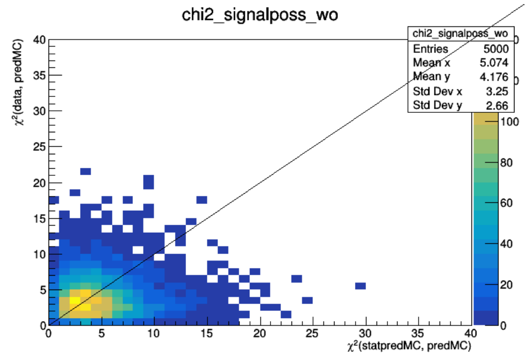

(b) PPP=0.574 for signal sample in water-out + RHC configuration

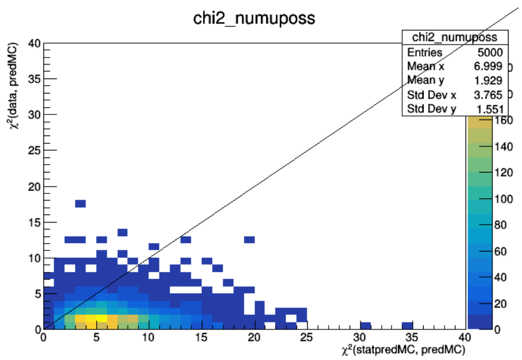

(c) PPP=0.931 for $\nu_\mu(\bar{\nu}_\mu)$ CC sideband in water-in + RHC configuration

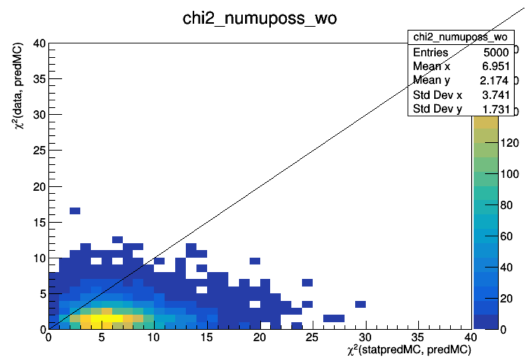

(d) PPP=0.908 for $\nu_\mu(\bar{\nu}_\mu)$ CC sideband in water-out + RHC configuration

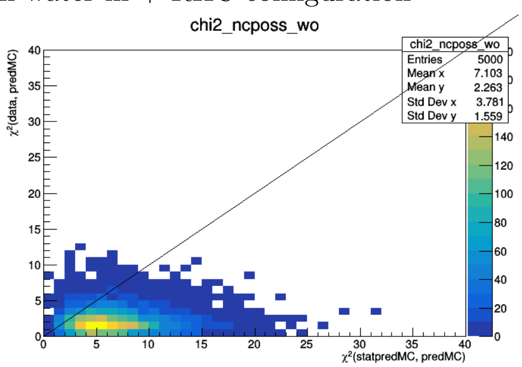

(e) PPP=0.916 for NC $1\pi^0$ sideband in water-in + RHC configuration

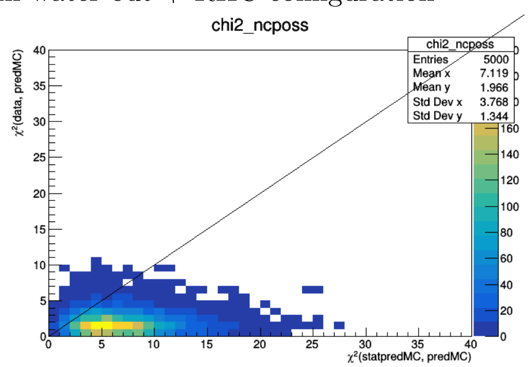

(f) PPP=0.936 for NC $1\pi^0$ sideband in water-out + RHC configuration

Figure 7.8: Posterior Predictive P-value (PPP) for each of all 6 samples in RHC after fitting with fake data set with biased CCDIS and Multiπ.

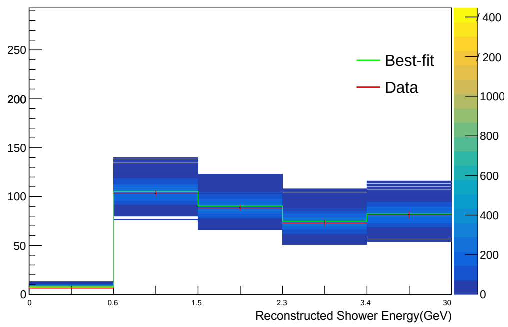

(a) Signal sample PPD in water-in + RHC configuration

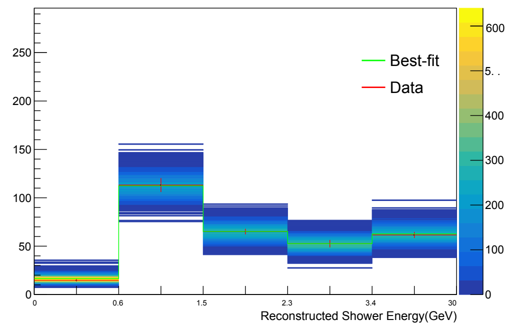

(b) Signal sample PPD in water-out + RHC configuration

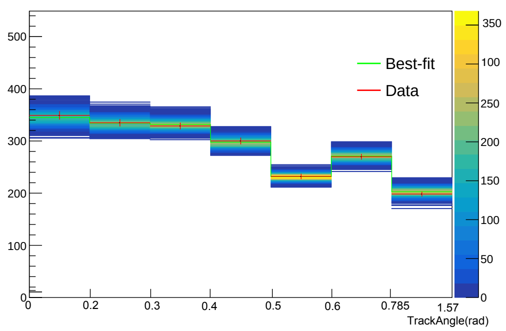

(c) $\nu_\mu(\bar{\nu}_\mu)$ CC sideband PPD in water-in + RHC configuration

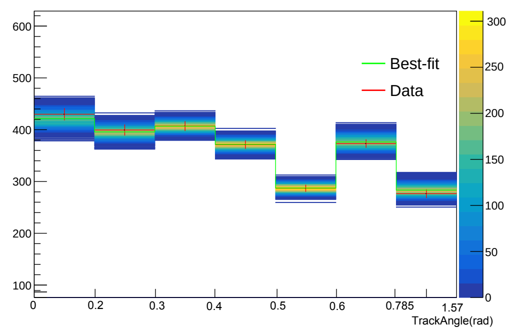

(d) $\nu_\mu(\bar{\nu}_\mu)$ CC sideband PPD in water-out + RHC configuration

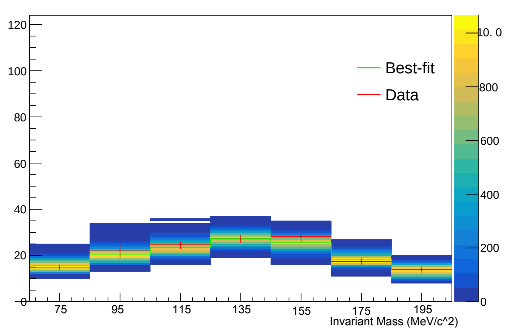

(e) NC $1\pi^0$ sideband PPD in water-in + RHC configuration

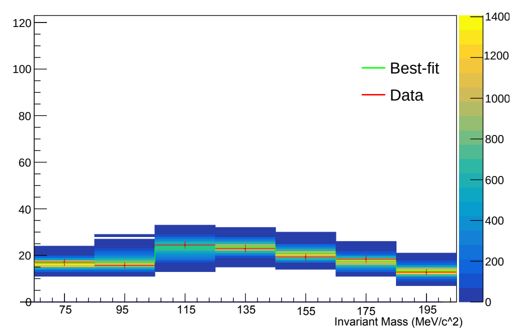

(f) NC $1\pi^0$ sideband PPD in water-out + RHC configuration

Figure 7.9: Posterior Predictive Distribution (PPD) of all 6 samples in RHC after fitting with fake data set with biased CCDIS and Multiπ. Red cross represent data and green lines are the "best-fit" values in MC. The distribution of each bin after sampling 5000 points on posterior distribution is shown as the colored 2D histogram.

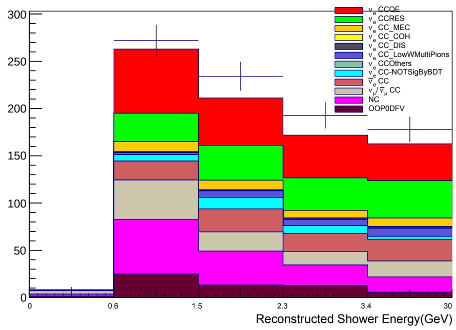

(a) Selected signal sample in water-in + FHC configuration

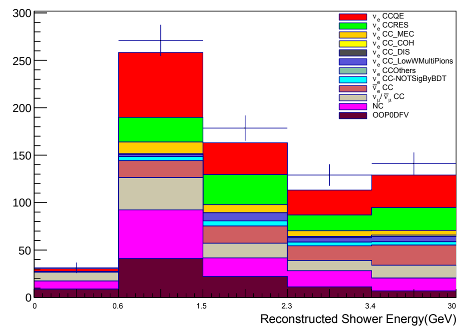

(b) Selected signal sample in water-out + FHC configuration

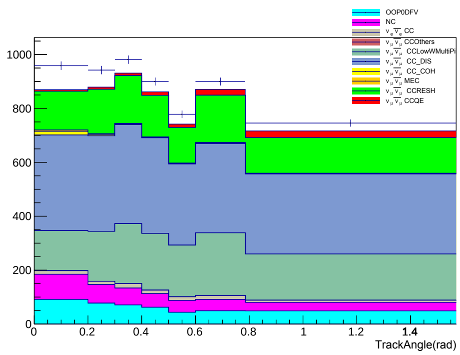

(c) Selected $\nu_\mu(\bar{\nu}_\mu)$ CC sidebands in water-in + FHC configuration

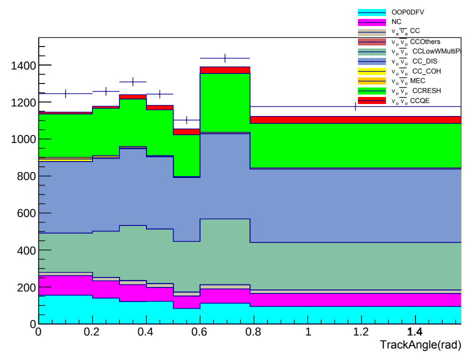

(d) Selected $\nu_\mu(\bar{\nu}_\mu)$ CC sidebands in water-out + FHC configuration

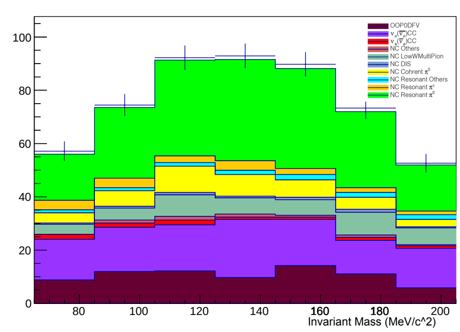

(e) Selected NC $1\pi^0$ sideband in water-in + FHC configuration

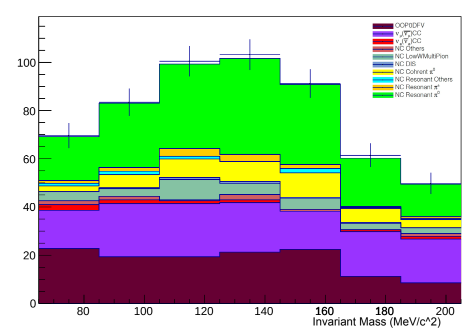

(f) Selected NC $1\pi^0$ sideband in water-out + FHC configuration

Figure 7.10: Comparison of selected nominal (pre-fit) MC and fake data with doubled NC DIS and Multiπ in FHC. Colorful Stack is the selected MC sample and the cross marker is the selected fake data sample. The binning in the plots of the signal sample are not equally divided. Refer to the labels on the x-axis for the value of each bin.

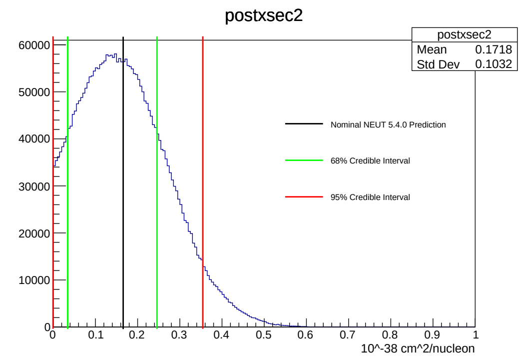

(a) Marginalized cross section distribution at bin2 in true space (0.6-1.5 GeV)

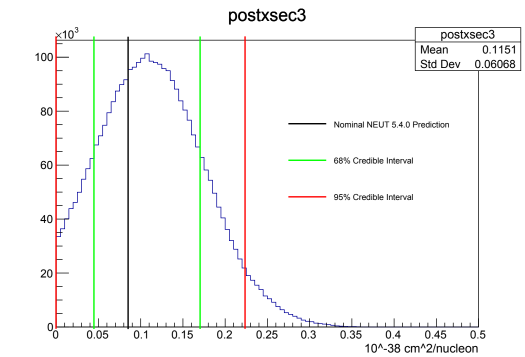

(b) Marginalized cross section distribution at bin3 in true space (1.5-2.3 GeV)

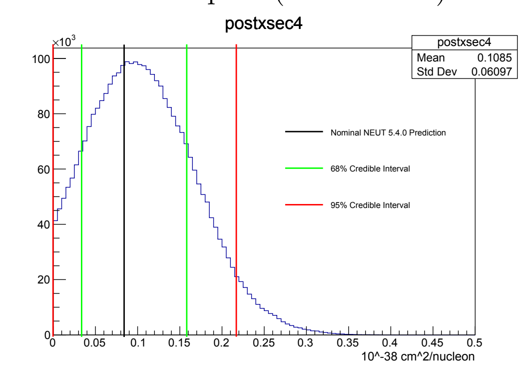

(c) Marginalized cross section distribution at bin4 in true space (2.3-3.4 GeV)

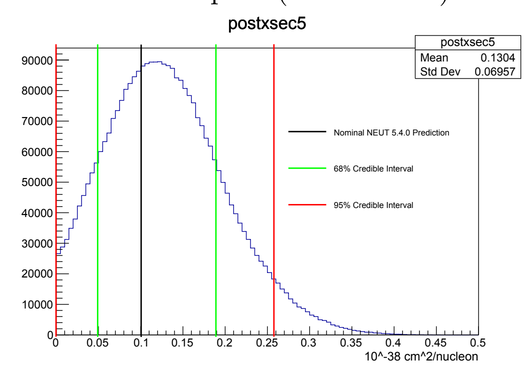

(d) Marginalized cross section distribution at bin5 in true space (>3.4 GeV)

Figure 7.11: Comparison of nominal cross section on water in NEUT 5.4.0 and marginalized posterior distribution of measured cross section on water using generated fake data set with biased NC DIS and Multiπ. Regions between green (red) lines are 68%(95%) credible intervals of the posterior distribution.

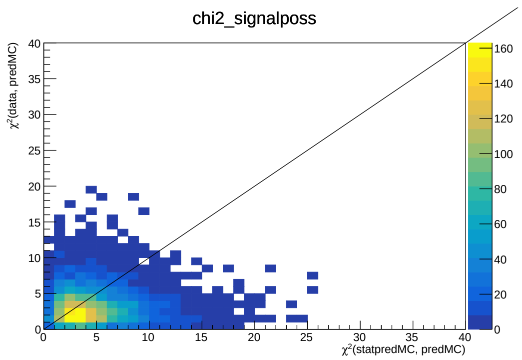

(a) PPP=0.657 for signal sample in water-in + FHC configuration

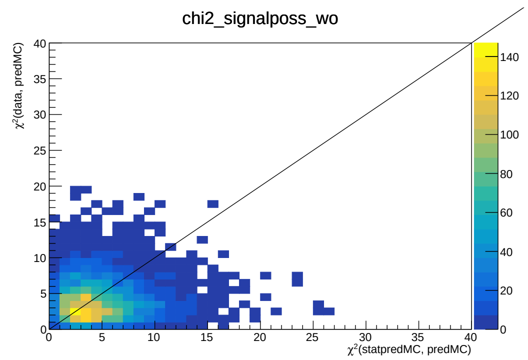

(b) PPP=0.571 for signal sample in water-out + FHC configuration

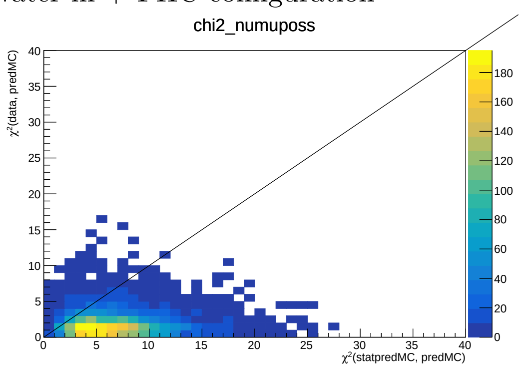

(c) PPP=0.930 for $\nu_\mu(\bar{\nu}_\mu)$ CC sideband in water-in + FHC configuration

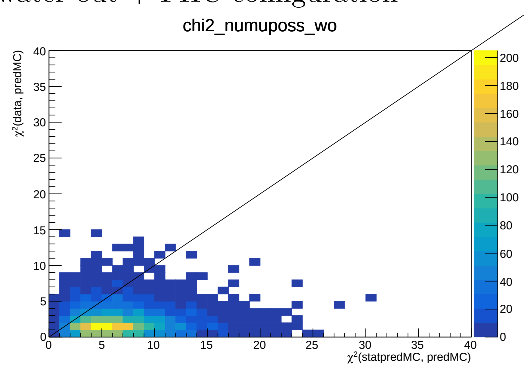

(d) PPP=0.906 for $\nu_\mu(\bar{\nu}_\mu)$ CC sideband in water-out + FHC configuration

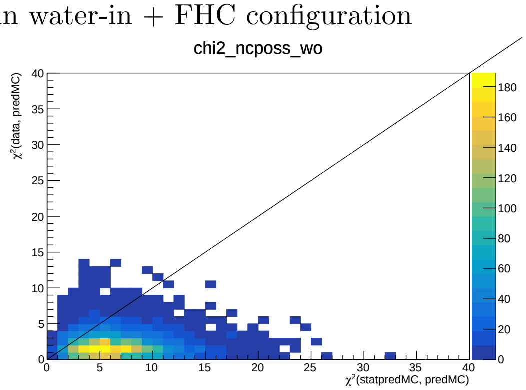

(e) PPP=0.910 for NC $1\pi^0$ sideband in water-in + FHC configuration

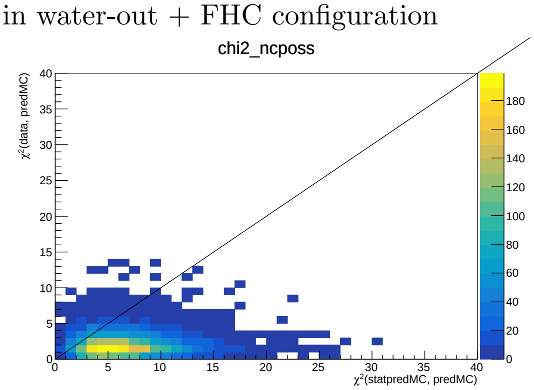

(f) PPP=0.908 for NC $1\pi^0$ sideband in water-out + FHC configuration

Figure 7.12: Posterior Predictive P-value (PPP) for each of all 6 samples in FHC after fitting with fake data set with doubled NC DIS and Multiπ.

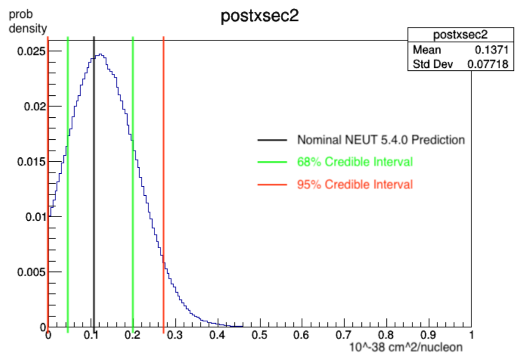

(a) Marginalized cross section distribution at bin2 in true space (0.6-1.5 GeV)

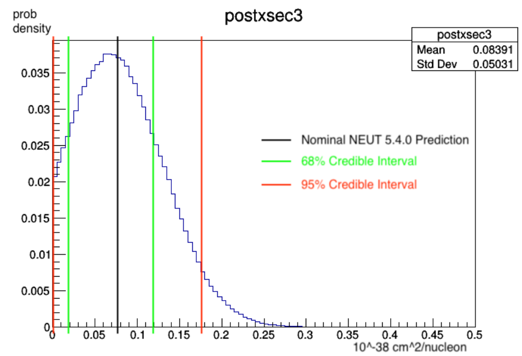

(b) Marginalized cross section distribution at bin3 in true space (1.5-2.3 GeV)

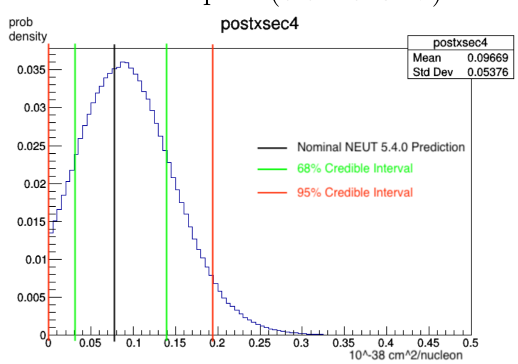

(c) Marginalized cross section distribution at bin4 in true space (2.3-3.4 GeV)

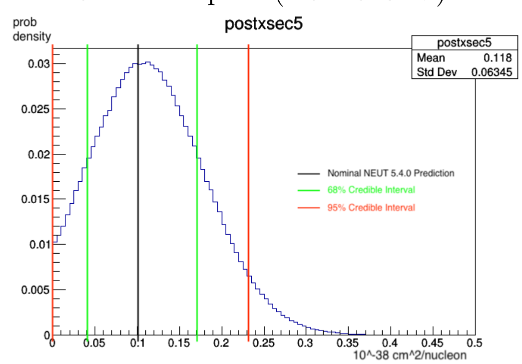

(d) Marginalized cross section distribution at bin5 in true space (>3.4 GeV)

Figure 7.13: Comparison of nominal cross section on water in NEUT 5.4.0 and marginalized posterior distribution of measured cross section on water using generated fake data set with biased NC DIS and Multiπ in RHC. Regions between green (red) lines are 68%(95%) credible intervals of the posterior distribution.

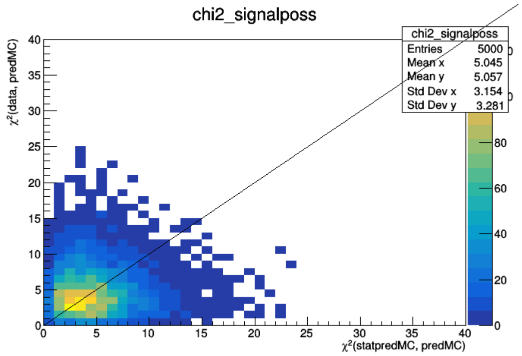

(a) PPP=0.505 for signal sample in water-in + RHC configuration

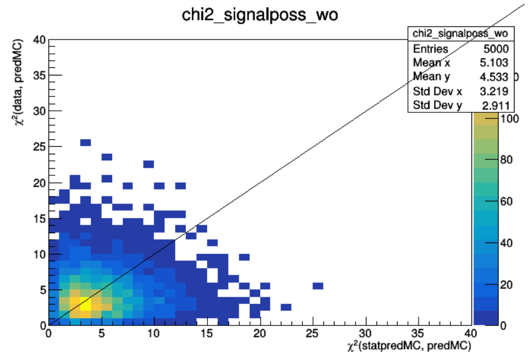

(b) PPP=0.555 for signal sample in water-out + RHC configuration

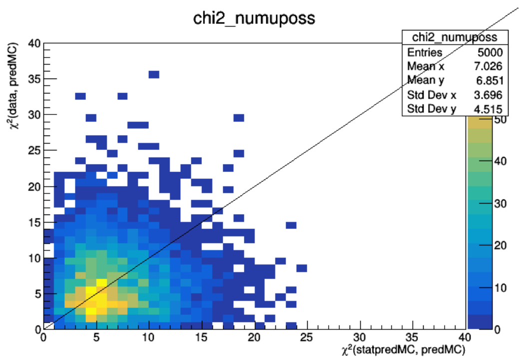

(c) PPP=0.526 for $\nu_\mu(\bar{\nu}_\mu)$ CC sideband in water-in + RHC configuration

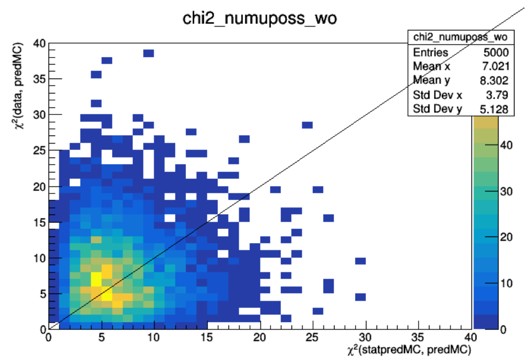

(d) PPP=0.437 for $\nu_\mu(\bar{\nu}_\mu)$ CC sideband in water-out + RHC configuration

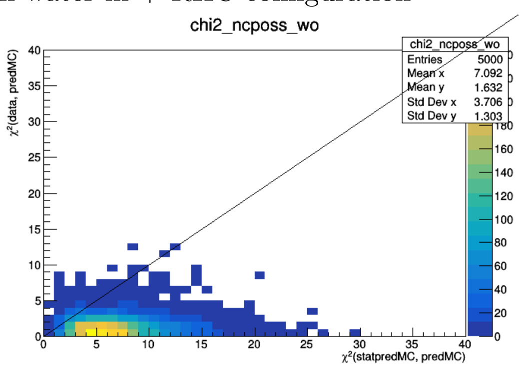

(e) PPP=0.954 for NC $1\pi^0$ sideband in water-in + RHC configuration

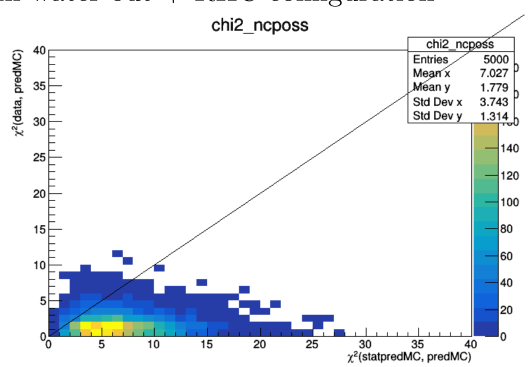

(f) PPP=0.942 for NC $1\pi^0$ sideband in water-out + RHC configuration

Figure 7.14: Posterior Predictive P-value (PPP) for each of all 6 samples in RHC after fitting with fake data set with doubled NC DIS and Multiπ.

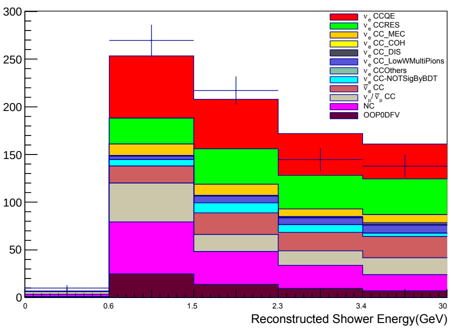

(a) Selected signal sample in water-in + FHC configuration

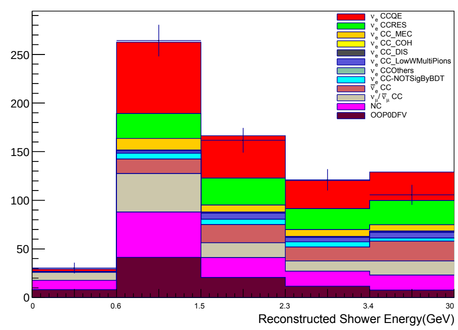

(b) Selected signal sample in water-out + FHC configuration

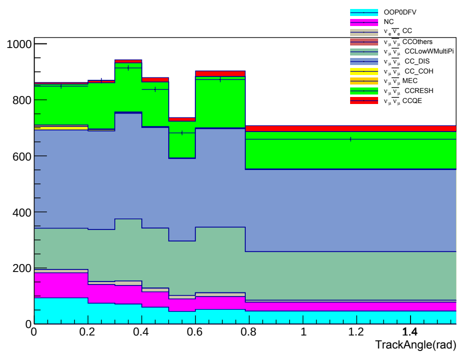

(c) Selected $\nu_\mu(\bar{\nu}_\mu)$ CC sidebands in water-in + FHC configuration

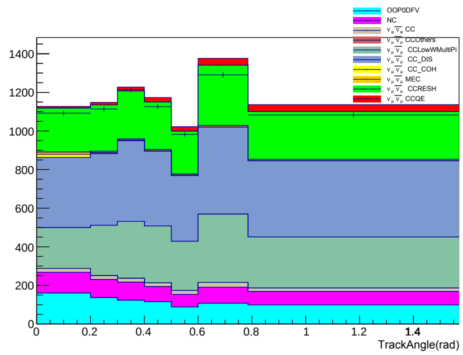

(d) Selected $\nu_\mu(\bar{\nu}_\mu)$ CC sidebands in water-out + FHC configuration

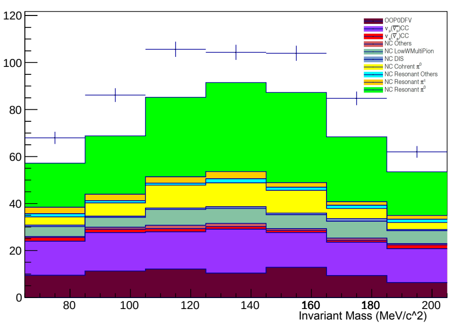

(e) Selected NC $1\pi^0$ sideband in water-in + FHC configuration

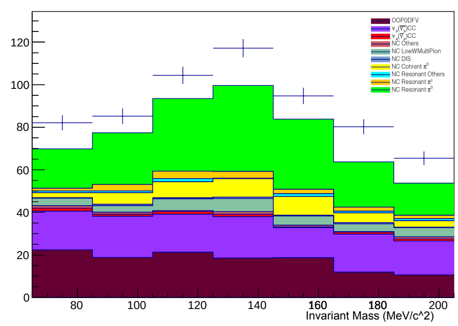

(f) Selected NC $1\pi^0$ sideband in water-out + FHC configuration

Figure 7.15: Comparison of selected nominal (pre-fit) MC and fake data using GENIE v2.8.0 in FHC. Colorful Stack is the selected MC sample and the cross marker is the selected fake data sample. The binning in the plots of the signal sample are not equally divided. Refer to the labels on the x-axis for the value of each bin.

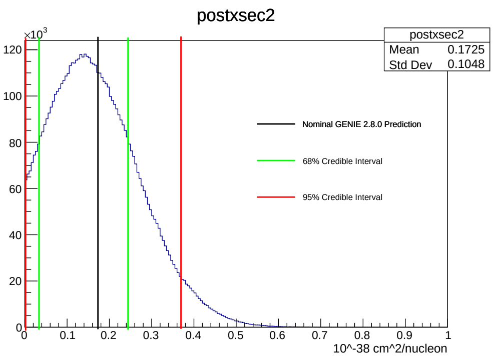

(a) Marginalized cross section distribution at bin2 in true space (0.6-1.5 GeV)

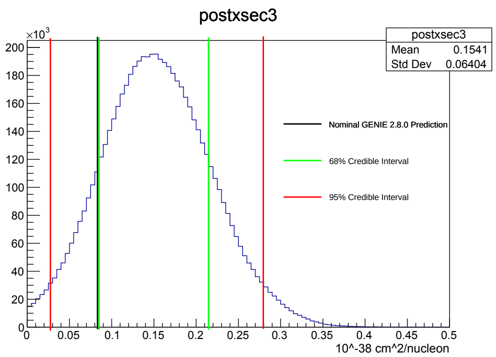

(b) Marginalized cross section distribution at bin3 in true space (1.5-2.3 GeV)

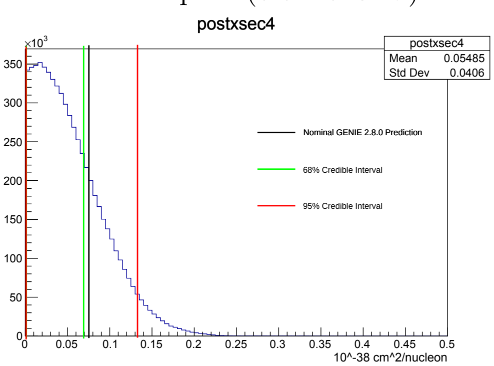

(c) Marginalized cross section distribution at bin4 in true space (2.3-3.4 GeV)

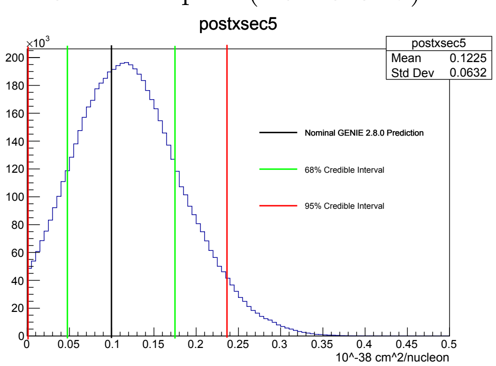

(d) Marginalized cross section distribution at bin5 in true space (>3.4 GeV)

Figure 7.16: Comparison of nominal cross section on water in GENIE 2.8.0 (truth in fake data) and marginalized posterior distribution of measured cross section on water using generated fake data set with GENIE in FHC. Regions between green (red) lines are 68%(95%) credible intervals of the posterior distribution.

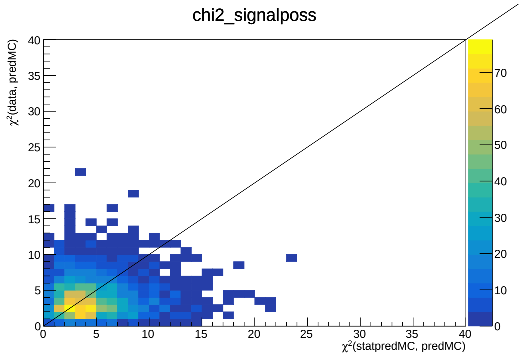

(a) PPP=0.581 for signal sample in water-in + FHC configuration

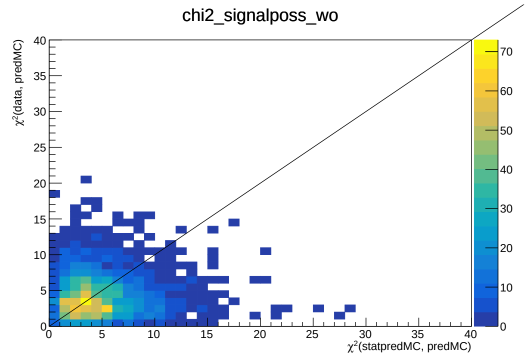

(b) PPP=0.552 for signal sample in water-out + FHC configuration

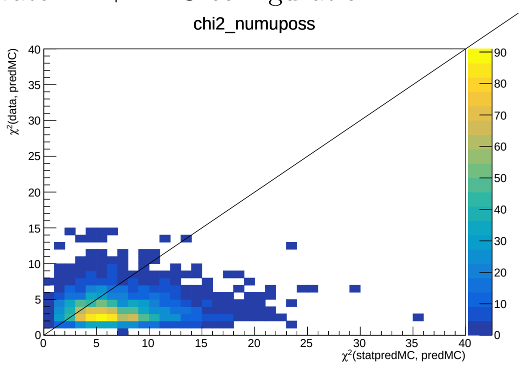

(c) PPP=0.778 for $\nu_\mu(\bar{\nu}_\mu)$ CC sideband in water-in + FHC configuration

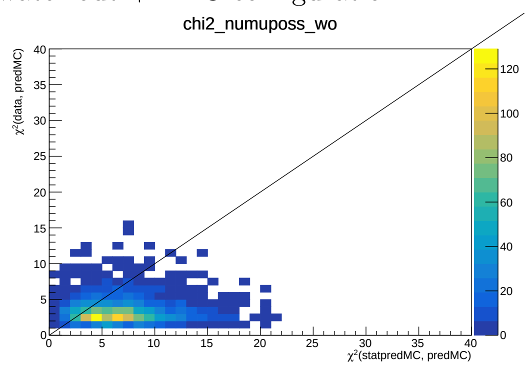

(d) PPP=0.827 for $\nu_\mu(\bar{\nu}_\mu)$ CC sideband in water-out + FHC configuration

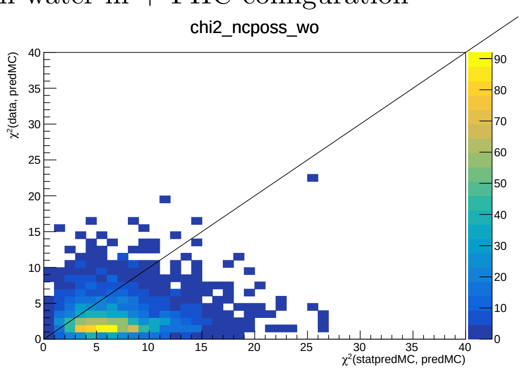

(e) PPP=0.822 for NC $1\pi^0$ sideband in water-in + FHC configuration

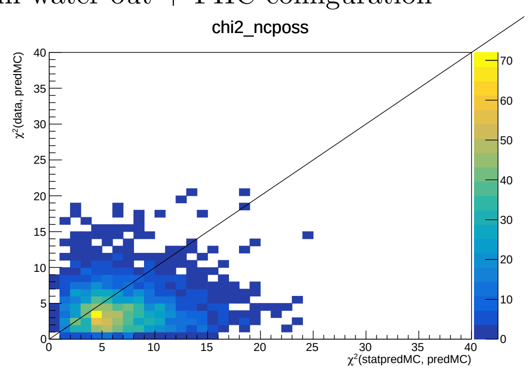

(f) PPP=0.72 for NC $1\pi^0$ sideband in water-out + FHC configuration

Figure 7.17: Posterior Predictive P-value (PPP) for each of all 6 samples in FHC after fitting with fake data set simulated with GENIE 2.8.0.

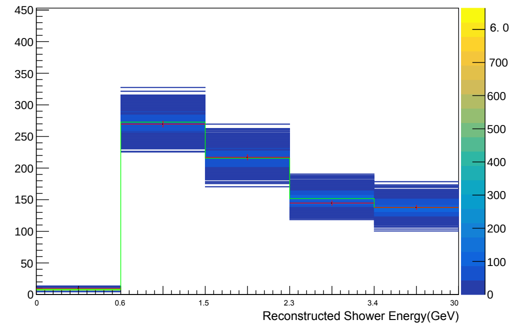

(a) Signal sample PPD in water-in + FHC configuration

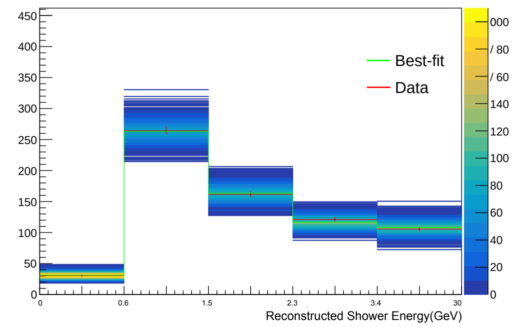

(b) Signal sample PPD in water-out + FHC configuration

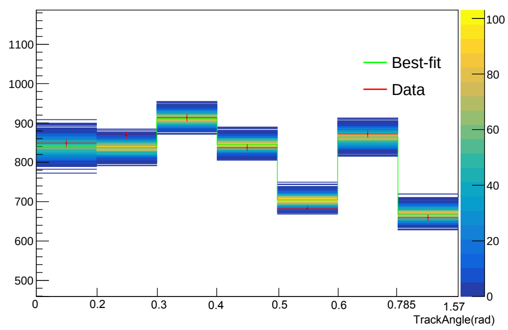

(c) $\nu_\mu(\bar{\nu}_\mu)$ CC sideband PPD in water-in + FHC configuration

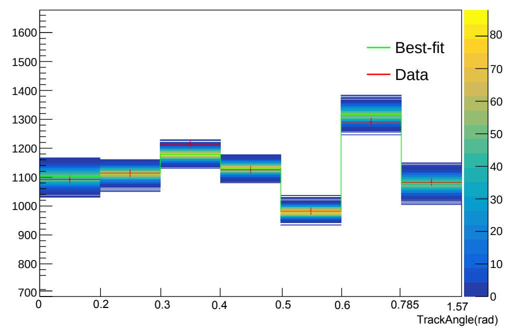

(d) $\nu_\mu(\bar{\nu}_\mu)$ CC sideband PPD in water-out + FHC configuration

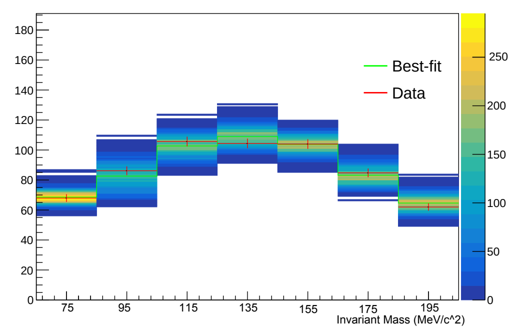

(e) NC $1\pi^0$ sideband PPD in water-in + FHC configuration

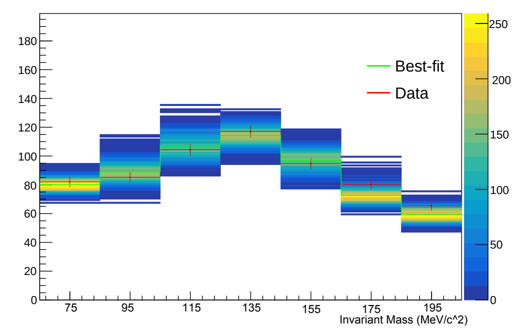

(f) NC $1\pi^0$ sideband PPD in water-out + FHC configuration

Figure 7.18: Posterior Predictive Distribution (PPD) of all 6 samples in FHC after fitting with fake data set with GENIE 2.8.0. Red cross represent data and green lines are the "best-fit" values in MC. The distribution of each bin after sampling 5000 points on posterior distribution is shown as the colored 2D histogram.

Chapter 8

Results

In this chapter, the same procedures applied on fake data shown in the previous chapter are applied to the real data collected by P0D. Measured cross section results will be present in this chapter.

8.1 ν_e CC signal cross section using FHC data

As discussed in chapter 4.2, signal in FHC is defined as ν_e CC interactions on-water generating $1e^-$ + 0 visible proton + 0 visible charged pion in true space, where the topology of $1e^-$ + 0 visible proton + 0 visible charged pion in true space is determined by a BDT criteria. In this chapter, the measured results using data collected in FHC configuration will be presented. Collected Data POTs in FHC used in this thesis which are in good data quality are shown in the table 8.1. MC POT is about ten times of the data POT for every run.

Table 8.1: Total Data POT in good quality used for P0D Analysis in FHC

POT	Water-in+FHC	Water-out+FHC
Data	3.7088e+20	5.81222e+20
MC	3.82809e+21	5.89477e+21

8.1.1 Data-MC Nominal (pre-fit) Comparison in FHC

Figures 8.1 show the comparisons of selected all 6 samples from data and nominal MC samples.

8.1.2 Fitted Results

Figures 8.3 show the distributions of marginalized posterior cross section on water of each bin. Table 8.2 shows the MC prediction of cross sections at each bin and credible intervals from marginalized cross section distributions. Figure 8.2 shows ν_e CC signal differential flux-integrated cross section on water.

Table 8.2: Comparison of MC prediction and measured cross section credible interval using FHC data

Cross Section at each bin $10^{-38} cm^2/nucleon$	MC Prediction	Measured 68% C.I.	Measured 95% C.I.
0.6-1.5 GeV	0.163	[0.055, 0.322]	[0, 0.472]
1.5-2.3 GeV	0.085	[0.090, 0.235]	[0.022, 0.300]
2.3-3.4 GeV	0.084	[0, 0.083]	[0, 0.152]
>3.4 GeV	0.100	[0.020, 0.146]	[0, 0.223]

Figures 8.4 show the distribution of all samples using the posterior predictive method described in section 6.4.3.

Posterior predictive p-value (PPP) was also calculated for each sample, using the method described in section 6.4.4. PPP of all samples together is calculated as 0.599 shown in figure 8.5. Figures 8.6 show the 2D distributions of $\chi^2(data, predMC_i)$ vs $\chi^2(statpredMC_i, predMC_i)$ for each sample. PPP for all samples but $\nu_\mu(\bar{\nu}_\mu)$ CC sideband in water-out and FHC configuration are accepted by the 5% p-value conventions. However, although the PPP for $\nu_\mu(\bar{\nu}_\mu)$ CC sideband in water-out and FHC configuration is about 2% which is less than 5%, a common number to choose as criteria by convention, it doesn't mean that the model should be rejected. There are 6 independent samples as inputs prior fit. It can be calculated that the probability of having one of the 6 samples to have PPP=2% is about 10.8% via combinations. Thus, having that the PPP for $\nu_\mu(\bar{\nu}_\mu)$ CC sideband in water-out and FHC configuration equals to 2% could be due to the statistical fluctuations. The model shouldn't be simply rejected when PPP of one out of the six samples is about 2%.

8.2 $\nu_e + \bar{\nu}_e$ CC signal cross section using RHC data

As discussed in chapter 3 and 4.2, e^- and e^+ are almost non-distinguishable in P0D and the number of ν_e CC and $\bar{\nu}_e$ CC interaction are comparable in RHC, so the signal is defined as ν_e and $\bar{\nu}_e$ Charged-Current (CC) interactions on-water generating $1e^{\pm}$ + 0 visible proton + 0 visible charged pion in true space. Similarly, collected Data POTs in RHC used in this thesis which are in good data quality are shown in the table 8.3 and MC POT is about ten times of the data POT for every run.

Table 8.3: Total Data POT in good quality used for P0D Analysis in FHC

POT	Water-in+RHC	Water-out+RHC
Data	2.43921e+20	3.50175e+20
MC	2.4313e+21	3.46977e+21

8.2.1 Data-MC Nominal (pre-fit) Comparison in RHC

Figures 8.7 show the comparisons of selected all 6 samples from data and nominal MC samples.

8.2.2 Fitted Results

Figures 8.9 show the distributions of marginalized posterior cross section on water of each bin. Table 8.4 shows the MC prediction of cross sections at each bin and credible intervals from marginalized cross section distributions. Figure 8.8 shows $\nu_e + \bar{\nu}_e$ CC signal differential flux-integrated cross section on water.

Figures 8.10 show the distribution of all samples using the posterior predictive method described in section 6.4.3.

Similarly, Posterior predictive p-value (PPP) was also calculated for each sample, using the method described in section 6.4.4. PPP of all samples together is calculated as 0.599 shown in figure 8.11. Figures 8.12 show the 2D distributions of $\chi^2(data, predMC_i)$ vs $\chi^2(statpredMC_i, predMC_i)$ for each sample. PPP for every sample indicates no disagreement between data and

Table 8.4: Comparison of measured cross section credible interval and MC prediction

Cross Section at each bin $10^{-38}cm^2/nucleon$	MC Prediction	Measured 68% C.I.	Measured 95% C.I.
0.6-1.5 GeV	0.113	[0, 0.113]	[0, 0.217]
1.5-2.3 GeV	0.071	[0.039, 0.160]	[0.001, 0.215]
2.3-3.4 GeV	0.078	[0, 0.062]	[0, 0.122]
$>$3.4 GeV	0.103	[0.099, 0.221]	[0.044, 0.286]

post-fit MC.

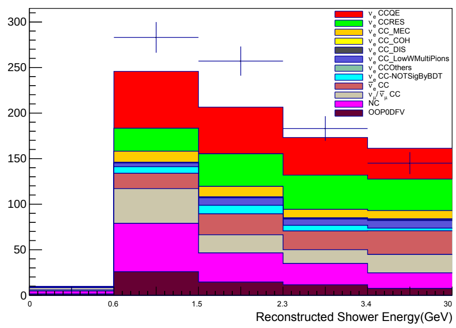

(a) Selected signal sample in
water-in + FHC configuration

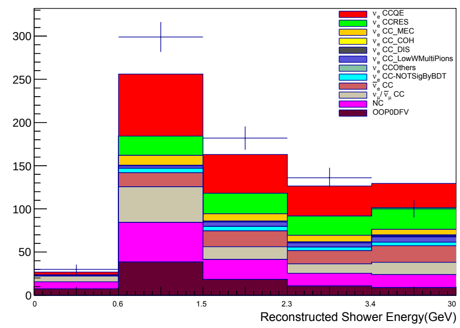

(b) Selected signal sample in
water-out + FHC configuration

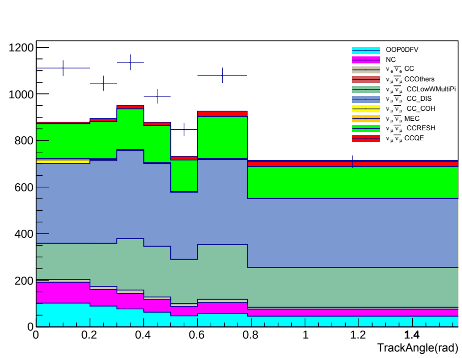

(c) Selected $\nu_\mu(\bar{\nu}_\mu)$ CC sidebands
in water-in + FHC configuration

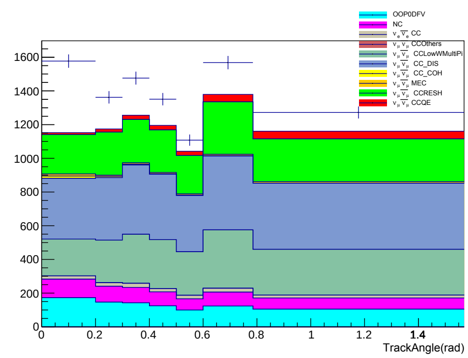

(d) Selected $\nu_\mu(\bar{\nu}_\mu)$ CC sidebands
in water-out + FHC configuration

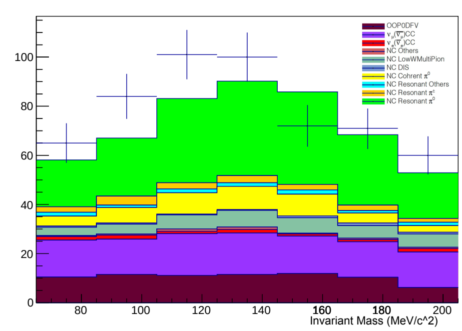

(e) Selected NC $1\pi^0$ sideband
in water-in + FHC configuration

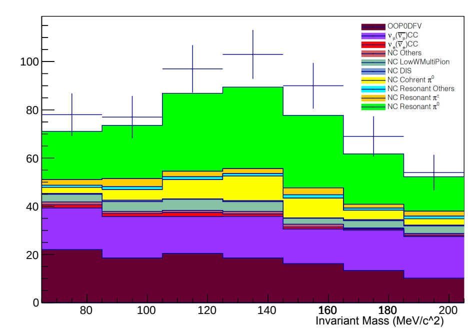

(f) Selected NC $1\pi^0$ sideband
in water-out + FHC configuration

Figure 8.1: Comparison of selected nominal (pre-fit) MC and data in FHC. Colorful stack is the selected MC sample and the cross marker is the selected data sample. The binning in the plots of the signal sample are not equally divided. Refer to the labels on the x-axis for the value of each bin.

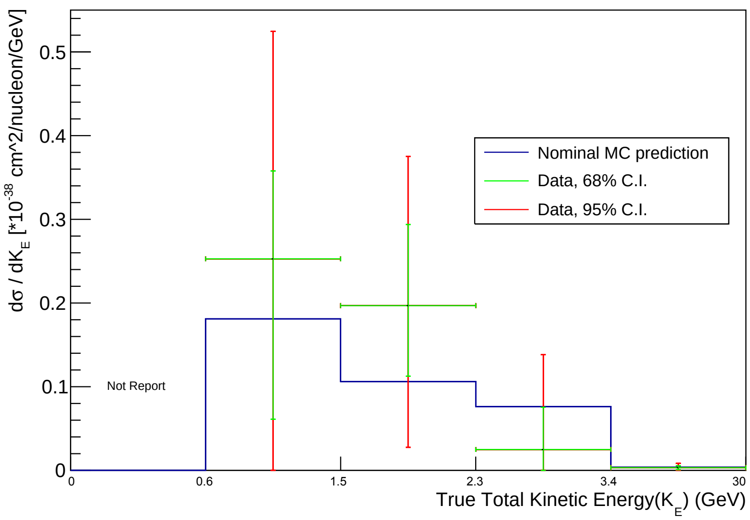

Figure 8.2: ν_e CC signal differential flux-integrated cross section on water using FHC data. The green and red bars represent the 68% and 95% credible intervals and the center is estimated by the peak of the distribution not the mean.

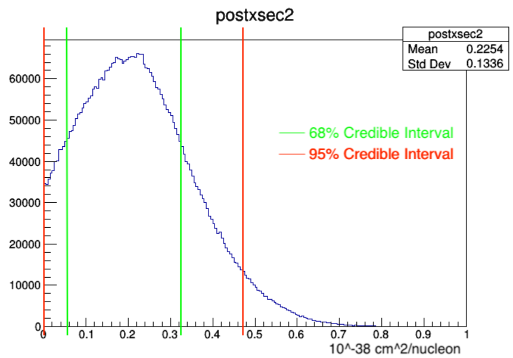

(a) Marginalized cross section distribution at bin2 in true space (0.6-1.5 GeV)

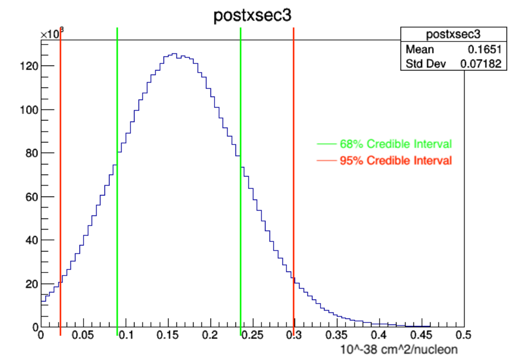

(b) Marginalized cross section distribution at bin3 in true space (1.5-2.3 GeV)

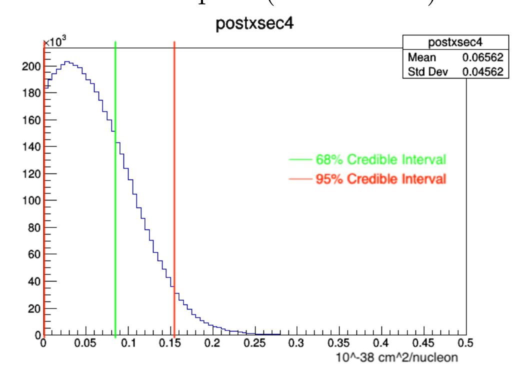

(c) Marginalized cross section distribution at bin4 in true space (2.3-3.4 GeV)

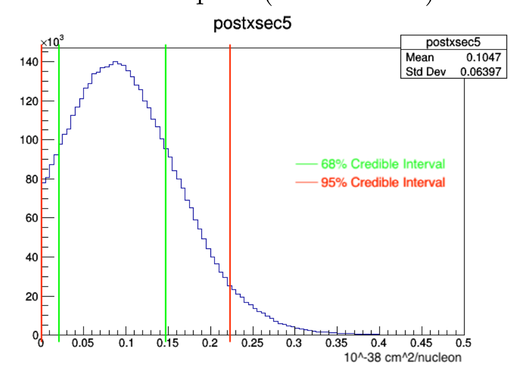

(d) Marginalized cross section distribution at bin5 in true space (>3.4 GeV)

Figure 8.3: Distributions of marginalized posterior cross section on water of each bin in the unit of $10^{-38} cm^2/nucleon$ using FHC data. Interval between green lines corresponds to 68% credible interval and between red lines are 95% credible interval.

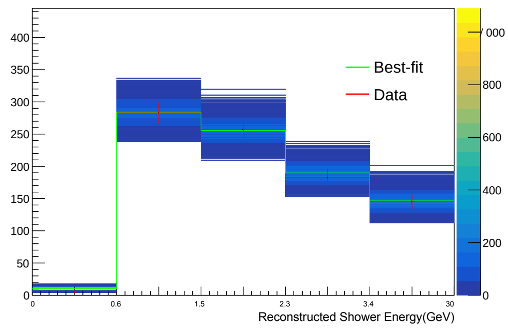

(a) Signal sample PPD in water-in + FHC configuration

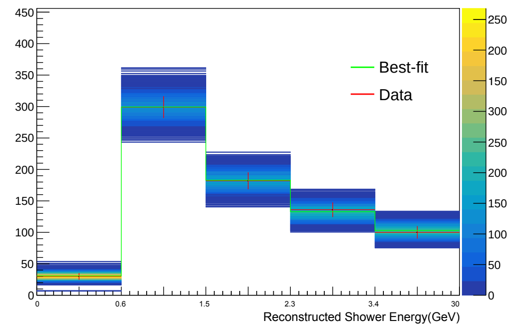

(b) Signal sample PPD in water-out + FHC configuration

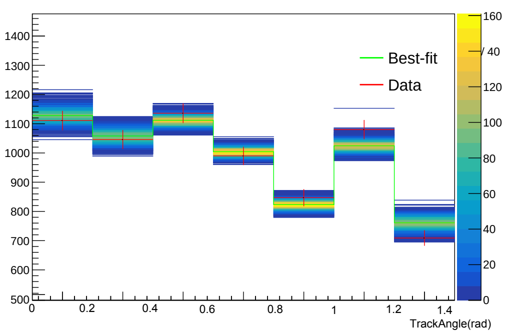

(c) $\nu_\mu(\bar{\nu}_\mu)$ CC sideband PPD in water-in + FHC configuration

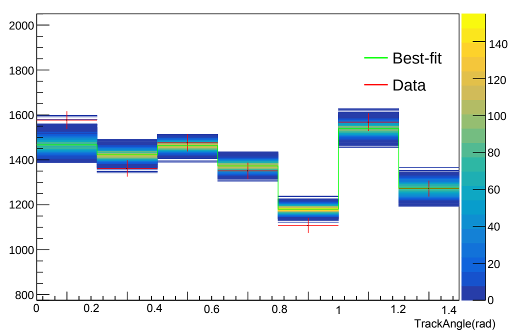

(d) $\nu_\mu(\bar{\nu}_\mu)$ CC sideband PPD in water-out + FHC configuration

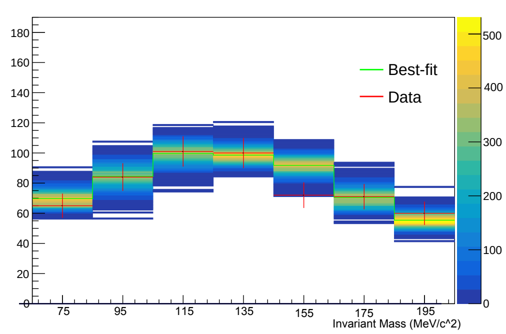

(e) NC $1\pi^0$ sideband PPD in water-in + FHC configuration

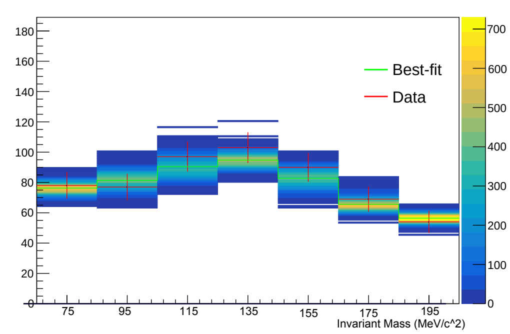

(f) NC $1\pi^0$ sideband PPD in water-out + FHC configuration

Figure 8.4: Posterior Predictive Distribution (PPD) of all 6 samples in FHC after fit. Red cross represent data and green lines are the "best-fit" values in MC. The distribution of each bin after sampling 5000 points on posterior distribution is shown as the colored 2D histogram.

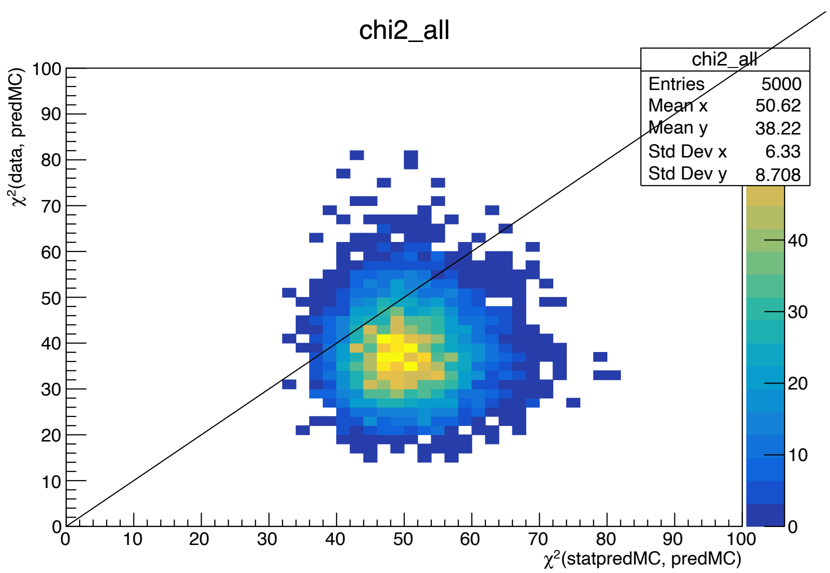

Figure 8.5: PPP=0.126 for all samples together in FHC after fit

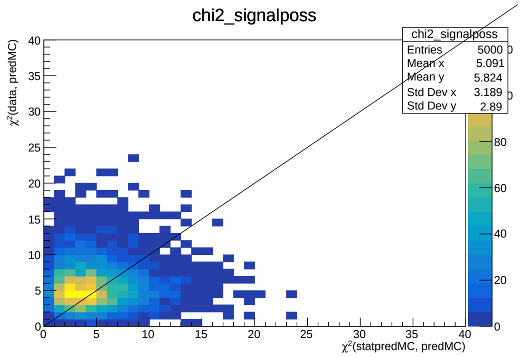

(a) PPP=0.416 for signal sample in water-in + FHC configuration

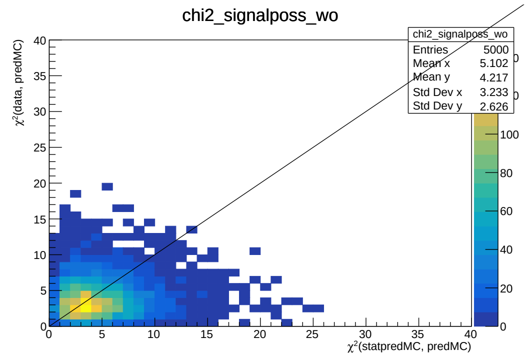

(b) PPP=0.585 for signal sample in water-out + FHC configuration

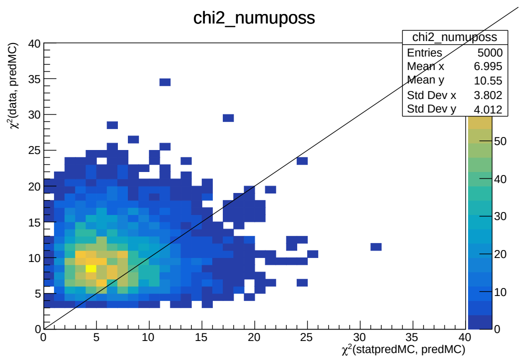

(c) PPP=0.242 for $\nu_\mu(\bar{\nu}_\mu)$ CC sideband in water-in + FHC configuration

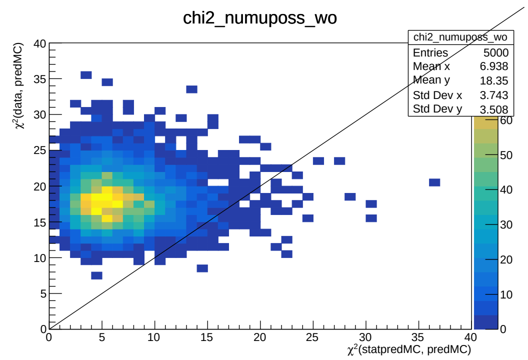

(d) PPP=0.021 for $\nu_\mu(\bar{\nu}_\mu)$ CC sideband in water-out + FHC configuration

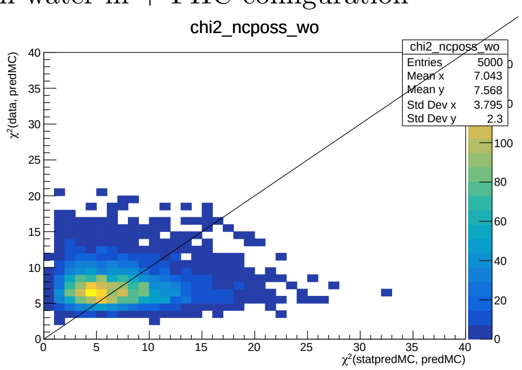

(e) PPP=0.412 for NC $1\pi^0$ sideband in water-in + FHC configuration

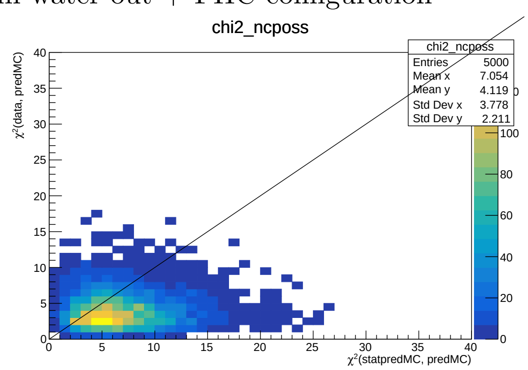

(f) PPP=0.758 for NC $1\pi^0$ sideband in water-out + FHC configuration

Figure 8.6: Posterior Predictive P-value (PPP) for each of all 6 samples in FHC after fit

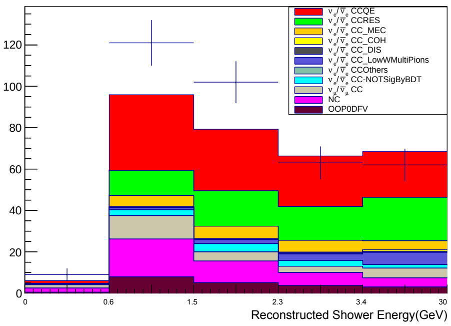

(a) Selected signal sample in water-in + RHC configuration

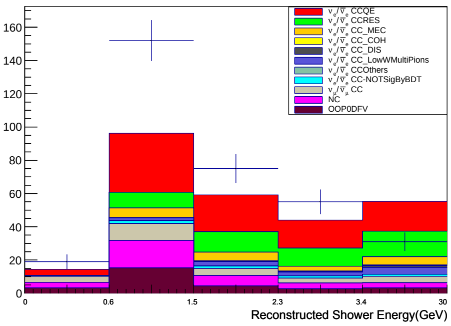

(b) Selected signal sample in water-out + RHC configuration

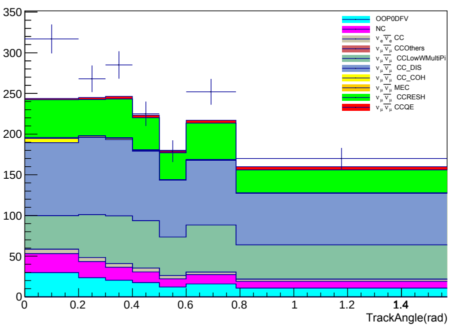

(c) Selected $\nu_\mu(\bar{\nu}_\mu)$ CC sidebands in water-in + RHC configuration

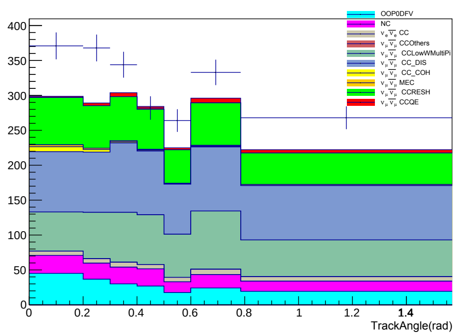

(d) Selected $\nu_\mu(\bar{\nu}_\mu)$ CC sidebands in water-out + FHC configuration

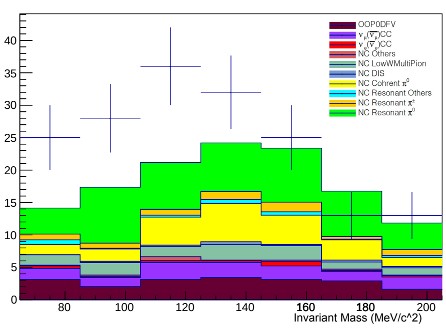

(e) Selected NC $1\pi^0$ sideband in water-in + RHC configuration

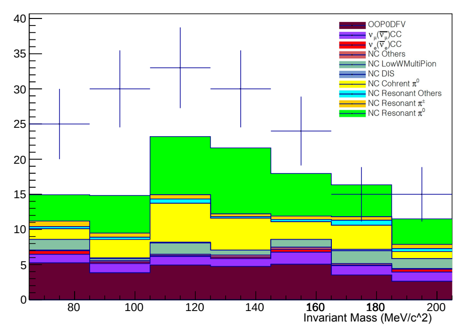

(f) Selected NC $1\pi^0$ sideband in water-out + RHC configuration

Figure 8.7: Comparison of selected nominal (pre-fit) MC and data in RHC. Colorful stack is the selected MC sample and the cross marker is the selected data sample. The binning in the plots of the signal sample are not equally divided. Refer to the labels on the x-axis for the value of each bin.

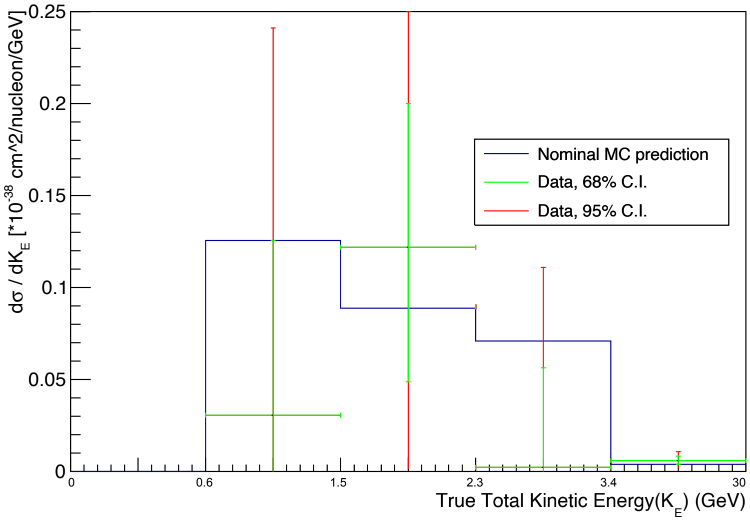

Figure 8.8: $\nu_e + \bar{\nu}_e$ CC signal differential flux-integrated cross section on water using RHC data. The green and red bars represent the 68% and 95% credible intervals and the center is estimated by the peak of the distribution not the mean.

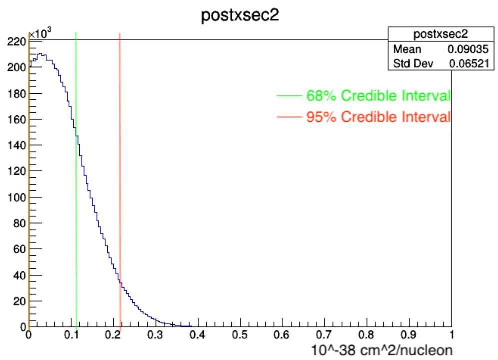

(a) Marginalized cross section distribution at bin2 in true space (0.6-1.5 GeV)

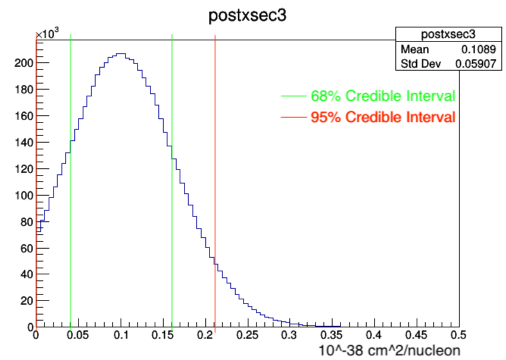

(b) Marginalized cross section distribution at bin3 in true space (1.5-2.3 GeV)

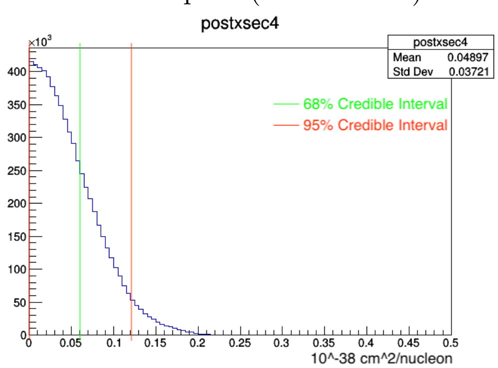

(c) Marginalized cross section distribution at bin4 in true space (2.3-3.4 GeV)

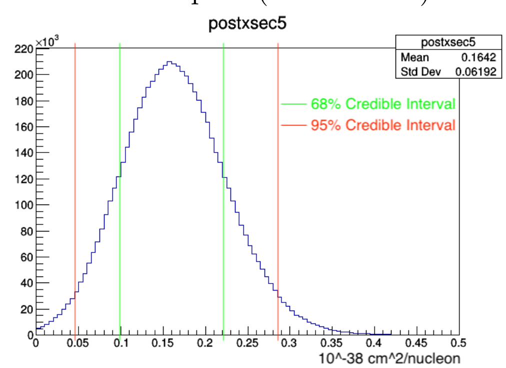

(d) Marginalized cross section distribution at bin5 in true space (>3.4 GeV)

Figure 8.9: Distributions of marginalized posterior cross section on water of each bin in the unit of $10^{-38} cm^2/nucleon$ using RHC data. Interval between green lines corresponds to 68% credible interval and between red lines are 95% credible interval.

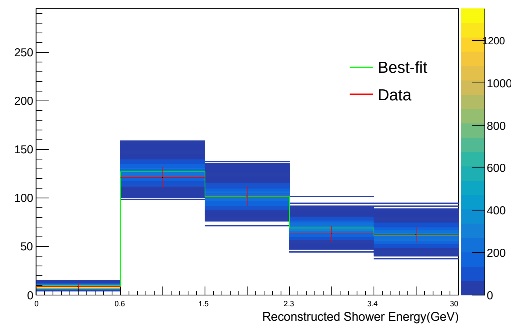

(a) Signal sample PPD in water-in + RHC configuration

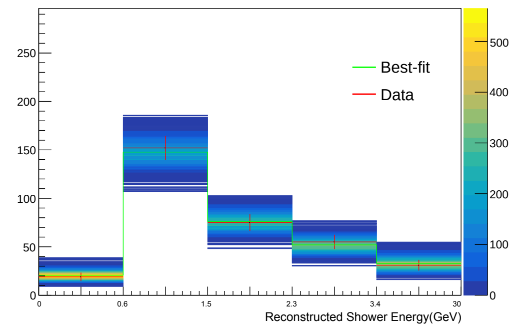

(b) Signal sample PPD in water-out + RHC configuration

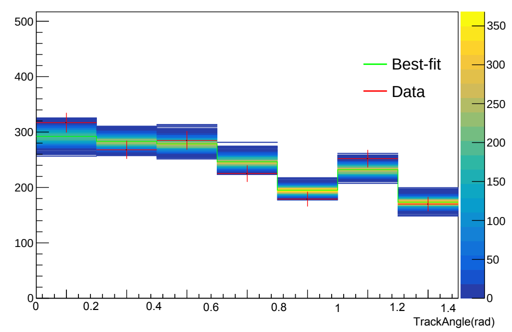

(c) $\nu_\mu(\bar{\nu}_\mu)$ CC sideband PPD in water-in + RHC configuration

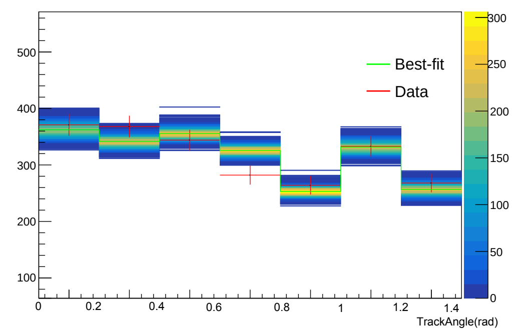

(d) $\nu_\mu(\bar{\nu}_\mu)$ CC sideband PPD in water-out + FHC configuration

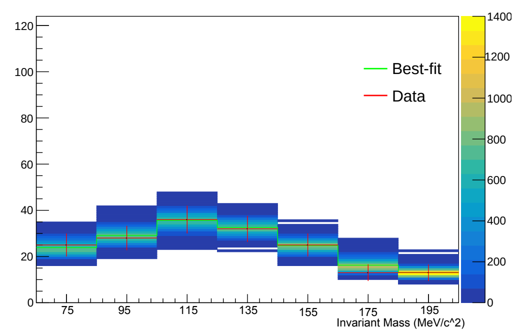

(e) NC $1\pi^0$ sideband PPD in water-in + RHC configuration

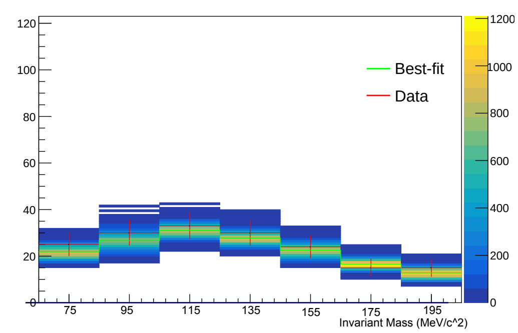

(f) NC $1\pi^0$ sideband PPD in water-out + RHC configuration

Figure 8.10: Posterior Predictive Distribution (PPD) of all 6 samples after fit. Red cross represent data and green lines are the "best-fit" values in MC. The distribution of each bin after sampling 5000 points on posterior distribution is shown as the colored 2D histogram.

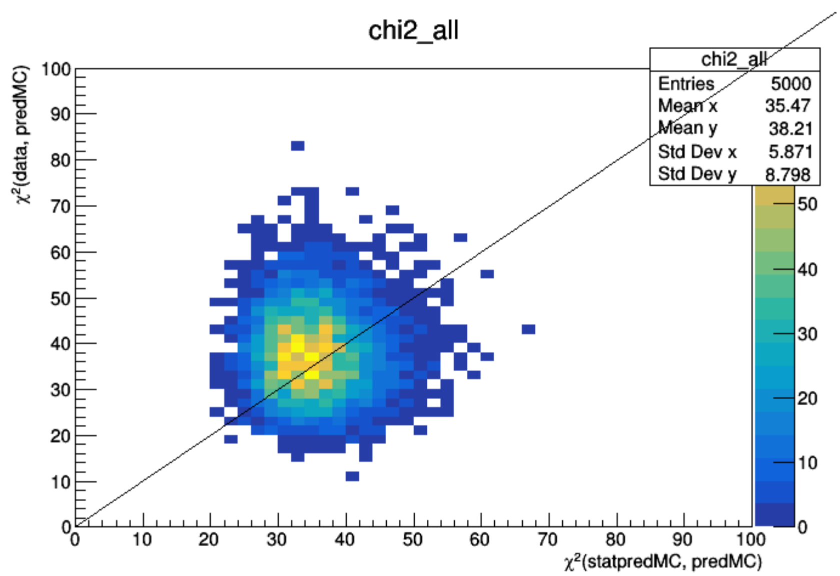

Figure 8.11: PPP=0.599 for all samples together in RHC after fit

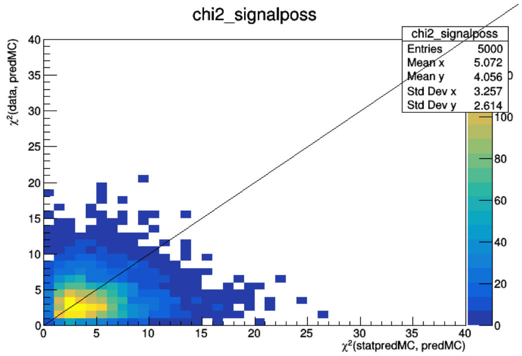

(a) PPP=0.599 for signal sample in water-in + RHC configuration

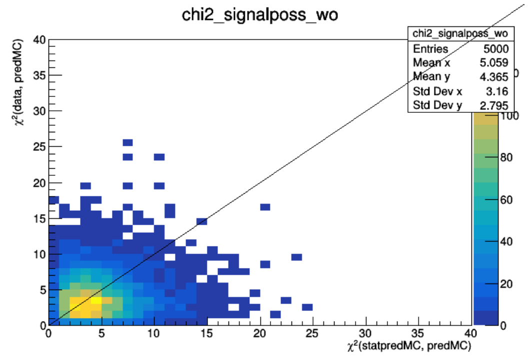

(b) PPP=0.570 for signal sample in water-out + RHC configuration

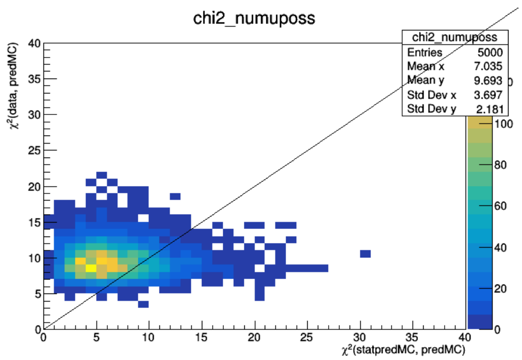

(c) PPP=0.241 for $\nu_\mu(\bar{\nu}_\mu)$ CC sideband in water-in + RHC configuration

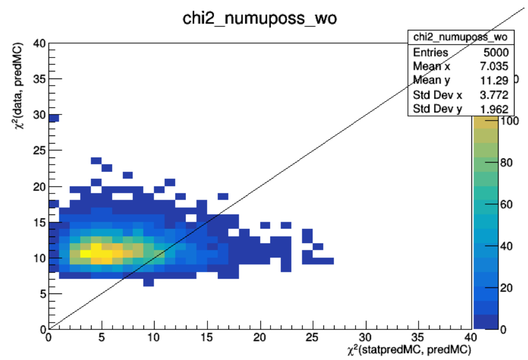

(d) PPP=0.146 for $\nu_\mu(\bar{\nu}_\mu)$ CC sideband in water-out + FHC configuration

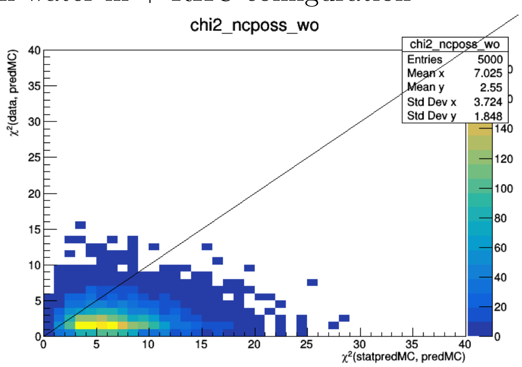

(e) PPP=0.887 for NC $1\pi^0$ sideband in water-in + RHC configuration

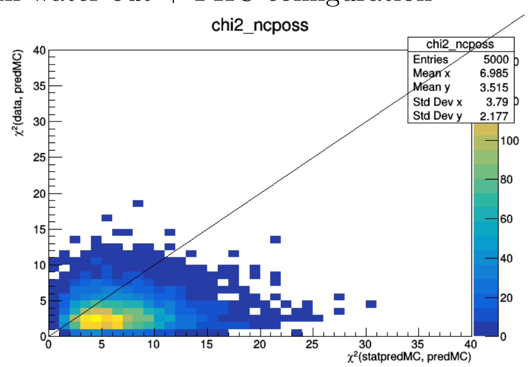

(f) PPP=0.808 for NC $1\pi^0$ sideband in water-out + RHC configuration

Figure 8.12: Posterior Predictive P-value (PPP) for each of all 6 samples after fit

Appendix A

PID Systematic Uncertainties

In this appendix, every variable used for PID likelihood calculation other than trackP0DuleAsymmetry will be introduced and then maps built from them will be listed.

A.1 trackMedianWidth

This is a 2D variable. Figure A.1 gives an example of the kEM likelihood distribution for this variable in water-in configuration and Water Target Contained region. The x-axis called MedianNodeWidth is same with TrackMedianWidth used in the selection in section 4.3.6. The y-axis, length index, is calculate using std::min((int(tracklength) / 500), 4). Figure A.2a and A.2b show disbribution of MedianNodeWidth with index value as 2 and 3 as examples. Almost all events are in the first bin. After normalization, data-MC matches very well. Thus, for this variable, if using the ratio of number of events in first bin between data and MC after normalization, it would be almost 1. As a results, the unitary matrix is taken as the map.

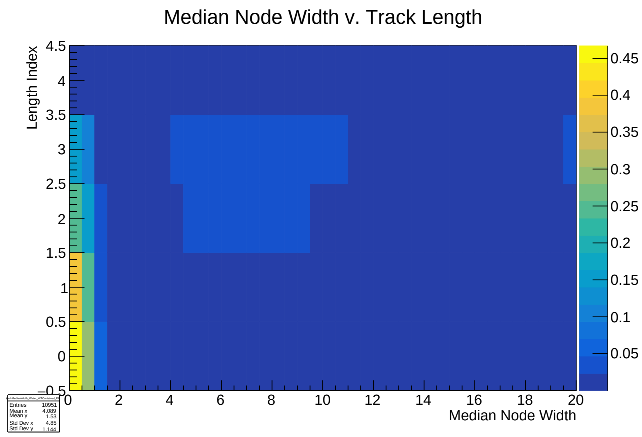

Figure A.1: Likelihood distribution of trackMedianWidth_waterinconfig_WatertargetContained_EM

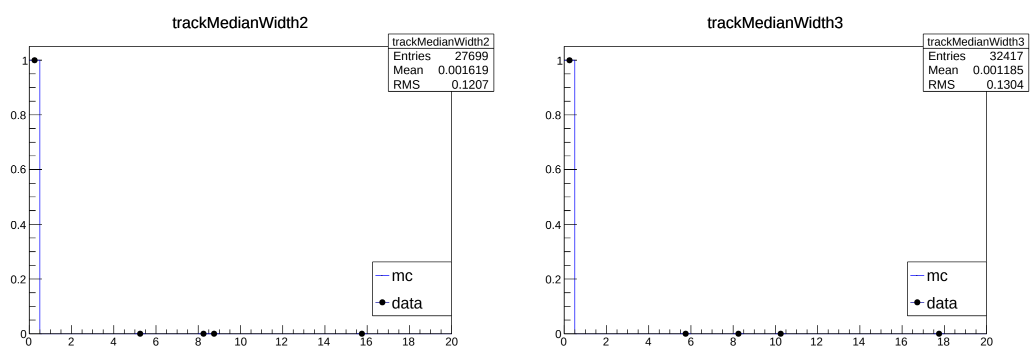

(a) Distribution of MedianNodeWidth when length index=2

(b) Distribution of MedianNodeWidth when length index=3

Figure A.2: Distribution of MedianNodeWidth

A.2 trackWTCharge

The variable, trackWTCharge, is Median WT Charge vs TrackLengh, where Median WT Charge is the median value of angle corrected charges in each layer in Water Target region. Figure A.3 shows the kEM likelihood distribution for this variable in water-in configuration. The binning of the length used in p0dRecon is $[250, 1750)$ with 6 bins. Taking the same binning and figures in A.8 show data-MC comparison of trackWTCharge in 4th , 5th and 6th bins. There is no events from first to third bin is found in our sand muon control sample. It is because that when selecting the control sample, a cut that requires selected objects pass >10 P0Dules in WT which mean that length of objects are at least approximately 1000mm.

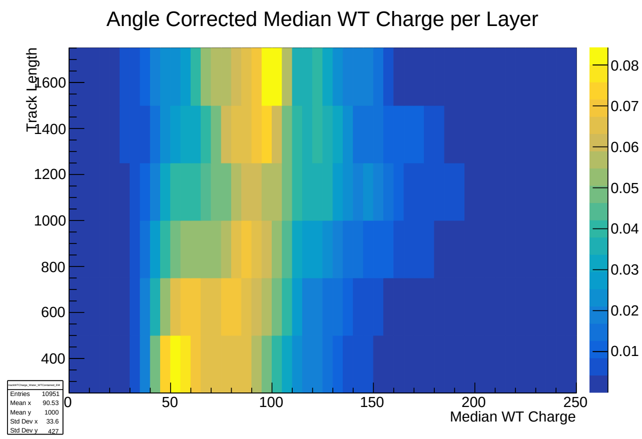

Figure A.3: Likelihood distribution of trackWTCharge_waterinconfig_WatertargetContained_EM

A.3 trackWTChargeRMS

As the name of the variable indicates, x-axis of this variable if the RMS of Median WT Charge. Like before, using the kEM likelihood distribution for this variable in water-in configuration as an example shown in figure A.4. Figures in A.9 show data-MC comparison.

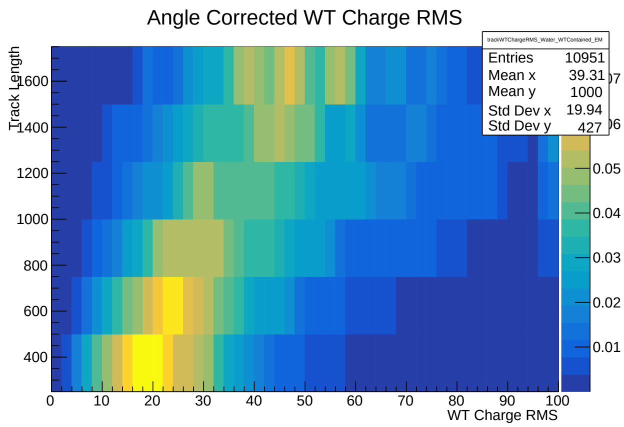

Figure A.4: Likelihood distribution of trackWTChargeRMS_waterinconfig_WatertargetContained_EM

A.4 trackECalCharge

The concept of this variable is similar to trackWTCharge. Figure A.5 is an example of Likelihood distribution. ECal charge on x-axis is the median value of of angle corrected charges in each layer in Central ECal. However, because Central ECal is smaller than WT along beam direction, the y-axis uses the number of layers objects pass in Central ECal rather than its length. Data-MC comparisons in water-in configuration are shown in figures A.10, A.11 and A.12. For the case of passing even last two scintillator layers shown in figure A.12e, due to the very small statistics, take the map as 1 for it rather than using its cumulative distribution.

A.5 trackECalChargeRMS

Similar with trackWTChargeRMS, this variable is the RMS of trackECalCharge. An example of likelihood distribution is shown in figure A.6. Maps are shown

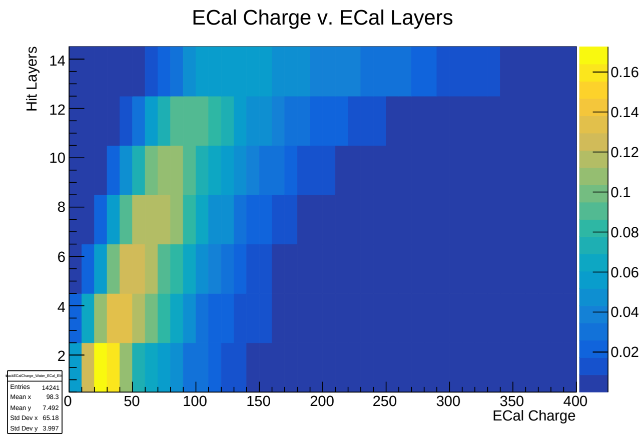

Figure A.5: Likelihood distribution of
trackECalCharge_waterinconfig_WatertargetContained_EM

in figure A.13, A.14 and A.15. Same with trackECalCharge, for last two layers, we take 1 as the map due to low statistics.

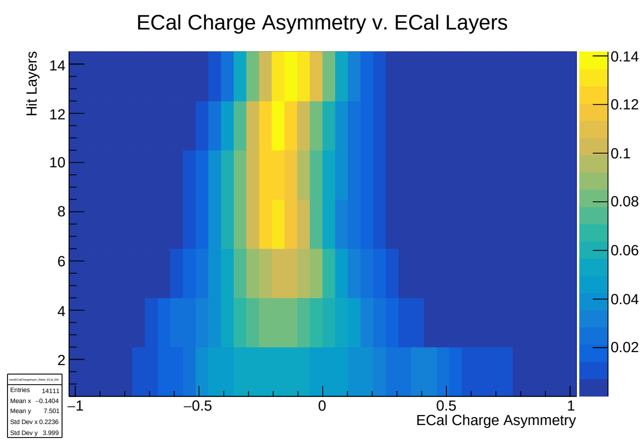

Figure A.6: Likelihood distribution of
trackECalChargeRMS_waterinconfig_WatertargetContained_EM

A.6 trackECalChargeAsym

ECalChargeAsymmetry study the charge aysmmetry among all layers in Central ECal. It is calculated in such a way: $\frac{\sum C_l(z_l - \bar{z})}{\sum C_l(0.5z_{max} - 0.5z_{min})}$, where C_l is the total charges in layer l, z_l is the position of the center of layer l, $\bar{z}$ is the average value of positions of all layers in Central ECal that the object passes and $z_{max} - z_{min}$ gives range the objects passes in Central ECal. See figure A.7 for a likelihood distribution example and A.16, A.17 and A.18 for the data-MC comparison.

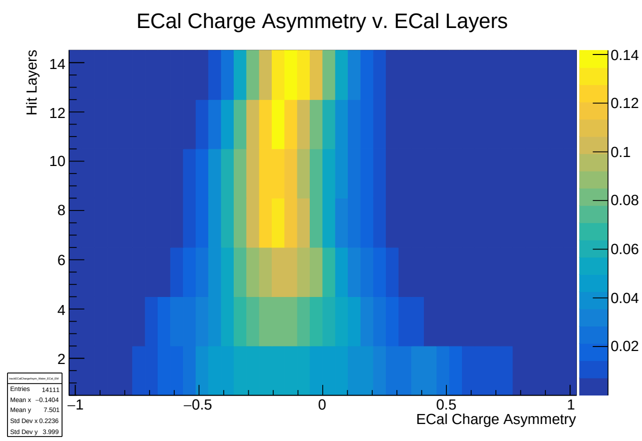

Figure A.7: Likelihood distribution of trackECalChargeAsym_waterinconfig_WatertargetContained_EM

A.7 trackLayerChargeVAngle

Unlike variables listed above, this variable id 3D. It consists of charge fraction in each P0Dule over total charges VS P0Dule from the End VS Angle. In p0dRecon, this variable is calculated and use to calculate pid likelihood only when the particle is geenerated in WT, which is contradicted to the selections of sand muon sample. Thus, this variable cannot be studied using sand muon sample. Take 1 as the map for now.

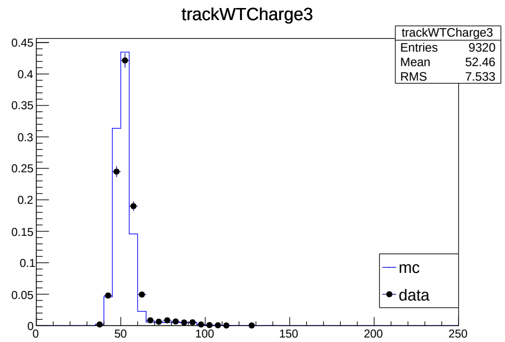

(a) Distribution of Median WT Charge of when track length is in 4th bin

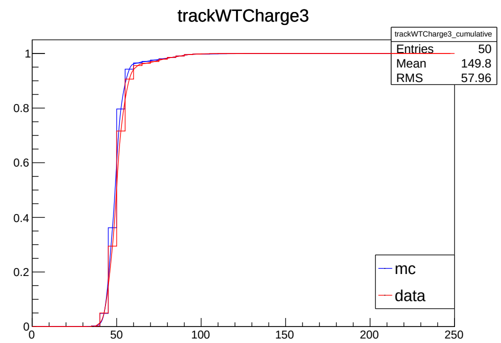

(b) Cumulative distribution of Median WT Charge of when track length is in 3th bin

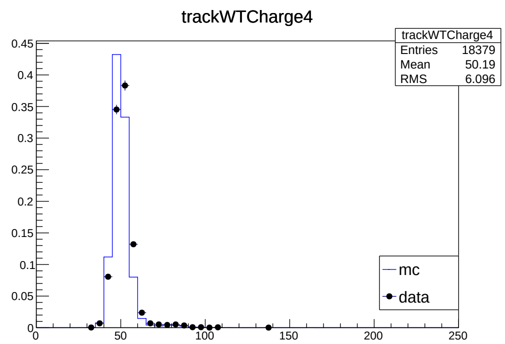

(c) Distribution of Median WT Charge of when track length is in 5th bin

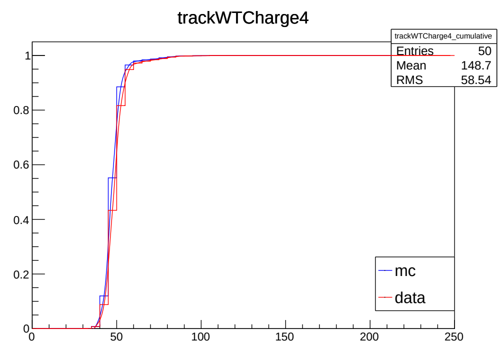

(d) Cumulative distribution of Median WT Charge of when track length is in 5th bin

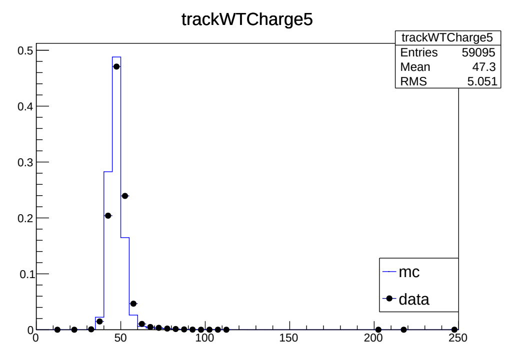

(e) Distribution of Median WT Charge of when track length is in 6th bin

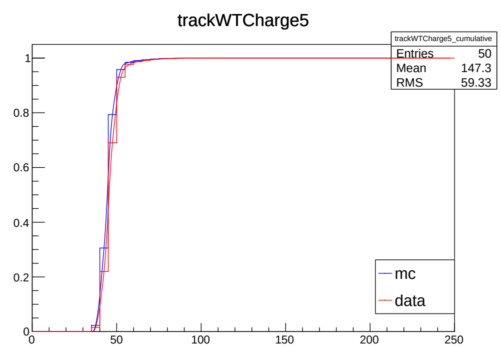

(f) Cumulative distribution of Median WT Charge of when track length is in 6th bin

Figure A.8: Data-MC comparision of Median WT Charge using sand muon control sample (waterin+FHC)

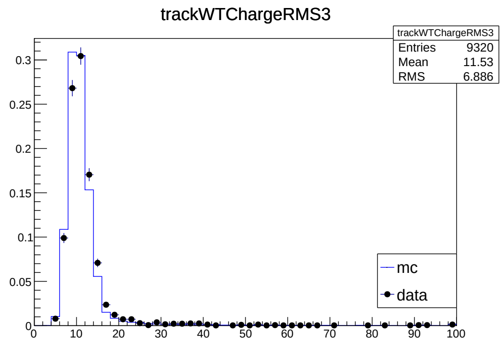

(a) Distribution of Median WT Charge RMS of when track length is in 4th bin

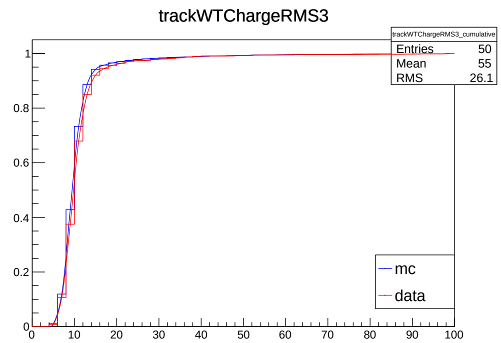

(b) Cumulative distribution of Median WT Charge RMS of when track length is in 3th bin

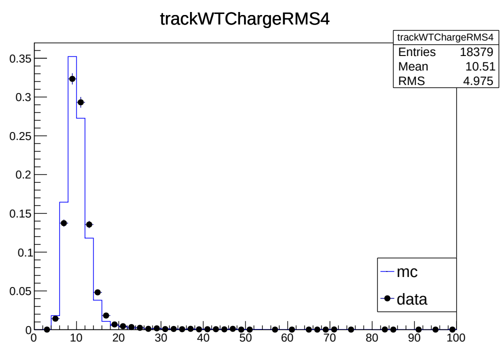

(c) Distribution of Median WT Charge RMS of when track length is in 5th bin

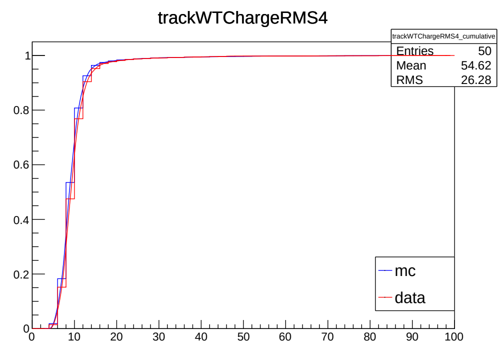

(d) Cumulative distribution of Median WT Charge RMS of when track length is in 5th bin

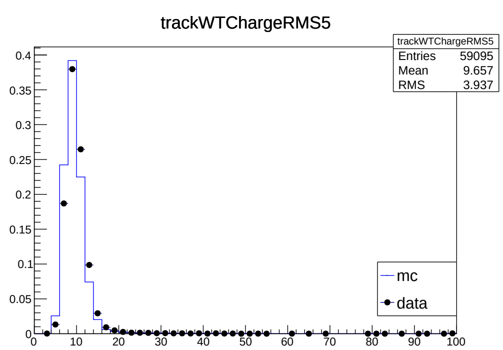

(e) Distribution of Median WT Charge RMS of when track length is in 6th bin

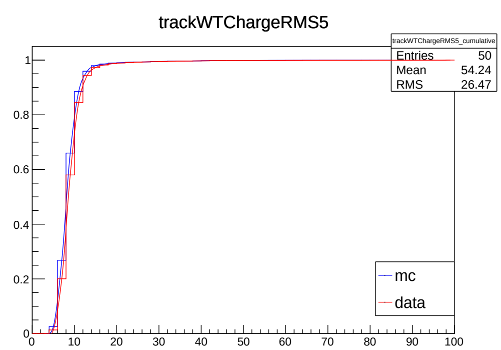

(f) Cumulative distribution of Median WT Charge RMS of when track length is in 6th bin

Figure A.9: Data-MC comparision of Median WT Charge RMS using sand muon control sample (waterin+FHC)

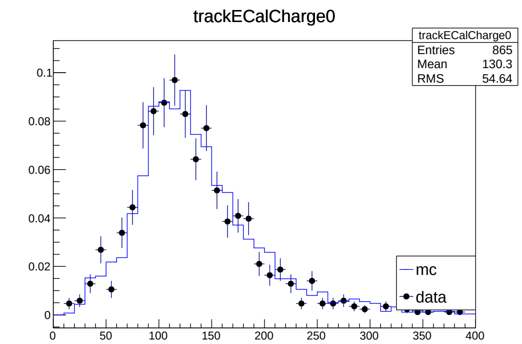

(a) Distribution of trackECalCharge when passing scintillator layers 0 and 1 in Central ECal

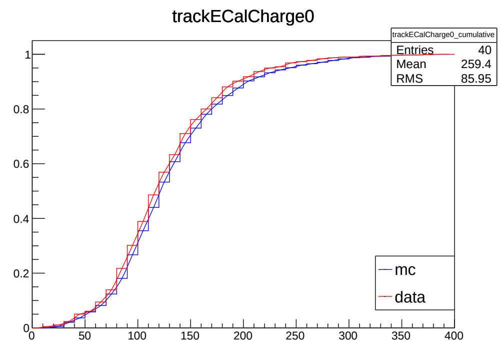

(b) Cumulative distribution of trackECalCharge when passing scintillator layers 0 and 1 in Central ECal

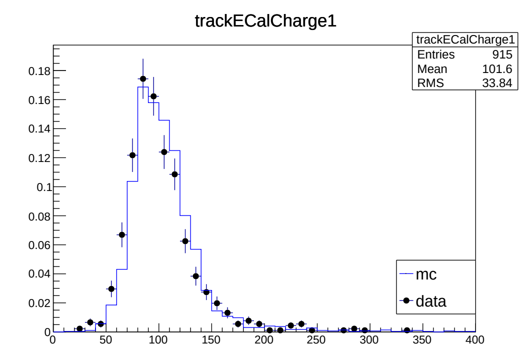

(c) Distribution of trackECalCharge when passing scintillator layers 2 and 3 in Central ECal

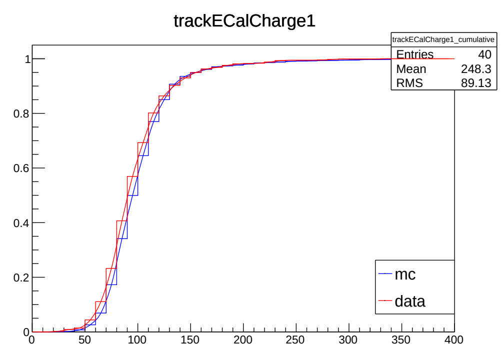

(d) Cumulative distribution of trackECalCharge when passing scintillator layers 2 and 3 in Central ECal

Figure A.10: Data-MC comparisons of Median ECal Charge using sand muon control sample (first half) (waterin+FHC). Part I

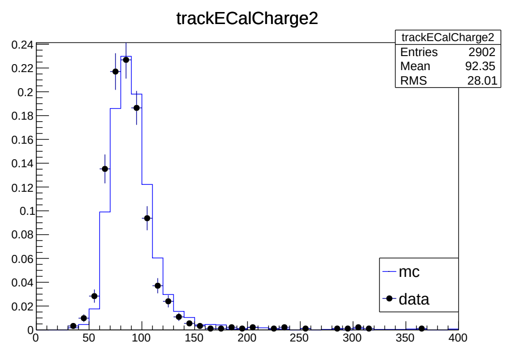

(a) Distribution of trackECalCharge when passing scintillator layers 4 and 5 in Central ECal

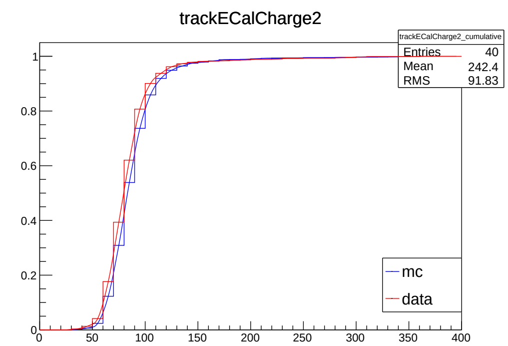

(b) Cumulative distribution of trackECalCharge when passing scintillator layers 4 and 5 in Central ECal

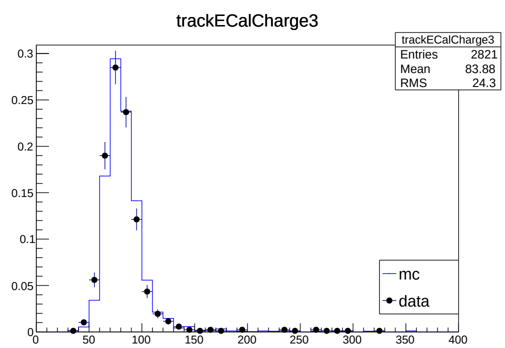

(c) Distribution of trackECalCharge when passing scintillator layers 6 and 7 in Central ECal

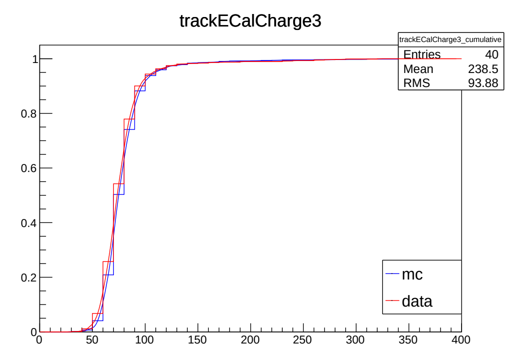

(d) Cumulative distribution of trackECalCharge when passing scintillator layers 6 and 7 in Central ECal

Figure A.11: Data-MC comparisons of Median ECal Charge using sand muon control sample (first half) (waterin+FHC). Part II

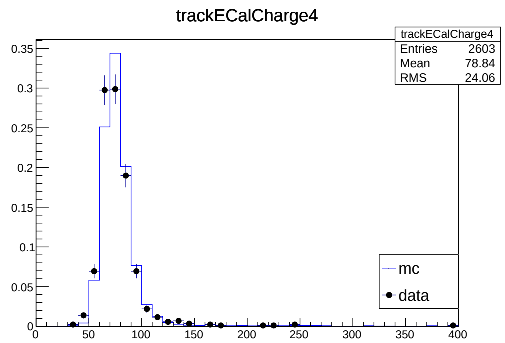

(a) Distribution of trackECalCharge when passing scintillator layers 8 and 9 in Central ECal

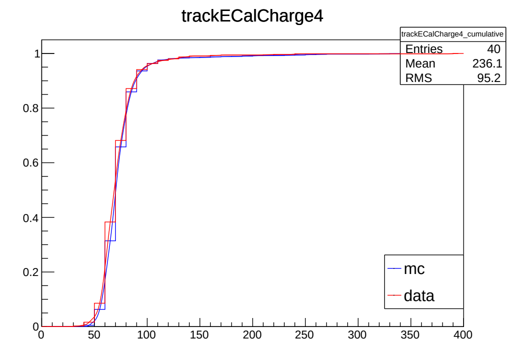

(b) Cumulative distribution of trackECalCharge when passing scintillator layers8 and9 in Central ECal

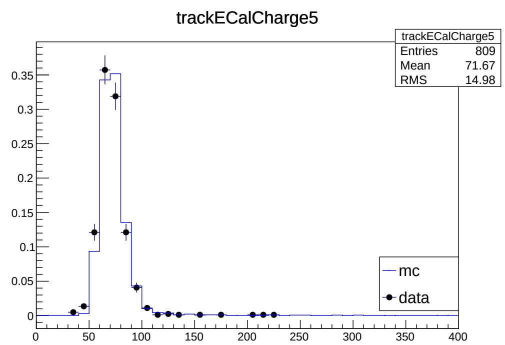

(c) Distribution of trackECalCharge when passing scintillator layers 10 and 11 in Central ECal

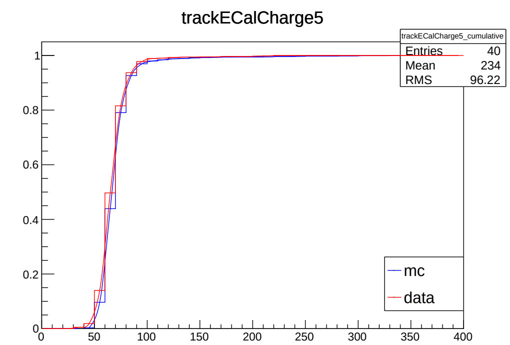

(d) Cumulative distribution of trackECalCharge when passing scintillator layers 10 and 11 in Central ECal

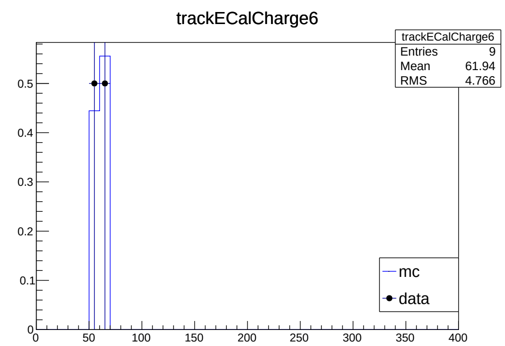

(e) Distribution of trackECalCharge when passing scintillator layers 12 and 13 in Central ECal

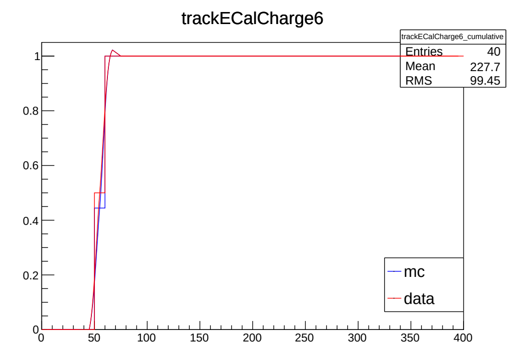

(f) Cumulative distribution of trackECalCharge when passing scintillator layers 12 and 13 in Central ECal

Figure A.12: Data-MC comparision of Median ECal Charge using sand muon control sample(second half) (waterin+FHC)

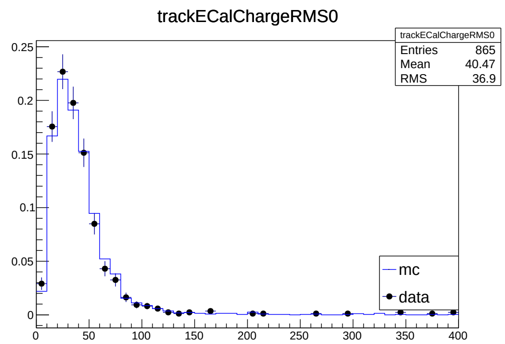

(a) Distribution of trackECalCharge RMS passing scintillator layers 0 and 1 in Central ECal

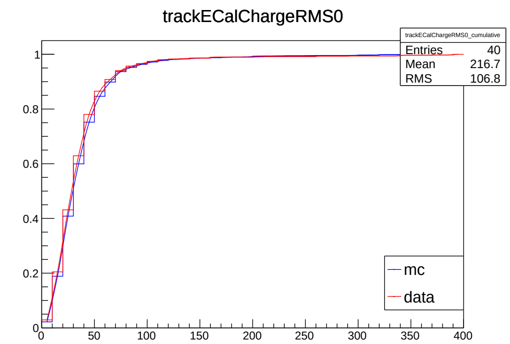

(b) Cumulative distribution of trackECalCharge RMS passing scintillator layers 0 and 1 in Central ECal

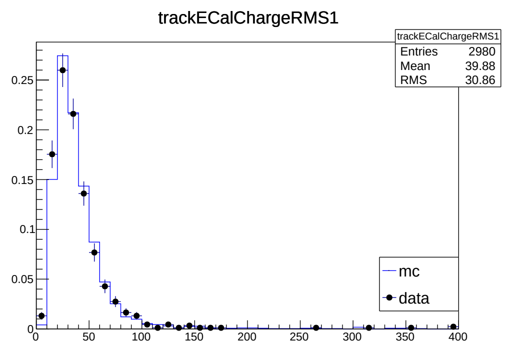

(c) Distribution of trackECalCharge RMS passing scintillator layers 2 and 3 in Central ECal

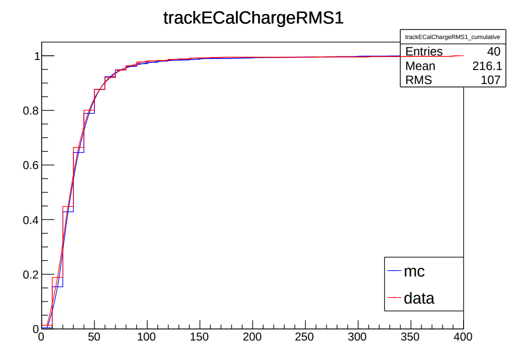

(d) Cumulative distribution of trackECalCharge RMS passing scintillator layers 2 and 3 in Central ECal

Figure A.13: Data-MC comparision of Median ECal Charge RMS using sand muon control sample (first half) (waterin+FHC). Part I.

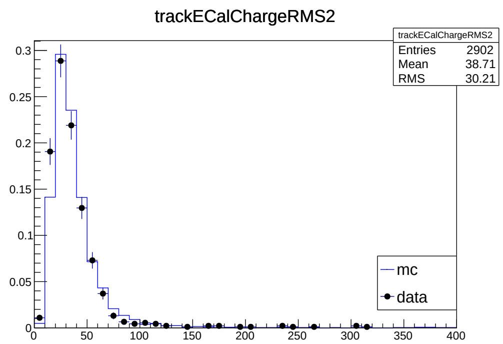

(a) Distribution of trackECalCharge RMS passing scintillator layers 4 and 5 in Central ECal

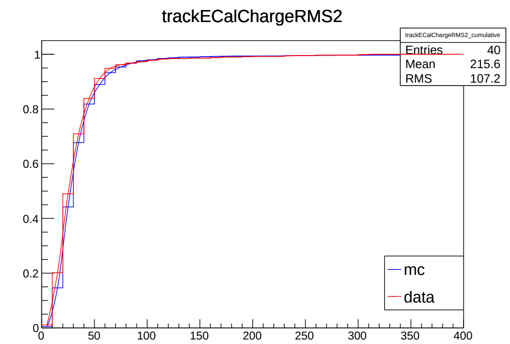

(b) Cumulative distribution of trackECalCharge RMS passing scintillator layers 4 and 5 in Central ECal

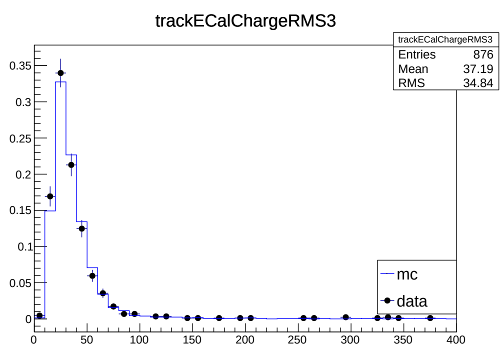

(c) Distribution of trackECalCharge RMS passing scintillator layers 6 and 7 in Central ECal

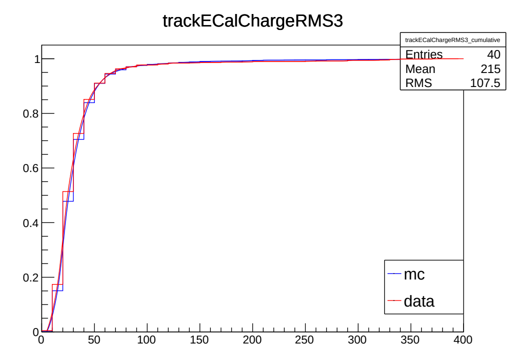

(d) Cumulative distribution of trackECalCharge RMS passing scintillator layers 6 and 7 in Central ECal

Figure A.14: Data-MC comparision of Median ECal Charge RMS using sand muon control sample (first half) (waterin+FHC). Part II.

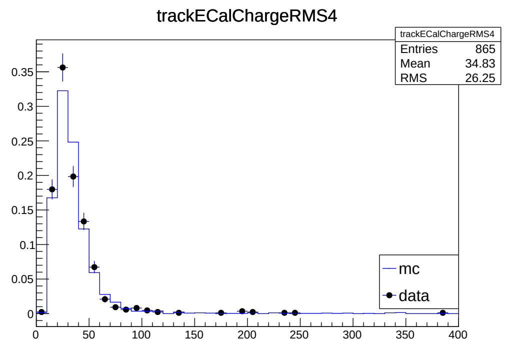

(a) Distribution of trackECalCharge RMS passing scintillator layers 8 and 9 in Central ECal

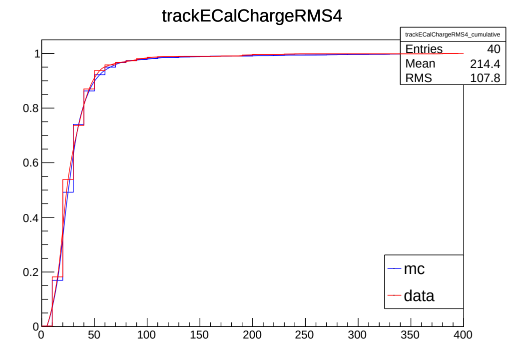

(b) Cumulative distribution of trackECalCharge RMS in scintillator layer8 and9 in Central ECal

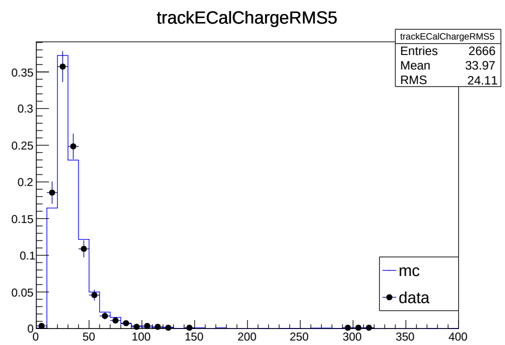

(c) Distribution of trackECalCharge RMS passing scintillator layers 10 and 11 in Central ECal

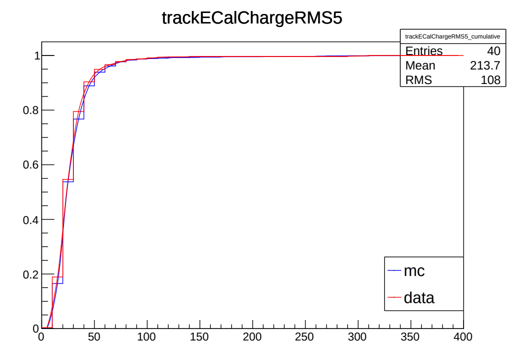

(d) Cumulative distribution of trackECalCharge RMS passing scintillator layers 10 and 11 in Central ECal

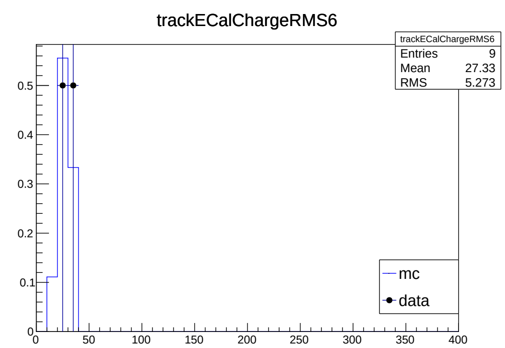

(e) Distribution of trackECalCharge RMS passing scintillator layers 12 and 13 in Central ECal

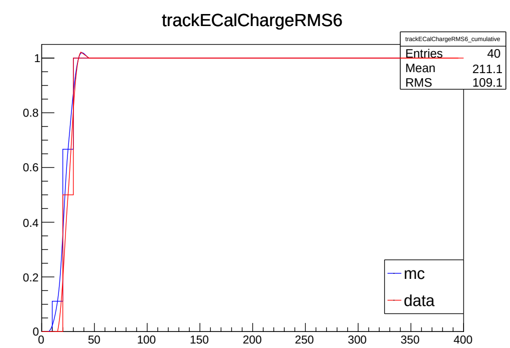

(f) Cumulative distribution of trackECalCharge RMS passing scintillator layers 12 and 13 in Central ECal

Figure A.15: Data-MC comparision of Median ECal Charge RMS using sand muon control sample(second half) (waterin+FHC)

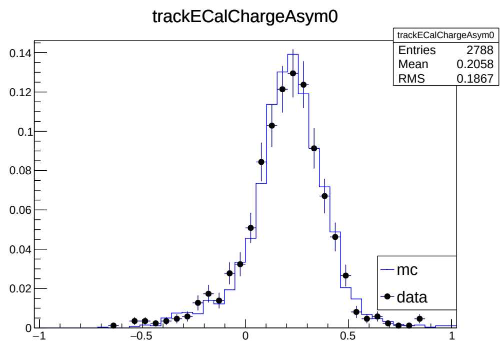

(a) Distribution of trackECalCharge Asym when passing scintillator layers 0 and 1 in Central ECal

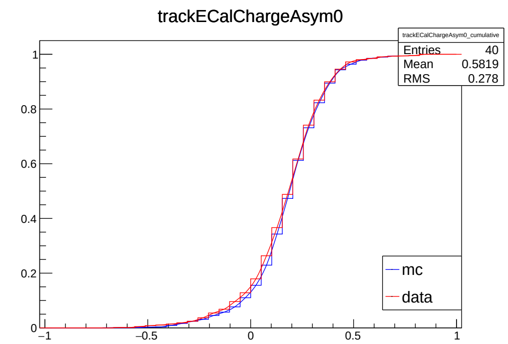

(b) Cumulative distribution of trackE-CalCharge Asym when passing scintillator layers 0 and 1 in Central ECal

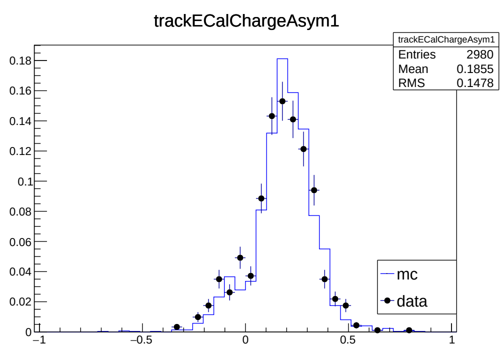

(c) Distribution of trackECalCharge Asym when passing scintillator layers 2 and 3 in Central ECal

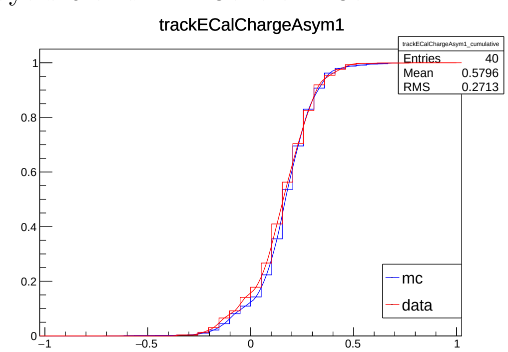

(d) Cumulative distribution of trackE-CalCharge Asym when passing scintillator layers 2 and 3 in Central ECal

Figure A.16: Data-MC comparision of Median ECal Charge Asym using sand muon control sample (first half) (waterin+FHC) Part I.

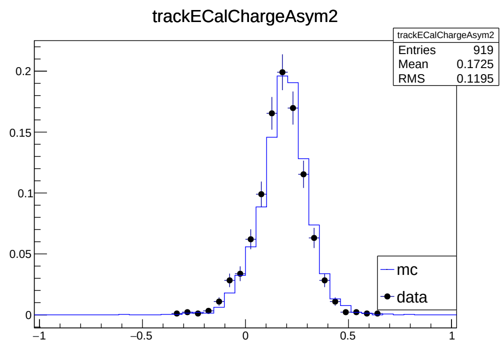

(a) Distribution of trackECalCharge Asym when passing scintillator layers 4 and 5 in Central ECal

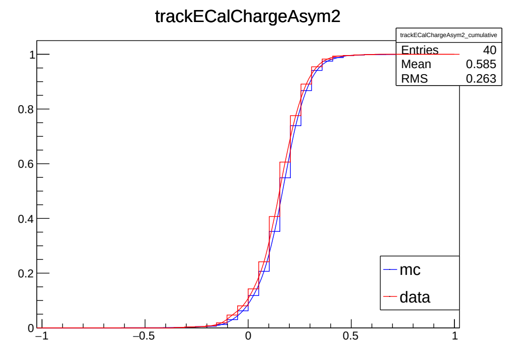

(b) Cumulative distribution of trackECalCharge Asym when passing scintillator layers 4 and 5 in Central ECal

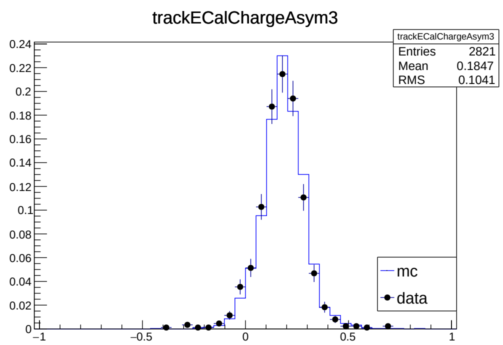

(c) Distribution of trackECalCharge Asym when passing scintillator layers 6 and 7 in Central ECal

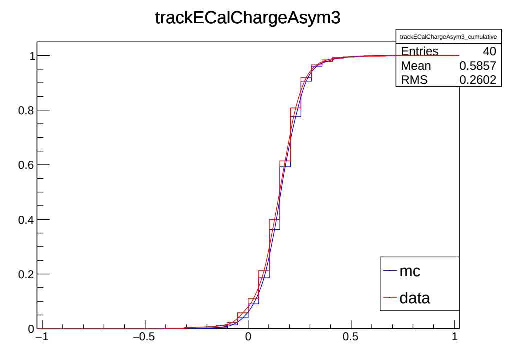

(d) Cumulative distribution of trackECalCharge Asym when passing scintillator layers 6 and 7 in Central ECal

Figure A.17: Data-MC comparision of Median ECal Charge Asym using sand muon control sample (first half) (waterin+FHC) Part II.

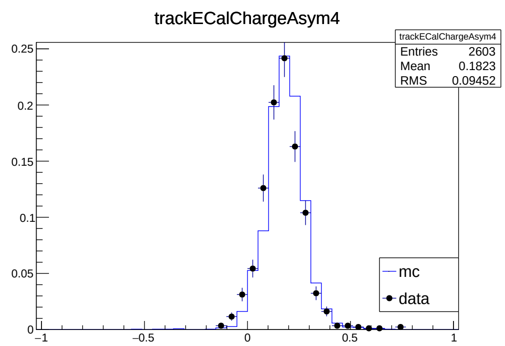

(a) Distribution of trackECalCharge Asym when passing scintillator layers 8 and 9 in Central ECal

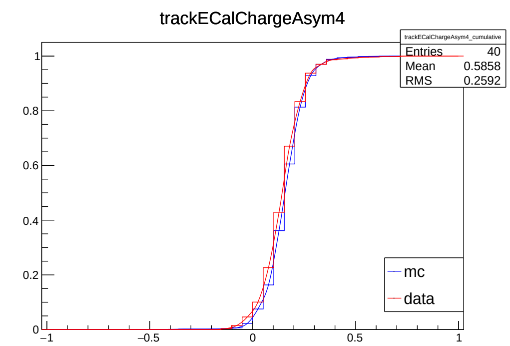

(b) Cumulative distribution of trackECalCharge RMS in scintillator layer8 and9 in Central ECal

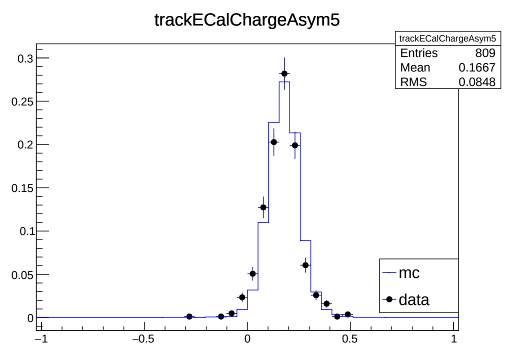

(c) Distribution of trackECalCharge Asym when passing scintillator layers 10 and 11 in Central ECal

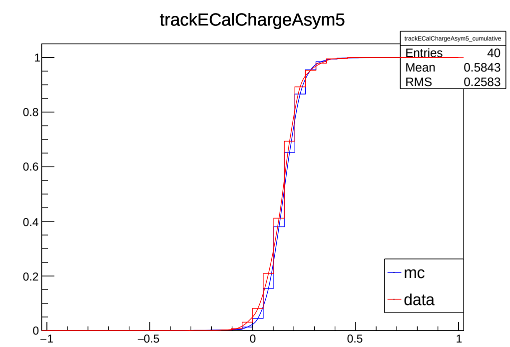

(d) Cumulative distribution of trackECalCharge Asym when passing scintillator layers 10 and 11 in Central ECal

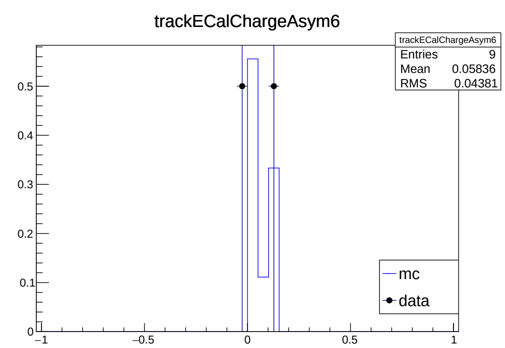

(e) Distribution of trackECalCharge Asym when passing scintillator layers 12 and 13 in Central ECal

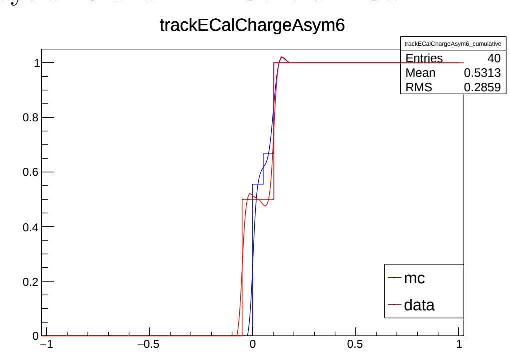

(f) Cumulative distribution of trackECalCharge Asym when passing scintillator layers 12 and 13 in Central ECal

Figure A.18: Data-MC comparision of Median ECal Charge Asym using sand muon control sample(second half) (waterin+FHC)

Bibliography

[1] W. Pauli. Letter to the T¨ubingen conference. http://www.library.ethz.ch/en/ms/Virtuelle-Ausstellungen/Wolfgang-Pauli-und-die-moderne-Physik, 1930.

[2] E. Fermi. Versuch einer theorie der -strahlen: I. *Zeitschrift fr Physik*, 88, 1934.

[3] F. Reines F. B. Harrison H. W. Kruse C. L. Cowan, Jr. and A. D. McGuire. Detection of the free neutrino: A confirmation. *Science*, 124, 1956.

[4] The Reines-Cowan Experiments, Detecting the Poltergeist. https://permalink.lanl.gov/object/tr?what=info:lanl-repo/lareport/LA-UR-97-2534-02.

[5] Peter W Higgs. Broken symmetries and the masses of gauge bosons. *Physical Review Letters*, 13(16):508, 1964.

[6] François Englert and Robert Brout. Broken symmetry and the mass of gauge vector mesons. *Physical Review Letters*, 13(9):321, 1964.

[7] Gerald S Guralnik, Carl R Hagen, and Thomas WB Kibble. Global conservation laws and massless particles. *Physical Review Letters*, 13(20): 585, 1964.

[8] Standard model. https://en.wikipedia.org/wiki/Standard$_{M}odel$.

[9] Mass and Width of the W Boson. https://pdg.lbl.gov/2020/reviews/rpp2020-rev-w-mass.pdf, 2020.

[10] Z Mass. https://pdg.lbl.gov/2020/listings/rpp2020-list-z-boson.pdf, 2020.

[11] Serguei Chatrchyan, Vardan Khachatryan, Albert M Sirunyan, Armen Tumasyan, Wolfgang Adam, Ernest Aguilo, Thomas Bergauer, M Dragicevic, J Erö, C Fabjan, et al. Observation of a new boson at a mass of 125 gev with the cms experiment at the lhc. *Physics Letters B*, 716(1): 30–61, 2012.

[12] Georges Aad, Tatevik Abajyan, B Abbott, J Abdallah, S Abdel Khalek, Ahmed Ali Abdelalim, R Aben, B Abi, M Abolins, OS AbouZeid, et al. Observation of a new particle in the search for the standard model higgs boson with the atlas detector at the lhc. *Physics Letters B*, 716(1):1–29, 2012.

[13] Bruno Pontecorvo. Neutrino experiments and the problem of conservation of leptonic charge. *Sov. Phys. JETP*, 26(984-988):165, 1968.

[14] Yoshiyuki Fukuda, T Hayakawa, E Ichihara, K Inoue, K Ishihara, Hirokazu Ishino, Y Itow, T Kajita, J Kameda, S Kasuga, et al. Evidence for oscillation of atmospheric neutrinos. *Physical Review Letters*, 81(8): 1562, 1998.

[15] Q Retal Ahmad, RC Allen, TC Andersen, JD Anglin, JC Barton, EW Beier, M Bercovitch, J Bigu, SD Biller, RA Black, et al. Direct evidence for neutrino flavor transformation from neutral-current interactions in the sudbury neutrino observatory. *Physical review letters*, 89(1): 011301, 2002.

[16] Ziro Maki, Masami Nakagawa, and Shoichi Sakata. Remarks on the unified model of elementary particles. *Progress of Theoretical Physics*, 28(5): 870–880, 1962.

[17] SP Mikheev and A Yu Smirnov. Resonance enhancement of oscillations in matter and solar neutrino spectroscopy. *Soviet Journal of Nuclear Physics*, 42(6):913–917, 1985.

[18] Lincoln Wolfenstein. Neutrino oscillations in matter. *Physical Review D*, 17(9):2369, 1978.

[19] Carlo Giunti and Chung W Kim. *Fundamentals of neutrino physics and astrophysics*. Oxford university press, 2007.

[20] Joseph A Formaggio and GP Zeller. From ev to eev: Neutrino cross sections across energy scales. *Reviews of Modern Physics*, 84(3):1307, 2012.

[21] SK Singh and E Oset. Quasielastic neutrino (antineutrino) reactions in nuclei and the axial-vector form factor of the nucleon. *Nuclear Physics A*, 542(4):587–615, 1992.

[22] Kenzo Nakamura. Review of particle physics. *Journal of Physics G: Nuclear and Particle Physics*, 37(7 A), 2010.

[23] Veronique Bernard, Latifa Elouadrhiri, and Ulf-G Meißner. Axial structure of the nucleon. *Journal of Physics G: Nuclear and Particle Physics*, 28(1):R1, 2001.

[24] T Leitner, O Buss, L Alvarez-Ruso, and U Mosel. Electron-and neutrino-nucleus scattering from the quasielastic to the resonance region. *Physical Review C*, 79(3):034601, 2009.

[25] C Maieron, MC Martinez, JA Caballero, and JM Udias. Nuclear model effects in charged-current neutrino-nucleus quasielastic scattering. *Physical Review C*, 68(4):048501, 2003.

[26] Andrea Meucci, Carlotta Giusti, and Franco Davide Pacati. Relativistic green's function approach to charged-current neutrino–nucleus quasielastic scattering. *Nuclear Physics A*, 739(3-4):277–290, 2004.

[27] Luke Pickering. Examining nuclear effects in neutrino interactions with transverse kinematic imbalance. In *Proceedings of the 10th International Workshop on Neutrino-Nucleus Interactions in Few-GeV Region (NuInt15)*, page 010032, 2016.

[28] Neutrino Cross Sections and Interactions. https://npc.fnal.gov/wp-content/uploads/2021/07/210624$_nuInteractionsCrossSections.pdf$, .

[29] SK Singh and E Oset. Inclusive quasielastic neutrino reactions in c 12 and o 16 at intermediate energies. *Physical Review C*, 48(3):1246, 1993.

[30] CW De Jager, H De Vries, and C De Vries. Nuclear charge-and magnetization-density-distribution parameters from elastic electron scattering. *Atomic data and nuclear data tables*, 14(5-6):479–508, 1974.

[31] Tomasz Golan, Jan T Sobczyk, and Krzysztof M Graczyk. *Modeling nuclear effects in NuWro Monte Carlo neutrino event generator*. PhD thesis, PhD thesis, University of Wroclaw, 2014.

[32] PKA de Witt Huberts. Proton spectral functions and momentum distributions in nuclei from high-resolution (e, e'p) experiments. *Journal of Physics G: Nuclear and Particle Physics*, 16(4):507, 1990.

[33] D Rohe, CS Armstrong, R Asaturyan, OK Baker, S Bueltmann, C Carasco, D Day, R Ent, HC Fenker, K Garrow, et al. Correlated strength in the nuclear spectral function. *Physical review letters*, 93(18):182501, 2004.

[34] Y. Hayato, S. Cao and V. Nguyen. The NEUT Neutrino Monte Carlo Generator: Physics and User Manual, T2K-TN-351. 2018.

[35] Juan Nieves, I Ruiz Simo, and MJ Vicente Vacas. Inclusive charged-current neutrino-nucleus reactions. *Physical Review C*, 83(4):045501, 2011.

[36] Marco Martini, Magda Ericson, Guy Chanfray, and Jacques Marteau. Unified approach for nucleon knock-out and coherent and incoherent pion production in neutrino interactions with nuclei. *Physical review C*, 80(6):065501, 2009.

[37] S Boyd, S Dytman, E Hernandez, J Sobczyk, and R Tacik. Comparison of models of neutrino-nucleus interactions. In *AIP Conference Proceedings*, volume 1189, pages 60–73. American Institute of Physics, 2009.

[38] Steven Dytman. Neutrino event generators. In *AIP Conference Proceedings*, volume 896, pages 178–184. American Institute of Physics, 2007.

[39] Dieter Rein and Lalit M Sehgal. Neutrino-excitation of baryon resonances and single pion production. *Annals of Physics*, 133(1):79–153, 1981.

[40] Dieter Rein and Lalit M Sehgal. Coherent $\pi 0$ production in neutrino reactions. *Nuclear Physics B*, 223(1):29–44, 1983.

[41] E Reya, A Vogt, et al. Dynamical parton distributions revisited. *arXiv preprint hep-ph/9806404*, 1998.

[42] A Bodek and UK Yang. Modeling neutrino and electron scattering inelastic cross sections. *arXiv preprint hep-ex/0308007*, 2003.

[43] Gargamelle Collaboration. Total cross-sections for electron-neutrino and anti-electron-neutrino interactions and search for neutrino oscillations and decay. *Nuclear Physics B*, 133:205–219, 1978.

[44] K Abe, J Adam, H Aihara, T Akiri, Constantinos Andreopoulos, S Aoki, A Ariga, S Assylbekov, D Autiero, M Barbi, et al. Measurement of the inclusive electron neutrino charged current cross section on carbon with the t2k near detector. *Physical review letters*, 113(24):241803, 2014.

[45] J Wolcott, L Aliaga, O Altinok, L Bellantoni, A Bercellie, M Betancourt, A Bodek, A Bravar, H Budd, T Cai, et al. Measurement of electron neutrino

quasielastic and quasielasticlike scattering on hydrocarbon at¡ e ν¿= 3.6 gev. *Physical review letters*, 116(8):081802, 2016.

[46] K Abe, N Akhlaq, R Akutsu, A Ali, C Alt, C Andreopoulos, L Anthony, M Antonova, S Aoki, A Ariga, et al. Measurement of the charged-current electron (anti-) neutrino inclusive cross-sections at the t2k off-axis near detector nd280. *Journal of High Energy Physics*, 2020(10):1–43, 2020.

[47] Melanie Day and Kevin S McFarland. Differences in quasielastic cross sections of muon and electron neutrinos. *Physical Review D*, 86(5):053003, 2012.

[48] The T2K Collaboration. The T2K experiment. *Nuclear Instruments and Methods in Physics Research Section A: Accelerators, Spectrometers, Detectors and Associated Equipment*, 659(1):106–135, 2011.

[49] The T2K Collaboration. Constraint on the matter–antimatter symmetry-violating phase in neutrino oscillations. *Nature*, 580:339–344, 2020.

[50] Thomas Campbell. *MEASUREMENT OF THE $\bar{\nu}_\mu$ CC-0π DOUBLE DIFFERENTIAL CROSS SECTION ON WATER USING THE π^0-DETECTOR AT T2K*. PhD thesis, 2018.

[51] Kou Abe, N Abgrall, H Aihara, T Akiri, JB Albert, C Andreopoulos, S Aoki, A Ariga, T Ariga, S Assylbekov, et al. T2k neutrino flux prediction. *Physical Review D*, 87(1):012001, 2013.

[52] Giuseppe Battistoni, F Cerutti, A Fasso, A Ferrari, S Muraro, J Ranft, S Roesler, and PR Sala. The fluka code: Description and benchmarking. In *AIP Conference proceedings*, volume 896, pages 31–49. American Institute of Physics, 2007.

[53] FLUKA version 2008.3c. http://www.fluka.org/fluka.php, 2008.

[54] GEANT3, A detector description and simulation tool. Application Software Group, Computing and Networks Division, CERN, Geneva, 1993.

[55] M. Friend et al. 1 Flux Prediction and Uncertainty with NA61/SHINE 2 2010 Replica Target Measurements. https://t2k.org/docs/technotes/401/v1.0, 2021.

[56] Kirsty Elizabeth Duffy. *Measurement of the neutrino oscillation parameters $\sin^2\theta_{23}$, Δm^2_{32}, $\sin^2\theta_{13}$ and δ_{CP} in neutrino and antineutrino oscillation at T2K*. PhD thesis, 2016.

[57] Georges Charpak, J Derre, Y Giomataris, and Ph Rebourgeard. Micromegas, a multipurpose gaseous detector. *Nuclear Instruments and Methods in Physics Research Section A: Accelerators, Spectrometers, Detectors and Associated Equipment*, 478(1-2):26–36, 2002.

[58] Nicolas Abgrall, B Andrieu, P Baron, P Bene, V Berardi, J Beucher, P Birney, F Blaszczyk, Alain Blondel, C Bojechko, et al. Time projection chambers for the t2k near detectors. *Nuclear Instruments and Methods in Physics Research Section A: Accelerators, Spectrometers, Detectors and Associated Equipment*, 637(1):25–46, 2011.

[59] Assylbekov, S and Barr, G and Berger, BE and Berns, H and Beznosko, D and Bodek, A and Bradford, R and Buchanan, N and Budd, H and Caffari, Y and others. The t2k nd280 off-axis π^0 detector. *Nuclear Instruments and Methods in Physics Research Section A: Accelerators, Spectrometers, Detectors and Associated Equipment*, 686:48–63, 2012.

[60] Passage of Particles Through Matter. https://pdg.lbl.gov/2019/reviews/rpp2018-rev-passage-particles-matter.pdf, 2019.

[61] Jay Hyun Jo. Measurement of CCNuE Interaction Rate on Water using the P0D. T2K-TN-240.

[62] Karin Gilje. Geometry and Mass of the π^0 Detector in the ND280 Basket. T2K-TN-073.

[63] Melanie Day, Steve Manly, Kevin McFarland, Philip Rodrigues, Ian Taylor. Crosscheck of high-energy ν_e event rate with the P0D, T2K-TN-053.

[64] Karin Gilje, Jeanine Adam, Clark McGrew and Helen O'Keeffe. Measurement of the NC1π^0 Rate on Water in the P0D, T2K-TN-144.

[65] Zoya Vallari. Measurement of NC1pi0 on water in P0D, T2K-TN-364.

[66] Tomislav Vladisavljevic, etc. Flux Prediction and Uncertainty with NA61/SHINE 2009 Replica-Target Data. T2K-TN-354.

[67] NIWG model and uncertainties for 2019-2020 oscillation analysis, T2K-TN-344.

[68] T2K-Reweight, Branch OA2021Development. https://github.com/t2k-software/T2KReWeight/tree/OA2021Development.

[69] NIWG-Reweight, Branch OA2021Tidy. https://github.com/t2k-software/NIWGReWeight/tree/OA2021Tidy.

[70] NEUT, Branch PreOA2021DevelopmentMerge. https://github.com/neut-devel/neut/tree/PreOA2021DevelopmentMerge, .

[71] Kou Abe, J Adam, H Aihara, C Andreopoulos, S Aoki, A Ariga, S Assylbekov, D Autiero, M Barbi, GJ Barker, et al. Measurement of the electron neutrino charged-current interaction rate on water with the t2k nd280 π 0 detector. *Physical Review D*, 91(11):112010, 2015.

[72] Nicholas Metropolis, Arianna W Rosenbluth, Marshall N Rosenbluth, Augusta H Teller, and Edward Teller. Equation of state calculations by fast computing machines. *The journal of chemical physics*, 21(6):1087–1092, 1953.

[73] W Keith Hastings. Monte carlo sampling methods using markov chains and their applications. 1970.

[74] Walter R Gilks, Sylvia Richardson, and David Spiegelhalter. *Markov chain Monte Carlo in practice*. CRC press, 1995.

[75] Kun Il Park and M Park. *Fundamentals of probability and stochastic processes with applications to communications*. Springer, 2018.

[76] Andrew Gelman, John B Carlin, Hal S Stern, and Donald B Rubin. *Bayesian data analysis*. Chapman and Hall/CRC, 1995.

[77] Andrew Gelman, Xiao-Li Meng, and Hal Stern. Posterior predictive assessment of model fitness via realized discrepancies. *Statistica sinica*, pages 733–760, 1996.

[78] Andrew Gelman. Two simple examples for understanding posterior p-values whose distributions are far from uniform. *Electronic Journal of Statistics*, 7: 2595–2602, 2013.

[79] Glen Cowan. *Statistical data analysis*. Oxford university press, 1998.

[80] A. Ajm, S. Bolognesi, V.Berardi, M.G. Catanesi, G. De Rosa, A. Longhin, L. Magaletti, E. Radicioni and C. Riccio. Measurement of ν_μ and $\bar{\nu}_\mu$ CC-0π cross-section on carbon.

List of Figures

List of Tables